Under-Dense Laser-Plasma Interactions in Relativistic Optical Vortices

by

Andrew M Longman

A thesis submitted in partial fulfillment of the requirements for the degree of

Doctor of Philosophy

in

Photonics and Plasmas

Department of Electrical and Computer Engineering
University of Alberta

Abstract

In the ever-evolving field of high-intensity laser interactions with matter, many approaches have been taken to control and enhance laser-plasma interactions. An alternative, and potentially beneficial approach to further controlling laser-plasma interactions comes from spatial structuring of the laser phase.

In this thesis, we explore high intensity ($> 1 \times 10^{18} W cm^{-2}$) structured light that carries orbital angular momentum (OAM) via a helical wavefront, also known as an optical vortex (OV). These beams have the unique property of carrying unprecedented amounts of angular momentum, even when linearly polarized. Coupling of this OAM to a plasma is of great interest for the generation of strong axial magnetic fields, particle guiding, enhanced radiation, and gaining an additional control parameter in the laser plasma interactions.

We introduce the concept of an off-axis spiral phase mirror for the mode conversion of ultra-fast high-intensity laser systems, and demonstrate the highest intensity OAM optical vortices to date. Diffraction models of the high-intensity OV's are developed analytically and then approximated using Laguerre-Gaussian basis functions for both symmetric and asymmetric modes. The interaction of high-intensity OV's with single

electrons and plasma is explored analytically, numerically and experimentally.

We show that linearly polarized OAM coupling to single electrons and plasma occurs from nonlinear mechanisms, and can be used to accelerate particles and enhance the laser-plasma interactions. We explore both numerically with particle in cell (PIC) simulations and experimentally new modes of relativistic self-focussing, wakefield acceleration, betatron radiation, and magnetic field generation in the presence of an OAM pulse. We find that angular momentum is indeed coupled to the electrons and that the critical energy of the emitted betatron spectrum is increased with an increase in beam OAM. Additionally, we demonstrate in realistic full scale 3D PIC simulations kilo-Tesla magnetic field generation from the inverse Faraday effect and characterize the spatial extent and temporal duration of these fields.

Preface

This thesis is an original work by Andrew Longman. Some of the work in this thesis was accomplished in collaboration with researchers from the University of Alberta, and some with researchers from other universities and institutes. The experiments described in Chapter's 5 and 6 were carried out at the Centros Laseres Pulsados Ultraintensos (CLPU) facility. All of the experiments were performed under the guidance and supervision of Professor Robert Fedosejevs. The introduction in chapter 1, the diffraction background in chapter 2, the theory in chapter's 3 and 4, the experimental methodologies in chapter 6, the simulation work in chapter 7, and the conclusion in chapter 8 was written by myself and edited by Prof. Fedosejevs.

Chapter 2 has been published in part as: A. Longman and R. Fedosejevs, "*Mode conversion efficiency to Laguerre-Gaussian OAM modes using spiral phase optics*", Opt. Express **25**(15), 17382-17932, (2017), and A. Longman and R. Fedosejevs, "*Optimal Laguerre-Gaussian modes for high intensity optical vortices*", J. Opt. Soc. Am. A **37**(5), 841-848, (2020). The manuscripts were written by A. Longman and edited by R. Fedosejevs.

Chapter 5 has been published in part as: A. Longman, C. Salgado, G. Zeraouli, J. Apiñaniz, J. A. Pérez-Hernández, M. Khairy Eltahlawy, L. Volpe, and R. Fedosejevs, "*Off-axis spiral phase mirrors for generating high-intensity optical vortices*", Opt. Lett. **45**(8), 2187-2190, (2020). A. Longman and R. Fedosejevs were responsible for conceiving, designing, and manufacturing the off-axis spiral phase mirrors, and for measuring the optical vortices. C. Salgado, G. Zeraouli, J. Apiñaniz, J. A. Pérez-Hernández, and L. Volpe assisted with measuring the optical vortices at CLPU, while M. Khairy Eltahlawy assisted with the experimental generation of low intensity vortices at the University of Alberta. The manuscript was written by A. Longman, and edited by R. Fedosejevs.

Dedicated to the memory of Susan Janet Longman (Plattner)

March 11th 1965 - December 22nd 2011

While she could not be there in person, she was was with me every step of the way

Acknowledgements

This work would not have been possible without the support of my friends, family, and colleagues at the University of Alberta, and at the Centros Laseres Pulsados Ultraintensos in Spain.

I was first introduced to high-power ultrafast laser systems in my junior and senior years of my undergraduate degree by Prof. Frank Hegmann, in which he had seeded an eternal interest in optics and lasers. As I transitioned to graduate school, I moved from physics to electrical engineering and found a near perfect match for my ambitions under the supervision of Prof. Robert Fedosejevs. Through his supervision, I learned determination, perseverance, and I have been able to flourish as a researcher both in physics, and in engineering.

I am thankful for the colleagues at the University of Alberta including Prof. Jason Myatt, Henry Tiedje, Shaun Kerr, Chandra Curry, Zach Tchir, Mohammed Eltahlawy, Ali Kiaee, Blaine Armstrong, Kyle Mckee, and Laila Manzoor for their friendship, support, and frequent discussions. Additionally, I would like to thank the support staff in the machine shop and the nanofab, in particular, Herbert Dexel, Terry Kugler, Reiner Schwarz, Aaron Hyrciw, and Les Schowalter who were all involved in the developemnt of the off-axis spiral phase mirrors, and the many diagnostics developed.

I spent a great deal of time on experiment in the United States at Lawrence Livermore National Laboratory, and also at the CLPU in Salamanca, for which I am very grateful for these opportunities. In particular, I would like to thank Shaun, Chandra, Art Pak, and Tony Link for helping with hosting and accommodations at Livermore. Living in Spain has been a great opportunity, but would not have been possible without the support of staff and friends at the CLPU. In particular, I would like to thank Jon Apinaniz, Marine Huault, Carlos Salgado, Ghassan Zeraouli, Sophia Malko, Diego de Luis, Jose Antonio Hernandez-Perez, Luca Volpe, Giancarlo Gatti,

and Luis Roso. Additionally I would like to thank Prof. Wendell Hill, and Calvin He, for both aiding, and hosting me on experiments at CLPU.

I would like to thank my family and friends who have been through the PhD process with me. I would like to thank my long term room mates Duncan Scott, and Paul Senegas-Lowe for many stimulating games of Age of Empires, and the neighbourhood cats Henry and Lady Whiskers. My Kodiak Taekwondo family, and in particular Dwayne Holmwood, and Lalo Pardo. I would like to thank my parents in-law Art and Dominique who have been fantastic support for me, and who have been kind enough to host me for a few months while I finished writing the thesis. I would also like to thank Emil Bizon for stimulating conversations, and for sharing his engineering experiences with me. My auntie Barbara Macrae, and her husband David for hosting me in Montanchez, Spain on much needed weekends away from CLPU. I am also thankful to my Dad, and my brothers Robert and Max who provided a home away from home whenever I needed to get out of Edmonton and clear my head.

Above all, I am most grateful to my wife Claire. Without her, I would not have been able to finish, let alone get half way through the program. Accompanying me on the many trips to Salamanca, listening to me type and work in our bedroom until the early hours of the morning, listening to me explain my calculations so I can understand where I went wrong, her physical and emotional support, and keeping me in good health, I couldn't have done it without her.

I would finally like to acknowledge funding and super computer time from the Natural Sciences and Engineering Research Council of Canada (NSERC), Alberta Innovates Technology Futures (AITF), ComputeCanada, and the EPOCH development team at the University of Warwick.

Contents

List of Figures

List of Tables

List of Abbreviations

CCD	Charge Coupled Device
CLPU	Centros Laseres Pulsados Ultraintensos
CPA	Chirped Pulse Amplification
D	Deuterium
FFT	Fast Fourier Transform
FWHM	Full-Width-Half-Maximum
HG	Hermite-Gaussian
ICF	Inertial Confinement Fusion
IFE	Inverse Faraday Effect
KHI	Kelvin-Helmholtz Instability
LG	Laguerre-Gaussian
LLE	Laboratory for Laser Energetics
LLNL	Lawrence Livermore National Laboratory
LWFA	Laser Wakefield Acceleration
NIF	National Ignition Facility
OAM	Orbital Angular Momentum
OASPM	Off Axis Spiral Phase Mirror
PIC	Particle in Cell
QED	Quantum Electrodynamics

RMI	Richtmeyer-Meshkov Instability
RTI	Rayleigh-Taylor Instability
SAM	Spin Angular Momentum
SMR	Small Modular Reactor
T	Tritium
fs	femto-second ($10^{-15}s$)
ns	nano-second ($10^{-9}s$)
ps	pico-second ($10^{-12}s$)
GW	Giga-Watt ($10^{9}W$)
PW	Peta-Watt ($10^{15}W$)
TW	Tera-Watt ($10^{12}W$)
μm	micrometers ($10^{-6}m$)
nm	nanometers ($10^{-9}m$)
keV	kilo-electronvolt ($10^{3}eV$)
MeV	Mega-electronvolt ($10^{6}eV$)
GeV	Giga-electronvolt ($10^{9}eV$)
TeV	Tera-electronvolt ($10^{12}eV$)

Chapter 1

Introduction

Probably the greatest problem facing human civilization today is the energy problem. Carbon dioxide emissions from power plants, transportation, and manufacturing has reached an all time high [2], with compelling evidence to suggest these emissions are accelerating the melting of the polar ice caps, permafrost, and glaciers that have been present since the last ice age. It is the responsibility of the current generation of scientists, engineers, and politicians to tackle this problem and avert the catastrophe of an increased global temperature.

The problem is not new, and many solutions have already been developed for zero carbon-dioxide energy emissions such as hydroelectricity, solar energy, wind turbines and nuclear fission energy to name just the primary contenders. However, there is no silver bullet to the problem, and each of the aforementioned solutions have advantages and disadvantages.

For instance, hydroelectric dams can only be built where there is a river of sufficient flow rate and volume, and energy losses from transmission lines to distant cities and villages can be high [19]. Additionally, the environmental impact of large hydroelectric dams has often been a source of controversy [42]. Wind turbines can be built almost anywhere that has a consistent wind flow, and also have long working lifetimes, but their intermittent power must be supplemented by a another power source, or a large energy storage facility.

Solar energy has increased in popularity dramatically over the past few decades due to large reductions in manufacturing and installation costs [28], and with high capacity battery systems being introduced by companies like Tesla [154], it is possible for houses to run *off-the-grid* almost entirely. However, it would be difficult to con-

vince a Canadian to convert there house entirely to solar when winter-time daylight hours are reduced to less than 6, outside temperatures plummet below -30°C, and there are several inches of snow covering the solar panels. There is also the problem of the limited working lifetime of silicon solar panels of roughly 25 years, and they degrade in efficiency slowly over time [77].

The discovery of nuclear fission in 1938 brought hope to an almost unlimited power source releasing far more energy per gram of material than any chemical burning reaction. By the 1960's, nuclear fission energy had been developed from the prototype 200W graphite moderator built be Fermi in 1942 [134], to widespread deployment of giga-watt (GW) nuclear power stations primarily using enriched uranium fuel rods. Many variations of fission reactors for burning different fuels and in different decay chains were developed including the heavy-water moderator CANDU reactors developed in Canada which required less-enriched uranium, and could even use spent fuel from other nuclear power plants [87]. However, with mounting concerns of waste material disposal, ever increasing costs to build reactors [1], and lack of public trust in the safety of the reactors following (but not limited to) the infamous Chernobyl accident, the three-mile accident and the recent incident in Fukushima, very few new nuclear fission power stations are being built. Currently, there is increasing interest to build small-modular-reactors (SMR's) which offer potentially safer, smaller nuclear reactors built at a factory rather than on site. These SMR's are expected to cost a fraction of a full scale GW plant, and are easily expanded to meet power needs [125].

Probably the biggest roadblock for fission reactors currently is their waste, and its corresponding storage and disposal which typically takes on the order of thousands of years. An alternative idea to that of splitting atoms through fission, is to combine them using fusion, the same process found with in stars. To fuse two nuclei together, they must be close enough together to overcome their Coulomb repulsion which requires significant forces to do so. The cross section for fusion (σ) varies depending on each nucleus and also scales as a function of particle energy [31]. Of the fusion of light elements and particles, the highest cross sections are found with the deuterium and tritium isotopes of hydrogen,

$$ {}^{2}_{1}H + {}^{2}_{1}H \rightarrow {}^{3}_{2}He + n + 3.27MeV \tag{1.1} $$

$$ {}^{2}_{1}H + {}^{2}_{1}H \rightarrow {}^{3}_{1}H + p + 4.03MeV \tag{1.2} $$

$$ {}^{2}_{1}H + {}^{3}_{1}H \rightarrow {}^{4}_{2}He + n + 17.62MeV \tag{1.3} $$

Here we see that the thermal energy released in the fusion of deuterium and tritium (D-T) is $17.62MeV$, which also has the highest fusion cross section when the particles have a temperature of approximately $10keV$. For a fusion reactor using D-T fuel, it only requires $91kg$ of fuel for $1GWy$ of energy. Unlike fission, fusion does not occur terrestrially, and as a result it is much more difficult to sustain fusion reactions suitable for power generation. Yet the advantages of using fusion energy are numerous, most notably the lack of radioactive waste. In fact, the helium produced in D-T and D-D fusion is a very useful resource.

Another advantage of fusion energy is the abundance of fuel on earth, with 0.015% of all natural hydrogen being a deuterium isotope. This is in stark contrast to the limited availability of U^{235} (0.72% isotope abundance) requiring large calutrons and centrifuges to separate it from uranium ore.

Given that the particles need to have energies upwards of $20keV$, they are in a plasma state. For fusion of the elements to occur, the Lawson criteria states that the product of plasma density and confinement time must exceed a given value depending on the plasma species and temperature. For a deuterium-tritium fusion at $26keV$, it is found that [31],

$$ n\tau \geq 1.5 \times 10^{14} \frac{s}{cm^3} \tag{1.4} $$

where τ is the energy confinement time, and n is the plasma density.

There are several methods of plasma confinement that can potentially meet this criteria, including of course gravitational confinement as found in stars. Unfortunately, the use of gravity to confine a plasma is not possible with current, or probably future technology. A suitable candidate instead of gravity is magnetic confinement through the use of tokamaks, spheromaks, and stellerators [65]. These large plasma containment devices use strong magnetic fields to confine the plasma into a torus shape and typically can confine the plasma on the order of ms to upwards of $300s$ with the new ITER project [73]. The resulting plasma density according to the Lawson criteria is typically low requiring $n \approx 1 \times 10^{14} cm^{-3}$.

The compressing and containment of plasma using magnetic fields is often compared with using rubber bands to compress a balloon, and the engineering of device to do this is not without problems. An alternative to magnetic field confinement is to use lasers from multiple angles to compress, and heat plasma in a fraction of the time.

Using Nd:glass laser systems packing mega-joules of energy into a few nanoseconds, inertial confinement fusion is a promising alternative that has already been able to release more energy than that used to confine and heat the fuel in a small ignition spot within the plasma ($Q > 1$) [71].

1.1 Inertial Confinement Fusion

In a similar fashion to magnetic confinement devices, there are several configurations that can be used for inertial confinement fusion. The direct-drive fusion approach, such as that used at the Laboratory for Laser Energetics in Rochester, NY [102], uses 60 frequency tripled lasers to directly compress a small plastic spherical target ($\approx 1mm$ diameter) filled with D-T mixture to densities of roughly 1000 times that of solid density. This results in a plasma density of order $10^{26}cm^{-3}$, corresponding to a confinement time τ of roughly $100ps$ - much shorter than the nanosecond timescale of the laser pulse. This gives great promise for fusion ignition, but so far efforts have fallen slightly short of achieving ignition and complete burning of the fuel.

Primary reasons for this are found due to two major factors, inhomogeneities in the laser wavefront, and surface roughness on the target surface. These factors seed instabilities such as the Rayleigh-Taylor (RTI), Richtmeyer-Meshkov (RMI), and Kelvin-Helmholtz instabilities (KHI) that ultimately become detrimental to the symmetry of the implosion.

One possible improvement to the direct-drive scheme is that of an indirect-drive scheme like that used at the National Ignition Facility (NIF) at Lawrence Livermore National Laboratory (LLNL) in California [71]. In this scheme, the spherical D-T fuel capsule is suspended within a gold cylinder with openings on either end. At the NIF, 192 laser beams of kJ, ns class are focussed on the inside walls of the the gold cylinder, also known as a hohlraum, which converts the incoming laser light into an x-ray oven with a near Planckian emission spectrum. The primary advantage in this scheme is the dramatic increase in radiation uniformity as compared to direct-drive schemes, however large scale non-uniformities such as the non spherical cylindrical x-ray source, target support structures and, target imperfections can still drive aforementioned instabilities.

In an ideal implosion, a central hot spot is generated at the centre of the compressed fuel with enough energy to ignite the fusion reaction. However instabilities in

the compression have prevented ignition requiring alternative approaches to igniting the fuel. A recent approach that increased the yield to beyond unity (energy incident into the ignition hot spot was less than that released) used a high foot laser pulse to drive the implosion [71]. In this scheme, the laser pulse is shaped temporally in an attempt to mitigate the RTI [36].

Another alternative is the fast-ignition approach in which the compression and ignition processes are decoupled [152]. In this process, the conventional ICF compression is used to compress the fuel, but is done in such a way that a central hot spot is not formed. A second energy source is then used to ignite the fuel through use of either photons or a particle beam. The advantage of this method is that the total laser energy threshold for ignition is lowered, it yields a higher gain, and the sensitivity to hydrodynamic instabilities is lower.

A typical fast ignition scheme would use a PW class high intensity laser to produce electrons in the surrounding plasma of the compressed core with a suitable energy spectrum such that they deposit their energy at the central hot spot of the fuel at the end of their energy range. The major problem in this scheme comes from filamentation, resistive effects and resultant electron beam divergence. Recent studies have shown that when a strong magnetic field ($2kT$) is imposed across the target, the electrons can be guided by this field and the coupling efficiency of the hot electron energy to the hot spot can be increased sevenfold up to 14% [169, 152, 80, 155, 143, 17, 149, 139].

This is superior to previous fast ignition schemes that have utilized a cone inserted into the hohlraum causing anisotropy and uneven compression of the fuel. It is believed that the additional large magnetic field can effectively collimate and guide hot electrons to the hotspot. Previous studies have shown an electron beam divergence of around 50° half angle, so any collimation of this beam can significantly increase coupling efficiency [149, 139].

Generating magnetic fields of this strength in these conditions is no trivial matter, and methods for doing this are actively being investigated [171]. One goal of this thesis is to investigate magnetic fields generated from structured laser pulses carrying angular momentum, particularly the so called called orbital angular momentum (OAM) pulses. The absorption of angular momentum by plasma, also known as the inverse Faraday effect [64, 5], is potentially capable of generating $\approx 10kT$ magnetic fields using lasers available today. However this effect is only understood using ideal

analytic models for structured light, and needs both numerical and experimental confirmation. This thesis will explore the numerical verification of these fields for underdense plasmas and present some preliminary experimental investigation of the interaction of OAM pulses with underdense targets at high intensities.

1.2 Laser Driven Particle Accelerators

The development of high peak power, high-intensity lasers ($> 1 \times 10^{18} W cm^{-2}$) over the past 30 years has led to the application of lasers to many interesting high-energy areas beyond that of fusion energy discussed in the previous section. Of them, one of the most promising is that of table-top particle acceleration, in particular, the acceleration of protons, neutrons, positrons, and electrons.

Conventional microwave and radio-frequency accelerators like the past Large Electron-Positron (LEP) collider and the current Large-Hadron collider (LHC) typically operate with a maximum electric field gradient of $150 MV/m$ requiring many meters to accelerate electrons to even GeV energies [39]. It is possible to accelerate protons and ions to TeV energies in circular accelerators as the energy losses due to synchrotron radiation scales as $[mass]^{-4}$ [75], whereas electrons are currently limited to energies of around $100 GeV$. Circular accelerators like the LEP at CERN, and the linear accelerator at SLAC are able to accelerate electrons to 100's (10's) of $GeV's$, but in doing so, require 27 kilometers of circumference or a 3 kilometer straight line respectively.

If we instead consider the electric field of an intense laser pulse, we find that the peak electric field is much greater, for instance, a laser with peak intensity $1 \times 10^{19} W cm^{-2}$ has a peak electric field of

$$E = \sqrt{\frac{2I}{c\epsilon_0}} \approx 1 TV/m \tag{1.5}$$

This is clearly many orders of magnitude greater than the electric field strength of conventional accelerators, but the electric field is sinusoidal and any material brought into contact with it is ionized and changes to a plasma state. Plasma waves can sustain a maximum electric field of

$$E_0(V/m) \approx 96\sqrt{n_e(cm^{-3})} \tag{1.6}$$

before wave breaking. For instance, a plasma with electron density $n_e = 1 \times 10^{19} cm^{-3}$

can sustain a peak accelerating field of $300GV/m$, more than 3 orders of magnitude greater than that of a conventional accelerator. In theory, using plasma to accelerate particles instead of RF waves in vacuum could reduce the accelerator from kilometer lengths to meter lengths.

By exciting nonlinear plasma waves - past the wave breaking limit of Eq.1.6, it is possible to accelerate particles with yet higher electric field gradients - on the order of $1TV/m$ [39]. To excite a nonlinear plasma wave, a high-intensity laser pulse is used to drive a laser wakefield [153, 40] that trails behind the laser pulse with a group velocity equal to the laser pulse in the plasma. Electrons caught in this wake are accelerated to GeV energies on scale lengths of millimeters, and eventually outrun the laser pulse and wake once their energy becomes highly relativistic. Currently, laser driven wakefield accelerators (LWFA) have achieved peak electron energies of approximately 8 GeV using a pre-ionized plasma channel of length $\approx$20 cm [57]. There are some schemes in place that could potentially accelerate the electrons in a single stage to beyond this energy towards the $100GeV$ energy scale, such as the AWAKE experiment at CERN that uses a proton bunch to drive the wakefield as opposed to light pulses [63].

In addition one can cascade acceleration stages in series such as the Bella accelerator proposal of Lawrence Berkeley National Laboratory to use 100 stages of acceleration of 10 GeV each to achieve a TeV particle accelerator [163].

In addition to producing high energy, low divergence electron beams, high brightness and spatially coherent x-ray beams can be emitted from the interaction. Betatron radiation is a result of the electrons accelerated in the wakefield oscillating in radial electric fields and azimuthal magnetic fields generated in the so-called bubble regime of LWFA [4]. These betatron x-rays are of great interest as their pulse duration is short - on the order of the pulse duration ($\approx 30fs$), and comparable in brightness to current high brightness x-ray sources [129]. A review of the physics of wakefield acceleration, and betatron radiation will be given in Chapter 4.

1.3 Higher Order Laser Modes

When we talk about high peak-power laser systems, we are usually referring to peak powers greater than 1 TW. To achieve these very high powers, many techniques are used including multi-pass amplifiers, chirped pulse amplification, and optical para-

metric amplifiers [150].

Typically, the high powered lasers used to drive ICF compression, fast ignition and wakefield accelerators have been linearly polarized fundamental laser modes - typically focussed to Gaussian or Airy focal spots. There are multiple reasons for this, the first of which is that most often researchers want the highest peak intensity which is achieved using the fundamental laser mode (single Gaussian spot).

Another reason is inherent in the design of the laser amplifiers for high-power laser systems which are typically large slabs of lasing glass or crystals. This glass is often illuminated using pump lasers with a transverse profile designed to make optimal use of the glass shape. Given that the amplifiers are typically cylindrical, or square, the ejected beam typically is a super-Gaussian profile that is convolved with the shape of the amplifying glass. The wavefront of the ejected beam is flat, and often corrected after pulse compression using deformable mirrors to ensure this wavefront flatness [175]. Modification of a high-power laser system to change the laser mode is typically not desirable as the lasers are designed to operate within tight specifications and damage thresholds.

For smaller, low-power laser cavities it is possible to manipulate the ejected laser mode such that higher order lasers modes can be generated [145]. This can be done through several methods such as spot defect mirrors [74], curved mirrors, or a phase plate within the cavity. To mode convert a high-power laser, alternative methods external to the laser cavity are needed.

Using higher order laser modes and alternative polarization states to drive high-intensity laser-plasma interactions is an area of growing interest. While there has been little work done experimentally in this area due to challenges associated with generating higher order modes at high-intensity [24, 113, 86], there is a significant amount of theoretical and simulation work done to explore possible advantages of using higher order modes to drive laser-plasma interactions [165, 164, 105, 106, 117, 116, 21, 168, 141]. Primarily, the interest in using higher order laser modes is in using modes that carry an angular momentum, unlike that of linearly polarized Gaussian modes.

The angular momentum carried by a laser pulse can come from two sources - either spin angular momentum (polarization) or orbital angular momentum (spatial structure in the wavefront). Spin angular momentum (SAM) is limited to one $\hbar$ unit of angular momentum per photon in a given beam as a result of photons being spin-1

bosons [62]. On the other hand, orbital angular momentum (OAM) is essentially unlimited in the angular momentum a beam can carry, however as OAM is increased in the beam, its peak intensity decreases [6]. Coupling of laser angular momentum to plasma is of great interest as it gives us an additional control parameter in the interaction.

If angular momentum is transferred to a plasma, then the plasma may begin to rotate about the laser axis. The primary phenomenon expected to occur is magnetic field generation as electrons orbit about the axis like a plasma solenoid. This has been explored analytically [5, 64], but little work has been done in the numerical and experimental verification into this mechanism for linearly polarized OAM beams. Axial magnetic field generation in a laser plasma interaction is of particular interest to the ICF community as it could be used to guide and focus electron beams for fast ignition, or for magnetically assisted fusion [146]. Additionally, it could be used to enhance the betatron critical energy from laser driven wakefield acceleration due to the dependence on the electron oscillation radius on magnetic fields.

1.4 Goal and Outline of Thesis

The goal of this thesis is to explore the generation and interaction of high intensity orbital angular momentum laser beams with free electrons and plasma theoretically, numerically, and experimentally extending models currently used for Gaussian beams to the new family of OAM modes. Specifically, we are interested in how to mode convert high-power lasers efficiently and economically, and to fully characterize the generated OAM beams at focus. Once the high-intensity OAM beam is generated, we aim to investigate how this angular momentum can be transferred to free electrons, and plasma using analytic, numerical, and experimental methods.

Single particle relativistic electrodynamics and scattering will be explored using a code developed in MATLAB, while the dynamics of relativistic self-focussing, wakefield acceleration in the blow-out regime, and betatron radiation in linearly polarized Laguerre-Gaussian modes will be explored using the EPOCH particle-in-cell code [8]. We also aim to verify the generation of magnetic fields in plasma from linearly polarized OAM modes via the inverse Faraday effect numerically, and develop plasma parameters suitable for studying the phenomenon experimentally.

To verify the simulations, we will compare the results to experimental data ac-

quired at the CLPU laser facility from a 2018 campaign. This is the first time an extensive study covering both the theoretical and experimental aspects of linearly polarized OAM beams has been performed. The thesis chapters are summarized below.

Chapter 2 - The Orbital Angular Momentum of Light

In this chapter we review the angular momentum carried in electromagnetic waves, and the concept of orbital angular momentum (OAM). We then derive a generalized formula for the Fraunhofer diffraction of azimuthally symmetric beams carrying OAM. The far-field diffraction of lasers carrying OAM is then found for high-power lasers with Gaussian, super-Gaussian and flat-top near field profiles. These far-fields are then approximated for the first time using two methods with waist-optimized Laguerre-Gaussian basis functions. These fitted functions provide an improved basis for accurate modelling of high-power optical vortices in numerical simulations and for comparing to experimental results.

Chapter 3 - Relativistic Electrodynamics of Optical Vortices

In this chapter we review the fundamental single-particle electrodynamics in relativistic plane waves including the concepts of the ponderomotive force, relativistic effects, and the Lawson-Woodward theorem. We derive the fully symmetric paraxial field equations of generalized Laguerre-Gaussian modes and model relativistic single particle dynamics within the fields. The simulation results are used to verify for the first time angular momentum transfer to electrons scaling with the absorption.

The physics and simulation of relativistic Thomson scattering from free electrons is also derived and demonstrated for plane waves. The simulations are then post-processed to give the detailed spatial and spectral distributions as a function of intensity. While we do not demonstrate it in this thesis, we have developed capabilities to model nonlinear Thomson scattering from arbitrary LG modes, and plan to implement this into future work.

Chapter 4 - Under-Dense Plasma Interactions with Optical Vortices

Chapter 4 explores the interaction of high-intensity optical vortices with under-dense plasma numerically. We review the physics of plasma wakes and electron acceleration.

We then explore the relativistic self-focussing of an optical vortex and discuss the two modes of self-focussing that were observed. Wakefield acceleration in the blow-out regime is discussed comparing scaling laws associated with electron energy gain and bubble size for Gaussian driven wakefields and extending these models to Laguerre-Gaussian wakefields.

Chapter 5 - Generation of High Intensity Optical Vortices

In this chapter the current methods of generating low power OAM beams in laser systems is reviewed and a novel method for generating such modes in high power laser systems is presented. We investigate the mode conversion efficiency of stepped spiral phase optics and develop the off-axis spiral phase mirror (OASPM) as a new method to generate OAM modes. The implementation of the OASPM is demonstrated in a low power laser system, and then in a high-power laser system yielding the highest intensity optical vortices produced in the lab to date. A perturbative model is also developed for the numerical modelling of realistic, asymmetric optical vortices.

Chapter 6 - Wakefield Acceleration with Optical Vortices

Chapter 6 discusses the 2018 CLPU experimental campaign aimed at driving wakefield acceleration with optical vortices for the first time. The experimental setup and the CLPU VEGA2 laser is discussed. A review of the diagnostics used for measuring electron energy and divergence, as well as betatron x-ray energy and divergence is given. The results are discussed and compared to numerical simulations using realistic beam profiles.

Chapter 7 - Linearly Polarized Optical Vortices and the Inverse Faraday Effect

In Chapter 7, we investigate numerically the generation of magnetic fields from the coupling of linearly polarized OAM modes to plasma electrons. These fields are compared to analytic models, using both ideal symmetric OAM beams and realistic asymmetric OAM beams and regimes are found where fields of the order of 1000T can be generated.

Chapter 2

The Orbital Angular Momentum of Light

In this chapter, we introduce the notion of electromagnetic waves carrying angular momentum in two forms; spin and orbital angular momentum (OAM). We then review beams carrying well defined orbital angular momentum through scalar diffraction theory and in the paraxial basis of Laguerre-Gaussian modes.

By approximating the actual diffraction of OAM beams at focus with best fit standard Laguerre-Gaussian modes, we find simple models for describing high intensity OAM beams at focus for analytic and numerical models. This is done in two methods and the advantages and disadvantages of each are compared and allows much more accurate descriptions of the focal spot intensity than has been done to date so far.

This work has been summarized in two publications, the first describes the decomposition of Gaussian OAM beams into Laguerre Gaussian function that have been optimized for energy. The paper also consider mode conversion of OAM beams generated with stepped spiral phase optics, and lasers with broad bandwidth [93]. The second paper considers the generation of OAM beams with high intensity lasers, specifically the various near-fields common to the lasers, and then fits the optimal Laguerre-Gaussian mode to each of the cases [94].

2.1 Electromagnetic Waves

The classical interplay between the electric and magnetic field can be completely described using a set of four symmetrical equations known formally as Maxwell's

equations [75],

$$\nabla \cdot \boldsymbol{E} = \frac{\rho}{\epsilon_0} \tag{2.1}$$

$$\nabla \cdot \boldsymbol{B} = \mu_0 \rho_m \tag{2.2}$$

$$\nabla \times \boldsymbol{E} = -\frac{\partial \boldsymbol{B}}{\partial t} - \mu_0 \boldsymbol{J}_m \tag{2.3}$$

$$\nabla \times \boldsymbol{B} = \mu_0 \epsilon_0 \frac{\partial \boldsymbol{E}}{\partial t} + \mu_0 \boldsymbol{J} \tag{2.4}$$

Here, $\boldsymbol{E}$ gives the 3D electric field vector, ρ gives the electric charge density, and ϵ_0 gives the permittivity of free space as defined in the list of constants in this thesis. The current density vector $\boldsymbol{J}$ gives the flux of charge per unit time per unit area. In vacuum the presence of charges and sources are assumed zero and thus, ρ and $\boldsymbol{J}$ are assumed zero.

By symmetry, we define the magnetic field vector $\boldsymbol{B}$, the magnetic charge density ρ_m, and the permeability of free space μ_0. At the present time, the magnetic charge has yet to be observed and thus its non-existence is assumed. If the magnetic charge density is zero, then the corresponding magnetic current density $\boldsymbol{J}_m$ is also zero. Setting both ρ and ρ_m equal to zero results in the vacuum Maxwell equations.

Maxwell's equations are linear in vacuum for electric field strengths much less than the Schwinger field; $E_S = 1.32 \times 10^{18} V/m$ [23]. Close to and beyond this electric field strength, the electromagnetic field becomes nonlinear and new phenomena can arise. Of interest to the high-intensity laser community is the observation of vacuum birefringence, the effect where virtual electron-positron pairs are generated at the Schwinger field intensity in vacuum. The observation of vacuum birefringence and other nonlinear processes are hoped to be explored with the next generation of lasers that may drive intensities over $1 \times 10^{23} W cm^{-2}$ [67].

Some algebraic manipulation of Maxwell's equations in vacuum allows us to rewrite the four first order partial differential equations as two second order partial differential equations. Taking the curl of Eq's.2.3 and 2.4, using the identity

$$\nabla \times \nabla \times \boldsymbol{A} = \nabla(\nabla \cdot \boldsymbol{A}) - \nabla^2 \boldsymbol{A} \tag{2.5}$$

and noting that in vacuum, $\nabla \cdot \boldsymbol{E} = 0$ and $\nabla \cdot \boldsymbol{B} = 0$, we can write;

$$\mu_0\epsilon_0\frac{\partial^2\boldsymbol{E}}{\partial t^2} - \nabla^2\boldsymbol{E} = 0 \tag{2.6}$$

$$\mu_0\epsilon_0\frac{\partial^2\boldsymbol{B}}{\partial t^2} - \nabla^2\boldsymbol{B} = 0 \tag{2.7}$$

We note that these are simply wave equations that propagate at speed,

$$c = \frac{1}{\sqrt{\mu_0\epsilon_0}} = 2.99792 \times 10^8 m/s \tag{2.8}$$

the speed of light in vacuum.

The solutions of these equations are dependant on initial and boundary conditions. Due to the linearity of Maxwell's equations, we can use the superposition principle to construct complicated solutions from a set of fundamental solutions. A non-trivial, fundamental solution suitable for describing propagating electromagnetic beams is that of an infinite plane wave,

$$\boldsymbol{E} = \boldsymbol{E}_0 exp\left(i(\boldsymbol{k}\cdot\boldsymbol{r} - \omega t)\right)\hat{e_1} \tag{2.9}$$

$$\boldsymbol{B} = \boldsymbol{B}_0 exp\left(i(\boldsymbol{k}\cdot\boldsymbol{r} - \omega t)\right)\hat{e_2} \tag{2.10}$$

Here, we define the angular frequency of the electromagnetic wave as ω, and the wave-vector $\boldsymbol{k} = \hat{e_3}2\pi/\lambda$ where λ is the wavelength of the wave. We use $\boldsymbol{r}$ as a general position vector and an orthogonal unit vector $\hat{e_k}$. If we assume our wave to be propagating in the $\hat{z}$ direction, then it is easy to show via Eq.2.4 that for plane waves in vacuum, there can be no electric or magnetic fields in the direction of propagation and they must be orthogonal to each other. If the electric field is polarized in the $\hat{x}$ direction, then the corresponding magnetic field must be polarized in the $\hat{y}$ direction.

Direct substitution of the time-independent plane wave solutions into the electromagnetic wave equations yields the Helmholtz equation,

$$(\nabla^2 + k^2)\boldsymbol{E}, \boldsymbol{B} = 0 \tag{2.11}$$

This solution generally describes any propagating wave comprised of plane waves. Due to the linearity of Maxwell's equations in vacuum, it is possible to compose a solution of Maxwell's equations and the Helmholtz equation as a superposition of plane waves. We will look for specific scalar solutions to the Helmholtz equation relevant to this thesis in section 2.3.

2.2 Angular Momentum of Electromagnetic Waves

Electromagnetic waves carry energy and momentum. The wave energy propagated per unit time, per unit area is given by the Poynting vector [75, 61].

$$\boldsymbol{\mathcal{S}} = \frac{1}{\mu_0}\boldsymbol{E} \times \boldsymbol{B} \tag{2.12}$$

The linear momentum density carried by a classical electromagnetic wave can then be given as,

$$\wp = \mu_0\epsilon_0\boldsymbol{\mathcal{S}} = \epsilon_0(\boldsymbol{E} \times \boldsymbol{B}) \tag{2.13}$$

As an extension to classical mechanics, it is not surprising that it is possible for an electromagnetic wave to carry angular momentum, the density of which can be given by,

$$\boldsymbol{j} = \boldsymbol{r} \times \wp = \epsilon_0[\boldsymbol{r} \times (\boldsymbol{E} \times \boldsymbol{B})] \tag{2.14}$$

Not all waves carry angular momentum, but all waves propagate with a linear momentum. For example a linearly polarized plane wave given by Eq.2.9 propagates with a time-averaged linear momentum density of $E_0^2/(2\mu_0 c)$ but does not carry an angular momentum. The combination of two plane waves with a phase and polarization shift can carry angular momentum. Consider two plane waves given by the following,

$$\boldsymbol{E}_1 = E_0 exp\left(i(kz - \omega t)\right)\hat{x} \tag{2.15}$$

$$\boldsymbol{E}_2 = E_0 exp\left(i(kz - \omega t + \delta)\right)\hat{y} \tag{2.16}$$

where δ is an arbitrary phase. If δ is set to zero, then the sum of the two waves $\boldsymbol{E} = \boldsymbol{E}_1 + \boldsymbol{E}_2$ will produce a linearly polarized plane wave 45° relative to the $\hat{x}$ axis. However if δ is set an arbitrary value that is not equal to 0 or $n\pi$, then the wave can carry an angular momentum in the form of a rotating electric field vector, i.e. circular or elliptical polarization. An illustration of circular polarization is given in Fig.2.1.

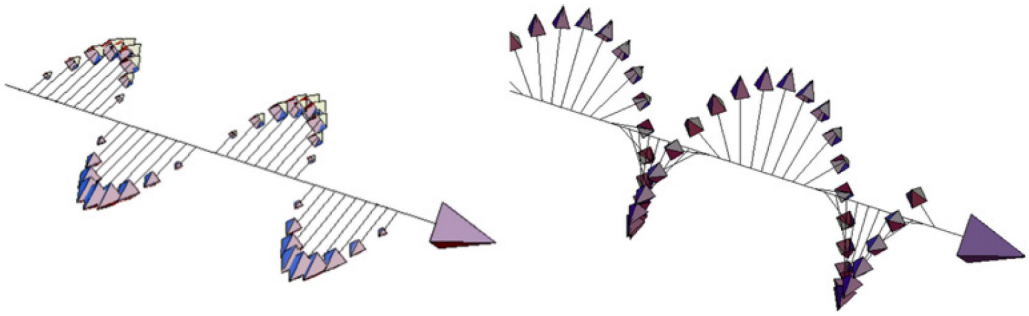

Figure 2.1: Electric field vectors for a linearly polarized beam (left), and a circularly polarized beam (right). Images reproduced with permission from [174]

It is a natural step to further consider that electromagnetic angular momentum may consist of two vector components, much like in classical mechanics. Consider the example of the Earth orbiting the sun which possesses a total angular momentum vector $\boldsymbol{J}$ - not to be confused with the current density. This angular momentum may be broken into its components of the spin angular momentum from the Earth rotating on its axis $\boldsymbol{S}$, and the orbital component of the Earth orbiting the Sun $\boldsymbol{L}$. The total angular momentum of the Earth orbiting the sun is simply the vector sum of the spin and orbital components.

$$\boldsymbol{J} = \boldsymbol{L} + \boldsymbol{S} \tag{2.17}$$

Electromagnetic waves can also be broken into spin and orbital angular momentum and add in the exact same way. As shown in Fig 2.1, the spin component arises from the rotation of the electric field vector about a point, typically arising from the combination of two orthogonal plane waves shifted in phase and polarization plane. The orbital angular momentum on the other hand may arise classically from a spatial variation in the phase of the beam which could be introduced by writing $\delta(x, y, z)$.

To prove this, we examine Eq.2.14, where it is possible to expand out the cross product into its constituent terms of spin and orbital angular momentum. We start

by introducing the magnetic vector potential $\boldsymbol{A}$ defined as

$$\boldsymbol{B} = \nabla \times \boldsymbol{A} \tag{2.18}$$

and,

$$\boldsymbol{E} = -\frac{\partial \boldsymbol{A}}{\partial t} - \nabla\varphi \tag{2.19}$$

where φ is some scalar potential set depending on the gauge. The magnetic vector potential is a powerful way of representing an electromagnetic wave as we can move the vector potential to a gauge that is more natural for describing waves. A useful gauge to do this is the Lorenz gauge given by,

$$\partial^{\mu} A_{\mu} = \nabla \cdot \boldsymbol{A} + \frac{1}{c^2}\frac{\partial \varphi}{\partial t} = 0 \tag{2.20}$$

Here, we introduce the 4-dimensional derivative ∂_{μ}, and the scalar potential φ freely chosen to satisfy the gauge condition. This is in contrast to Maxwell's equations as the divergence of the electric field which must always be zero as given in Eq.2.1. The use of a scalar potential removes this condition and we can write the full magnetic vector potential without loss of generality of an EM wave in a much simpler form,

$$\boldsymbol{A} = \Re\left[\psi(x,y,z)e^{i(kz-\omega t)}\hat{e}\right] \tag{2.21}$$

Here, we introduce a scalar wavefunction $\psi(x,y,z)$ and a generalized polarization vector $\hat{e}$. Eq.2.21 is a full description of a linearly polarized of arbitrary spatial shape and requires no additional terms to make it Maxwell consistent. A time harmonic magnetic vector potential can then be used to write the electric field in the Lorenz gauge as [66],

$$\boldsymbol{E} = i\omega\left[\boldsymbol{A} + \frac{1}{k^2}\nabla(\nabla \cdot \boldsymbol{A})\right] \tag{2.22}$$

Using the above definitions of the electric and magnetic field, it is possible to write Eq.2.14 in the following form [12].

$$\boldsymbol{j} = \epsilon_0\left[\sum_j E_j(\boldsymbol{r} \times \nabla)A_j - \boldsymbol{r} \times \nabla_j(E_j\boldsymbol{A})\right] \tag{2.23}$$

By inspection we see the right hand operator $\boldsymbol{r} \times \nabla$ is reminiscent of the orbital angular momentum operator in quantum mechanics [25], while the second term can

be written assuming the fields drop off sufficiently quickly as $\boldsymbol{E} \times \boldsymbol{A}$ [12]. Integrating over all space gives the total angular momentum of a time harmonic electromagnetic wave as [12],

$$\boldsymbol{J} = \epsilon_0 \int \left[\sum_j E_j (\boldsymbol{r} \times \nabla) A_j + \boldsymbol{E} \times \boldsymbol{A} \right] dV \tag{2.24}$$

With the orbital angular momentum defined as,

$$\boldsymbol{L} = \epsilon_0 \int \sum_j E_j (\boldsymbol{r} \times \nabla) A_j dV \tag{2.25}$$

and the spin angular momentum as,

$$\boldsymbol{S} = \epsilon_0 \int \boldsymbol{E} \times \boldsymbol{A} dV \tag{2.26}$$

It is possible for an EM wave to carry OAM by having a simple phase tilt or any anisotropic structure in its phase, however these can be difficult to define and in general, are not of interest.

A simple way for an electromagnetic wave to carry a well defined orbital angular momentum (OAM) is by imprinting the wavefront to contain a helix centred about the laser axis. The pitch of the helix Q can be written in terms of the wavelength as $Q = \lambda L$. The topological charge L of the beam can be any number, but for now we will assume it is equal to an integer such that we can define the azimuthal mode number $\ell = L$. In doing this, we can write the scalar wave amplitude as a function of ℓ,

$$\psi(r, \theta, z) = \psi(r, z) e^{i\ell\theta} \tag{2.27}$$

where θ and r are the polar coordinates in the transverse plane. Here, we have assumed that the wavevector is independent of θ and as such has an azimuthally symmetric amplitude profile short of the helical phase. While this may seem restricting as there are many laser modes that are not azimuthally symmetric, we shall see that the laser modes carrying a well defined OAM are azimuthally symmetric. A beam carrying OAM via a helical phase is illustrated in Fig.2.2.

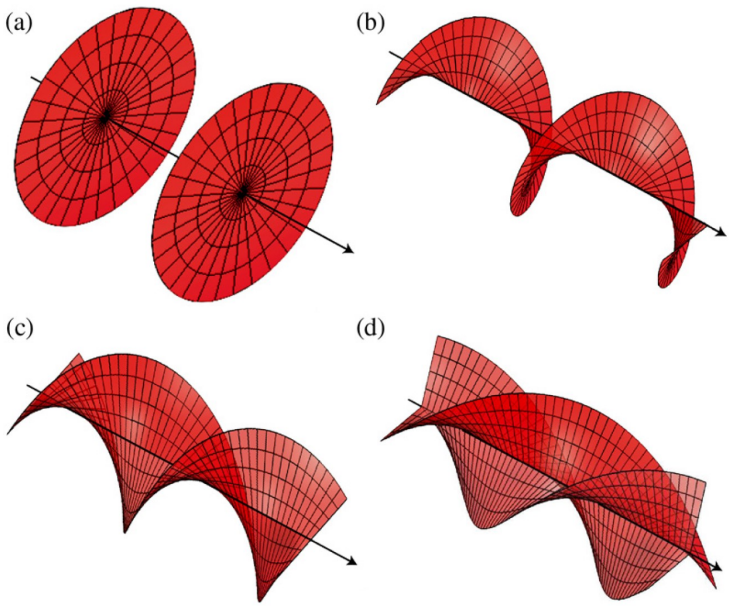

Figure 2.2: Helical wavefronts for beams with various orbital angular momentum. a). $\ell = 0$, b). $\ell = 1$, c). $\ell = 2$, and d). $\ell = 3$. Images reproduced with permission from [174]

It was shown in the seminal paper by Allen et al.[6] that the angular momentum density in the propagation direction carried by a wave with both spin and orbital angular momentum in the form of a helical wavefront can be given by,

$$j_z = \frac{\ell}{\omega}|\psi|^2 + \frac{\sigma_z r}{2\omega}\frac{\partial|\psi|^2}{\partial r} \tag{2.28}$$

Here, we use σ_z to denote the polarization state of the beam; $+1$ for right hand circular polarization, -1 for left, and 0 for a linearly polarized beam. Other values between 1 and -1 compose an elliptically polarized beam.

Eq.2.28 gives deep insight into the nature of electromagnetic angular momentum. For instance, integrating over all space and utilizing the fact that each photon carries $\hbar\omega$ energy, we reach the famous result for the total angular momentum per photon,

$$J_z = (\ell + \sigma_z)\hbar \tag{2.29}$$

The spin angular momentum of a photon is well known to be $\sigma_z\hbar$ as photons are spin 1 bosons [62]. However, the surprising result is that a single photon may contain an

additional intrinsic angular momentum in the form of an orbital component equivalent to $\ell\hbar$. This notion is counter intuitive as classical OAM is associated with something rotating around an axis or point. We know that photons are mass-less, and charge-less, so what are they rotating around as there can be no binding force?

It is well understood that the spin of a photon is an intrinsic property of the photon and there is no classical analogue. Considering many spin 1 photons in a beam comprises a circularly polarized beam with a rotating electric field vector.

Similarly, we find that the OAM of a single photon is an intrinsic property and arises in the form of a helical phase in the photon wavefunction. Much like the intrinsic spin of a photon, there is no classical analogue to the intrinsic OAM of a photon, and its interpretation is dependant on the interpretation of quantum mechanics.

A remarkable feature of this is result is the allowed range of values of ℓ. In theory, ℓ is unbounded as we can make the pitch of the helix infinitely tight (perhaps limited to the Planck length), and therefore a single photon could in theory carry a massive amount of intrinsic orbital angular momentum. This has been demonstrated experimentally for values fo ℓ up to 10000 [46], and is being widely researched as a method to enhance communication bandwidth in optical, infra-red, microwave, and radio frequencies [112].

2.3 The Paraxial Approximation and Laguerre-Gaussian Modes

A useful property of the Lorenz gauge is that if a vector potential satisfies the gauge condition, then it also satisfies the wave equation,

$$\partial^\mu \partial_\mu A^\mu = 0 \tag{2.30}$$

where $\partial^\mu \partial_\mu = \mu_0 \epsilon_0 \partial_{tt} - \nabla^2$. Direct substitution of the time harmonic vector potential into Eq. 2.30 yields,

$$\frac{\partial^2 \psi}{\partial x^2} + \frac{\partial^2 \psi}{\partial y^2} + 2ik\frac{\partial \psi}{\partial z} + \frac{\partial^2 \psi}{\partial z^2} = 0 \tag{2.31}$$

In general, this partial differential equation is difficult to solve analytically and typically requires a numerical solution. However, if we can make the assumption that the laser is not diverging with a large angle, then the beam will satisfy the paraxial

approximation,

$$\left|\frac{\partial^2\psi}{\partial z^2}\right| \ll \left|k\frac{\partial\psi}{\partial z}\right| \tag{2.32}$$

such that we can drop the second derivative in z. Rewriting Eq. 2.31 in polar coordinates under the paraxial approximation yields the following,

$$\frac{\partial^2\psi}{\partial r^2} + \frac{1}{r}\frac{\partial\psi}{\partial r} + \frac{1}{r^2}\frac{\partial^2\psi}{\partial\theta^2} + 2ik\frac{\partial\psi}{\partial z} = 0 \tag{2.33}$$

The solution of this equation can be given by the well-known Laguerre-Gaussian modes [6],

$$\begin{aligned}\psi_{\ell,p}(r,\theta,z) = \sqrt{\frac{2p!}{\pi(p+|\ell|)!}}\frac{1}{w(z)}\left[\frac{r\sqrt{2}}{w(z)}\right]^{|\ell|} exp\left(\frac{-r^2}{w(z)^2}\right) L_p^{|\ell|}\left(\frac{2r^2}{w(z)^2}\right) \\ exp\left[i\ell\theta - ik\frac{r^2 z}{2\left(z_0^2+z^2\right)} - i\Psi(z,p,\ell)\right]\end{aligned} \tag{2.34}$$

Here we introduce the azimuthal and radial mode numbers ℓ and p respectively, and the generalized Laguerre polynomial

$$L_p^{|\ell|}(x) = \sum_{n=0}^{p}(-1)^n\frac{(p+|\ell|!)}{(p-n)!(|\ell|+n)!n!}x^n \tag{2.35}$$

The Rayleigh range is the distance at which the beam width increases its radius by $\sqrt{2}$ as shown in Fig.2.3 and is given by the formula $z_0 = kw_0^2/2$ where w_0 is the Gaussian beam waist for the fundamental mode.

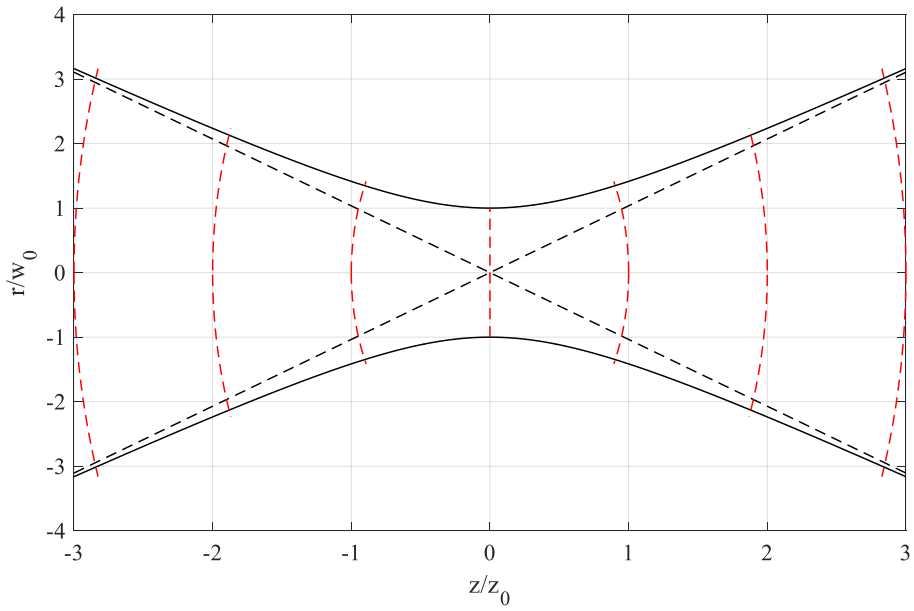

Figure 2.3: Illustration of a Gaussian beam close to focus with $w_0 = \lambda$. The solid black lines represent the radius at $w(z)$ while the dashed black lines represent the diffraction-less solution of a beam focussing to a singularity at $z = 0$. The dashed red lines represent the wavefront curvature ignoring the phase shift due to the helical phase.

The beam waist at any given point along the propagation axis is given by,

$$w(z) = w_0 \sqrt{1 + \frac{z^2}{z_0^2}} \tag{2.36}$$

Additionally, we define the Gouy phase is given as,

$$\Psi(z, p, \ell) = (2p + |\ell| + 1) \tan^{-1}\left(\frac{z}{z_0}\right) \tag{2.37}$$

The solutions for the first few azimuthal and radial modes are plotted in Fig.2.4 indicating both the field amplitude, time averaged intensity, and the phase of a few-low order modes.

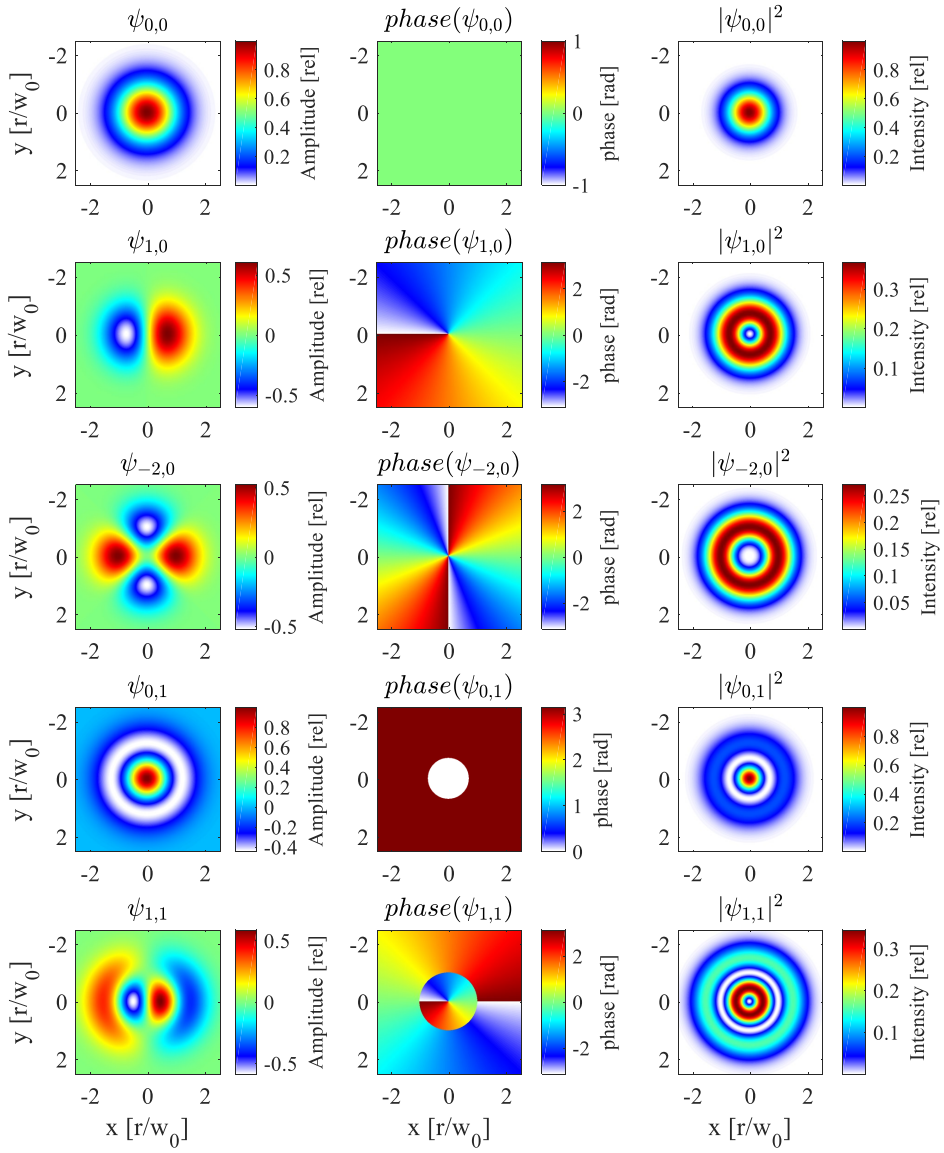

Figure 2.4: From left to right; instantaneous amplitude, phase, and time averaged intensity of various low order Laguerre-Gaussian modes $\psi_{\ell,p}$ at $z = 0$ according to Eq.2.34.

Combining the field amplitudes of Eq.2.34 with the magnetic vector potential given in Eq.2.21 yields a complete description of the electric and magnetic fields of the OAM beam close to focus within the paraxial approximation. Analytic expressions of these

fields is given in section 3.3.1.

While this model has been employed extensively in the literature both in theoretical and numerical models of OAM beams, it is not necessarily a good representation of realistic OAM beams. For realistic descriptions of OAM beams, we need to verify that the LG modes match the results of diffraction theory, or find modes that represent the diffraction theory accurately.

2.4 Scalar Diffraction of Optical Vortices

While the Laguerre-Gaussian modes are valid solutions to the wave equation in the paraxial approximation and the Helmholtz equation, they do not completely describe OAM beams at focus in their given form.

Scalar diffraction allows for the electric and magnetic fields to become decoupled in the Helmholtz equation if the following conditions are met; the propagation medium is linear, isotropic, homogeneous, non-dispersive, and non-magnetic, as is vacuum [121]. From the vector Helmholtz equation given in Eq. 2.11, we write the scalar Helmholtz equation as,

$$(\nabla^2 + k^2)U(\boldsymbol{x}) = 0 \tag{2.38}$$

where $U(\boldsymbol{x})$ is some scalar field that describes the wave amplitude. The problem we are interested in solving is the far-field diffraction of an OAM beam for a given near-field profile. This is illustrated in Fig.2.5.

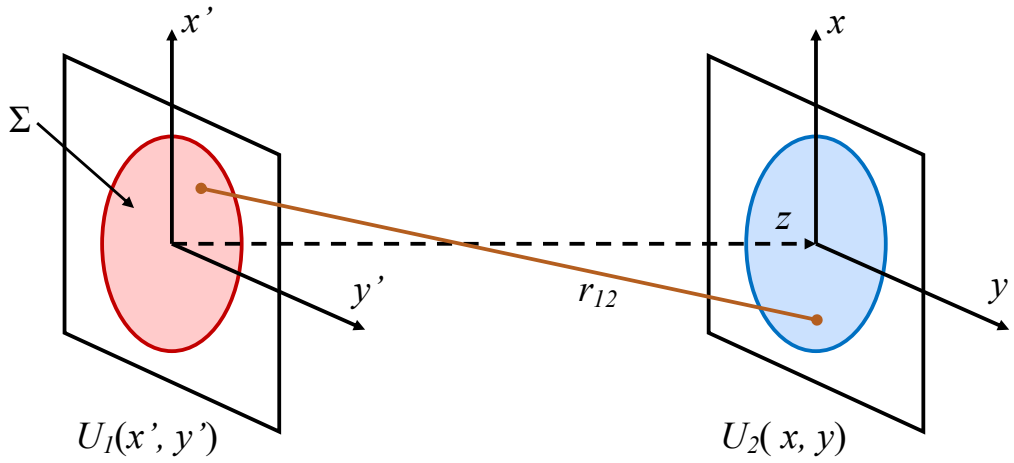

Figure 2.5: Propagation geometry from source plane $U_1(x', y')$ to a parallel observation plane $U_2(x, y)$

If we take the amplitude in the source plane as $U_1(x', y')$, it is possible to write the amplitude in a second plane $U_2(x, y)$ some distance z away by the Rayleigh-Sommerfeld diffraction solution [121],

$$U_2(x, y) = \frac{z}{i\lambda} \iint_{\Sigma} U_1(x', y') \frac{exp(ikr_{12})}{r_{12}^2} dx'dy' \tag{2.39}$$

where Σ defines the limits of the integrals by some aperture function. We use the variable r_{12} to denote the distance between any two points on the two planes. Formally we can define this distance by,

$$r_{12} = \sqrt{z^2 + (x - x')^2 + (y - y')^2} \tag{2.40}$$

In essence, this is a statement of Huygen's principle; every point on the aperture acts a spherical source of waves which are then summed at the observation point U_2 allowing for the effects of constructive and destructive interference to take place. If the two planes containing U_1 and U_2 are parallel, then Eq.2.40 becomes a convolution

integral written as [58],

$$U_2(x,y) = \iint U_1(x',y')h(x-x',y-y')dx'dy' \tag{2.41}$$

where $h(x,y)$ is the impulse response. In this case the Rayleigh-Sommerfeld impulse response can be written as,

$$h(x,y) = \frac{z}{i\lambda}\frac{exp(ikr)}{r^2} \tag{2.42}$$

with $r = \sqrt{x^2+y^2+z^2}$. Using the Fourier covolution theorem, we can rewrite Eq.2.41 as,

$$U_2(x,y) = \Im^{-1}\left[\Im\{U_1(x,y)\}\Im\{h(x,y)\}\right] \tag{2.43}$$

Here we denote the Fourier transform and inverse Fourier transform as $\Im$ and $\Im^{-1}$ respectively.

Eq.2.43 is the basis for Fourier optics, and in simple cases can be solved exactly. The Fourier transform of Eq.2.42 is analytic and yields the Rayleigh-Sommerfeld transfer function,

$$H(f_x,f_y) = exp\left(ikz\sqrt{1-(\lambda f_x)^2-(\lambda f_y)^2}\right) \tag{2.44}$$

where f_x, f_y are the coordinates in k space.

2.4.1 Near-field and Far-field Diffraction

The inverse Fourier transform of Eq.2.43 is in general not solvable and must be computed by numerical methods such as the Fast Fourier Transform (FFT). However, we can take two limits of Eq.2.43 to obtain the near-field and far-field diffraction approximations. The first approximation to obtain the near-field solution, often referred to as the Fresnel approximation, can be used when the Fresnel number F is greater than one.

$$F = \frac{R_0^2}{z\lambda} \tag{2.45}$$

Here we introduce the characteristic size of the aperture R_0 or the radius of the beam being focussed, and z is the distance of propagation from the source plane. Clearly for F to be greater than 1; $z < R_0^2/\lambda$. In this region, we can take the approximation

that the beam has not diverged significantly and as such $z \approx r$. Taylor expanding Eq.2.40 then yields,

$$r = z\sqrt{1 + \frac{(x-x')^2 + (y-y')^2}{z^2}} \approx z\left[1 + \frac{(x-x')^2 + (y-y')^2}{2z^2} + ...\right] \tag{2.46}$$

Plugging this into Eq.2.39 gives the Fresnel diffraction formula,

$$U_2(x,y) = \frac{e^{ikz}}{i\lambda z}\iint_\Sigma U_1(x',y') exp\left\{i\frac{k}{2z}\left[(x-x')^2 + (y-y')^2\right]\right\} dx'dy' \tag{2.47}$$

This simplifies the Fourier transforms drastically as the impulse response is now simply a Gaussian function,

$$h(x,y) = \frac{e^{ikz}}{i\lambda z} exp\left\{i\frac{k}{2z}\left[(x-x')^2 + (y-y')^2\right]\right\} \tag{2.48}$$

from which we can write the transfer function,

$$H(f_x, f_y) = e^{ikz} exp\left[-i\pi\lambda z\left(f_x^2 + f_y^2\right)\right] \tag{2.49}$$

The Fresnel approximation is therefore useful for modelling beams close to the source plane, and can be computed for many cases as an analytical inverse Fourier transform problem.

After a collimated beam passes through an achromatic lens (or off-axis parabola), it is focussed to a finite diffraction-limited size some distance f away from the lens, where f is the focal length of the lens. It is possible to show, although not done here, that focussing a collimated beam to a focal spot is equivalent to modelling the beam very far from its source plane where the Fresnel number is much less than 1. This region, often referred to as Fraunhofer diffraction, can be modelled via another approximation.

In the Fraunhofer approximation, we assume the beam has propagated sufficiently far such that the wavefronts are effectly planar - much like they are in the focal plane of a lens. As such, we can make the approximation in the phase of the Rayleigh-Sommerfeld formula,

$$exp\left[i\frac{k}{2z}(x'^2 + y'^2)\right] \approx 1 \tag{2.50}$$

Plugging this into Eq.2.39 yields the Fraunhofer diffraction integral,

$$U_2(x,y) = \frac{exp(ikz)}{i\lambda z} exp\left[i\frac{k}{2z}(x^2+y^2)\right] \iint U_1(x',y') exp\left[-i\frac{2\pi}{\lambda z}(xx'+yy')\right] dx'dy' \tag{2.51}$$

We note that the Fraunhofer diffraction integral is simply the inverse Fourier transform of the initial profile U_1 over the aperture function. We can further generalize this formula for lenses by replacing the variable z with the focal length of the lens f.

The irradiance in the image plane is more useful for practical use as in principle it is generally not possible to directly measure the electric or magnetic field of an electromagnetic wave at optical frequencies as modern electronics are typically limited to GHz frequencies. CCD and CMOS cameras can measure the irradiance of the beam given by $I = U^*U$ where U^* is the complex conjugate of the field amplitude. The far-field irradiance of an electromagnetic wave from a lens of focal length f is therefore given by,

$$I(x,y,z=f) = \left| \iint \frac{U_1(x',y')}{\lambda f} exp\left[-i\frac{2\pi}{\lambda f}(xx'+yy')\right] dx'dy' \right|^2 \tag{2.52}$$

Using this formula to compute the far-field diffraction patterns for some given near-field amplitude function imprinted with OAM will allow us to compare the paraxial solutions of the Helmholtz equation to the diffraction theory.

2.4.2 Fraunhofer Diffraction of Optical Vortices

Assuming the laser near-field profile is cylindrically symmetric and collimated - a good approximation for almost all real lasers, we can write the near-field amplitude as a function of radius $U(r)$ alone. If we imprint a perfect helical wavefront of topological charge ℓ into the near-field by some method that will be described later, we can write the near-field amplitude of the laser as,

$$U(r,\theta,\ell) = U(r)e^{i\ell\theta} \tag{2.53}$$

Here, r and θ represent the radius and azimuthal angle in the near-field (source) plane. If the beam has a central wavelength λ and is focussed by an achromatic optic

of focal length f, the intensity profile in the far-field can be found via the Fraunhofer approximation utilizing the 2D Fourier transform in polar coordinates,

$$I(\rho,\phi,\ell) \propto \left| \iint \frac{U(r)}{\lambda f} exp\left(\frac{-i2\pi}{\lambda f} r\rho\cos(\theta-\phi) + i\ell\theta\right) r dr d\theta \right|^2 \tag{2.54}$$

This equation is found simply by substituting $x' = r\cos\theta$, $x = \rho\cos\phi$, $y' = r\sin\theta$, and $y = \rho\sin\phi$ into Eq.2.52. We use the variables ρ and ϕ to denote the polar coordinates in the far-field. The standard procedure to integrate this function is to start with the azimuthal integral. We first make a change of variables such that $\psi = \theta - \phi$ as we can then rewrite the azimuthal integral as,

$$e^{i\ell\phi} \int_0^{2\pi} exp\left(\frac{-2\pi}{\lambda f} r\rho\cos(\psi) + i\ell\psi\right) d\psi \tag{2.55}$$

This allows us to make use of the definition listed in the identities section of the first order Bessel function of the ℓ^{th} kind [22]:

$$J_\ell(a) = \frac{i^{-\ell}}{2\pi} \int_0^{2\pi} e^{-iacos(\psi)+i\ell\psi} d\psi \tag{2.56}$$

We then write the far-field diffraction in the following form,

$$I(\rho,\ell) \propto \left| \frac{2\pi}{\lambda f} \int_0^\infty U(r) J_{|\ell|}\left(\frac{2\pi r\rho}{\lambda f}\right) \right|^2 \tag{2.57}$$

This result is the Hankel transform of order ℓ and scaling factor $2\pi\rho/\lambda f$ of the laser near-field. This powerful result allows use to calculate to intensity profile of an arbitrary OAM beam from almost any laser system. We shall explore the intensity profile generated by the three most common cylindrically symmetric laser near-fields.

2.4.3 Gaussian Optical Vortices

The simplest case to consider is that of a Gaussian near-field, common to laboratory lasers such as the helium-neon gas laser, small titanium:sapphire systems and most fiber based lasers. We can describe the Gaussian near-field of a laser by the following,

$$U(r) = U_0 exp\left(-\frac{r^2}{R_0^2}\right) \tag{2.58}$$

Here, R_0 is the characteristic near-field beam radius and U_0 is an arbitrary near-field amplitude. The power contained within the near-field can be computed as,

$$P \propto \iint U^*(r)U(r)rdrd\theta = \frac{|U_0|^2\pi R_0^2}{2} \tag{2.59}$$

In the following sections, we assume that the laser near-field and far-field all contain the same power, regardless of beam near-field shape. If the beam was not imprinted with a helical wavefront ($\ell = 0$) and we assume the beam focusses with no power lost, the Hankel transform can be computed analytically to give the well known Gaussian focal spot:

$$I(\rho, \ell = 0) = I_0 e^{-2\xi^2} \tag{2.60}$$

Here, I_0 is the peak intensity which is maximal on axis, ξ is the normalized radius $\xi = \rho/w_0$ where w_0 is the Gaussian beam waist defined as:

$$w_0 = \frac{\lambda f}{\pi R_0} \tag{2.61}$$

This result is shown in Fig.2.6 indicated by the solid blue line.

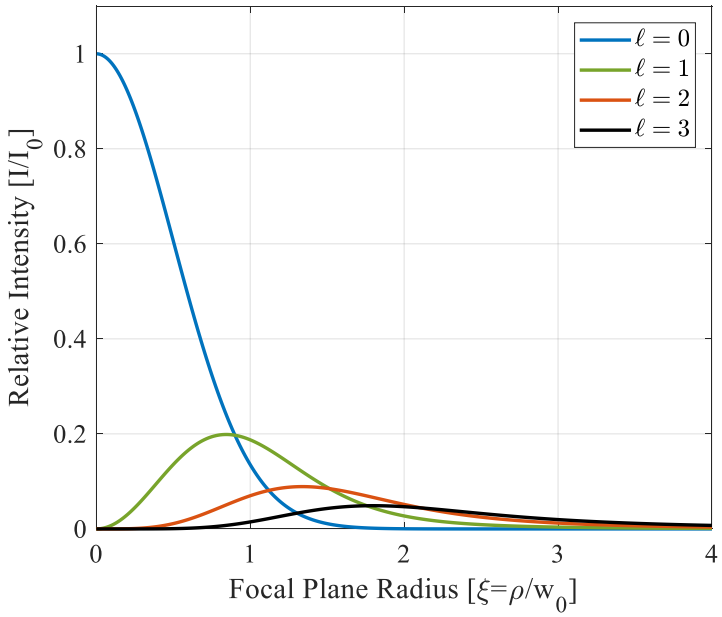

Figure 2.6: Fraunhofer diffraction of a near-field Gaussian beam carrying OAM for the first four topological charges.

Table 2.1: Properties of Gaussian and flat-top driven OAM beams; column 1). OAM content of beam ℓ, column 2). Peak intensity relative to I_0 for Gaussian near-field OAM beams, column 3). Normalized radial position of peak intensity for Gaussian near-field beams, column 4). Peak intensity relative to I_0 for flat-top near-field beams, column 5). Normalized radial position of peak intensity for flat-top driven beams.

ℓ	I_{Gp}/I_0	ξ_{Gp}	I_{Fp}/I_0	ξ_{Fp}
0	1.000	0.000	0.500	0.000
1	0.199	0.845	0.129	1.228
2	0.089	1.337	0.073	1.967
3	0.049	1.798	0.049	2.632
4	0.030	2.250	0.036	3.271
5	0.020	2.711	0.028	3.885

It is possible to solve the ℓ^{th} order Hankel transform of Eq.2.58 analytically using the identity [60],

$$\int_0^\infty e^{-ar^2} J_\ell(\beta r) r dr = \frac{\sqrt{\pi}\beta}{8\alpha^{3/2}} exp\left(\frac{-\beta^2}{8\alpha}\right)\left[I_{\frac{\ell-1}{2}}\left(\frac{\beta^2}{8\alpha}\right) - I_{\frac{\ell+1}{2}}\left(\frac{\beta^2}{8\alpha}\right)\right] \tag{2.62}$$

where $I_n(x)$ is the modified Bessel function of the first kind as given in the identities section. After some algebra, we can now write the analytical expression for the intensity distribution at focus,

$$I(\rho,\ell) = I_0\frac{\pi}{4}\xi^2 e^{-\xi^2}\left[I_{\frac{|\ell|-1}{2}}\left(\frac{\xi^2}{2}\right) - I_{\frac{|\ell|+1}{2}}\left(\frac{\xi^2}{2}\right)\right]^2 \tag{2.63}$$

This result has been normalized such that it contains the same total power in the focal spot as the result given in Eq.2.60. As a result, the value of I_0 is identical in both cases.

As the value of ℓ increases, the radius at the peak intensity is increased. As a result of this, the peak intensity of the ring must decrease to conserve total power in the focal spot. The first three non-zero intensity profiles are given in Fig.2.6. The decrease in peak intensity is clear as the ℓ number of the near-field is increased. The ratio of the peak intensity for the first four ℓ modes as compared to the $\ell = 0$ mode are given in column 2 of Table 2.1 and their corresponding radial positions are given in column 3. The subscript of G inidcates that the beam were driven with a Gaussian beam. These results will be compared to the Laguerre-Gaussian modes in section 2.5.

2.4.4 Flat-top Optical Vortices

Another common model for a laser near-field is that of a flat-top beam. In this model, the intensity is constant across the near-field profile until it reaches some radius R_0 at which it immediately drops to zero. While it is impossible to generate a laser near-field like this in practice, it is actually a good approximation to super-Gaussian lasers which behave more like a flat-top beam than they do a Gaussian beam.

We write the near-field profile of a flat-top beam in the following form,

$$U(r) = \frac{U_0}{\sqrt{2}} circ\left(\frac{r}{R_0}\right) \tag{2.64}$$

where the *circ* function is defined as,

$$circ\left(\frac{r}{R_0}\right) = \begin{pmatrix} 1, & r < R_0 \\ \frac{1}{2}, & r = R_0 \\ 0, & r > R_0 \end{pmatrix} \tag{2.65}$$

The *circ* function can be easily implemented by making the radial boundary of the Hankel transform finite. The near-field is normalized to contain the same power as in the previous case and as a result, the value of R_0 and U_0 are the same. As before, we first consider a beam without OAM to obtain the classical result. The $\ell = 0$ Hankel transform of Eq.2.64 yields the well known Airy spot at focus given by,

$$I_F(\rho, \ell = 0) = \frac{I_0}{2}\left[\frac{J_1(2\xi)}{\xi}\right]^2 \tag{2.66}$$

The normalization factor of $1/2$ ensures the power is consistent with the result in Eq.2.60 and as a result, the peak intensity of the focus is half of what is found when using a Gaussian near-field with the same parameters. This reduction of peak intensity comes as a result of additional laser power in surrounding Airy rings. The fundamental Airy focus is plotted in Fig.2.7 and indicated by the blue line.

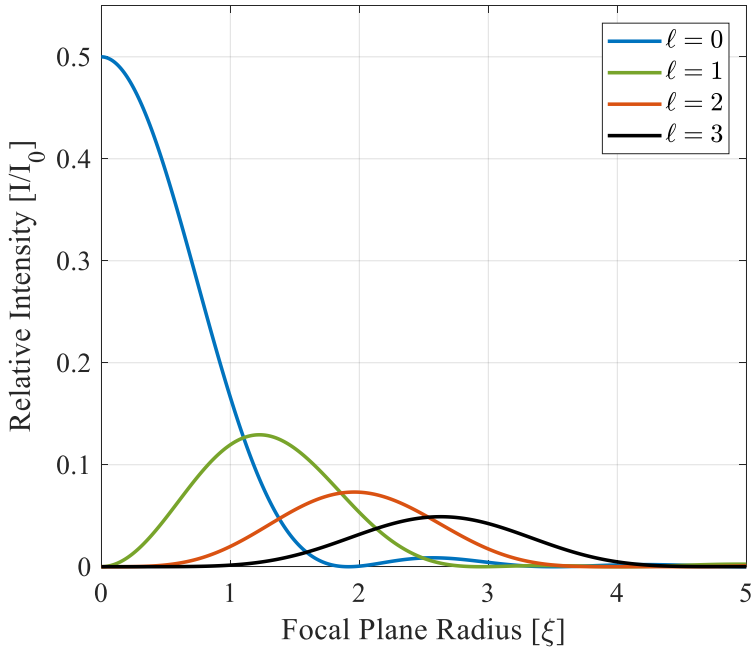

Figure 2.7: Fraunhofer diffraction of a near-field flat-top beam carrying OAM for the first four topological charges.

A solution of the ℓ^{th} order Hankel transform of Eq.2.64 becomes more challenging, for which analytical solutions only exist when ℓ is even. In general, there seems to be no closed form to the integral, but it is possible to represent the solution as a generalized hypergeometric function ${}_1F_2(a; b, c; z)$:

$$I_F(\rho, \ell) = \frac{I_0}{2} \left| \frac{\xi^{|\ell|}}{|\ell|! \left(\frac{|\ell|}{2} + 1\right)} {}_1F_2 \left(\frac{|\ell|}{2} + 1; |\ell| + 1, \frac{|\ell|}{2} + 2; -\xi^2 \right) \right|^2 \tag{2.67}$$

Again, the result is normalized to ensure the total power is conserved and hence the value of I_0 remains the same. The results of the first 3 non-zero ℓ modes are given in Fig.2.7. We note that compared to the Gaussian near-field, the flat-top driven OAM focal spots have a higher peak intensity relative to the $\ell = 0$ focal spot. These relative intensities are summarized in column 4 of Table 2.1 and their corresponding normalized radii in column 5. This is likely a result of the donut modes overlapping with the Airy rings, and due to the increased power at larger radii in the laser near-field leading to better matching to higher ℓ modes with larger radii.

2.4.5 Super-Guassian Optical Vortices

In reality, high-power laser's have neither a flat-top beam or a Gaussian near-field beam. Rather, a convolution of the two resulting in the well known super-Gaussian beam. By generalizing the previous two near-fields, it is possible to construct a near-field profile for the super-Gaussian mode,

$$U(r) = U_0 \sqrt{\frac{2^{1/n} n}{2\Gamma(1/n)}} exp\left[-\left(\frac{r}{R_0} \right)^{2n} \right] \tag{2.68}$$

Here, we introduce the super-Gaussian integer n, and the gamma function $\Gamma(x)$. Again, this result is normalized such that it contains the same power as the previous near-fields. This is possible to see if one takes the limit as $n \to \infty$, we retrieve the flat-top case and if we set $n = 1$, we retrieve the Gaussian case.

In general there is no known analytical solution to the Hankel transform of Eq.2.68, so we must restrict this near-field to a numerical study only. Based on previous expressions that we derived, we maintain representing the far-field intensity pattern with the dimensionless variable ξ. The results for the first few values of n including both the $n = 1$ and $n = \infty$ case are shown in Fig's.2.8 and 2.9 for the $\ell = 0$ and $\ell = 1$ modes respectively.

From the figures, the evolution of the focal spot as it transforms from a Gaussian near-field to a flat-top near-field is well illustrated. For the $\ell = 0$ case, we see the focal spot broadening as n increases until about $n = 4$ when the results quickly converge to that of a flat-top driven beam. This highlights the point made earlier in that a flat-top beam is well representative of a super-Gaussian beam of $n > 3$. Typical high-power lasers have a super-Gaussian parameter of order $n = 4$ [166]. For the $\ell = 1$ case as shown in Fig.2.9, we find good agreement between the $n = 3$ super-Gaussian beam and the flat-top beam.

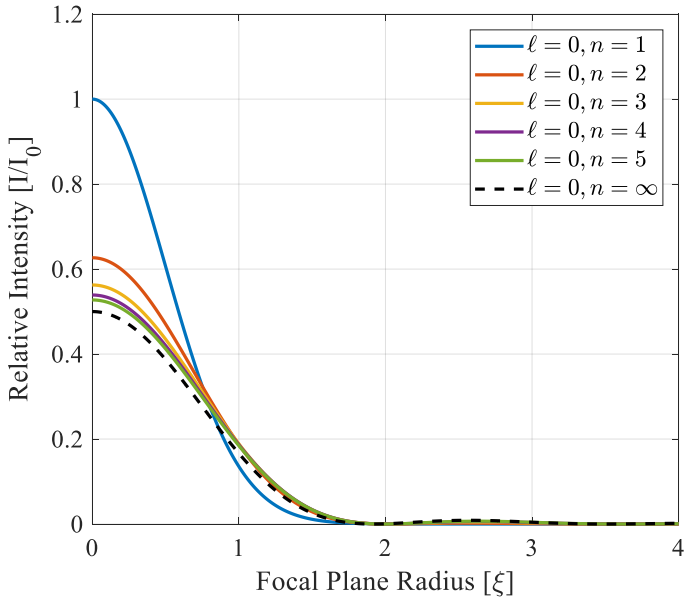

Figure 2.8: The first 5 super-Gaussian focal spots for an $\ell = 0$ beam. The dashed black line represents a flat-top driver. The blue line corresponds to a Gaussian driver.

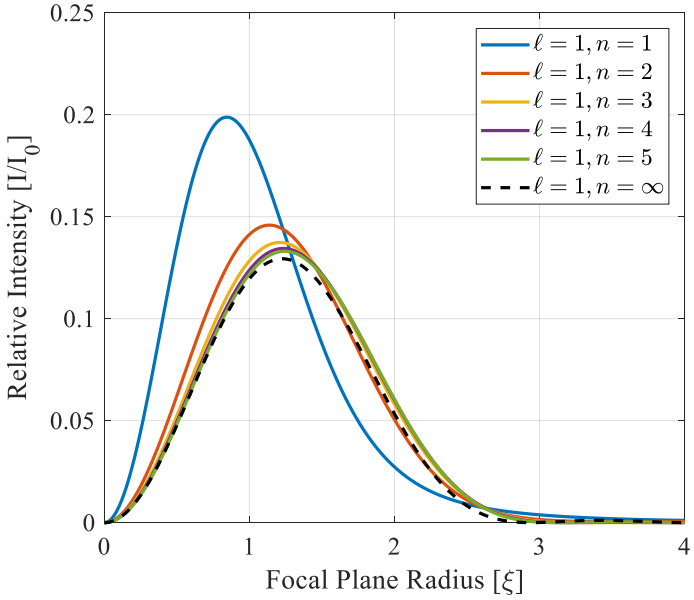

Figure 2.9: The first 5 super-Gaussian focal spots for an $\ell = 1$ beam. The dashed black line represents a flat-top driver. The blue line corresponds to a Gaussian driver.

2.5 Optimal Descriptions of Optical Vortices

In the previous section, we used diffraction theory to derive the far-field intensity patterns of OAM modes driven by various laser near-field profiles. While we were able to describe these beams by (mostly) analytic formulae, the formulae themselves use complicated functions such as the modified Bessel functions, or hypergeometric functions. If we wish to model these beams either analytically or numerically, these forms are not suitable as they can add computational overhead, or difficult expressions to differentiate or integrate. We therefore return to the Laguerre-Gaussian modes as these are much simpler to work with, and look for approximate LG modes to best represent this complicated diffraction solutions.

We start by first restating the intensity of the LG modes in the focal plane in a modified form,

$$I_{LG}(\rho,\ell,p) = I_0 \frac{\eta p!}{(p+|\ell|)!}\left(\frac{w_0}{w_{LG}}\right)^2\left(\frac{\rho\sqrt{2}}{w_{LG}}\right)^{2|\ell|} exp\left(\frac{-2\rho^2}{w_{LG}^2}\right)\left[L_p^{|\ell|}\left(\frac{2\rho^2}{w_{LG}^2}\right)\right]^2 \quad (2.69)$$

where we have introduced two new variables; the mode conversion efficiency parameter η, and the modified LG beam waist parameter given by,

$$w_0 = \gamma w_{LG} \quad (2.70)$$

The value of γ is optimally chosen such that the LG mode best fits the diffraction result of a given near-field. The value of η is then chosen to scale the mode energy. Throughout the literature, the equivalent values of γ and η have been mostly left as unity.

We can approach the problem of optimizing the value of η and γ in two different ways. The first of which is through a mode converter, where we decompose the near-field imprinted with a helical phase into LG modes. We can then optimize the energy into a single mode by varying the beam waist parameter. The second approach is slightly simpler in that we simply fit the LG mode to the focal spot intensity distribution and tabulate the results from numerical fits. While this is not as rigorous as the first method, it is more robust in getting a first-order approximation of the diffraction theory result and can be applied to any function.

2.5.1 Energy Optimized Laguerre-Gauss Beams

The conversion efficiency from one orthogonal mode to another through the use of a transmission operator T can be given by the modal decomposition inner product,

$$\eta_{\ell p} = |\langle \psi_{\ell p} | T | \psi_{mn} \rangle|^2 \tag{2.71}$$

Here, we denote the orthogonal modes as ℓ, p of the output beam and m, n of the input beam, and ψ is given by Eq.2.35. For a perfect helical phase imprinted on the beam, we find the transmission operator to be given by,

$$T = e^{-iL\phi} \tag{2.72}$$

where L is the topological charge of the beam. For now, we will assume $L = \ell$, but we will later show that this is not necessarily the case and explore solutions for the non-integer case. We first explore the case of a fundamental Gaussian input beam where $m = n = 0$. This yields the equation in the focal plane as,

$$\begin{aligned}\langle \psi_{\ell p} T \psi_{00} \rangle = \sqrt{\frac{p!}{(p+|\ell|)!}} \frac{\gamma}{w_0^2} \iint \left(\frac{\rho\sqrt{2}\gamma}{w_0} \right)^{|\ell|} \\ exp\left[-\frac{r^2(1+\gamma^2)}{w_0^2} \right] L_p^{|\ell|} \left(\frac{2r^2\gamma^2}{w_0^2} \right) e^{i(\ell - L)\phi} \rho d\rho d\phi\end{aligned} \tag{2.73}$$

We can separate this integral into two products; the radial integral and the azimuthal integral. Using the definition of the generalized Lagurre polynomial given in Eq.2.36, we can write the radial integral as,

$$\begin{aligned}R_{|\ell| p} = \sqrt{\frac{p!}{(p+|\ell|)!}} \frac{2^{|\ell|/2} \gamma^{|\ell|+1}}{w_0^{|\ell|+2}} \\ \int_0^\infty \rho^{|\ell|+1} e^{-\beta\rho^2} \sum_{m=0}^{p} \frac{(-1)^m (p+|\ell|)!}{(p-m)!(|\ell|+m)!m!} \left(\frac{\sqrt{2}\rho\gamma}{w_0} \right)^{2m} d\rho\end{aligned} \tag{2.74}$$

where,

$$\beta = \frac{1+\gamma^2}{w_0^2} \tag{2.75}$$

To integrate this function, we make use of the identity [60],

$$\int_0^\infty x^n exp\left(-ax^b\right) dx = \frac{1}{b} a^{-1/b(n+1)} \Gamma\left(\frac{n+1}{b}\right) \tag{2.76}$$

Pulling the sum out of the integral makes this expression straight-forward to integrate. The azimuthal integral is trivial to solve for the case of $L = \ell$,

$$\Phi_{\ell L} = \int_0^{2\pi} exp\left[i(\ell - L)\phi\right] d\phi = 2\pi|_{\ell=L} \tag{2.77}$$

Finally, combining the two integrals and solving them, we obtain the result,

$$\eta_{\ell p} = \left|R_{|\ell|p}\Phi_{\ell=L}\right|^2 = 2^{|\ell|+2} p!(|\ell| + p)!\gamma^2 \left|\sum_{m=0}^{p} \frac{(-2)^m \Gamma(\mu)}{(p-m)!(|\ell| + m)!m!(1+\gamma^2)^\mu}\right|^2 \tag{2.78}$$

where we define $\mu = m + |\ell|/2 + 1$.

If we consider an OAM beam with $L = \ell = 1$, we can plot the conversion efficiency as a function of the beam waist ratio for the first few LG p modes as shown in Fig. 2.10. One may note that the maximum conversion efficiency to a single LG mode exists when $\gamma \neq 1$. We also note that where the maximum beam waist ratio occurs, the conversion efficiency to some odd p modes also goes exactly to zero. This is true for any integer value of L.

It is possible to analytically differentiate and optimize Eq.2.78. As we are interested in representing our diffraction spot in the minimum number of LG modes, we look primarily at the $p = 0$ case. In doing so, we find the optimal beam waist to maximize the energy in the first ℓ LG mode is given by,

$$\gamma = \frac{1}{\sqrt{|\ell| + 1}} \tag{2.79}$$

Plugging this value of γ into Eq.2.78, we find that a maximal conversion efficiency of $\eta = 0.9308$ is possible for the $\ell = 1$ mode. This is a vast improvement on using the default value of $\gamma = 1$ in which a maximal conversion efficiency of $\eta = 0.785$ is possible. The remaining 7% of the focal spot energy is found in higher order radial p modes. We find that as the topological charge of the beam increases, the conversion efficiency to maximize the focal spot energy into a single mode decreases. This is illustrated for the first 6 p modes in Fig. 2.11.

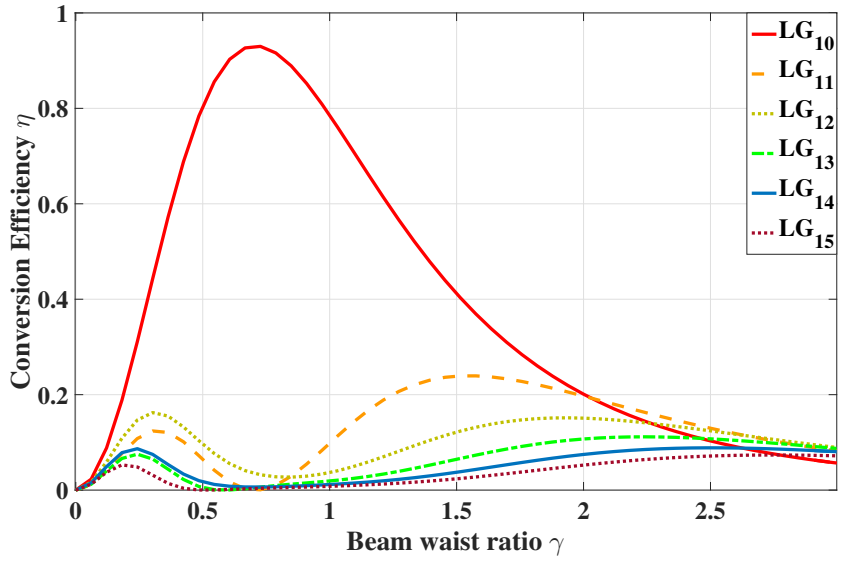

Figure 2.10: Mode conversion efficiency of an OAM beam with topological charge $L = \ell = 1$ for the first five LG p modes. The peak of the LG_{10} mode is located at $\gamma = 1/\sqrt{2}$.

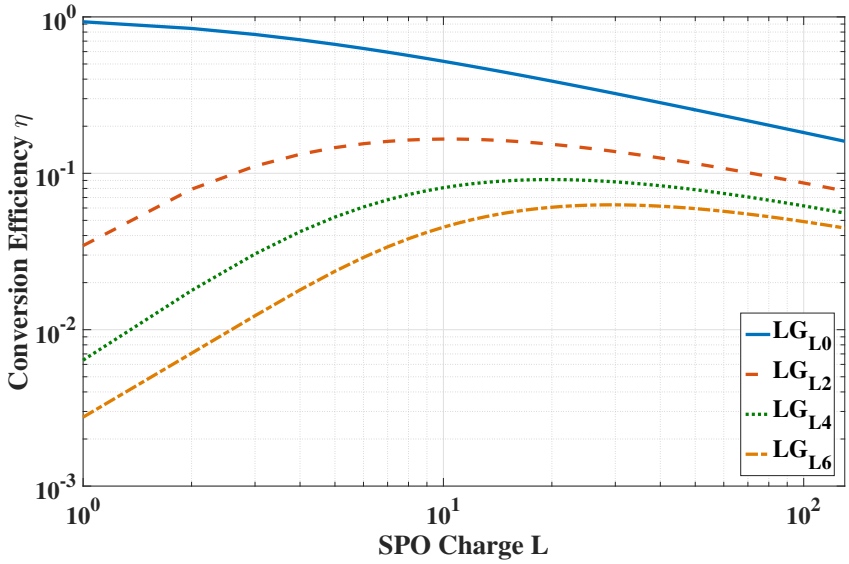

Figure 2.11: Conversion efficiency for various topological charges L to the first non-trivial p modes using optimal beam waists.

We find that for $L = \ell > 11$, the conversion efficiency to a single LG mode

becomes less than 50%. This become problematic for modelling OAM beams as now we need many LG p modes to accurately describe the focal spot intensity distribution. We thus seek an alternate method describe OAM beams that are non-integrable, and require less p modes to accurately describe OAM beams of large topological charge.

We summarize the quality of the fits found by this method in Fig. 2.12. We note that as ℓ increases, the accuracy of the energy optimized fit becomes worse - this is due to less energy being contained with the mode as ℓ increases. We also note that there is a large discrepancy between the peak intensity value of the LG mode and the diffraction result, aswell as the the radial position of this peak. We do note however that while these fits may not be exact, the modes are more optimal as opposed to leaving the LG mode with unity value of η and ℓ as can be seen by the blue dash-dot line in Fig.2.12.

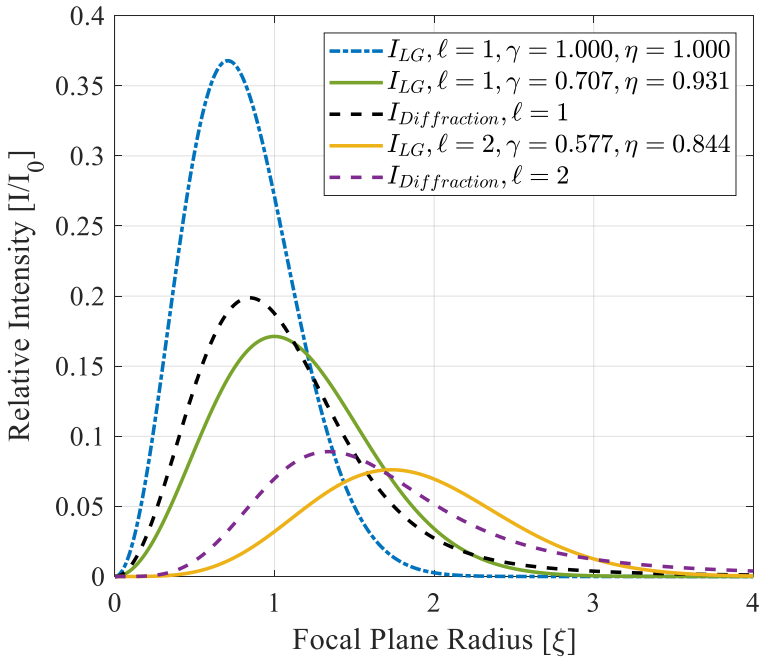

Figure 2.12: Laguerre-Gaussian beams fitted to the diffraction results via energy optimization. The diffraction results are indicated by dashed lines. The dash-dot blue line represents a non-optimized LG mode.

2.5.2 Intensity Optimized Laguerre-Gauss Beams

The second approach in which we seek to fit LG modes directly to the OAM focal spots is somewhat more straight-forward. We note that the peak intensity radial position and magnitude of the diffraction results are listed in Table 2.1, from which we can match a $p = 0$ LG modes of equivalent topological charge to. The peak intensity of an LG mode as given by Eq.2.69 is given by,

$$\frac{r_{max}}{w_0} = \xi_{max} = \sqrt{\frac{|\ell|}{2\gamma^2}} \tag{2.80}$$

while the peak intensity of the $p = 0$ LG mode is directly proportional to the mode conversion efficiency given by,

$$\frac{I_{LG}(\xi_{max}, \ell)}{I_0} = \frac{|\ell|^{|\ell|} e^{-|\ell|} \gamma^2 \eta}{|\ell|!} \tag{2.81}$$

The radial position of the peak of the LG mode is then matched to the radial position of the peak of the diffraction solutions in Eq's.2.63 and 2.67. The conversion efficiency, or in this case scaling factor, is then found by matching the peak intensity value of the LG mode to the peak intensity of the diffraction solution. This is found by using the formula,

$$\eta = \frac{I(\xi_{max}, \ell)|\ell|!}{|\ell|^{\ell} e^{-|\ell|} \gamma^2} \tag{2.82}$$

where $I(\xi_{max}, \ell)$ is the peak intensity of the diffraction solution. The peak intensity and its corresponding radial position of the diffraction solutions cannot be found analytically and thus we use a numerical root finding solution accurate to 3 decimal places. The results of η and γ by fitting LG modes to the first 5 ℓ modes are given in Tables 2.2 and 2.3. We remark that the values of n correspond to all 3 near-field profiles studied; $n = 1$ represents a Gaussian near-field, $n = \infty$ represents a flat top near-field, and we also calculate γ and η values for useful super-Gaussian beams. These tables therefore summarize the results of the near-fields entirely.

We first examine the results of the Gaussian near field fitted with the LG modes in Fig. 2.13. It is clear to see that a non-optimized LG mode (shown in dash-dot blue) is a poor representation of the OAM modes at focus. The solid green line shows a very good approximation to the blacked dashed line which gives the diffraction result.

Table 2.2: Optimal beam waist ratios γ of the first 6 ℓ numbers for Gaussian ($n = 1$), flat-top ($n = \infty$), and useful super-Gaussian mode numbers.

$\ell \backslash n$	1	2	3	4	5	10	∞
0	1.000	0.797	0.766	0.758	0.756	0.759	0.771
1	0.837	0.622	0.584	0.574	0.569	0.568	0.576
2	0.746	0.554	0.519	0.508	0.504	0.503	0.508
3	0.680	0.508	0.477	0.466	0.460	0.459	0.465
4	0.629	0.475	0.443	0.434	0.430	0.426	0.432
5	0.583	0.447	0.418	0.409	0.404	0.401	0.407

Table 2.3: Optimal conversion efficiencies η of the first 6 ℓ numbers for Gaussian ($n = 1$), flat-top ($n = \infty$), and useful super-Gaussian mode numbers.

$\ell \backslash n$	1	2	3	4	5	10	∞
0	1.000	0.986	0.960	0.939	0.924	0.885	0.841
1	0.772	1.023	1.094	1.110	1.116	1.101	1.061
2	0.589	0.892	1.001	1.046	1.062	1.070	1.047
3	0.472	0.778	0.908	0.970	1.005	1.035	1.010
4	0.391	0.680	0.828	0.901	0.939	0.996	0.980
5	0.338	0.603	0.756	0.837	0.882	0.952	0.946

Beyond the radius of the peak intensity the fit deviates from the diffraction result. We find this as a result of reduction of power in the focal spot due to the fit.

By integrating over all space of Eq.2.69, we find that the total power (or energy) in the laser focus is directly proportional to η:

$$P \propto \int_0^{2\pi} \int_0^{\infty} I_{LG} \rho d\rho d\phi = \frac{I_0 \eta \pi w_0^2}{2} \tag{2.83}$$

Because the value of η was less than 1 for our fits to diffraction result in Fig.2.13, the power in each focal spot was reduced, hence the reduction in intensity for radii greater than the peak intensity radii.

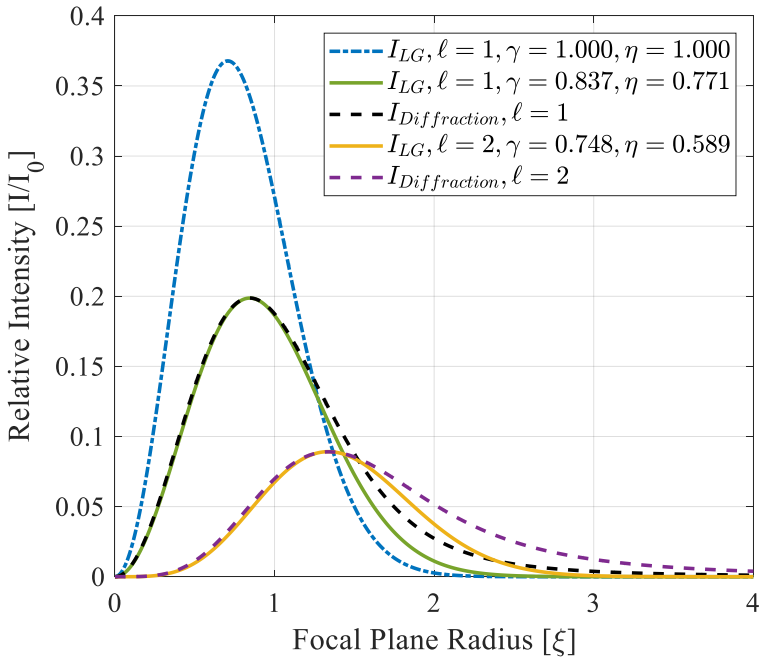

Figure 2.13: Laguerre-Gaussian beams fitted to the exact diffraction result (dashed) for OAM beams driven by Gaussian near-field beams for both $\ell = 1$ and $\ell = 2$ topological charges. The dash-dot blue line represents a non-optimized LG mode.

If we instead consider the results of the flat-top driven OAM beams given in Fig.2.14, we find even better fits, with the additional energy in the fitted LG beams for $\ell > 0$ as a result of the value of η being greater than unity. We have also fitted the Airy focal spot for $\ell = 0$ with an LG_{00} mode with non-unity η and ℓ values. This was done by matching the beam waist position of the LG mode with that of the diffraction solution. This result itself is useful for when modelling Airy foci in numerical models that we will later explore.

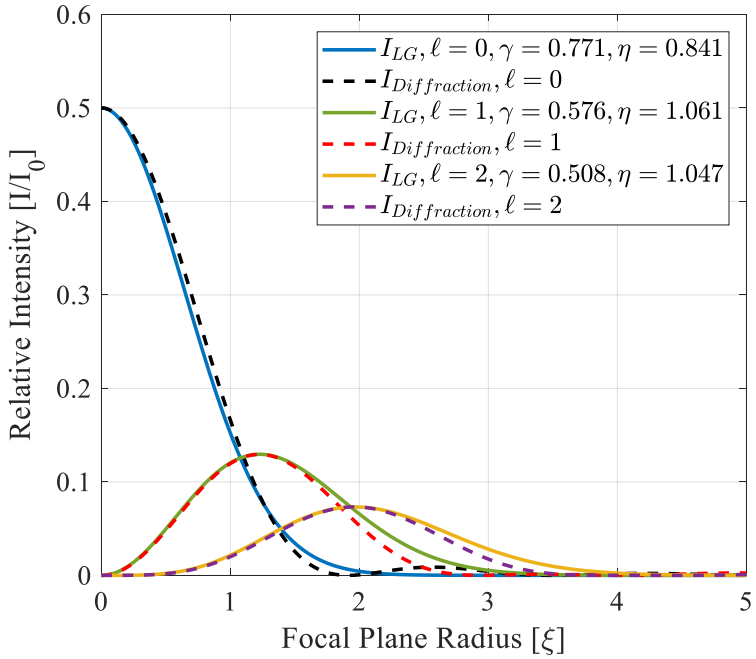

Figure 2.14: Laguerre-Gaussian beams fitted to the exact diffraction results (dashed) for OAM beams driven by flat-top near-field beams for $\ell = 0$, $\ell = 1$, and $\ell = 2$ topological charges.

We have summarized some of the LG fits to the diffraction result of the super-Gaussian driven OAM beams in Fig.2.15. We find an almost exact agreement with the fitted LG modes to the diffraction theory of the $n = 2$ driven super-Gaussian beams. This is emphasized by the close to unity values of η for OAM beams driven by super-Gaussian beams with $n = 2, 3$ as shown in Table 2.3.

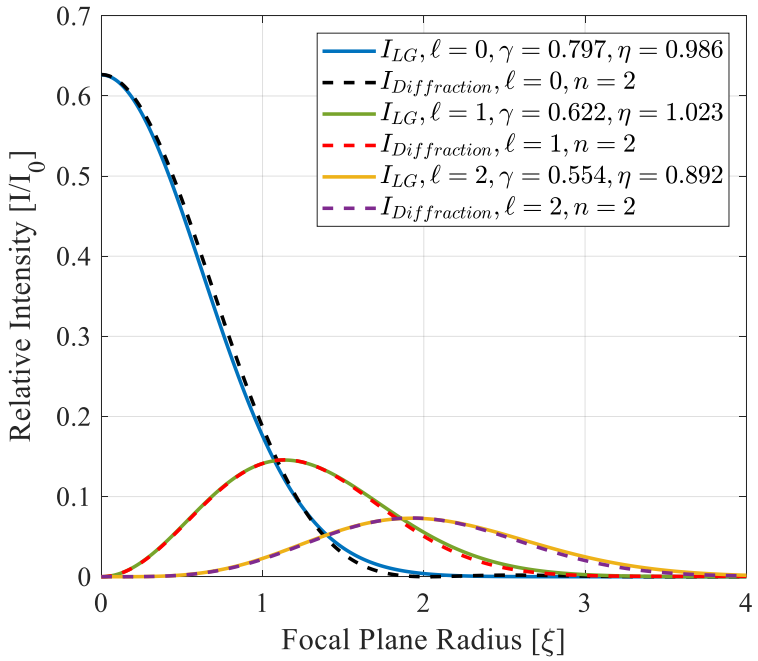

Figure 2.15: Laguerre-Gaussian beams fitted to the exact diffraction results (dashed) for OAM beams driven by $n = 2$ super-Gaussian near-field beams for $\ell = 0$, $\ell = 1$, and $\ell = 2$ topological charges.

It is quite clear to see that while the energy optimized LG modes are a rigorous method for describing the OAM beam at focus, the result is not suitable as a first order approximation. This is clear from examining Fig. 2.12. We therefore opt for the intensity fit LG modes for the rest of the thesis as these represent the diffraction solution reasonably well from the laser axis to some distance beyond the peak intensity. As we will see in the next chapters, this is primarily the region of interest when an OAM beam interacts with matter.

In this chapter, the proper diffraction intensity distribution at focus for OAM beams has been investigated with exact results given for Gaussian and flat top beam profiles. However in order to more conveniently calculate the actual interactions in the focal region, novel best fit LG mode solutions are found which can readily be applied in analysis of laser plasma interactions.

2.6 Conclusions

In this chapter, we reviewed the origins of spin and orbital angular momentum in electromagnetic waves. We explored the diffraction theory of OAM beams generated by high power laser systems, and the beam near-field profiles typically associated with them. We found that the far-field diffraction patterns produced by various near-field beams feature different relative intensity and spot sizes relative to one another.

Given the complex formulas to describe the diffraction theory far-fields, we explored two different methods of fitting paraxial Laguerre-Gaussian modes to the far-field diffraction patterns. The Laguerre-Gaussian modes offer a simpler alternative to the diffraction result and can be used for analytic and numerical modelling purposes. The fitting parameters of low-order LG modes to the far-field diffraction results for Gaussian, super-Gaussian and flat top lasers are given in Tables 2.2 and 2.3.

Chapter 3

Relativistic Electrodynamics of Optical Vortices

The interaction of electromagnetic waves with matter is largely dominated by its interaction with electrons, either as free electrons in a metal or as bound electrons in a gas or dielectric material. To understand the nature of the interaction of intense electromagnetic radiation with electrons - both bound and unbound, it is also important to understand the ionization of electrons from atoms and then how these ionized electrons respond to intense electromagnetic waves.

In this chapter, we approach this problem from a classical viewpoint where we treat the electrons as massive point-like charged particles and the incident radiation as a wave rather than a set of discrete photons. The quantum mechanics of the interaction of photons, specifically those carrying both spin and orbital angular momentum, with atoms and free electrons is beyond the scope of this work. There is a significant amount of literature on the problem of the interaction of OAM photons with bound and free electrons [123], and more recently on exploring the relativistic quantum electrodynamics of OAM photons with electrons [10, 20].

We review some of the literature on current models of electric and magnetic fields at focus, and then derive the symmetric first order paraxial fields of a general Laguerre-Gaussian mode at focus for the first time. We then study the trapping of electrons within these fields due to the ponderomotive force, and the subsequent scattering and net angular momentum transfer in the nonlinear regime. In addition, a calculation of relativistic Thomson scattering is given which can be extended to the case of OAM modes in the future.

The work in this chapter has not yet been published, however it has formed much of the basis for an experimental study of relativistic Thomson scattering of electrons from high intensity Gaussian beams published in 2019 [67]. Future work hope to extend this work to include beams carrying OAM as outlined in this chapter.

3.1 Electrodynamics of Plane Waves

We begin by reviewing the well-understood interaction of an infinite plane-wave with a free electron as outlined in almost every laser-plasma physics textbook.

We define the electric and magnetic fields of an elliptically polarized infinite plane wave by a magnetic vector potential propagating in the $\hat{z}$ direction in the Lorenz gauge,

$$\boldsymbol{a} = a_0 \left[(1-\delta^2)^{1/2} \sin(\omega t - kz)\hat{x} + \delta \cos(\omega t - kz)\hat{y}\right] \tag{3.1}$$

Here we introduce the normalized wave amplitude a_0,

$$a_0 = \frac{eA_0}{m_e c} = \frac{eE_0}{m_e c\omega} \tag{3.2}$$

and the polarization parameter δ such that when $\delta = (\pm 1, 0)$ the wave is linearly polarized, and for $\delta = \pm 1/\sqrt{2}$, the wave is circularly polarized. We also introduce the electron mass m_e, and the peak laser electric field strength E_0.

The primary force acting on a charged particle in an electromagnetic field is given by the relativistic Lorentz force equation,

$$\frac{d\boldsymbol{p}}{dt} = q(\boldsymbol{E} + \boldsymbol{v} \times \boldsymbol{B}) \tag{3.3}$$

where $\boldsymbol{v}$ is the instantaneous particle velocity, q is the particle charge, and $\boldsymbol{p}$ is the relativistic momentum vector:

$$\boldsymbol{p} = \gamma m_0 \boldsymbol{v} = \frac{m_0 \boldsymbol{v}}{\sqrt{1 - \frac{v^2}{c^2}}} \tag{3.4}$$

where γ is the Lorentz factor for relativistic motion, not to be confused with optimal beam waist parameter from the last chapter. Additionally, it is possible to show that the time evolution of the energy of a charged particle in an electromagnetic wave may

be given by [84],

$$\frac{d}{dt}(\gamma m_0 c^2) = q(\boldsymbol{v} \cdot \boldsymbol{E}) \tag{3.5}$$

We define the mass of the particle as m_0 so not to be confused with the relativistic mass $m = \gamma m_0$.

Using the relation from Eq.2.18 and the plane wave relation $\boldsymbol{E} = -\partial \boldsymbol{A}/\partial t$, we can rewrite the perpendicular Lorentz force in terms of the magnetic vector potential for a linearly polarized plane-wave,

$$\frac{d\boldsymbol{p}_\perp}{dt} = q\frac{\partial \boldsymbol{A}}{\partial t} + qv_z\frac{\partial \boldsymbol{A}}{\partial z} \tag{3.6}$$

Noting that the Eulerian derivative can be given by,

$$\frac{d}{dt} = \frac{\partial}{\partial t} + \boldsymbol{v} \cdot \nabla \tag{3.7}$$

we can write the first constant of motion:

$$\frac{d}{dt}\left(\boldsymbol{p}_\perp - q\boldsymbol{A}\right) = 0 \tag{3.8}$$

This result is also true for elliptical and circular polarization. A similar method can be applied to the longitudinal motion of a charged particle by subtracting Eq.3.5 from Eq.3.3 to yield the second constant of motion,

$$\frac{d}{dt}\left(\boldsymbol{p}_z - \gamma m_0 c\right) = 0 \tag{3.9}$$

These results are fundamental to the general study of charged particles in plane waves, however the results can be extended to more general waves that can be treated *locally* like plane waves - that is, the spatial variation of the electric field strength is much larger than the oscillation length of the electron.

If we consider the solutions of the constants of motion for an electron, it is possible to write the momentum in an elliptically polarized plane electromagnetic wave as [56],

$$\frac{\boldsymbol{p}_\perp}{m_e c} = a_0\left[\delta\cos(\omega t - kz)\hat{x} + \left(1-\delta^2\right)^{1/2}\sin(\omega t - kz)\hat{y}\right] \tag{3.10}$$

and,

$$\frac{p_z}{m_e c} = \frac{a_0^2}{4}\left[1 + \left(2\delta^2 - 1\right)\cos(2(\omega t - kz))\right] \tag{3.11}$$

These equations are then simply integrated over time to obtain the position as a function of time in the laboratory frame,

$$kx = \delta a_0 \sin(\omega t - kz) \tag{3.12}$$

$$ky = -\left(1-\delta^2\right)^{1/2} a_0 \cos(\omega t - kz) \tag{3.13}$$

$$kz = \frac{a_0^2}{4}\left[(\omega t - kz) + \frac{2\delta^2 - 1}{2}\sin(2(\omega t - kz))\right] \tag{3.14}$$

While the transverse oscillations are a direct result of the charged particle interacting with the electric field of the laser, the forward velocity of the particle is a result of the magnetic field term in the Lorentz force. Time averaging Eq's.3.10 and 3.11 over one laser period yields no net momentum in the transverse direction, however we find a forward drift velocity of the electron,

$$\left\langle \frac{p_z}{m_e c} \right\rangle = \frac{a_0^2}{4} \tag{3.15}$$

These results are summarized in Fig.3.1. Here, Fig.3.1 a), gives the evolution of the particle position in the polarization plane of a linearly polarized beam. The momentum in the transverse plane in summarized in the phase space given in Fig.3.1 c) which shows a closed loop indicating no net momentum gain or loss over one laser cycle. The z momentum phase space is give in Fig.3.1 e) where the red dotted line gives the average drift velocity.

The right hand side panel in Fig.3.1 (b,d,e) give similar plots but for an electron in a circularly polarized laser field carrying spin angular momentum. The trajectory of the electron is fundamentally different following orbits around an axis of radius $k\delta a_0$. Just like the case of a linearly polarized wave, the electron gains no net momentum in the transverse direction, but does still retain an average drift velocity forward from the Lorentz force. In addition, the electron gains an orbital angular momentum. While the electron does have a spin angular momentum of $\hbar/2$, we do not consider the spin-orbit interaction here and are only concerned with the orbital angular momentum the electron gains. Using the definition of orbital angular momentum given in Eq.2.14 we find the value to be given by,

$$L_z\left(\delta = \frac{1}{\sqrt{2}}\right) = (\boldsymbol{r} \times \boldsymbol{p})_z = \frac{a_0^2 m_e c}{2k} = \frac{a_0^2 m_e c^2}{2\omega} \tag{3.16}$$

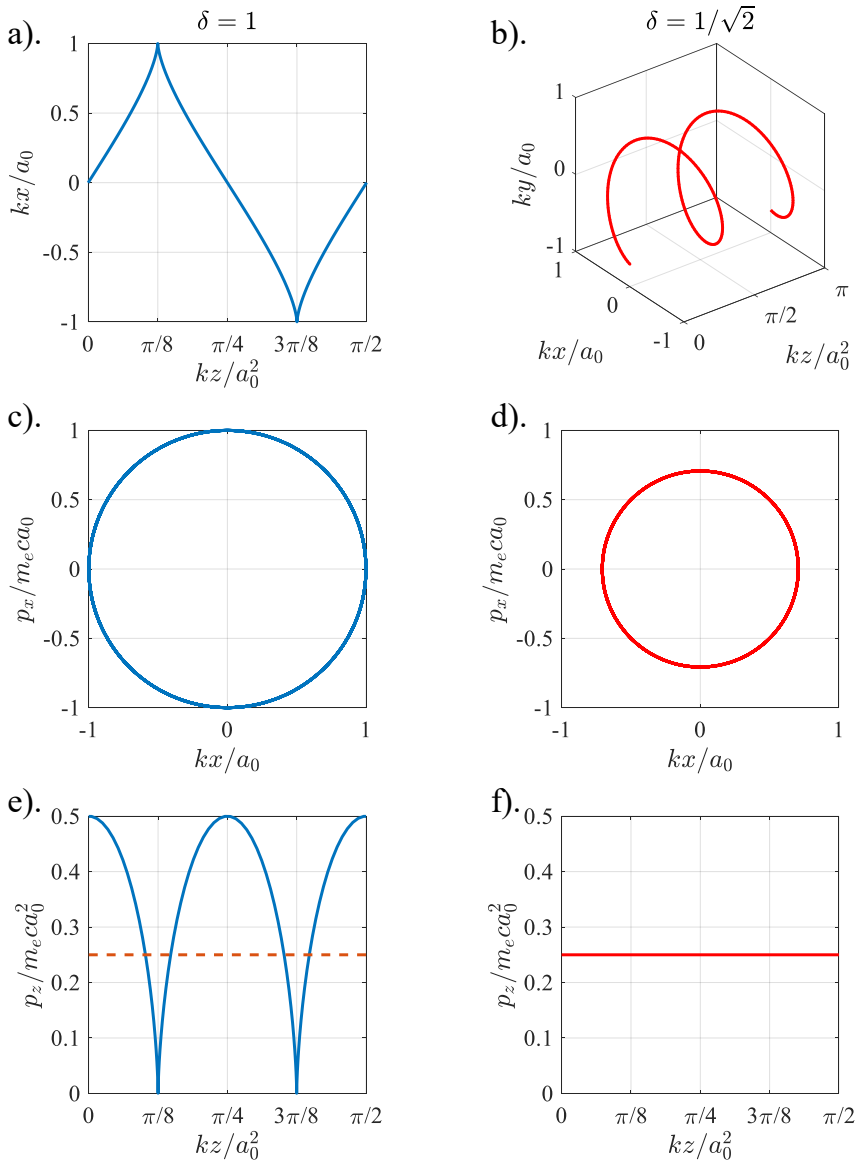

Figure 3.1: Phase space diagrams for an electron in a linearly polarized plane wave (left-blue), and in a circularly polarized plane wave (right-red).

Each photon in the incident wave carries an energy of $\hbar\omega$, and a spin angular momentum of $\pm\hbar$. Relating the wave vector k of the incoming beam to each photons energy allows us to estimate the angular momentum absorption of the incoming beam per electron. For instance, if we consider a laser with wavelength 800nm and a peak intensity of $a_0 = 1$, we find the total orbital angular momentum absorbed by the electron is,

$$L_z(800nm, a_0 = 1) = 1.739 \times 10^{-29} \frac{kgm^2}{s} \approx 164859\hbar \tag{3.17}$$

or roughly, it absorbs 164859 photons. We can compare this number of photons absorbed with the estimate given by the energy absorbed by the electron. The peak kinetic energy the electron reaches is found from,

$$U = (\gamma - 1)m_e c^2 \tag{3.18}$$

where γ is found from Eq.3.9. Taking the the phase of the plane wave to be zero; $\omega t - kz = 0$, we find the peak kinetic energy of the electron in the same laser to have a similar form to the result in Eq.3.16 bar a factor of ω,

$$U(800nm, a_0 = 1) = \frac{a_0^2}{2} m_e c^2 = 4.094 \times 10^{-14} \frac{kgm^2}{s^2} \approx 164859\hbar\omega \tag{3.19}$$

The electron therefore absorbs both energy and spin angular momentum from the photons at the same rate. It is therefore possible for an electron in a plane electromagnetic wave to absorb energy, linear momentum, and angular momentum.

From the given relations, the value of a_0 can be seen to have an important effect on the motion of electrons in an electromagnetic wave. By its definition, we find that the value of a_0 corresponds to the value of A_0 normalized to the rest-mass energy of an electron (in the Gaussian unit system). In this sense, we understand that an electromagnetic field of strength $a_0 \approx 1$ can accelerate an electron from rest, to its rest mass energy in half a laser cycle. We therefore say that a beam with $a_0 \geq 1$ is relativistic. A beam where the opposite is true; $a_0 < 1$, is non relativistic. A useful formula for determining the strength of a laser field is given by [97],

$$a_0 = 0.85 \left(\frac{I\lambda_{\mu m}^2}{10^{18} W cm^{-2}} \right)^{1/2} \tag{3.20}$$

For instance, a titanium:sapphire laser typically lases with a wavelength of $0.8\mu m$,

and can produce laser intensities above $10^{21} W cm^{-2}$ [132]. To obtain an a_0 of 1, the peak intensity should be no less than $2.16 \times 10^{18} W cm^{-2}$ which is certainly obtainable on many large scale titanium:sapphire laser systems. At relativistic intensities, the contribution from the magnetic field also becomes important as can be seen by Eq.3.15 due to the squaring of the a_0 parameter.

One issue with our model so far is that it assumes infinite plane waves. We have already argued that plane waves can be useful to approximate a laser beam if the transverse spatial extent of the laser and its associated gradients are much larger than the oscillation range of the electron, such that we can model laser beams reasonably accurately as plane waves. However we are still assuming that the laser is infinite in is longitudinal extent - that is it is a continuous beam. In order for a laser to obtain these relativistic intensities, it is necessary for the laser to be pulsed such that the peak power of the laser can reach the multi-terawatt level. Typically, the laser pulses emitted from an amplifier are Gaussian in shape but can in principle be shaped to any temporal profile desirable.

We introduce a temporal envelope to the continuous laser by convolving the normalized temporal pulse shape to the magnetic vector potential,

$$\boldsymbol{A} = a_0 g(t) \cos(\omega t - kz) \tag{3.21}$$

where $g(t)$ is the temporal envelope. While this is a simple method of shaping the pulse for analytic models, it is not adiabatic if the pulse shape is comparable to the laser frequency. For the pulse shape to satisfy the adiabatic approximation, the pulse shape must change slowly relative to the laser frequency,

$$\frac{dg(t)}{dt} \ll \omega g(t) \tag{3.22}$$

Assuming the laser pulse temporal shape can be given by,

$$g(t) = exp\left(-\frac{t^2}{w_t^2}\right) \tag{3.23}$$

and taking the point of steepest gradient,

$$\frac{d^2 g(t)}{dt^2} = 0 \tag{3.24}$$

we find the fastest changing point in the Gaussian shape to be at $t = w_t/\sqrt{2}$. Plugging this value of time into Eq. 3.22, we find the relation,

$$\sqrt{2} \ll \omega w_t \tag{3.25}$$

For a Gaussian temporal pulse shape in the optical frequency, we typically find the temporal beam waist $2w_t$ ranging from roughly 30 femtoseconds up to and beyond nanoseconds. For an 800nm beam, we find the product of $w_t\omega \approx 35 \gg \sqrt{2}$, such that the adiabatic approximation is satisfied for the pulse duration's common to the methods presented in this thesis.

To simulate the evolution of the electron in a short laser pulse and to test the adiabatic approximation, we integrate the Lorentz force numerically using an adaptive Runge-Kutta algorithm developed in MATLAB. Fig.3.2 shows the evolution of an electron through a pulsed, linearly polarized plane wave of duration 30fs. It is clear to see the electron gains energy according to Eq.3.19 in tile b), but as the electron leaves the laser pulse, it gives the energy back to the laser and there is no net transfer of energy to first order. We also observe the phase space of the electron in tile c) to be no longer confined to a circle as in Fig. 3.1. The electron slowly gains momentum as the laser intensity increases, and as such, the phase space radius increases. As the electron gives its energy back to the laser, the radius decreases and the electron closes the loop. As expected, tile d). shows the electron gains no angular momentum while interacting with a linearly polarized plane wave.

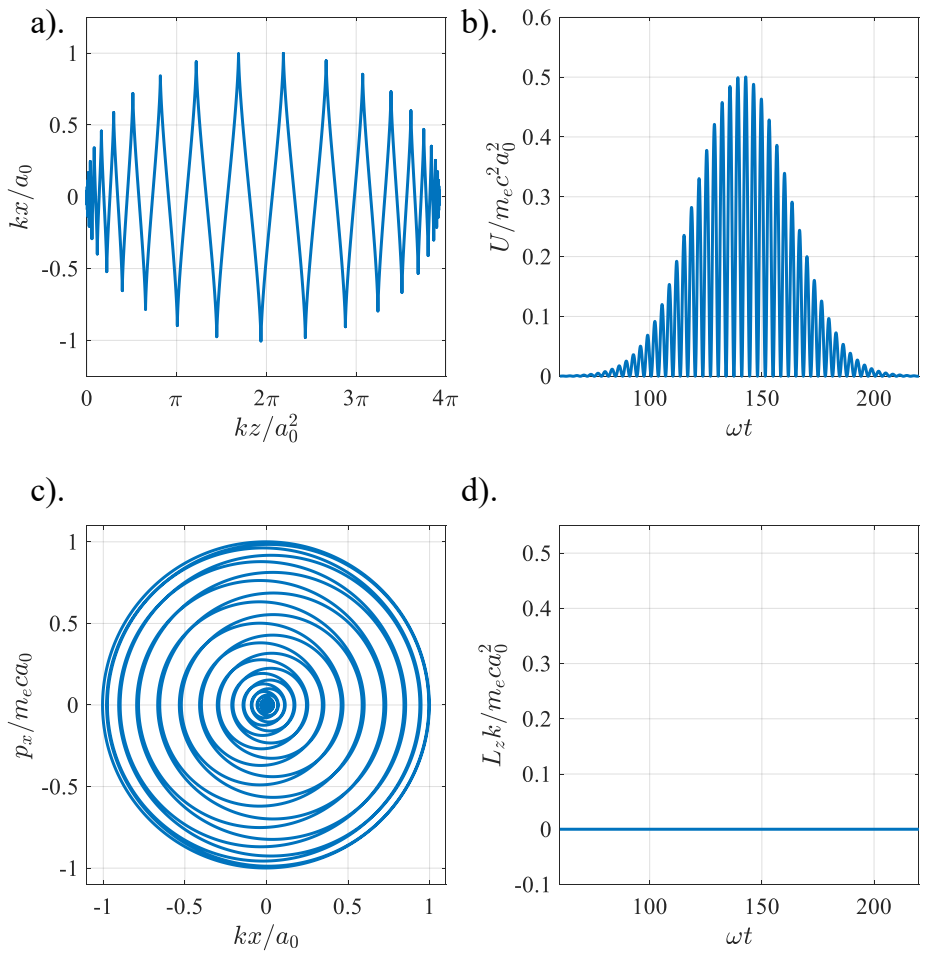

Figure 3.2: Phase space diagrams for an electron in an 800nm, linearly polarized plane wave with a Gaussian temporal shape and a full-width half maximum of 30fs. The axes have been normalized to the relevant parameters in the given equations.

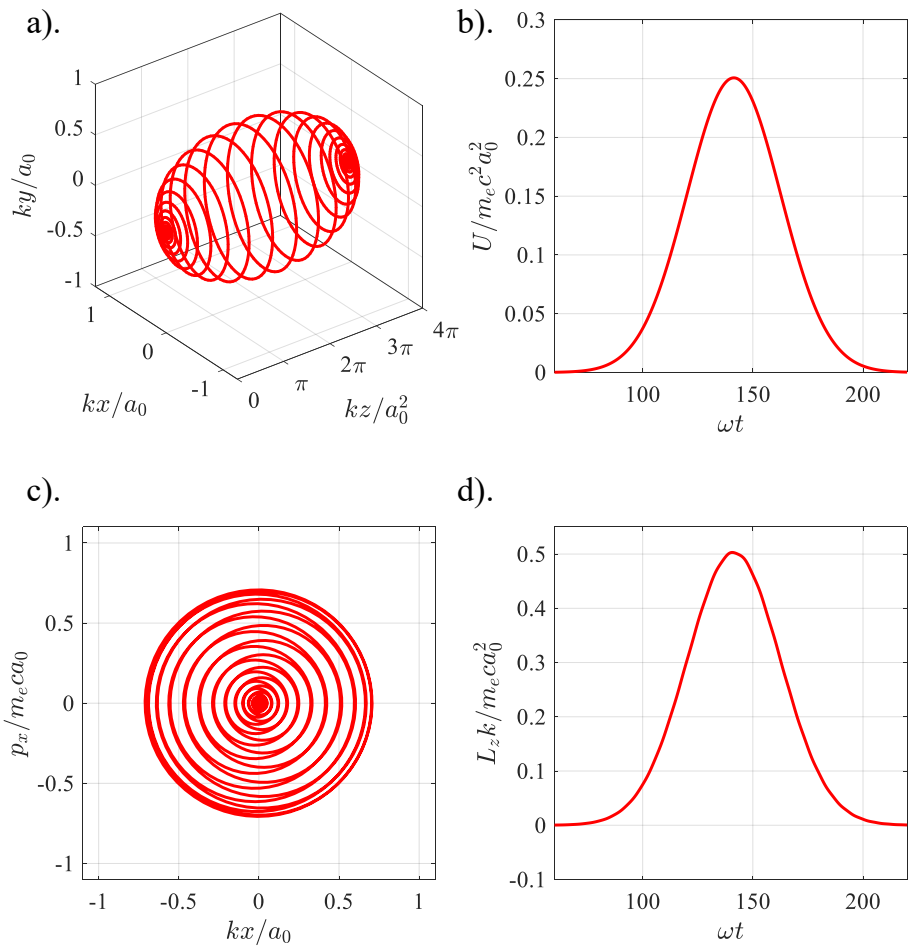

Figure 3.3: Phase space diagrams for an electron in an 800nm, circularly polarized plane wave with a Gaussian temporal shape and a full-width half maximum of 30fs. The axes have been normalized to the relevant parameters in the given equations.

If we examine the case of a finite circularly polarized plane wave, we find the electron behaves as expected and follows a helical motion as shown in tile a) of Fig.3.3. The peak energy acquired by the electron in tile b) is half of that of a linearly polarized pulse but does not oscillate as the case before. Most interestingly is tile d) which shows the orbital angular momentum of the electron as a function of time. Here we see good agreement with the peak value of the orbital angular momentum given by Eq. 3.17.

We find that in both linear and circular polarization cases, the energy of the electron before and after interacting with the laser pulse remains zero in agreement with the adiabatic approximation. We note that the initial conditions for the simulation require that the electron be at rest and sufficiently far from the laser. If this were not the case, and the electron were born in the laser - perhaps through ionization, then the final energy of the electron will be non-zero.

The phenomenon that an electron given the right initial conditions cannot gain energy from a laser pulse has stirred controversy in the literature over the years, and many schemes have been put forward to develop direct-laser acceleration schemes that circumvent this. For instance, an 800nm laser with $a_0 = 1$ has an electric field strength of $\approx 4TV/m$, much greater than that of a conventional accelerator ($\approx 100MV/m$). If this electric field could be exploited directly, the size and cost of accelerators could be reduced greatly. In the next section we explore the governing physics of this problem and some of the proposed solutions.

3.1.1 Lawson-Woodward Theorem

Perhaps one of the most important results of single particle electrodynamics is the Lawson-Woodward theorem [85]. In essence, it is a simple proof that shows that there can be no net energy transferred to an electron from a finite laser pulse. While we omit the proof here, there is a great deal of literature exploring the subject [41]. In summary, the Lawson-Woodward theorem states that there can be no net transfer of energy to an electron if the following conditions are met [56, 41];

1. the laser field is in vacuum, with no interfering walls or boundaries,
2. the electron is highly relativistic along the acceleration path,
3. no static electric or magnetic fields are present,
4. the interaction region is infinite,
5. ponderomotive forces are neglected.

Of course, it is clear on how we can break some of rules with ease, some being more effective than others. We will address point 5 in the next section, but the other points will be discussed here.

In order to accelerate an electron directly from the laser electric field, we can consider firstly that the laser could be propagating in a media, perhaps a dielectric in which we would violate the first point. When a laser reaches high intensities, particularly above $1 \times 10^{14} Wcm^{-2}$, it is able to ionize material and as such cannot propagate through the media without turning it into a plasma. Alternatively one could consider reflecting a high intensity laser from an ionizable surface like a dielectric or metallic mirror. In this case electrons can be ionized and injected into the laser pulse close to the peak intensity and as a result be accelerated to high energy breaking both rules 1 and 4. The final energy of the electron is however sensitive to the phase of the laser and can lead to a large bandwidth in the ejected electron energies [156]. This is illustrated by injecting an electron into various phases of the laser in Fig.3.4. It is clear to see that the optimal injection point into the pulsed plane wave is found to be at $z_0 = \lambda/4$. Increasing the injection point beyond this position only decreases the final electron energy but is not shown here.

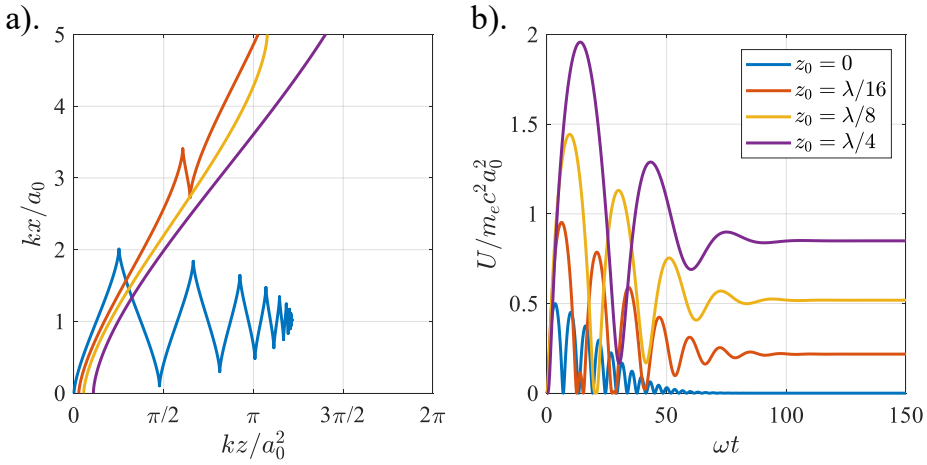

Figure 3.4: Electron position (a) and energy (b) for various injection points (z_0) into a linearly polarized plane wave 30fs laser pulse. Here, z_0 corresponds to $\cos(\phi) = 1$, and the field is maximal.

Of the other items on the list, point 3 holds large potential for accelerating electrons to very high energies. In this scenario, a background static electric or magnetic

field is imposed on the interaction region breaking the symmetry of the laser pulse electric and magnetic fields. This could be imposed in many different ways, either with some high voltage plates around the interaction region to generate the desired electric field, or by some method to generate a strong axial magnetic field such as a high current coil.

An interesting case is that of a static magnetic field aligned along the laser propagation axis. The magnetic field strength is tuned such that the electron cyclotron frequency is matched to that of the laser frequency,

$$\omega_L = \omega_c = \frac{eB}{\gamma m_e} \tag{3.26}$$

where ω_L is the laser frequency. Assuming that the electron is initially non-relativistic ($\gamma = 1$), we can write the required magnetic field strength for the laser cyclotron heating of an electron,

$$B = \frac{2\pi m_e c}{e\lambda} \tag{3.27}$$

For a laser wavelength of 800nm, we find a required magnetic field of ≈13387T which is far above what is currently available in the laboratory. The energy as a function of time for the electron in this case is given in Fig.3.5 for various laser intensities. A surprising result is that an electron will acquire more energy from a lower intensity than than one at relativistic intensity. As one can see from the tile a) in Fig.3.5, the electron becomes relativistic quickly and the matching condition of Eq.3.27 is no longer valid. As the electron acceleration is lower with the lower intensity, it can maintain its phase with the laser for a longer period of time, and gain an overall increase in energy.

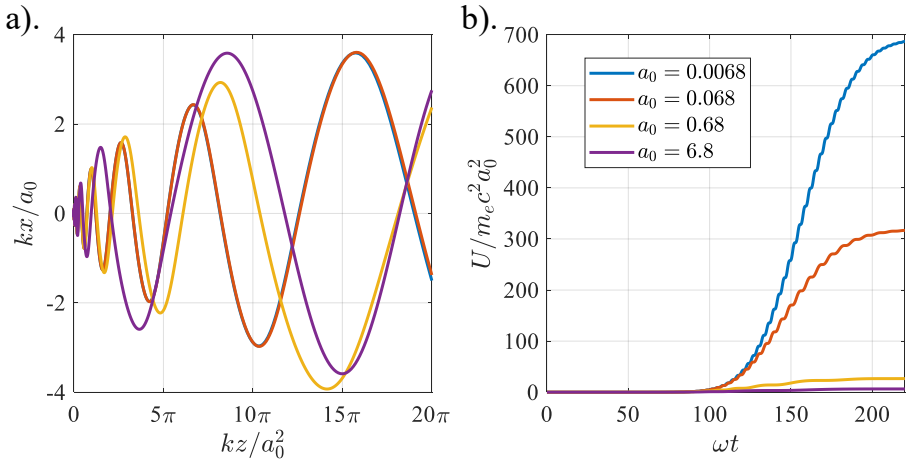

Figure 3.5: Electron position (a) and energy (b) for various laser intensities in a 30fs linearly polarized plane wave of wavelength 800nm and axial magnetic field of $B_z = 13387T$.

This is all assuming that the laser be infinitely wide and as we go to finite sized pulses, we will find that other effects such as ponderomotive forces can eject the electron from the laser before it has had sufficient time to gain energy. This is overcome by simply focussing the laser to a larger spot size. Another key challenge in laser-cyclotron resonance acceleration is the high B-field requirement. As one can clearly see, the magnetic field required for an 800nm beam is currently beyond the capabilities of laboratory magnetic fields. Noting the required magnetic field is inversely proportional to the laser wavelength, we could lower the B-field requirement significantly by using a longer wavelength. A carbon dioxide laser for instance typically lases at $10.6\mu m$ requiring a magnetic field of 1010T which is obtainable with today's technology [142]. Current research is also exploring the use of THz radiation to drive electron cyclotron acceleration which would only require a B field on the order of 10's of Tesla which is certainly obtainable using superconducting magnets and pulsed power coils.

Most direct laser acceleration schemes with the exception of laser cyclotron heating involve injecting the electron somehow into the laser beam through an ionization

process that allows the electron to be born at the optimal point. Once inside the laser, the laser electric and magnetic fields can accelerate the electron to relativistic speeds typically by the transverse electric field.

As we will show in section 3.3, a finite laser pulse and more so, a tightly focussed laser pulse can have a large axial electric field component. The shape and size of this axial electric field depends on many parameters, including the mode of the laser. Higher order laser modes, like the Laguerre-Gaussian modes can have structured axial electric fields, some of which can be useful for direct laser acceleration. Of particular interest is the axial fields of a radially polarized Laguerre-Gaussian mode which look to be the most promising candidate for direct laser acceleration due to their long non-oscillating axial electric field [41]. Alternatively, people have looked at beating two modes together [41] which may be simpler than generating high intensity radially polarized beams in the lab.

3.2 Relativistic Ponderomotive Force

Contrary to the conclusion of the Lawson-Woodward theorem, it is in fact possible to transfer energy to electrons while obeying the first 4 criteria from the last section. The radiation pressure of a light wave can be thought of as the exchange of photon momentum ($p = \hbar k$) when reflecting from a surface. Due to the conservation of momentum, an equal and opposite momentum must be imposed on the reflecting surface and given the number of photons in a high-power laser can be on the order of 10^{20}photons, there can be a significant momentum transferred to the reflector.

The ponderomotive force is similar but rather a result of gradient of the electric field instead. Consider a tightly focussed Gaussian beam with an electron oscillating close to the axis of the laser. The symmetry of the electric field in the laser pulse is broken due to the decrease in electric field strength as the radius increases. As the electron oscillates back and forth in this field, it will see a stronger electric field on one half of its oscillation than the other. This will in turn cause the electron to drift, and in fact be accelerated away from the region of high field. As the ponderomotive force is a function of the shape of the electric field, it changes for higher order laser modes and as such it is fundamentally different to a Gaussian mode.

As we have shown in the last chapter, non-planar solutions to the Helmholtz equation that do not constitute an infinite amount of energy have a finite spatial

extent both radially, and temporally. If we consider a non-relativistic beam ($a_0 \ll 1$) that is polarized in the $\hat{x}$ direction, then a good approximation to the particle motion can be given purely by the electric field term of the laser,

$$\frac{dp_x}{dt} = qE_x(\boldsymbol{r}) \tag{3.28}$$

where $\boldsymbol{r}$ denotes the radial dependence of the electric field shape,

$$E_x(\boldsymbol{r}) = E_0(\boldsymbol{r})\cos(kz - \omega t) \tag{3.29}$$

If we Taylor expand the electric field in one dimension (x), then we can rewrite the electric field as,

$$E_x(\boldsymbol{r}) \approx E_0(x)\cos(kz - \omega t) + x\frac{\partial E_0(x)}{\partial x}\cos(kz - \omega t) + ... \tag{3.30}$$

To first order, we can write the momentum of the electron as,

$$p_x^{(1)} = -v_{os}\sin(kz - \omega t) \tag{3.31}$$

where $v_{os} = a_0 c$, and the electron position is given as,

$$x^{(1)} = \frac{v_{os}}{\omega}\cos(kz - \omega t) \tag{3.32}$$

Plugging these results back into Eq.3.28, we find the second order correction to the Lorentz force as,

$$\frac{dp_x^{(2)}}{dt} = -\frac{e^2}{m_e\omega^2}E_0\frac{\partial E_0(x)}{\partial x}\cos^2(kz - \omega t) \tag{3.33}$$

Time averaging over one laser cycle we find the non-relativistic ponderomotive force for an electron,

$$F_p = -\frac{e^2}{4m_e\omega^2}\frac{\partial}{\partial x}\left|E_0(x)\right|^2 \tag{3.34}$$

This can be further generalized to 3 dimensions,

$$\boldsymbol{F}_p = -\frac{e^2}{4m_e\omega^2}\nabla\left|E\right|^2 = -m_e c^2\nabla\left|\frac{a}{2}\right|^2 \tag{3.35}$$

Extending this to include relativistic field intensities is not trivial and is quite

involved as the magnetic $\boldsymbol{v} \times \boldsymbol{B}$ term has to be included [56]. As such we just state the relativistic result here [97],

$$\boldsymbol{F}_p = \frac{dp_s}{dt} = -m_e c^2 \nabla \left(\sqrt{1 + \langle a^2 \rangle} - 1 \right) \tag{3.36}$$

where p_s is the slow (non oscillatory) motion of the electron and $\langle a^2 \rangle = a_0^2/2$. There are alternate formulations of this result such as that in Quesnel [126]. In general, we find the electron gains a maximal velocity equal to,

$$\frac{p_s}{m_e c} = \frac{a_0^2}{4} \tag{3.37}$$

which is the same result we found in Eq.3.15. As one can see, the force is dependant on the gradient of the electric field squared, or the intensity. Given the nature of an OAM beam with an intensity null on axis, it becomes possible to trap and guide particles within the beam. We will explore this trapping in section 3.4, but we must first determine the electric and magnetic fields of the OAM modes.

3.3 The Electric and Magnetic Fields of a Laguerre-Gaussian Mode

While the electric and magnetic fields of the plane wave can be written down simply as a single polarization component, it is not clear as to what the full field equations of a laser beam are at this point. It is a simple proof to show that any beam containing a transverse dependence cannot satisfy Maxwell's equations with a single polarization component. For instance if we consider a beam with some radial dependence polarized only in one direction,

$$\boldsymbol{E} = E_0 f(r, \theta) e^{i(kz - \omega t)} \hat{x} \tag{3.38}$$

We find that the divergence of the electric field cannot be satisfied in vacuum,

$$\nabla \cdot \boldsymbol{E} = \frac{\partial E_x}{\partial x} = E_0 e^{i(kz - \omega t)} \frac{\partial f(r, \theta)}{\partial x} \neq 0 \tag{3.39}$$

In general, for any beam of finite radius there must be more than one component of the electric field in order to satisfy Maxwell's equations in vacuum. As previously shown, we know that a beam must satisfy the Helmholtz equation (Eq.2.11). In the

paraxial Helmholtz equation (Eq.2.34), we found cylindrical scalar solutions in the form of the Laguerre-Gaussian basis set, but we have not yet given the polarization components of the fields required to satisfy Maxwell's equations.

There are multiple methods available to derive the components of the fields, each with their advantages and disadvantages. Fortunately for the work completed in this thesis, we are mostly concerned with beams that are paraxial and do not require the high-order accuracy of non-paraxial solutions that usually consist of non-analytic integrals and Hankel transforms.

3.3.1 Paraxial Fields

As previously discussed, the paraxial approximation is satisfied when the beam is not tightly focussed which is implied from Eq.2.32. A good rule of thumb is that a beam focussed with an f-number of $f/\# \geq 4$ can be treated as paraxial, where the f-number is given by,

$$f/\# \approx \frac{f}{2w_0} \tag{3.40}$$

where f is the focal length of the optic.

If we use the Lorenz gauge such that,

$$\partial^\mu A_\mu = 0 \tag{3.41}$$

then we can define a vector potential that satisfies the Helmholtz equation, Maxwell's equations, and the gauge condition with one polarization component,

$$\boldsymbol{A} = \psi(x, y, z)e^{i(kz-\omega t)}\hat{x} \tag{3.42}$$

The magnetic field is then easily found from the curl of the vector potential to give the full 3D polarization components,

$$\boldsymbol{B} = \nabla \times \boldsymbol{A} = \frac{\partial A_x}{\partial z}\hat{y} - \frac{\partial A_x}{\partial y}\hat{z} \tag{3.43}$$

If we ignore $\partial\psi/\partial z$ compared to the $k\psi$ term, we are left with a simple but elegant formula [66],

$$\boldsymbol{B} = B_0 \left[\hat{y} + \frac{i\hat{z}}{k}\frac{\partial}{\partial y}\right] \psi(x, y, z)e^{i(kz-\omega t)} \tag{3.44}$$

This is valid for any wavefunction ψ that satisfies the paraxial Helmholtz equation.

Moving on to solve for the electric field becomes a little more difficult due to the multiple vector calculus operators in Eq.2.22,

$$\boldsymbol{E} = i\omega \left[\boldsymbol{A} + \frac{1}{k^2} \nabla(\nabla \cdot \boldsymbol{A}) \right] = i\omega \left[A_x + \frac{1}{k^2} \left(\hat{x} \frac{\partial^2}{\partial x^2} + \hat{y} \frac{\partial^2}{\partial x \partial y} + \hat{z} \frac{\partial^2}{\partial x \partial z} \right) A_x \right] \quad (3.45)$$

On inspection, we see an issue with the fields being anti-symmetric - the B field has components in $\hat{y}$ and $\hat{z}$, whereas the electric field has components in $\hat{x}$, $\hat{y}$, and $\hat{z}$. This is due to the choice of the vector potential only existing in one polarization plane. Upon simplifying Eq.3.44, we find the asymmetric terms to be small and the remaining field can be approximately written as,

$$\boldsymbol{E} = E_0 \left[\hat{x} + \frac{i\hat{z}}{k} \frac{\partial}{\partial x} \right] \psi(x, y, z) e^{i(kz - \omega t)} \quad (3.46)$$

Using these two simple formulas, we can obtain the first order fields of the paraxial approximation given ψ. The derivatives are first order and are mostly analytical.

Some efforts have been made to add higher order terms to these expressions which has been well summarized in the paper by Peatross [122]. In this paper, Peatross takes the Ignatovsky diffraction model in which the fields are computed at focus using vector diffraction theory from the parabola, and compares it to various paraxial models. Of the methods presented, the model adopted by Erikson and Singh [38] appears to have the best reproduction of the Ignatovsky result, and luckily is one of the simplest models.

The Erikson and Singh model adds only one extra term to the previous model and is of second order,

$$\boldsymbol{E} = E_0 \left[\hat{x} + \frac{\hat{y}}{2k^2} \frac{\partial^2}{\partial x \partial y} + \frac{i\hat{z}}{k} \frac{\partial}{\partial x} \right] \psi(x, y, z) e^{i(kz - \omega t)} \quad (3.47)$$

$$\boldsymbol{B} = B_0 \left[\frac{\hat{x}}{2k^2} \frac{\partial^2}{\partial x \partial y} + \hat{y} + \frac{i\hat{z}}{k} \frac{\partial}{\partial y} \right] \psi(x, y, z) e^{i(kz - \omega t)} \quad (3.48)$$

The second derivative adds some considerable complexity to the calculation but it remains an analytic formula. The existence of $\hat{y}$ component to the electric field for a laser polarized in the $\hat{z}$ may seem a little confusing. This can be understood as a component that emanates from the focussing of the laser, and as we shall see, is

a small fraction of the intensity of the main polarization component. A useful tool introduced by Peatross for calculating these fields is to introduce the complex beam parameter,

$$Z = z_0 + iz \tag{3.49}$$

This allows us to separate the r and z dependence in Eq.2.34, yielding the Laguerre-Gaussian mode in the modified (elegant) form [11],

$$\psi_{\ell,p}(r,\theta,z) = C\left(\frac{r\sqrt{2}}{w(z)}\right)^{|\ell|}\left(\frac{z_0}{Z}\right)^{2p+|\ell|+1} exp\left(-\frac{kr^2}{2Z}\right) L_p^{|\ell|}\left(\frac{kr^2}{Z}\right) e^{i\ell\theta} \tag{3.50}$$

where C is a normalization constant. In order to solve the analytic expressions of the electric and magnetic fields above, we need to solve three differentials; ∂_x, ∂_y, and ∂_{xy}.

We derive the the following differentials,

$$\frac{\partial\psi}{\partial x} = \psi\left[\frac{|\ell|\cos(\theta)}{r} - \frac{i\ell\sin(\theta)}{r} - \frac{kx}{Z} - \frac{2kx}{Z}L_1\right] \tag{3.51}$$

$$\frac{\partial\psi}{\partial y} = \psi\left[\frac{|\ell|\sin(\theta)}{r} + \frac{i\ell\cos(\theta)}{r} - \frac{ky}{Z} - \frac{2ky}{Z}L_1\right] \tag{3.52}$$

$$\begin{aligned}&\frac{\partial^2\psi}{\partial x\partial y} = \\ &[|\ell|\sin(2\theta) + i\ell\cos(2\theta)]\left[\frac{|\ell|-1}{r^2} - \frac{k(1+2L_1)}{Z}\right] + \frac{k^2xy}{Z^2}\left[1+4(L_1+L_2)\right]\end{aligned} \tag{3.53}$$

where,

$$L_1 = \frac{L_{p-1}^{|\ell|+1}\left(\frac{kr^2}{Z}\right)}{L_p^{|\ell|}\left(\frac{kr^2}{Z}\right)} \tag{3.54}$$

$$L_2 = \frac{L_{p-2}^{|\ell|+2}\left(\frac{kr^2}{Z}\right)}{L_p^{|\ell|}\left(\frac{kr^2}{Z}\right)} \tag{3.55}$$

Plugging the differentials into Eq 's.3.46 and 3.47 allows us to give analytic formulas for the electric and magnetic field to second order in the paraxial approximation.

Setting the normalization constant as,

$$C = \sqrt{\frac{\eta p! \bar{\gamma}^2}{(p+|\ell|)!}} \tag{3.56}$$

allows us to use the modified Laguerre-Gaussian basis set given in Eq.2.69 which has been scaled to the diffraction result. Note that here, $\bar{\gamma}$ is the beam waist parameter and not the Lorentz factor and as such has been denoted with a bar. For completeness, we will write the full electric and magnetic fields of a Laguerre Gaussian mode here,

$$\boldsymbol{E} = E_0 \begin{pmatrix} \hat{x} \\ \hat{y}\left[\frac{|\ell|\sin(2\theta)}{2} + \frac{i\ell\cos(2\theta)}{2}\right]\left[\frac{|\ell|-1}{k^2r^2} - \frac{(1+2L_1)}{kZ}\right] + \frac{xy[1+4(L_1+L_2)]}{2Z^2} \\ \hat{z}\left[\frac{\ell\sin(\theta)}{kr} + \frac{i|\ell|\cos(\theta)}{kr} - \frac{ix}{Z}(1+2L_1)\right] \end{pmatrix} \psi e^{i(kz-\omega t)} \tag{3.57}$$

$$\boldsymbol{B} = \frac{E_0}{c} \begin{pmatrix} \hat{x}\left[\frac{|\ell|\sin(2\theta)}{2} + \frac{i\ell\cos(2\theta)}{2}\right]\left[\frac{|\ell|-1}{k^2r^2} - \frac{(1+2L_1)}{kZ}\right] + \frac{xy[1+4(L_1+L_2)]}{2Z^2} \\ \hat{y} \\ \hat{z}\left[-\frac{\ell\cos(\theta)}{kr} + \frac{i|\ell|\sin(\theta)}{kr} - \frac{iy}{Z}(1+2L_1)\right] \end{pmatrix} \psi e^{i(kz-\omega t)} \tag{3.58}$$

We note that the beam waist in Z and in $\psi_{\ell,p}$ is the modified beam waist as given by Eq. 2.70. The fields are plotted in Fig.3.6 for the three polarization components for the $z = 0$ position and also plotted in Fig.3.7 for the $z = \lambda/4$ position.

These fields are in good agreement with the results of 3D PIC simulations using second order Maxwell solvers and will be discussed later. For the first time, we have developed analytic formulas that are in good agreement with the paraxial approximation to second order. A subtle result also mentioned in [122], is that the Erikson and Singh model is accurate to f-numbers below $f/2$ making this model also suitable for analytically modelling tightly focussed LG modes.

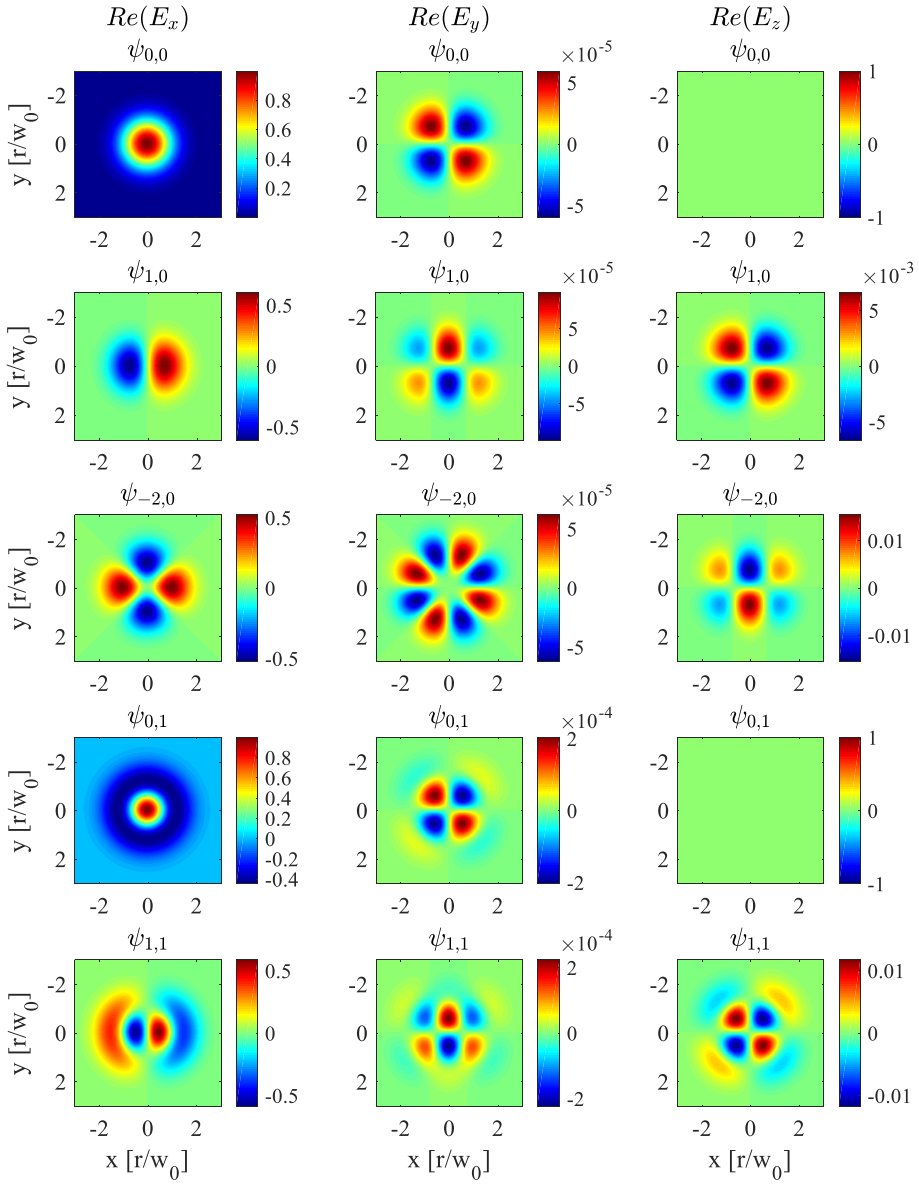

Figure 3.6: Electric field distributions various LG modes $\psi_{\ell,p}$ for $z = 0$. From left to right; $Re(Ex)$, $Re(Ey)$, and $Re(Ez)$. Colourbars are relative.

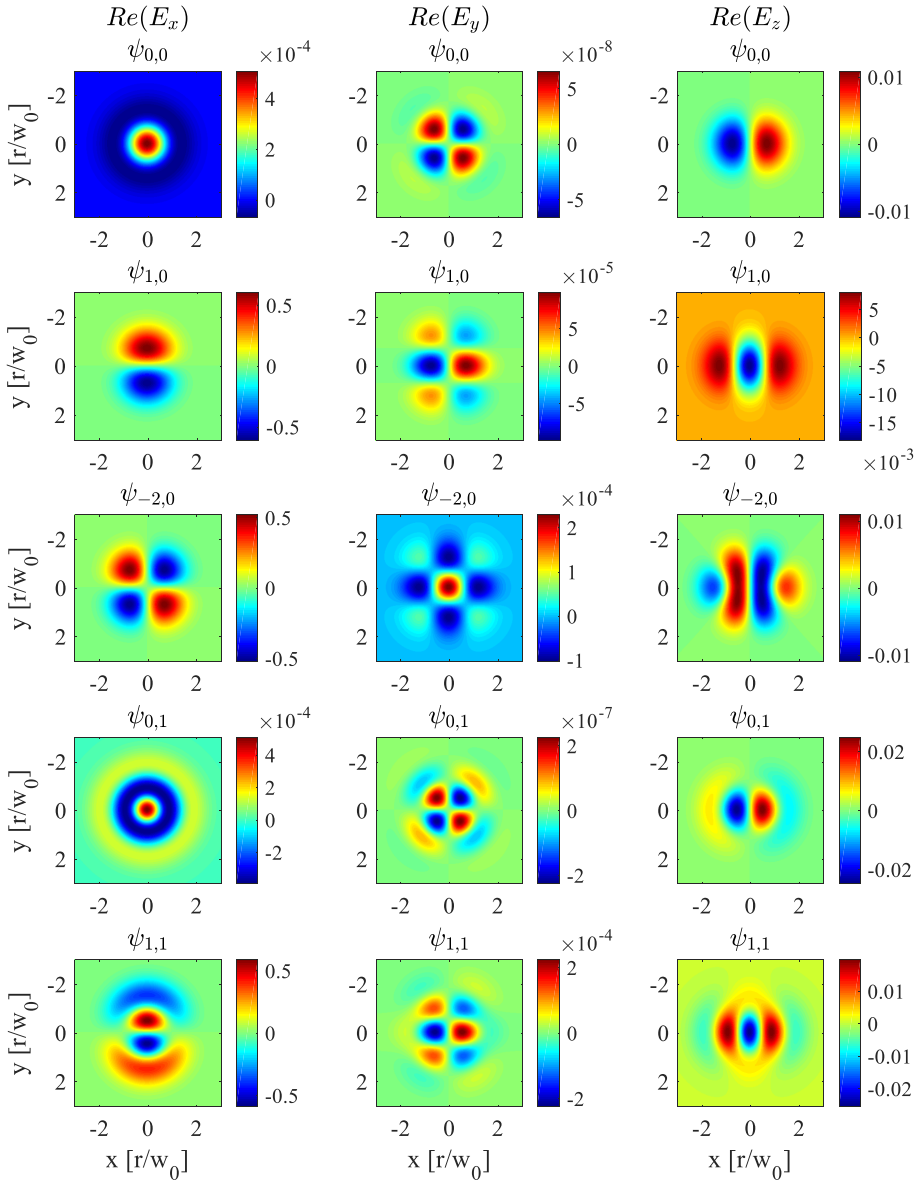

Figure 3.7: Electric field distributions various LG modes $\psi_{\ell,p}$ for $z = \lambda/4$. From left to right; $Re(Ex)$, $Re(Ey)$, and $Re(Ez)$. Colourbars are relative.

3.3.2 Non-Paraxial Fields

To go one step further and calculate the non-paraxial fields, we take the approach of using the angular spectrum representation of plane waves [58, 126]. In this method, we transform the Laguerre Gaussian mode into the spectral space via a Fourier transform. Maxwell's equations become much easier to manipulate in k space, and the complex spatial derivatives become multiplication operations. An inverse Fourier transform then brings the fields back to real space to propagate the field in the focal plane to any z position for all components.

This is easily seen by Maxwell's vacuum equations in k space,

$$\frac{\partial \tilde{\boldsymbol{E}}}{\partial t} = c^2 i\tilde{\boldsymbol{k}} \times \tilde{\boldsymbol{B}} \tag{3.59}$$

$$\frac{\partial \tilde{\boldsymbol{B}}}{\partial t} = -i\tilde{\boldsymbol{k}} \times \tilde{\boldsymbol{E}} \tag{3.60}$$

$$i\tilde{\boldsymbol{k}} \cdot \tilde{\boldsymbol{E}} = 0 \tag{3.61}$$

$$i\tilde{\boldsymbol{k}} \cdot \tilde{\boldsymbol{B}} = 0 \tag{3.62}$$

Where the tilde denotes the Fourier transformed variable. If we assume a linearly polarized Laguerre Gaussian mode that is purely an ℓ mode, we can write a simplified expression for the electric field in the $z = 0$ plane as,

$$E_x = C\left(\frac{r}{w_0}\right)^{|\ell|} exp\left(\frac{-r^2}{w_0^2}\right) e^{i\ell\theta} \tag{3.63}$$

where C is a normalization constant. Using the Fourier field allows us to propagate the solution in the focal plane to any point along z assuming the field is time harmonic. To do this, we first normalize the $\boldsymbol{k}$ vector such that,

$$\boldsymbol{k} = k(p\hat{k_x} + q\hat{k_x} + w\hat{k_z}) \tag{3.64}$$

where k is the wavevector magnitude. The Fourier transform in Cartesian coordinates is then given as,

$$\tilde{E_x}(p,q) = \frac{1}{\lambda^2}\iint E_x(x,y,0)e^{-ik(px+qy)}dxdy \tag{3.65}$$

however the Fourier transform is more suitably calculated using the polar form of the Fourier transform as given in Eq.2.54. Using our previous integration methods, and the Fourier polar coordinates, $p = \rho\cos(\phi)$ and $q = \rho\sin(\phi)$ we then yield the following integral,

$$\tilde{E_x}(\rho,\phi) = \frac{C2\pi i^\ell}{\lambda^2 w_0^{|\ell|}} e^{i\ell\phi} \int_0^\infty r^{|\ell|+1} exp\left(\frac{-r^2}{w_0^2}\right) J_\ell\left(kr\rho\right) dr \tag{3.66}$$

The integral has an analytical solution given by [60],

$$\int_0^\infty x^{\nu+1} e^{-\alpha x^2} J_\nu(\beta x) dx = \frac{\beta^\nu}{(2\alpha)^{\nu+1}} exp\left(-\frac{\beta^2}{4\alpha}\right) \tag{3.67}$$

Solving the integral and simplifying, we find the Laguerre-Gaussian field in the Fourier plane,

$$\tilde{E_x}(\rho,\phi) = \frac{Ci^\ell}{4\pi\epsilon^2} e^{i\ell\phi} \left(\frac{\rho}{2\epsilon}\right)^{|\ell|} exp\left(-\frac{\rho^2}{4\epsilon^2}\right) \tag{3.68}$$

where ϵ is given by,

$$\epsilon = \frac{1}{kw_0} \tag{3.69}$$

Propagating the field in the z direction and then taking the inverse Fourier transform,

$$E_x(r,\theta,z) = \iint \tilde{E_x}(\rho,\phi) e^{ikr\rho\cos(\theta-\phi)} e^{ikw(\rho)z} \rho d\rho d\phi \tag{3.70}$$

gives the $\hat{x}$ component of the electric field in all space. Here, $w(\rho)$ is the aperture function defined as,

$$w(\rho) = \begin{pmatrix} \sqrt{1-\rho^2} & if & \rho^2 \leq 1 \\ i\sqrt{\rho^2-1} & if & \rho^2 > 1 \end{pmatrix} \tag{3.71}$$

As we are only interested in the real field and not the evanescent solutions, we disregard solutions where $\rho^2 > 1$ and set them equal to zero. Again using the same method of integrating over the azimuthal coordinate first, we derive the following Hankel transform,

$$E_x(r,\theta,z) = \frac{Ce^{i\ell\theta}}{2\epsilon^2} \left(\frac{1}{2\epsilon}\right)^{|\ell|} \int_0^1 J_\ell(kr\rho) exp\left(-\frac{\rho^2}{4\epsilon^2}\right) e^{ik\sqrt{1-\rho^2}z} \rho^{|\ell|+1} d\rho \tag{3.72}$$

Clearly this is a non-analytic Hankel transform and must be computed numerically. However, we could use the paraxial approximation here and check we get the paraxial

result as in Eq.3.56. The paraxial equation in k space can be given as [115],

$$w(\rho) = \sqrt{1-\rho^2} \approx 1 - \rho^2/2 \tag{3.73}$$

The integral then becomes analytic using Eq.3.66 and results in the same equation as in Eq3.57.

The orthogonal components of the electric field in k space in the $z = 0$ plane can be easily found from Maxwell's equations for a linearly polarized beam,

$$\tilde{E}_z(\rho, \phi, 0) = -\frac{k_x}{k_z}\tilde{E}_x(\rho, \phi, 0) \tag{3.74}$$

The E_z field can then be given as [126],

$$E_z(r, \theta, z) = \frac{i}{k}\frac{\partial}{\partial x}\iint \tilde{E}_x(\rho, \phi, 0)\frac{e^{ikr\rho\cos(\theta-\phi)}e^{ikw(\rho)z}}{\sqrt{1-\rho^2}}\rho d\rho d\phi \tag{3.75}$$

which is clearly a non-analytic integral. The paraxial approximation could be applied here, but the algebra is challenging and will result in what we have already found in Eq.3.57.

As before, we have a problem with symmetry in this solution as we assumed that there was no $\hat{y}$ component in Eq.3.73 even though we have previously shown that this is a requirement for symmetric fields. The solution to this using the angular spectrum method is to compute the $\boldsymbol{E}$ and $\boldsymbol{B}$ fields from a known E_x field at focus, and then again from a known B_y field at focus. The average of each field is then taken to obtain the 6 vector field components.

Given the complexity, and little advantage in having non-paraxial solutions for our problems, we do not pursue this any further. The fields must be computed via a numerical Hankel transform, and while there are fast algorithms for this [144], the additional computational overhead when computing 1000's of time steps can be too much. One approach could be to compute the fields at regular nodes in 3D space, and then interpolate the fields in between, but the fields must be pre-computed and will only be valid within the initial boundaries computed.

3.4 Trapping Within an Optical Vortex

We have now derived the analytic second order paraxial field equations for an arbitrary Laguerre-Gaussian mode, giving us the necessary tools to model how an electron will move through these fields. Given the form of Eq's 3.57 and 3.58, it is not possible to integrate these fields in the Lorentz equations analytically. We must therefore use an adaptive Runge-Kutta algorithm developed in MATLAB as outlined in the appendix. As a result, the physics of the ponderomotive force is implicit in the solutions and as such we can start to explore the fundamental differences between a Gaussian and Laguerre-Gaussian beam.

Given the donut shape of the LG mode as shown in Fig.2.4, particularly the $p = 0$ modes, it is unsurprising that the ponderomotive force acts radially inwards inside of the peak intensity radius $r_{peak} = w_0\sqrt{|\ell|/2}$. If we take the simplified $\hat{x}$ component of the electric field of a $p = 0$ laser as,

$$E_x = E_0\sqrt{\frac{1}{|\ell|!}}\left(\frac{r\sqrt{2}}{w_0}\right)^{|\ell|} exp\left(-\frac{r^2}{w_0^2}\right)e^{i\ell\theta} \tag{3.76}$$

we can derive the radial ponderomotive force associated with this beam as,

$$F_p(r) = -\frac{e^2}{4m_e\omega^2}|E_x(r)|^2\left(\frac{2|\ell|}{r} - \frac{4r}{w_0^2}\right) \tag{3.77}$$

The normalized radial ponderomotive force for the $|\ell| = 0$ and $|\ell| = 1$ modes are given in Fig.3.8 and emphasize the change in the sign of the force as a function of radius.

Electrons that are in the negative ponderomotive force radius bounded at $r = w_0\sqrt{|\ell|/2}$, will oscillate in the laser field but will also drift towards the laser axis. As the electrons oscillate back and forth, they will accelerate to a peak transverse momentum proportional to the laser intensity parameter a_0 according to Eq.3.10, but will also drift forward with the laser pulse at an average velocity given by (Eq.3.15),

$$\beta_z\gamma = \frac{a_0^2}{4} \tag{3.78}$$

where $\beta_z = v_z/c$. In a Gaussian laser, as the ponderomotive force is acting always radially outward, few electrons experience the peak a_0 of the laser as they are swept

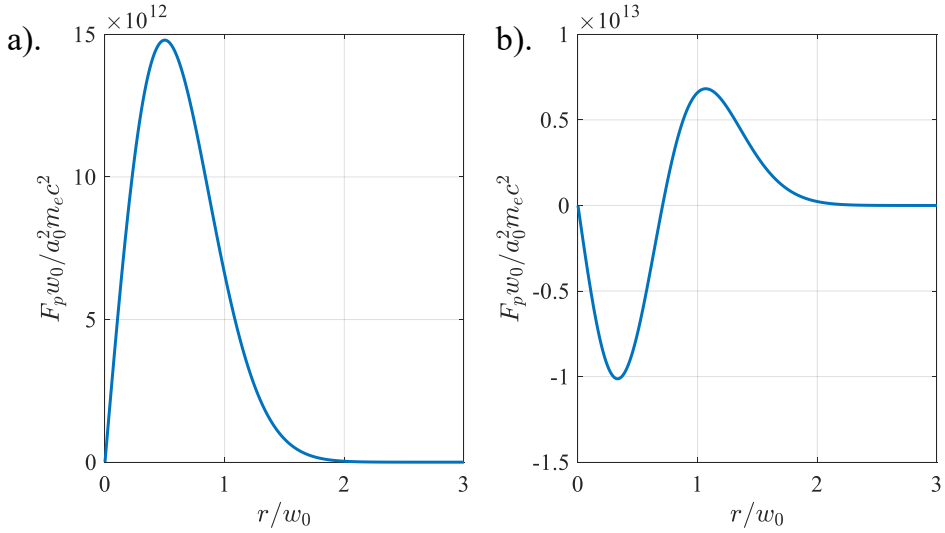

Figure 3.8: Normalized ponderomotive force for an electron in a), an $\ell = 0$ Gaussian mode and b), an $|\ell| = 1, p = 0$ Laguerre Gaussian mode.

away from the areas of high intensity. In the Laguerre-Gaussian mode however, the electrons are confined radially but often slip through the "hole" of the donut mode and dephase as the laser pulse outruns them. If the laser intensity were sufficiently high such that the forward drift velocity is close to c, then the electrons are not only trapped radially in the laser pulse, but are also pushed forward close to the laser group velocity such that they can potentially extract more energy.

Rewriting Eq. 3.78 as,

$$\frac{v_z}{c} = \frac{a_0^2}{\sqrt{a_0^4 + 16}} \tag{3.79}$$

we find that for the electron to be accelerated to an average velocity of $v/c = 0.9$, we require $a_0 \approx 2.8$. If we require that the peak laser intensity is 10 times this such that the majority of the laser field within the peak intensity radius is above this criteria, we find a peak intensity of roughly $1 \times 10^{21} W cm^{-2}$. While this intensity is high, it is obtainable with modern high power laser systems using the optics outlined in Chapter 5.

To test the trapping theory, we first look at solutions to the numerical simulations run in the MATLAB integrator. We start with a single electron at rest at a point in space: $x = w_0/2, y = 0, z = 0$ far from the laser. The laser has a Gaussian temporal function and a full-width half-maximum of 100fs, it is polarized in the $\hat{x}$ plane and is initialized 1ps away.

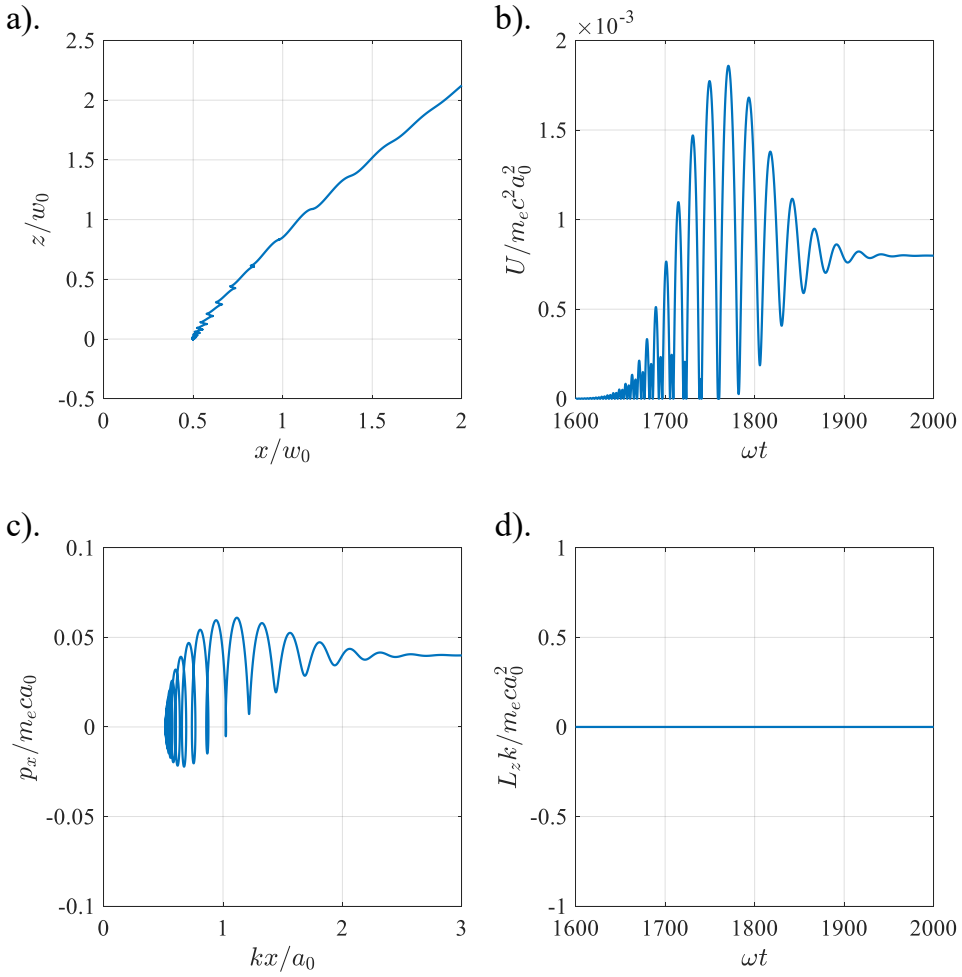

Figure 3.9: Phase space plots for an electron scattered from a linearly polarized Gaussian laser pulse with peak intensity $5 \times 10^{21} W cm^{-2}$, or $a_0 = 60.1$, pulse duration 100fs, and a beam waist of $w_0 = 10 \mu m$.

Two lasers are considered, the first is a $1\mu m$ linearly polarized Gaussian ($\ell = 0$) with peak intensity $5 \times 10^{21} W cm^{-2} = 60.1$ and a beam waist of $w_0 = 10\mu m$. The phase space for the Gaussian case is given in Fig.3.9. As is clear from tile a), the electron is kicked sideways away from the laser axis. The ejected energy is found to be $\approx 1.5 MeV$ which is considerable given the spatial extent of the interaction. As expected, the laser gains no angular momentum as shown in tile d).

The second laser is a linearly polarized Laguerre-Gaussian pulse of equal pulse duration and equal energy. As a requirement to contain the same energy, the laser beam waist and intensity should be scaled according to Table's 2.2 and 2.3. If we assume a Gaussian near-field, then $\eta = 0.772$ and $\bar{\gamma} = 0.837$. This results in a beam waist of $w_0 = 11.94$ and a peak intensity of $1 \times 10^{21} W cm^{-2}$, or $a_0 = 26.9$. The results for the same initial electron is given in Fig.3.10 in which it is clear to see that the electron is initially kicked inwards towards the laser axis as expected. The electron then rebounds from the opposite wall and oscillates back and forth in the laser channel until it finally escapes from the laser and is ejected with significantly more energy than the Gaussian case.

The final energy ejected from the electron is given in tile b) and converts to roughly $15 MeV$, or 10 times the energy of a Gaussian laser with the same energy. The electron also gains considerable angular momentum as can be seen from tile d). Increasing the pulse duration could extend the interaction length before the laser passes the electron and in theory increase the energy, however this is not the case. As the pulse length is increased, the ponderomotive force associated with the temporal shape of the laser decreases, and as a result the ejected electron energy is decreased. For an electron in the same initial position, but for a Laguerre-Gaussian laser with a 1ps duration, the ejected energy is reduced to roughly $0.5 MeV$. However, if the pulse duration is decreased to 30fs, the ejected energy increases to roughly $51 MeV$.

However, these results are quite unrealistic as the electron is placed at a specific place, something we cannot do in the laboratory. Rather we must consider an ensemble of non-interacting electrons that are randomly placed in a given distribution. We therefore consider a spherical distribution of 2000 electrons with zero initial energy. The electrons are normally distributed with a Gaussian width of $w_0/2$ around $x = y = z = 0$ and the laser is initialized 1ps away.

Again, two lasers will be used of the same energy, but now a 30fs pulse duration to maximize scattered electron energy. The results for the Gaussian case are given

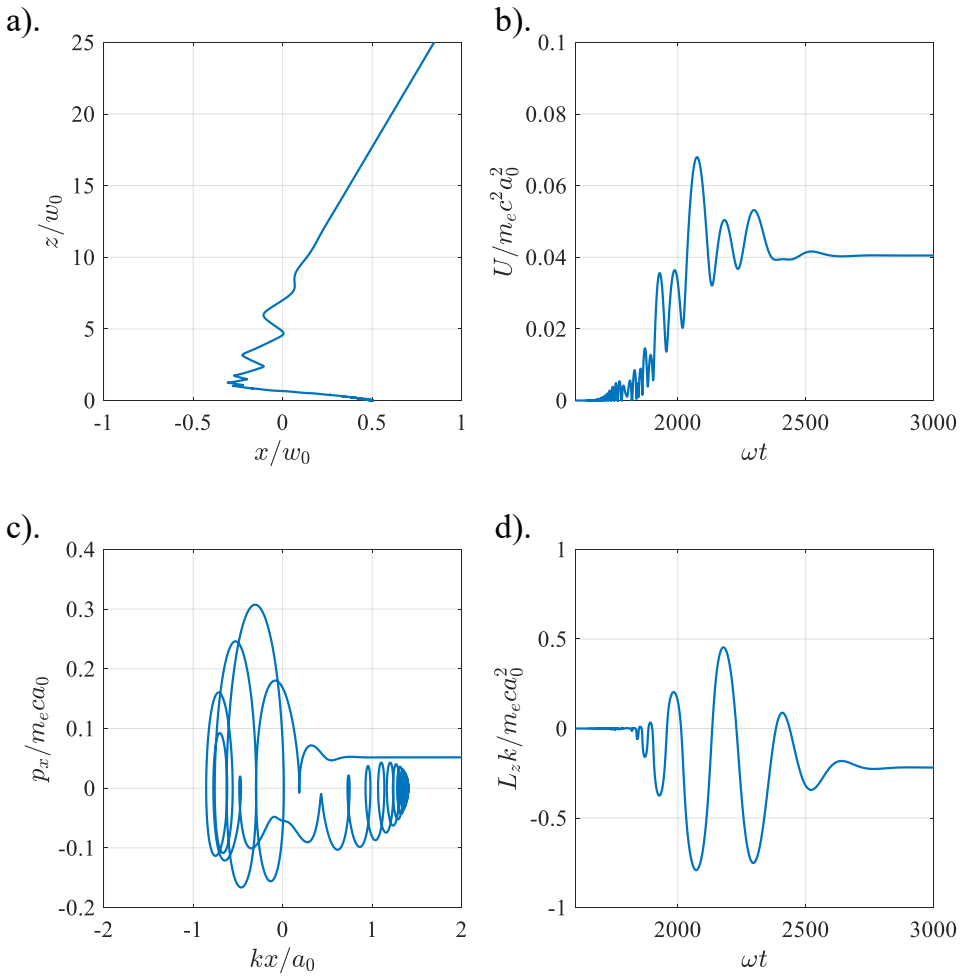

Figure 3.10: Phase space plots for an electron scattered from a linearly polarized Laguerre-Gaussian ($\ell = 1$) laser pulse with peak intensity $1 \times 10^{21} W cm^{-2}$, or $a_0 = 26.9$, pulse duration 100fs, and a beam waist of $w_0 = 11.94 \mu m$.

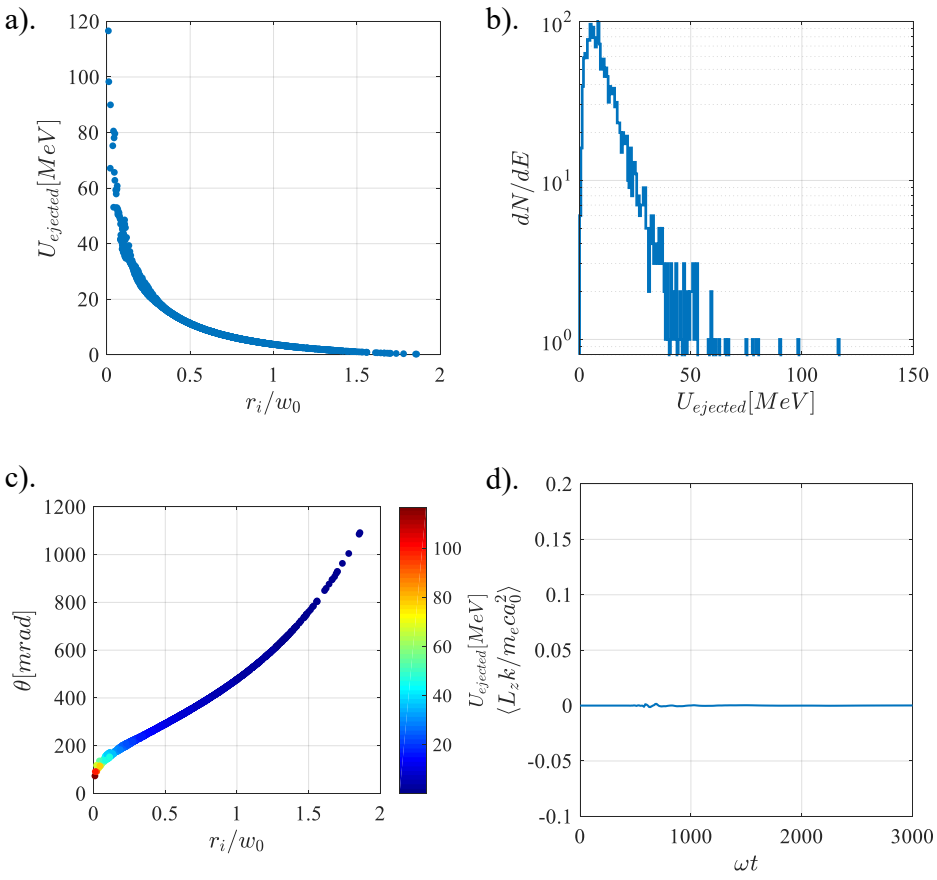

Figure 3.11: Ejection plots for 2000 electrons from a 30fs linearly polarized Gaussian laser pulse, $a_0 = 60.1$. Tile a) gives the ejected energy as a function of initial radius from the laser axis, b) gives the spectral distribution of the ejected electron, c) the ejected divergence angle of the electrons as a function of initial radius from the laser axis, and d) the average electron angular momentum as a function of time for the ensemble.

in Fig.3.11. Tile a) plots the ejected energy as a function of initial radial position showing strong acceleration for electrons close to the laser axis and rapidly decaying as the radius is increased. It was found that the initial z position played little role in the scattering energy as expected. Tile b) gives the histogram of electron energy showing that the majority of scattered electrons are scattered with an energy of approximately $10MeV$ and cutoff at roughly $50MeV$ with a few outliers beyond $50MeV$. Tile c) shows the ejected divergence as a function or initial radius and is colour coded to show the final energy of the electron. It is clear that there is a small cross section for the electron to be accelerated to high energy with most electrons being scattered into a large cone angle with little energy. This indicates that the Gaussian beam would be inefficient at generating high energy electrons in a small cone angle. Tile d) gives the average angular momentum of the electrons as a function of time, remaining zero throughout the interaction as expected.

The results of the $\ell = 1$ Laguerre-Gaussian pulse are given in Fig.3.12, where the laser intensity and beam waist have been scaled by the parameters η and $\bar{\gamma}$ to satisfy the requirements found in Chapter 2. Tile a) gives the ejection energy as a function of initial electron radius. Electrons within the peak intensity radius of the beam have a high probability of being accelerated to high energy and the effective cross section for electron acceleration is increased. This is also seen in tile b) where the total number of electrons accelerated to energies greater than $50MeV$ is much greater than that of the Gaussian case. Tile c) shows the divergence of the electrons as a function of input radius and are colour coded to ejection energy. It is possible to see that there is a wide range of initial radii that the electrons can be injected in and be accelerated forward with a minimal divergence angle. Therefore the Laguerre-Gaussian mode could be more optimal for vacuum particle acceleration due to its increase in high energy electron flux, and the minimal divergence of the electrons.

For a particle accelerator to be of use, it is ideal if the electron source is collimated, which is certainly not the case here. However, due to the finite size of the electron source, effectively a point source, it would be possible to use a quadrupole electron lens to re-image the high energy electrons onto a target or sample. Tile d) shows the interesting result of a finite orbital angular momentum transferred to the electrons. We find the average angular momentum transferred to the electrons roughly 10% of the result in Fig.3.3. This is due to the range of a_0's over which the electrons interact, while rarely interacting with the peak intensity directly.

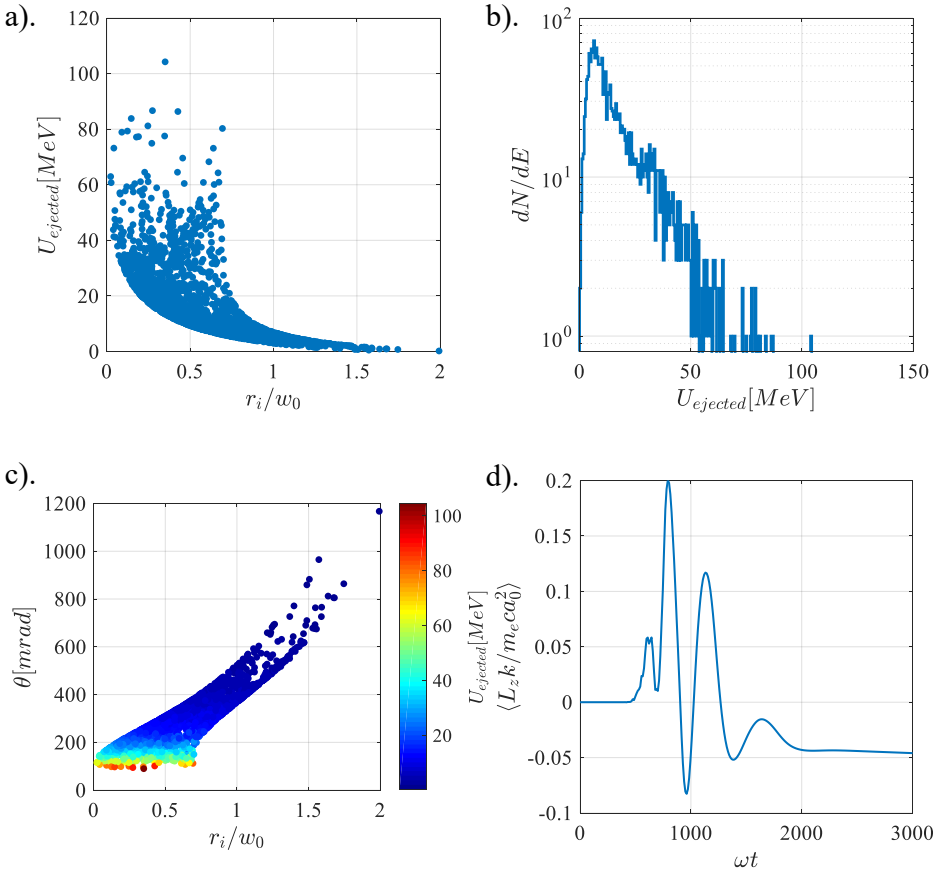

Figure 3.12: Ejection plots for 2000 electrons from a 30fs linearly polarized Laguerre Gaussian laser pulse, $a_0 = 26.9$. Tile a) gives the ejected energy as a function of initial radius from the laser axis, b) gives the spectral distribution of the ejected electron, c) the ejected divergence angle of the electrons as a function of initial radius from the laser axis, and d) the average electron angular momentum as a function of time for the ensemble.

To estimate the angular momentum absorbed per electron, we compare it to the energy absorbed per electron as shown in Fig.3.13. Tile a) and b) show the average energy and angular momentum as a function of time for an LG pulse with the previous intensity and beam waist, and with a topological charge of $\ell = 1$. The y axes have been both normalized such that they correspond to the average number of photons absorbed per electron. The final value for each is found to be roughly the same (≈ 7000) photons per electron indicating that like spin angular momentum, orbital angular momentum is absorbed at the same rate as the energy of the photons.

Tiles c) and d) show the same results, but rather for a laser with the opposite topological charge ($\ell = -1$). Here, we see essentially the same result in average ejected energy of the electrons as expected, however as the electrons are placed randomly, there is a small discrepancy of the total energy absorbed by the electrons when compared to the $\ell = 1$ result. The main difference is the absorbed angular momentum and is equal, but opposite in direction as expected. This indicates that indeed, the orbital angular momentum is coupling to the electrons.

3.5 Relativistic Radiation and Nonlinear Thomson Scattering

As shown, charged particles respond to electromagnetic waves given by the Lorentz equation (Eq.3.3), however this is not yet the full picture. Electrons in motion can generate electromagnetic waves, particularly if they are accelerating. In the classical picture, we can analyze the motion of an electron as a current source in Maxwell's equations and omit any presence of background electromagnetic fields that may be driving the particle. From this one can derive the Lienard-Wiechert four-potentials of the emitted radiation given by,

$$\Phi(\boldsymbol{r}, t) = \left[\frac{e}{(1 - \boldsymbol{\beta} \cdot \boldsymbol{n})R}\right]_{ret} \tag{3.80}$$

and,

$$\boldsymbol{A}(\boldsymbol{r}, t) = \left[\frac{e\boldsymbol{\beta}}{(1 - \boldsymbol{\beta} \cdot \boldsymbol{n})R}\right]_{ret} \tag{3.81}$$

where R is the distance from the electron to the the detector, $\boldsymbol{n}$ is the unit vector in the direction of R, and ret indicates that the computations should be performed in

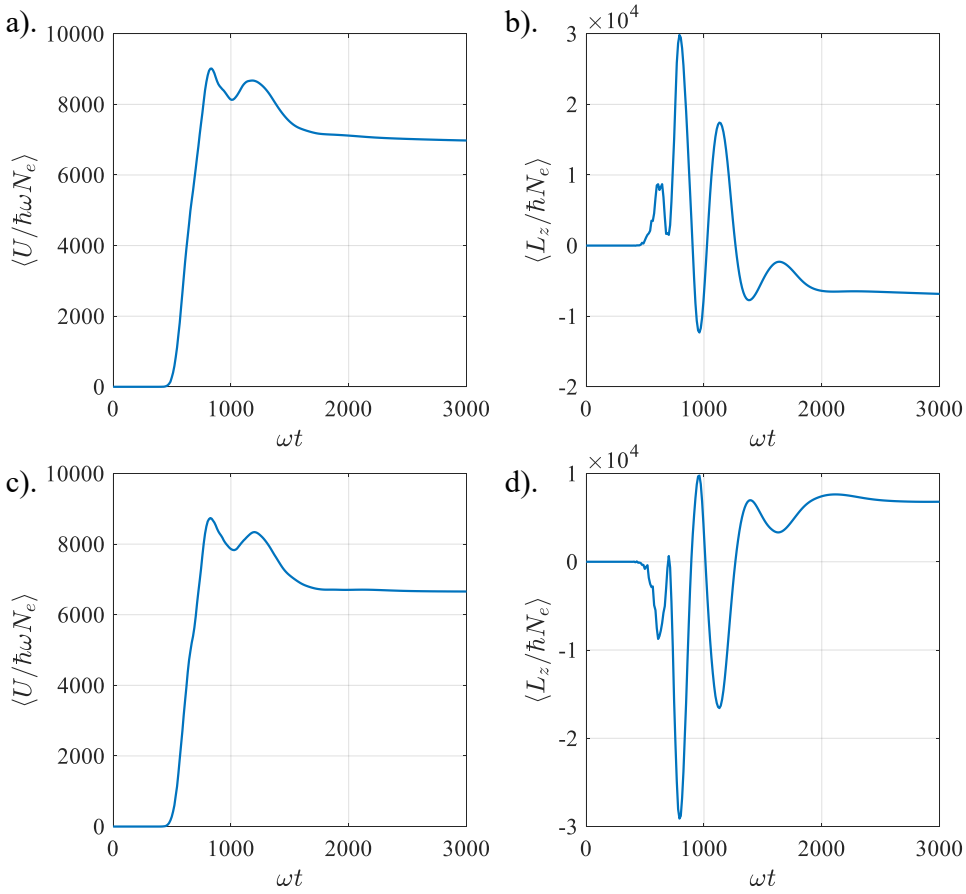

Figure 3.13: Average energy and angular momentum of per electron of 2000 electrons in two oppositely charged Laguerre-Gaussian modes. a) and b), average energy and angular momentum in an $\ell = 1$ mode respectively. c) and d), average energy and angular momentum in an $\ell = -1$ mode respectively.

the retarded time.

Using these potentials and Maxwell's equations, it is possible to write the radiated electric field from an electron in motion as [75],

$$\boldsymbol{E}(\boldsymbol{r},t) = \frac{e}{4\pi\epsilon_0}\left[\frac{\boldsymbol{n}-\boldsymbol{\beta}}{\gamma^2(1-\boldsymbol{\beta}\cdot\boldsymbol{n})^3R^2}\right]_{ret} + \frac{e}{4\pi c\epsilon_0}\left[\frac{\boldsymbol{n}\times\left((\boldsymbol{n}-\boldsymbol{\beta})\times\dot{\boldsymbol{\beta}}\right)}{(1-\boldsymbol{\beta}\cdot\boldsymbol{n})^3R}\right]_{ret} \tag{3.82}$$

This formula is often re-written in the more enlightening Heaviside-Feynman formula [45],

$$\boldsymbol{E}(\boldsymbol{r},t) = \frac{e}{4\pi\epsilon_0}\left[\frac{\hat{R}}{R^2} + \frac{R}{c}\frac{\partial}{\partial t}\left(\frac{\hat{R}}{R^2}\right) + \frac{1}{c^2}\frac{\partial^2}{\partial t^2}\hat{R}\right] \tag{3.83}$$

From this formula, we can see the three components of the source of radiation. The first term corresponds to the source for the electrostatic fields, the second term corresponds to the velocity of the electron and is responsible for magnetostatic fields, while the third term is the acceleration term and gives rise to radiated electromagnetic waves. As we are interested in the radiated power from an electron, we are only concerned with the acceleration (second) term in Eq.3.82. As shown in Eq.2.12, the energy radiated per unit time is given by the Poynting vector in the retarded time,

$$[\boldsymbol{\mathcal{S}}\cdot\boldsymbol{n}]_{ret} = \frac{e^2}{16\pi^2\epsilon_0 c}\left[\frac{1}{R^2}\left|\frac{\boldsymbol{n}\times\left((\boldsymbol{n}-\boldsymbol{\beta})\times\dot{\boldsymbol{\beta}}\right)}{(1-\boldsymbol{\beta}\cdot\boldsymbol{n})^3}\right|^2\right]_{ret} \tag{3.84}$$

In our previous numerical calculations using MATLAB, we were able to calculate the trajectory of the electron in its time t' with a time-step $\Delta t'$. Integrating over a infinitesimal time-step and changing from retarded time to electron time, we find the instantaneous power radiated per steradian as,

$$\frac{dP(t')}{d\Omega} = \frac{e^2}{16\pi^2\epsilon_0 c}\frac{\left|\boldsymbol{n}\times\left((\boldsymbol{n}-\boldsymbol{\beta})\times\dot{\boldsymbol{\beta}}\right)\right|^2}{(1-\boldsymbol{n}\cdot\boldsymbol{\beta})^5} \tag{3.85}$$

where Ω is the solid angle.

From Eq.3.85, it is possible to calculate the scattered power in any given direction of an electron. If the electron is oscillating in the field of a plane wave of a given power, then it is possible to calculate the scattering *cross section* of the electron in a plane wave. We define the scattering cross section as the ratio of the number of

photons scattered per unit solid angle to the number of incident photons per unit area. This is given [75] for a low intensity ($a_0 \ll 1$) linearly polarized plane wave as,

$$\frac{d\sigma}{d\Omega} = \left(\frac{e^2}{4\pi\epsilon_0 m_e c^2}\right)^2 \frac{1+\sin^2\Theta}{2} \tag{3.86}$$

Where Θ is the scattering angle relative to the oscillation axis. This is integrated over all area to give the Thomson scattering cross section,

$$\sigma_T = \frac{8\pi}{3}\left(\frac{e^2}{4\pi\epsilon_0 m_e c^2}\right)^2 = 0.665 \times 10^{-24} cm^2 \tag{3.87}$$

where $e^2/4\pi\epsilon_0 m_e c^2$ is the classical electron radius. This is valid for incident photons with energies sufficiently smaller than that of the rest mass of the electron, $\hbar\omega \ll m_e c^2$, otherwise the Compton scattering formulas must be used.

The cosine squared dependence of the Thomson scattering cross section gives some indication of the radiation pattern. We verify this relationship by adding in a radiation post-processor script to the MATLAB particle integrator. As the code cannot compute infinitely small differential areas or time steps, it calculates the power radiated on a dynamic time-step basis. The radiation is calculated per steradian on a spherical grid with cell sizes $\Delta\phi$ and $\Delta\theta$ for the azimuthal and polar coordinates respectively. While the code can compute instantaneous power, it is computed over a finite time step creating a discrepancy, so instead we look to find the total scattered energy by integrating over time. The total energy scattered per electron is then calculated as,

$$U_{total} = \iiint \frac{dP(t')}{d\Omega}\sin(\theta)d\theta d\phi dt' \approx \sum_{i,j,k}\frac{\Delta P_{i,j,k}}{\Delta\Omega}\cos(\theta'_j)\Delta\phi_i\Delta\theta_j\Delta t'_k \tag{3.88}$$

where them sums are computed as trapezoidal sums to minimize error. We remark on the change from the $\sin(\theta)$ used commonly in physics standard definitions of spherical Jacobian's, to $\cos(\theta')$ as used in mathematics standards and also in MATLAB. In this case, we find that $\theta' = \theta + \pi/2$.

The radiation pattern of a single electron oscillating in a low intensity linearly polarized plane wave of wavelength 800nm and Gaussian pulse duration 100fs is given in Fig.3.14. Tile a) gives the true spherical mapping of the radiation detected 1

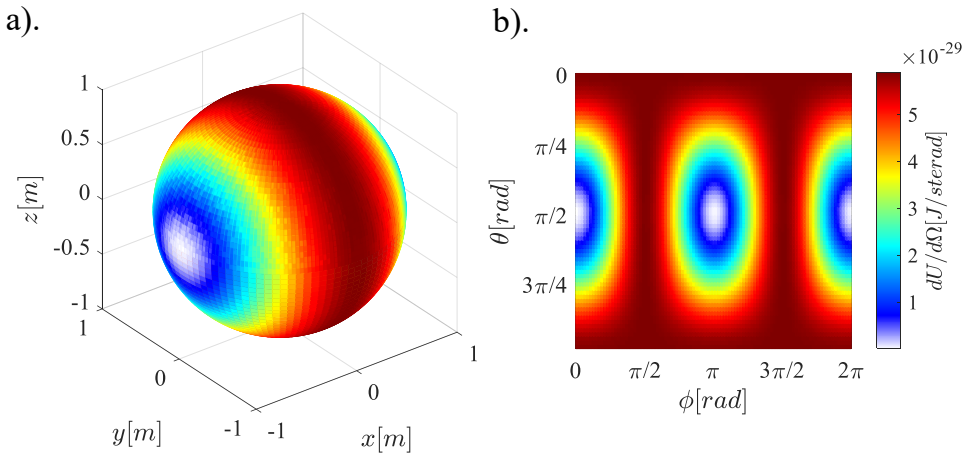

Figure 3.14: Thomson scattered radiation from an electron in a $1\times10^{10}Wcm^{-2}$ infinite plane wave of pulse duration 100fs. The laser is propagating in the z direction and is polarized in the x direction.

meter from the interaction region, whereas tile b) gives the mercator projection of the radiation onto a 2D plane. Here, ϕ denotes the azimuthal coordinate from the polarization plane ($\hat{x}$), while θ denotes the polar coordinate measured from the laser k vector in the $\hat{z}$ direction. In the far-field it is clear that the radiation emitted appears to be very similar to that of a dipole antenna oriented along the $\hat{x}$ axis. The intensity null on the poles of the dipole antenna are in agreement with the sine-squared radiation law.

From Eq.3.85, we see that there is some relativistic dependence to the direction of the Thomson scattering. This is found from the denominator with the $\boldsymbol{n}\cdot\boldsymbol{\beta}$ term. For electron speeds much less than c ($\beta \approx 0$), the denominator plays little role. As the electron becomes relativistic, the denominator tends towards infinity in the direction of β which bends forwards as the laser becomes more relativistic.

Increasing the beam to relativistic intensities causes the radiation to "bend" in the direction of laser propagation. Fig.3.15 shows the result for an electron in a linearly polarized 800nm plane wave of intensity $a_0 = 0.83$ with pulse width 100fs.

Further increasing the laser intensity to more extreme values results in further bending of the radiation to the laser propagation direction. Fig.3.16 shows the more extreme case of nonlinear Thomson scattering with quite extreme bending towards the propagation axis. This was computed with a 100fs laser pulse and peak intensity

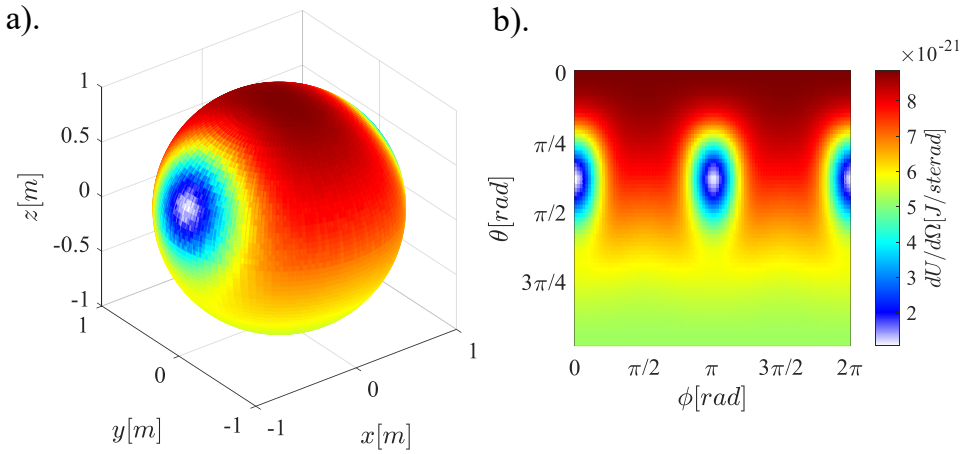

Figure 3.15: Thomson scattered radiation from an electron in an infinite plane wave of intensity $a_0 = 0.83$ and pulse duration 100fs. The laser is propagating in the z direction and is polarized in the x direction.

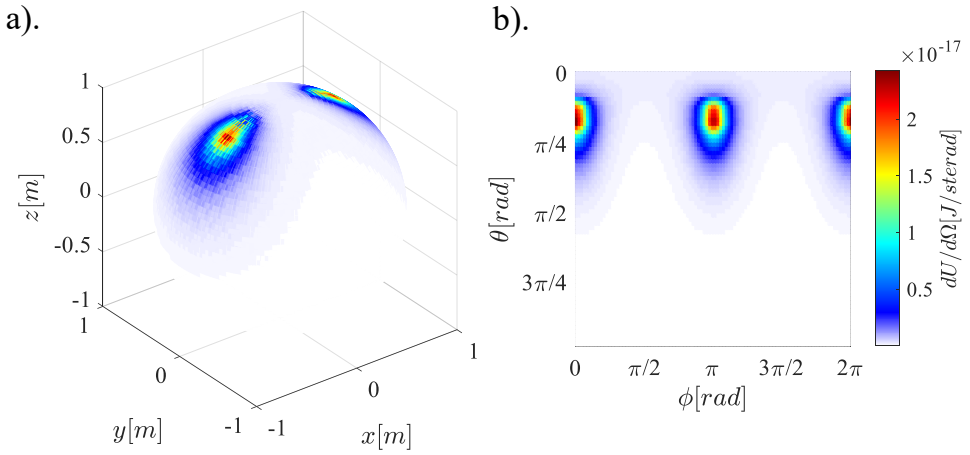

Figure 3.16: Thomson scattered radiation from an electron in an infinite plane wave of intensity $a_0 = 4.81$ and pulse duration 100fs. The laser is propagating in the z direction and is polarized in the x direction.

of $a_0 = 4.81$. While it is clear there is some spatial dependence to the radiation far-field as a function of the laser intensity, we still have to analyze the spectrum of the radiation.

If we know the power delivered to a point in space as a function of time, then it is straight-forward to find the corresponding frequency of the emitted beam by means of a Fourier transform. Given the relation [75],

$$\frac{dP(t)}{d\Omega} = |\boldsymbol{A}(t)|^2 \tag{3.89}$$

we can find the frequency spectrum of the emitted radiation as,

$$\boldsymbol{A}(\omega) = \frac{1}{\sqrt{2\pi}} \int \boldsymbol{A}(t) e^{i\omega t} dt \tag{3.90}$$

From this we can write the energy emitted per unit steradian as,

$$\frac{dU}{d\Omega} = \int |\boldsymbol{A}(\omega)|^2 d\omega \tag{3.91}$$

where,

$$\boldsymbol{A}(\omega) = \sqrt{\frac{e^2}{32\pi^3 \epsilon_0 c}} \int e^{i\omega t} \left[\frac{\boldsymbol{n} \times \left[(\boldsymbol{n} - \boldsymbol{\beta}) \times \dot{\boldsymbol{\beta}} \right]}{(1 - \boldsymbol{\beta} \cdot \boldsymbol{n})^3} \right]_{ret} dt \tag{3.92}$$

We can transform this to the frame of the particle where the trajectory in the particle time is computed by the MATLAB code,

$$\boldsymbol{A}(\omega) = \sqrt{\frac{e^2}{32\pi^3 \epsilon_0 c}} \int e^{i\omega(t' - \boldsymbol{n} \cdot \boldsymbol{R}(t')/c)} \frac{\boldsymbol{n} \times \left[(\boldsymbol{n} - \boldsymbol{\beta}) \times \dot{\boldsymbol{\beta}} \right]}{(1 - \boldsymbol{\beta} \cdot \boldsymbol{n})^2} dt' \tag{3.93}$$

This is the standard radiation spectrum integral in most texts, however it is not suitable for the task at hand. One may notice that Eq.3.92 is a perfect Fourier transform for which the fast Fourier transform (FFT) is a suitable technique for calculating this quickly and with minimal error. Eq.3.93 on the other hand is a difficult integral to compute numerically and the FFT cannot be applied. This can lead to massive computational requirements and overall time increase in the calculation. We therefore opt to compute the radiation spectra in the retarded time of the particle which

requires an interpolation of the particle time to the retarded time. This is given by,

$$t_{ret} = t' + \frac{R(t')}{c} \tag{3.94}$$

where t' is the particle time.

The energy radiated per unit solid angle per unit frequency is then given as,

$$\frac{d^2I}{d\omega d\Omega} = \frac{e^2}{16\pi^3\epsilon_0 c}\left|\int e^{i\omega t}\frac{\boldsymbol{n}\times\left[(\boldsymbol{n}-\boldsymbol{\beta})\times\dot{\boldsymbol{\beta}}\right]}{(1-\boldsymbol{\beta}\cdot\boldsymbol{n})^3}dt\right|^2_{ret} \tag{3.95}$$

It is more useful however to convert this equation into radiation per unit wavelength as opposed to frequency which is difficult to directly measure in the lab. We therefore make a change of variables taking care with the differential of the frequency to yield,

$$\frac{d^2I}{d\lambda d\Omega} = \frac{e^2}{8\pi^2\epsilon_0\lambda^2}\left|\int e^{i\omega t}\frac{\boldsymbol{n}\times\left[(\boldsymbol{n}-\boldsymbol{\beta})\times\dot{\boldsymbol{\beta}}\right]}{(1-\boldsymbol{\beta}\cdot\boldsymbol{n})^3}dt\right|^2_{ret} \tag{3.96}$$

We could also rewrite the equation such that it gives the yielded energy in terms of number of photons in a frequency band but it will not be shown here. In the form of Eq.3.96, it is possible to discretize the formula such that it is suitable for use in the numerical MATLAB code. This allows us to pick any point on the previous figures and plot the frequency spectrum for it.

The result for the low intensity, linear Thomson scattering spectrum in a 100fs duration, infinite width plane wave of intensity $1\times10^{10}Wcm^{-2}$ is given in Fig.3.17. Tile a) gives the total radiation spatial distribution which is sampled at two points indicated by the blue and black squares. The black square indicates the radiation emitted in the polarization which we expect to be essentially zero, however due to its finite size, and the small effects from the field strength, we find it to be roughly 300 times weaker than the radiation emitted in the blue square. The blue square is located on the $\phi = \pi/2$ position and measures the strongest linear Thomson scattering.

At low intensity ($a_0 \ll 1$), we find that the radiation scattered in tile b) is almost entirely at the laser central frequency. There is a bandwidth associated with the scattered radiation that matches the bandwidth of the laser pulse exactly. Using a log scale, although not shown, we find an extremely weak 2nd harmonic of the laser

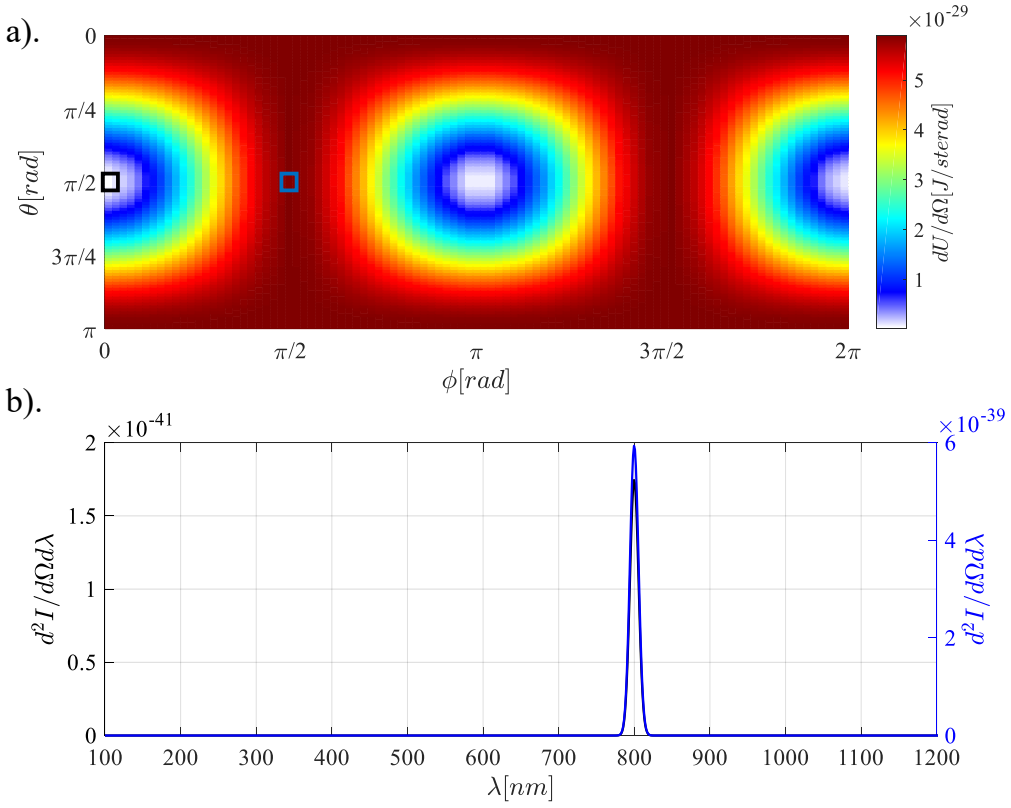

Figure 3.17: Linear Thomson scattering of an electron in an infinite plane wave of duration 100fs and peak intensity $1\times10^{10}Wcm^{-2}$. Tile a) gives the spatial distribution of the radiation and shows the two spectral sample points in the black and blue squares. Tile b) gives the radiation spectra for these points with the colours of the lines corresponding to the colour of the boxes in tile a). The scales in tile b) are relative arbitrary units.

radiation at 400nm in the polarization direction.

Increasing the intensity to relativistic levels makes this second harmonic, and many others appear quite strong, and in fact can become stronger than the first harmonic emission. Fig.3.18 gives the nonlinear Thomson spectra of an electron in an infinite plane wave of strength $a_0 = 0.96$ in the two perpendicular planes as described before. It is clear to see the drastic change in the spectra, the black (laser polarization plane) shows many red shifted harmonics. Using a log scale shows the FFT is capable of resolving down to the 17th harmonic using a $167as$ time-step. A finer time-step could be used but at great cost to the computational time. The minimum frequency that can be resolved is calculated from the Shannon-Nyquist theorem. Interestingly, the

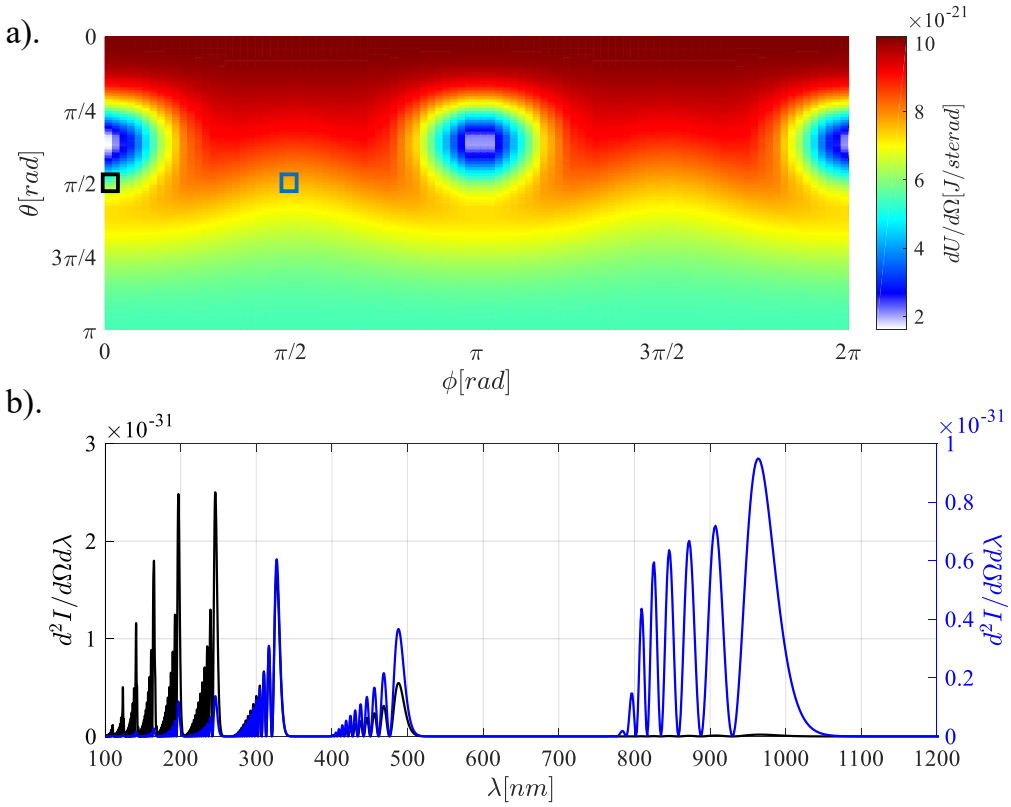

Figure 3.18: Nonlinear Thomson scattering of an electron in an infinite plane wave of duration 100fs and peak field amplitude $a_0 = 0.96$. Tile a) gives the spatial distribution of the radiation and shows the two spectral sample points in the black and blue squares. Tile b) gives the radiation spectra for these points with the colours of the lines corresponding to the colour of the boxes in tile a). The scales in tile b) are relative arbitrary units.

radiation emitted in the perpendicular (blue) direction is red-shifted all the way out to 1000nm. The red shift is due to special relativity and can be described quite qualitatively as follows. Much like the space-time invariant, the phase of the laser is invariant under a Lorentz transform,

$$\Phi = \omega t - kz \tag{3.97}$$

If the time the electron experiences is the proper time $\tau = t/\gamma$ then for the phase to be invariant, the frequency of the laser must be red shifted to account for this. Similarly, the z distance is Lorentz contracted causing an increase in the wavevector k to compensate. Thus the electron sees a red-shifted laser. Upon scattering the light, the relative motion of the electron to the observer is also Lorentz transformed and further red-shifted again. If the laser intensity were to keep increasing, the harmonics would be red shifted so much that they would overlap with each other.

While it is possible to derive analytic models for the radiation scattered from electrons in infinite plane waves as we have shown [135], it is not necessarily an accurate representation of the nonlinear Thomson scattering from a real laser beam with multiple electric field components, ponderomotive forces, and electron trapping properties. Nonlinear Thomson scattering can give a rich amount of information about the laser field when scattered from single electrons, or plasma parameters such as electron temperature and density if the laser is scattering from a plasma.

These techniques developed have been used for multiple applications in my research, including the characterization of laser intensity with relativistic Thomson scattering [67] in Gaussian and Laguerre-Gaussian modes. We do not present this work here however as it is still in early stages, and needs more work. The second use for this code is in estimating radiation from laser driven plasma accelerators discussed in the next chapter.

3.5.1 The Lorentz-Abraham-Dirac Equation

Eq. 3.3 is valid for scenarios where the intensity of the laser is relativistic, but only to intensities of roughly $1 \times 10^{22} W cm^{-2}$. After this intensity, the nonlinear Thomson scattered light starts to emit harmonics that extend into the UV and even x-ray range. It is common to find scenarios such as in synchrotron accelerators where the electron is accelerated such that it emits x-ray photons with energies approaching the

rest mass energy of an electron ($511keV$). At these energies, the photons that are scattered, or radiated away can cause a recoil on the electron modifying its trajectory.

We therefore need to add an additional force term to the Lorentz equation in the form of a radiation damping (or reaction) term. Writing the Lorentz equation in covariant form allows us to write the Lorentz-Abraham-Dirac (LAD) equation as [84],

$$\frac{dp_\mu}{d\tau} = eF_{\mu\nu}u^\nu + \frac{1}{4\pi\epsilon_0}\frac{2e^2}{3m_e c^3}\left[\frac{d^2p_\mu}{d\tau^2} + \frac{p_\mu}{m_e^2c^2}\left(\frac{dp_\nu}{d\tau}\frac{dp^\nu}{d\tau}\right)\right] \tag{3.98}$$

where p_μ and u^ν are the momentum and velocity four vectors respectively, and $F_{\mu\nu}$ is the field strength tensor given by [75],

$$F_{\mu\nu} = \begin{pmatrix} 0 & E_x & E_y & E_z \\ -E_x & 0 & -B_z & B_y \\ -E_y & B_z & 0 & -B_x \\ -E_z & -B_y & B_x & 0 \end{pmatrix} \tag{3.99}$$

The LAD equation has been the source of much controversy for some time including its non-relativistic case. Eq.3.98 admits non-physical and paradoxical solutions such as the electron reacting to the emission of the photon before it was emitted breaking causality. There have been many attempts to address these issues [167], but none have been entirely satisfactory.

As it turns out, the approximations and possible solutions of Eq.3.98 depend on the quantum-electrodynamical (QED) strength parameter χ defined as,

$$\chi = \frac{\gamma}{E_s}\left|(\boldsymbol{\beta}\cdot\boldsymbol{E})^2 - (\boldsymbol{E} + \boldsymbol{v}\times\boldsymbol{B})^2\right|^{1/2} \tag{3.100}$$

where E_s is the Schwinger field strength given at the beginning of Chapter 2 as $E_s = 1.32\times10^{18}V/m$. As the strength parameter χ approaches 1, the emitted photons are on the order of the rest mass energy of the electron and relativistic quantum mechanics is required to solve the problem. Typically this is done numerically using a Monte-Carlo algorithm with some pre-populated tables of scattering cross sections. For the parameters accessible with lasers in the laboratory today, the values of χ is typically small when interacting with low energy electrons, and is often on the order of $10^{-3} - 10^{-2}$ for a_0's between 10 and 100.

In this case, it is possible to use the Landau-Lifshitz approximation to Eq.3.98

given by [84],

$$\frac{d\boldsymbol{p}_{RR}}{dt} = \frac{2e^3}{3m_e c^3}\left[\gamma\left(\frac{d\boldsymbol{E}}{dt} + \boldsymbol{v}\times\frac{d\boldsymbol{B}}{dt}\right)\right] + \\ \frac{2\gamma e^4}{3m_e^2 c^4}\left[\boldsymbol{E}\times\boldsymbol{B} + \boldsymbol{B}\times(\boldsymbol{B}\times\boldsymbol{v}) + \boldsymbol{E}(\boldsymbol{v}\cdot\boldsymbol{E}) - \boldsymbol{v}\left((\boldsymbol{E}+\boldsymbol{v}\times\boldsymbol{B})^2 - (\boldsymbol{E}\cdot\boldsymbol{v})^2\right)\right] \tag{3.101}$$

where d/dt is the material derivative. For lasers of many frequency cycles and a large beam waist, it is possible to drop the material derivatives and compute the reduced Landau-Lifshitz equation as used in PIC codes like OSIRIS [48]. Including the reduced Landau-Lifshitz correction to the Lorentz equation, and normalizing the variables, we have the equation of motion given by,

$$\frac{d\boldsymbol{p}}{dt} = \left(\boldsymbol{E} + \frac{\boldsymbol{p}}{\gamma}\times\boldsymbol{B}\right) + \alpha\left[\boldsymbol{E}\times\boldsymbol{B} + \boldsymbol{B}\times\left(\boldsymbol{B}\times\frac{\boldsymbol{p}}{\gamma}\right) + \boldsymbol{E}\left(\boldsymbol{E}\cdot\frac{\boldsymbol{p}}{\gamma}\right)\right] - \\ \alpha\gamma\boldsymbol{p}\left[\left(\boldsymbol{E} + \frac{\boldsymbol{p}}{\gamma}\times\boldsymbol{B}\right)^2 - \left(\frac{\boldsymbol{p}}{\gamma}\cdot\boldsymbol{E}\right)^2\right] \tag{3.102}$$

where,

$$\alpha = \frac{1}{4\pi\epsilon_0}\frac{2e^2\omega}{3c^3 m_e} \tag{3.103}$$

and the variables are normalized such that, $\boldsymbol{E} = e\boldsymbol{E}/\omega m_e c$, $\boldsymbol{B} = e\boldsymbol{B}/\omega m_e$, $\boldsymbol{x} = k\boldsymbol{x}$, $\boldsymbol{p} = \boldsymbol{p}/m_e c = \gamma\boldsymbol{v}/c$, and $t = \omega t$. This normalization ensures that the variables are all similar in terms of magnitude which minimizes numerical rounding errors.

The form of Eq.3.102 may appear daunting and is certainly difficult to analytically integrate for almost any scenario, but it is simple to implement in the Runge-Kutta algorithm and while is mostly not needed for the laser intensities used in the laboratory throughout this thesis, it is a first order correction that is easily introduced.

The effects of radiation damping can be subtle, and its effect can become important in high intensity interactions, or when there is a strong magnetic field present in which case the electron will experience magnetic braking. In this scenario, the electron is strongly bending in the magnetic field emitting high energy photons in the process. This radiation of x-rays, while in a strong static magnetic field leads to an eventual decrease in the electron energy, hence the term magnetic breaking [167].

3.6 Ionization and Electron Injection

To this point, we have largely been concerned with electrons "placed" at a given point and time from which we have then studied the evolution of the electron in a laser field given the exact initial conditions. Physically this can't be the case as we cannot manipulate electrons to this level of precision. If we were to place an electron at an exact place and time, then according to the Heisenberg uncertainty principle the electron would have an infinite momentum [62].

Experimentally, electrons must first be ionized from their binding atom either by collisions, photon absorption, or by tunneling. For ultrafast lasers ($< 1ps$), in low density ($\approx 1 \times 10^{19} cm^{-3}$) plasma as used throughout this thesis, the collision times associated with plasmas are much longer than the pulse duration as will be discussed in the next chapter. We are then left with two major ionization processes present - photoionization and tunnel-ionization. Of these two processes, the dominant mechanism is usually characterized by the Keldysh parameter [56],

$$\gamma_K = \omega \sqrt{\frac{2U_{ion}}{I(\boldsymbol{r},t)}} \approx \omega \sqrt{\frac{U_{ion}}{\Phi_p}} \tag{3.104}$$

where E_{ion} is ionization potential of the atom and electron of interest, $I(\boldsymbol{r},t)$ is the intensity of the incident laser and Φ_p is the ponderomotive potential given in Eq.3.34 and rewritten here as,

$$\Phi_p = \frac{e^2 |I(\boldsymbol{r},t)|^2}{4 m_e \omega^2} \tag{3.105}$$

If $\gamma_K > 1$, then the atom is most likely to be ionized through photoionization in which one, or multiple photons are absorbed by the atom and ionize the electron in the process. To ionize the electron, the total energy of the photons absorbed must be equal to, or exceed the binding potential of the electron. The binding energy of electron can be calculated for simple single and double electron atoms using the Schrodinger equation [62], but the problem becomes intractable for atoms with many electrons. The values are then usually measured experimentally and empirically and can be accessed in databases such as that used by NIST [147]. Ionization potentials relevant to this thesis are given in column 2 of Table 3.1.

If we consider a laser with a wavelength of 800nm, then each photon has an energy (not including laser bandwidth) of roughly $1.55eV$. From Table 3.1, it is clear to see that no single photon can ionize an electron of the given elements, and many

Table 3.1: Ionization potentials and equivalent appearance laser intensities required for tunneling ionization for gases used in this thesis.

Ion	$U_{ion}[eV]$	$I_{app}[W/cm^2]$
H^+	13.61	1.4×10^{14}
He^+	24.59	1.4×10^{15}
He^{2+}	54.42	8.8×10^{15}
N^+	14.53	1.8×10^{14}
N^{2+}	29.60	7.7×10^{14}
N^{3+}	47.45	2.3×10^{15}
N^{4+}	77.47	9.0×10^{15}
N^{5+}	97.89	1.5×10^{16}
N^{6+}	552.07	1.0×10^{19}
N^{7+}	667.05	1.6×10^{19}

photons must therefore be required. For hydrogen to be ionized via multi-photon ionization, at least 9 photons must be simultaneously absorbed. The cross section for this interaction is quite small and a large laser intensity is required for this to be feasible.

For the laser intensities used throughout this work, we are often working at relativistic intensities in which the Keldysh parameter becomes much less than 1. In this case, electrons tunnel through the potential trapping barrier. This is made possible by the presence of a strong laser field where the electric field acts to "tilt" the potential barrier such that it has a barrier of finite width. Fig.3.19 shows the two cases of an electron trapped within the potential well of a singly charged atom. Tile a) shows the electron with the presence of an electric field indicated by its potential energy with the black dotted line. The only way for the electron to escape in this case is by the absorption of energy through either a photon or a collision. Tile b) shows the potential barrier of the atom in the presence of a strong electric field indicated by the dotted red line. The potential is tilted to one side creating a finite barrier width. It is now possible for the electron to tunnel through this barrier (indicated by the green dashed line) to which the electron can then escape.

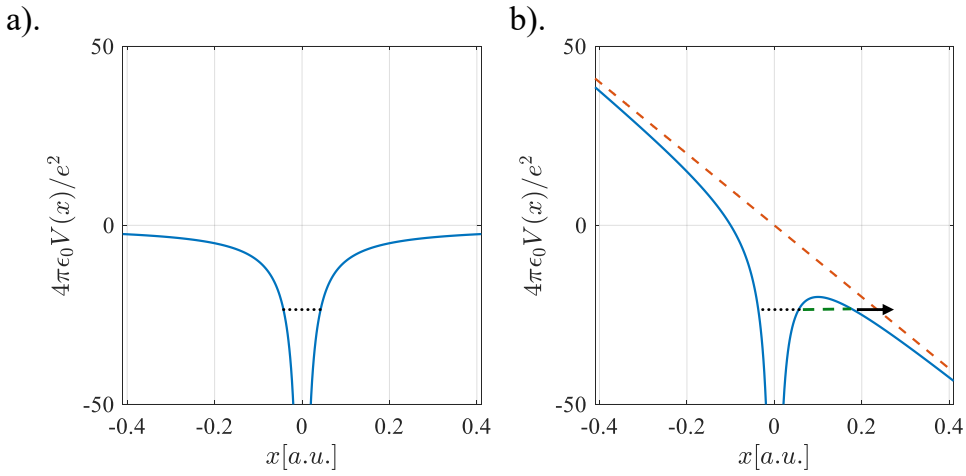

Figure 3.19: Over the barrier ionization illustration. Tile a) shows the potential well of an isolated atom and the binding energy of an electron trapped within given by the black dotted line. Tile b) shows the same potential perturbed by a strong laser electric field given in red. The bound electron is now able to tunnel through the finite barrier indicated by the green dashed line, or is able to escape if the barrier is reduced to a potential lower than the potential energy of the electron.

If we define the trapping potential for a simple hydrogen like electron as,

$$V(x) = \frac{-Ze^2}{4\pi\epsilon_0 x} \tag{3.106}$$

where Z is the charge is the ion [25], we can apply the electric field of a laser as $V_L(x) = e\epsilon x$ indicated by the red dotted line in Fig.3.19. It is possible to find the local maximum of the potential in the presence of the laser by simply differentiating the potential and equating to zero. Setting this peak potential equal to the value of the bound energy potential gives threshold electric field value for over the barrier ionization. At this intensity it is possible for the electron to effectively "leak" out of the side of the potential. The intensity of the laser required to do this can be given by [56],

$$I_{app} = 4 \times 10^9 \left(\frac{U_{ion}}{eV}\right)^4 Z^{-2} W cm^{-2} \tag{3.107}$$

A few values for relevant ion states are given in column 3 of Table3.1. It is clear that

even a moderate laser intensity of $10^{14} W cm^{-2}$ can ionize an atom through barrier suppression ionization. Ionization of inner shell electrons becomes more difficult and for nitrogen can require laser intensities over $1 \times 10^{19} W cm^{-2}$ to ionize the 6th and 7th electrons.

Further suppression of the electron binding potential further increases the ionization probability. The physics behind the ionization probability can become quite complex and involves solving the time-dependant Schrodinger equation, something that is not suitable to do in numerical codes where there can be millions to billions of electrons present.

Instead, we opt to use a simple ionization probability model as suggested by L. Roso. In this model, the electron cannot be ionized until the laser reaches an intensity that satisfies Eq.3.107. At this intensity, the probability to ionize the electron is still 0, however there is now a linear increase in probability to ionize the electron until the laser reaches an electric field strength of $2E_{app}$, after which the probability of ionization is 1. By randomly generating a number between zero and one, we can estimate the ionization process using a Monte Carlo algorithm, which finds the time at which the electron is injected according to the random number value.

The cumulative distribution function of this process is given by,

$$F(X) = \begin{pmatrix} 0 & X < 1 \\ X - 1 & 1 \leq X \leq 2 \\ 1 & X > 2 \end{pmatrix} \tag{3.108}$$

where $X = E_{laser}/E_{app}$. This is summarized in Fig.3.20 where the probability of ionization is given as a function of laser electric field strength over the appearance electric field strength.

The barrier suppression ionization model has been implemented into the Runge Kutta MATLAB algorithm for providing more accurate results of electron injection and accelerating from the beam. We have now generated a MATLAB code that is capable of simulating the injection, radiation, and acceleration of electrons (or any charged particle) in a generalized Laguerre-Gaussian mode on a single particle basis. While the code is not sufficient to solve more complicated problems with plasmas that involve the interaction of electrons within the laser field, the code is extremely useful for studying the fundamental physics of angular momentum transfer, radiation, and acceleration of electrons in high order laser modes.

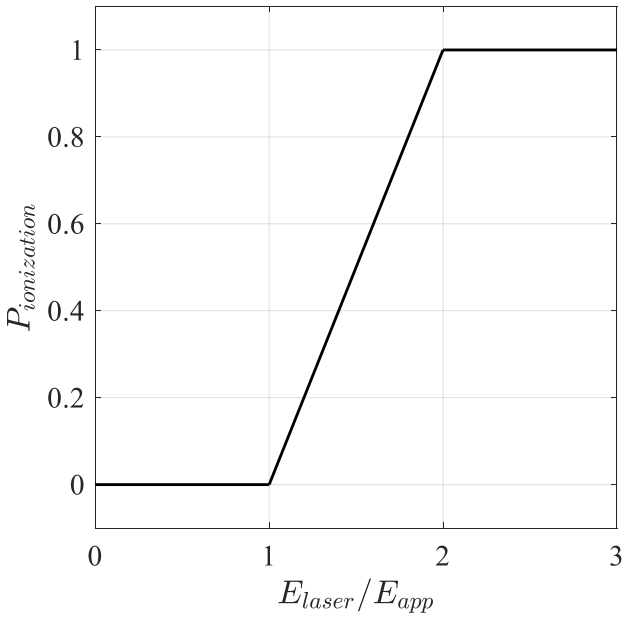

Figure 3.20: Cumulative distribution function of the barrier suppression ionization probability for an electron in a high intensity laser field.

3.7 Conclusions

In this chapter, we explored the already known electrodynamics of free electrons in plane waves. This was then extended to free electron motion in LG modes using a newly-derived paraxial equation based on the model of Erikson and Singh [38]. From this model, we were able to show that in addition to the energy gained by a scattering electron from the ponderomotive force, an angular momentum was gained with a direct scaling to the ponderomotive scattering.

The trapping of electrons for energy gain within the optical vortex was also investigated indicating that electrons may be optimally accelerated from a wide variety of initial radii within the peak intensity ring of the donut.

Chapter 4

Under-Dense Plasma Interactions with Optical Vortices

In this Chapter, we begin to study the interaction of optical vortices with plasma. In itself, the physics of laser-plasma interactions is difficult to study analytically at higher intensities due to the nonlinear partial differential equations governing more than 10^{19} electrons, and thus often requires numerical simulations. In this case, particle in cell (PIC) simulations are employed and the problems of propagation, self focussing and wakefield acceleration of electrons are investigated for Laguerre-Gaussian modes. The results are compared to some analytical scaling laws also.

While no publications have yet been made with the material in this Chapter, the results of Laguerre-Gaussian self focussing in plasma, the scaling of electron energies in laser wakefield accelerators and the subsequent radiation emission will be published shortly after this thesis is published. The wakefield theory and simulations are used to support the results of Chapter 6, while the inverse Faraday effect theory is used to support the numerical simulations in Chapter 7.

4.1 Plasma Characteristics

We begin this chapter with a brief review of basic plasma parameters and how we can use them to study the interactions of interest correctly and effectively. A plasma is often defined as an ensemble of electrons and ions - typically charge neutral, that exhibits a collective behaviour. While plasma's can exist in a variety of conditions, it is defined primarily by its temperature and density.

The concept of temperature can be related to the average energy of a particle in an ensemble. For simplicity, we will assume that our ensemble of electrons is in thermodynamic equilibrium and the electron velocity can be described by the Maxwell-Boltzmann distribution [29]. The distribution of electron velocities in 3D can then be given by,

$$f(v_x, v_y, v_z) = n_e \left(\frac{m_e}{2\pi k_B T}\right)^{3/2} exp\left[-\frac{m_e\left(v_x^2 + v_y^2 + v_z^2\right)}{2k_B T}\right] \tag{4.1}$$

where k_B is the Boltzmann constant, and T is the electron temperature. The number density n_e is found via,

$$n_e = \int_{-\infty}^{\infty} f(\boldsymbol{v}) d\boldsymbol{v} \tag{4.2}$$

The expectation value of an operator on an ensemble is given by [120],

$$\langle A \rangle = \frac{\int A f(\boldsymbol{v}) d\boldsymbol{v}}{\int f(\boldsymbol{v}) d\boldsymbol{v}} \tag{4.3}$$

The mean non-relativistic kinetic energy of the electron ensemble (in 3D) can then be given by,

$$\langle KE \rangle = \frac{\int 1/2 m_e |\boldsymbol{v}|^2 f(\boldsymbol{v}) d\boldsymbol{v}}{\int f(\boldsymbol{v}) d\boldsymbol{v}} = \frac{3}{2} k_B T \tag{4.4}$$

We then can define the thermal velocity of a (1D) plasma as,

$$v_{th} = \sqrt{\frac{2k_B T}{m_e}} \tag{4.5}$$

Typical plasmas created in the laboratory in high intensity laser-plasma interactions can have temperatures from a few eV to tens of keV required for inertial confinement fusion. Here we note that $1eV \approx 11600K$. This corresponds to thermal electron velocities on the order of $0.002c - 0.2c$, indicating that the Maxwell-Boltzmann distribution is sufficient to describe the plasma without having to implement the more complicated relativistic Maxwell-Jüttner distribution.

Given the temperature of the plasma and the ionization potential of the element of interest U_{ion}, it is possible to estimate the ratio of ions (n_i) to the total number of

neutral atoms (n_n) in thermodynamic equilibrium via the Saha equation [29],

$$\frac{n_i}{n_n} = \frac{3 \times 10^{27}}{n_i[m^3]}(T[eV])^{3/2} exp\left(-\frac{U_{ion}[eV]}{T[eV]}\right) \tag{4.6}$$

We find that for the simple case of hydrogen at atmospheric pressure, the atoms are almost entirely ionized with a temperature of roughly $3eV$.

A second parameter that arises as a function of the electron temperature and density is the Debye length given by [29],

$$\lambda_D = \left(\frac{\epsilon_0 k_B T}{n_e e^2}\right)^{1/2} \tag{4.7}$$

The Debye length describes the sheath distance in a plasma. If a positive charge was placed in a plasma, the electrons would arrange such to shield and mitigate the distance this charge's potential can be felt. The distance places an effective scale length on the plasma which may or may not need to be resolved numerically depending on the problem and the physics of interest. For instance, the Debye length of a $1eV$ plasma at a density of $1 \times 10^{19} cm^{-3}$ - a typical density used in wakefield acceleration experiments, is approximately 2.35nm. If the plasma was to be simulated over a large region - on the order of 100's of microns, the number of cells required would be on the order of 100,000 which is certainly computational demanding. The problem becomes more difficult if you are required to simulate in 3D. Increasing the plasma temperature in the simulation to 100's if not 1000's of eV's will increase the Debye length and decrease the numerical load.

The Debye length becomes very small as the plasma approaches solid density. For instance, a plasma of temperature $1eV$ and density $1 \times 10^{22} cm^{-3}$, we find a Debye length of 0.074nm. This is beyond the resolution capability of many particle-in-cell (PIC) codes which are the primary tool for studying underdense plasmas. Modelling high density, solid target plasma's can be studied via other techniques such as modelling the plasma as a fluid, using a kinetic code modelling the evolving spatially dependant distribution function in time, or using hybrid codes implementing dynamic meshes and that can choose between the particle-in-cell solver or a fluid solver.

The next parameter we must investigate is how the plasma responds to an electromagnetic wave of frequency ω_0. If we consider the plasma as a ensemble of electrons

that collectively move together in the field of a laser, we can think of each electron using the simple mass on a spring oscillator model. If an electron is perturbed in position by a time harmonic electric field we can write Newton's second law for the electron as [49],

$$m_e \frac{d^2x}{dt^2} + m_e \Gamma \frac{dx}{dt} = -eE_0 e^{-i\omega t} \tag{4.8}$$

where we have added a damping term to the electron of strength Γ. As with any driven ODE of this form, we assume a solution of the form $x = x_0 e^{-i\omega t}$. Plugging this in, we find the displacement of the electron in the EM wave as,

$$x = \frac{eE_0 e^{-i\omega t}}{m_e(\omega^2 + i\Gamma\omega)} \tag{4.9}$$

The polarizability of the plasma is given by $P = -n_e e x$, and when related to the electric displacement, we can find the relative permittivity of the plasma,

$$D = \epsilon_r \epsilon_0 E = \epsilon_0 E + P \tag{4.10}$$

We therefore find the relative permittivity of the plasma as,

$$\epsilon_r(\omega) = 1 - \frac{n_e e^2}{\epsilon_0 m_e} \frac{1}{\omega^2 + i\Gamma\omega} \tag{4.11}$$

If the plasma has zero damping, we then find the permittivity in a useful form,

$$\epsilon_0(\omega) = 1 - \frac{\omega_p^2}{\omega^2} \tag{4.12}$$

where ω_p is the plasma frequency,

$$\omega_p = \left(\frac{n_e e^2}{\epsilon_0 m_e} \right)^{1/2} \tag{4.13}$$

The plasma frequency is one of the most important characteristics of a plasma and is purely a function of the plasma density. Much like a capacitor, electromagnetic waves with a frequency above the plasma frequency are able to penetrate and propagate through the plasma, whereas electromagnetic waves with a frequency below the plasma frequency are reflected strongly, and any wave penetrating into the plasma is strongly damped.

An interesting case arises when the laser frequency matches the plasma frequency. In this case, it is possible to derive the critical density at which this occurs by setting the laser frequency equal to the plasma frequency,

$$n_c = \frac{\omega^2 \epsilon_0 m_e}{e^2} \tag{4.14}$$

Plasma densities below this critical density are considered to be underdense and allow for the propagation of EM waves through the medium. Plasma densities above this density are considered to be overdense and do not permit EM waves to propagate through them. The physics of laser absorption, and particle acceleration is quite different for both cases.

This thesis is focused on coupling of OAM to plasma, in particular in underdense regimes. In the following sections, we will focus mostly on underdense interactions.

4.2 Underdense Propagation

In this section, we will briefly review some of the fundamental concepts of nonlinear propagation of a beam in an underdense plasma, and its application to particle acceleration, magnetic field generation and as a light source.

To first order, when an electromagnetic wave interacts with an underdense plasma, the electrons collectively oscillate in the laser field driving electron plasma waves. The waves can be large in amplitude far surpassing the electric field strengths of conventional accelerators [136]. In the linear regime, the maximum electric field of the electron plasma wave before wave breaking can be given by,

$$E_0[V/m] = 96\sqrt{n_e[cm^{-3}]} \tag{4.15}$$

For instance, a plasma with a density of roughly 1% critical density has an electron density of $1 \times 10^{19} cm^{-3}$ which corresponds to an electric field of $3 \times 10^{11} V/m$. If the laser field is increased in strength to where a_0 approaches 1, the plasma wave can become nonlinear and forces like the ponderomotive force can become dominant. In this case, the electrons initially oscillate in the laser electric field but are quickly expelled from the high intensity regime by the ponderomotive force as we saw in the previous chapter.

In the case of a Gaussian pulse, the electrons are swept out radially leaving a void

(or bubble) in the wake of the laser pulse, until the electrons are able to eventually fill the void some time later. The void of electrons behind the laser pulse in the nonlinear regime can lead to a very high potential accelerator with acceleration gradients of multiple TeV/m. These acceleration gradients have been the focus of much study [4, 40, 39], and show alot of promise in delivering a table-top scale particle accelerator.

While we do not expect the acceleration gradients of OAM driven plasmas to be increased due to the decrease in laser intensity for the same pulse power, we do expect a change in the laser wakefield structure. In the previous chapter, we already demonstrated that laser OAM can couple to electrons through ponderomotive-like interactions, and as such we expect the OAM to couple to the plasma when the ponderomotive force becomes dominant. Diagnosing a nonlinear plasma interaction is not trivial however as the interactions are extremely chaotic and noisy both in simulations and in the laboratory. We therefore look for global changes in the interaction that can possibly be measured in the lab and verified by particle in cell simulations. These changes could be in the shape of the wakefield bubble, orbital motions of electrons driving magnetic fields, and possible changes in the betatron radiation emitted from the interaction.

4.3 Self-Focussing

From the previous section, we were able to derive the permittivity of the plasma given by Eq.4.11. From optical theory, it is possible to the show that the complex index of refraction of a material is given by $\eta = \sqrt{\epsilon_r}$ [49]. For the case where $\Gamma = 0$, we find the non-relativistic plasma index as

$$\eta = \sqrt{1 - \frac{\omega_p^2}{\omega^2}} \tag{4.16}$$

As the plasma frequency is a function of electron density, this simple relationship turns out to be quite formidable. If the electron density is perturbed by strong electric fields and the ponderomotive force, as well as electrons being ionized into the laser, the problem is complicated to solve in general and typically needs a numerical method such as a PIC code, or a split-step Fourier transform code.

Employing a simple model by only including the effects of density modification

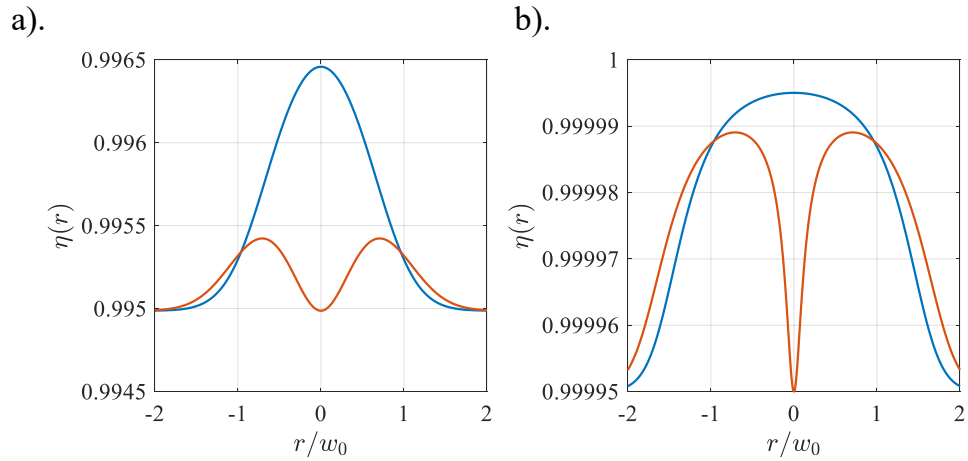

Figure 4.1: Plasma index of refraction for a Gaussian (blue) and an $\ell = 1$ Laguerre Gaussian (red) for $\omega_p/\omega = 0.1$. Tile a), $a_0 = 1$. Tile b), $a_0 = 10$.

due to the presence of a laser, we can write the refractive index as approximately [56],

$$\eta(r) \approx 1 - \frac{\omega_p^2}{\omega^2} \frac{n_e(r)}{n_0 \gamma(r)} \tag{4.17}$$

where $\gamma \approx \sqrt{1 + a(r)^2}$ and n_0 is the initial unperturbed electron density. Much like a variable index lens, the plasma index response can be used to focus (or defocus) the beam. The index of refraction for both a Gaussian (blue) and an $\ell = 1$ LG beam (red) are plotted in Fig. 4.1 assuming $n_e(r)$ is constant and assuming the beams contain the same energy. Tile a) gives the result for the slightly relativistic $a_0 = 1$ case whereas tile b) gives the very relativistic $a_0 = 10$ case. It is clear to see there is a vast difference between the two intensities where the $a_0 = 1$ case indicates a similar refractive index to the intensity shape of the laser, where as the $a_0 = 10$ case gives a highly modified refractive index profile.

The slope of the index as a function of radius indicates where the focussing and defocussing properties of the plasma will predominantly occur. If $d\eta(r)/dr < 0$ then the beam will focus, and if $d\eta(r)/dr > 0$ then the beam will defocus. From Fig. 4.2 tile a), it is clear to see that the Gaussian (blue) beam always has a focussing plasma profile, whereas the Laguerre-Gaussian beam (red) alternates between a focussing and defocussing index gradient. What this indicates is that for relativistic intensities

($a_0 \geq 1$), we expect the Gaussian beam to self-focus in the plasma, whereas the LG case will instead "pinch" into a tighter ring.

The LG beam also has an odd feature that the slope of the intensity is not symmetric about the peak intensity radius, that is, the slope of the intensity inside the peak intensity radius is different to that outside of the peak intensity. This contrasts the Gaussian beam which clearly has a symmetric intensity profile about its peak intensity at $r = 0$. From this, we could expect that the LG beam will have much more dynamic and complex self focussing properties than the Gaussian case.

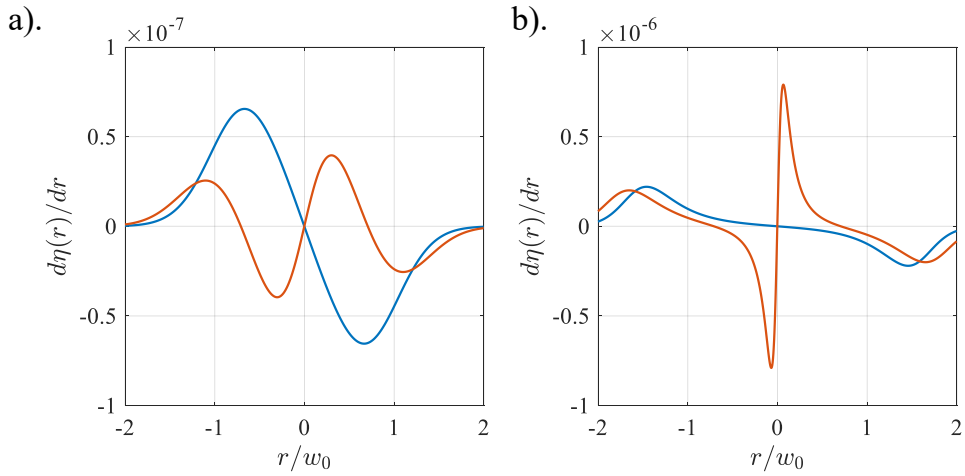

Figure 4.2: Rate of change of plasma index of refraction for a Gaussian (blue) and an $\ell = 1$ Laguerre Gaussian (red) for $\omega_p/\omega = 0.1$. Tile a), $a_0 = 1$. Tile b), $a_0 = 10$.

In vacuum, according to to Fig. 2.3, the laser will focus to a finite beam waist, and then diffract in a cone angle proportional to the f-number of the focussing optic regardless of the laser mode. We can write the general diffraction half angle as,

$$\theta_D = \frac{2}{kw_0} \tag{4.18}$$

In the case of the Gaussian beam, it is possible to maintain a balance between the vacuum diffraction of the laser, and the relativistic self focussing in the plasma. By matching the focussing angle of the plasma to the diffraction angle of the beam in the plasma, the minimum power of a Gaussian laser to balance diffraction with self

focussing is found to be [39],

$$P_c[GW] = 17.4\left(\frac{\omega}{\omega_p}\right)^2 = 17.4\frac{n_c}{n_e} \tag{4.19}$$

For a standard case of $\omega/\omega_p = 10$, we find the critical power for self focussing to be roughly 1.74TW. The laser energy for an ultrashort laser pulse to obtain this turns out to be quite low (60mJ for 30fs) indicating this can be done on smaller scale lasers. For large multi-terawatt lasers, their power is far beyond this level (100TW+). When we consider a $p = 0$ LG beam, the critical power for self focussing is modified and given by the following [133, 83],

$$P_{c\ell}[GW] = 17.4\frac{n_c}{n_e}4^{|\ell|}\frac{|\ell|!(|\ell|+1)!}{(2|\ell|)!} \tag{4.20}$$

For an LG beam of charge $\ell = \pm 1$, we find the critical power is 4 times higher than the Gaussian case, while the $\ell = \pm 2$ is 8 times higher. This is relative agreement with our diffraction model from Chapter 2 which shows that for the same laser power, the intensity of the LG $\ell = 1$ is approximately 4 times less than the Gaussian case and 8 times less for the $\ell = 2$ case.

This model of critical power assumes no modification to the plasma density as a result of the presence of the laser pulse and its inclusion is difficult. In the low intensity limit, we can estimate the refractive index to be [39],

$$\eta(r) \approx 1 - \frac{\omega_{p0}^2}{2\omega^2}\left(1 - \frac{a^2}{2} + \frac{\Delta n_p}{n_0} + \frac{\delta n}{n_0}\right) \tag{4.21}$$

where δn is the plasma wave density response, and Δn is the response due to an initial plasma density profile before interaction.

To explore the self focussing of OAM beams at relativistic intensities, two 3D simulations have been run using the particle in cell code EPOCH [8]. The details of the input parameters used are given in the appendix. However we will state the relevant parameters in Table4.1.

Table 4.1: Simulation parameters used to compare self-focussing between Gaussian and Laguerre Gaussian beams in underdense plasma.

Parameter	Gaussian Drive	Laguerre Gaussian Drive
Temporal FWHM	$100fs$	$100fs$
Peak Intensity	$2.5 \times 10^{19} Wcm^{-2}$	$2.5 \times 10^{19} Wcm^{-2}$
a_0	4.25	4.25
w_0	$8\mu m$	$9.6\mu m$
ℓ	0	1
Peak Power $[TW]$	25	97
$U[J]$	2.7	9.0
$\lambda[nm]$	1000	1000
n_0	$3 \times 10^{19} cm^{-3}$	$3 \times 10^{19} cm^{-3}$
$P_c[TW]$	0.58	2.3
Polarization	Linear $(\hat{y})$	Linear $(\hat{y})$

A pre-ionized helium plasma was initialized on a gird of $150\mu m$ by $40\mu m$ by $40\mu m$ with $4000 \times 500 \times 500$ cells respectively. This gave the simulation a grid resolution of 37.5nm in the propagation $(\hat{x})$ direction, and 80nm per cell in the transverse $(\hat{y}, \hat{z})$ directions. As the lasers are propagating at the group velocity in the plasma at roughly c/η, we employ a tracking window to follow the evolution of the laser pulse until 850fs after which the window stops and we study the evolution of the residual magnetic fields in the plasma after the laser pulse leaves. This will be studied in more detail in Chapter 7.

The electron density in the helium plasma was initialized to ramp up to the maximal value using a super-Gaussian profile of width $600\mu m$ and super-Gaussian parameter $n = 10$,

$$n_e(x) = n_{e0} exp\left[-\left(\frac{x - 350\mu m}{300\mu m}\right)^{10}\right] \tag{4.22}$$

This was chosen to mimic the density profile given by a gas jet in the laboratory as outlined in Chapter 6. Using this profile, the laser is initially launched into vacuum from the $x = 0$ boundary from which the plasma density ramps up to peak value over roughly $100\mu m$. This also enables us to mimic how the laser, and accelerated electrons are ejected on the plasma density down ramp. We have chosen for this study to use an electron density of $3 \times 10^{19} cm^{-3} \approx 0.03 n_c$. This gives a linear plasma

wavelength of $\lambda_p \approx 6\mu m$ or roughly $20.33fs * c$. This is five times shorter than the 100fs of the laser pulse we are injecting and so it should be possible to observe the effects of self focussing.

To resolve the Debye length in the simulation, we initialize the electrons with a temperature of $3 \times 10^7 K \approx 2.6keV$. This results in a Debye length of 120nm, which is larger than our grid resolution. While it may not be important to resolve the Debye length now, it will be necessary later when we study magnetic field generation in plasma. This electron temperature is hotter than the bulk plasma temperature we may generate in the lab, but the electrons that are accelerated in the laser field will surpass this temperature as they are accelerated to relativistic speeds with energies of over $511keV$. The helium ions are assumed frozen ($0keV$) as their inertia is much larger than the electrons. On the time scale of an ultrafast laser, this assumption of "immobile" ions is often made.

Fig. 4.3 shows the initial launched Gaussian laser shortly after it starts to interact with the plasma at time 267fs. The peak electric field in the polarization direction is found to be roughly $1.6 \times 10^{13} V/m$ which is equivalent to $3.4 \times 10^{19} Wcm^{-2}$. After propagating through the plasma for another 367fs, we find the peak intensity to increase due to the relativistic self focussing to a maximal value of roughly $5.8 \times 10^{13} V/m$ or $4.5 \times 10^{20} Wcm^{-2}$ as shown in Fig. 4.4. We also find the beam waist to be much smaller at roughly $3 - 4\mu m$.

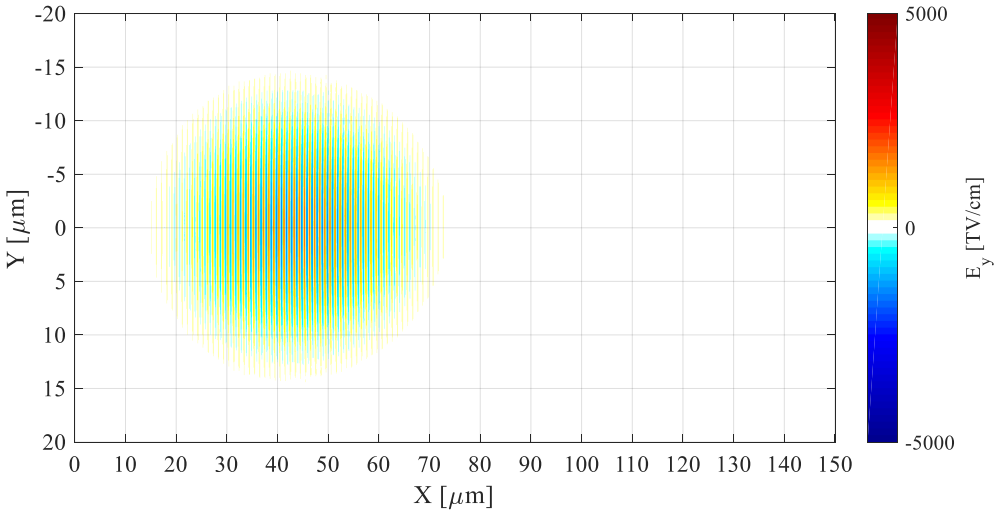

Figure 4.3: Initial electric field slice of a linearly polarized Gaussian laser pulse launched in a 3D PIC simulation. The time stamp for this frame is 267fs after simulation start.

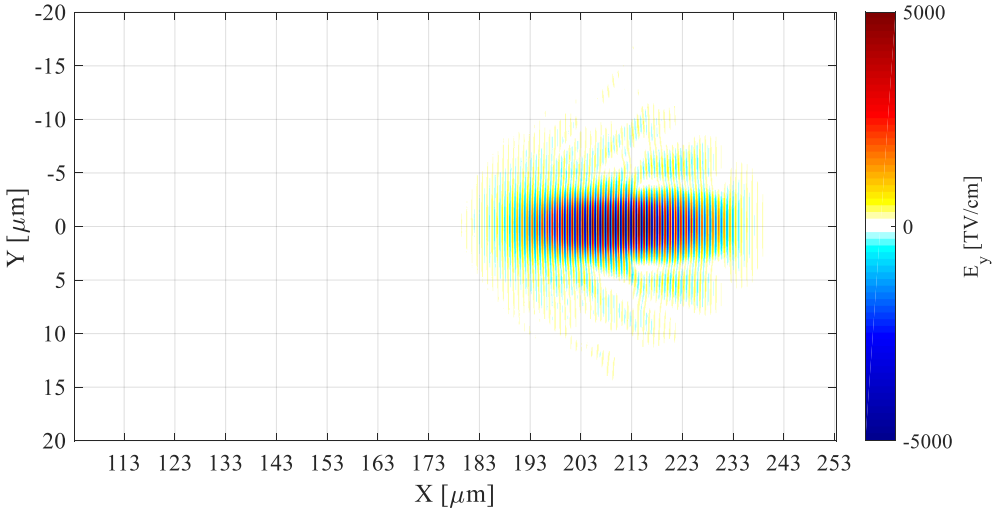

Figure 4.4: Relativistic self focussing of a linearly polarized Gaussian laser pulse launched in a 3D PIC simulation. The time stamp for this frame is 634fs.

Theoretically, under the self-guiding condition, we expect the peak intensity of the laser to scale as [96],

$$a_0 \approx 2\left(\frac{P}{P_c}\right)^{1/3} \tag{4.23}$$

Given the input parameters of the simulation, we find $P_c \approx 580GW$. The corresponding peak power of a laser can be computed via [94],

$$P \approx \frac{I_0 \pi w_0^2}{2} \tag{4.24}$$

For the Gaussian case, the peak power of the laser is found to be roughly $25TW$. According to the Eq.4.23, we find $a_0 \approx 7$ which corresponds to a peak intensity of $6.8 \times 10^{19} Wcm^{-2}$. While this is significantly lower than the result we observed, we note that the result in Fig.4.4 is the peak intensity reached during self focussing and is not necessarily the steady state result that Eq.4.23 is based on.

Fig.4.5 shows the same time frame as Fig.4.3 (267fs), however this time we have launched a Laguerre-Gaussian $\ell = 1$ beam. As we are taking a slice through a 3D simulation, we see the cross section of the donut mode, and the corresponding zero on axis. The peak electric field in this case is $1.6 \times 10^{13} V/m$, similar to the Gaussian case. This is because they were launched with the same intensity, but the LG mode has roughly 4 times the total power in order to achieve this same intensity. Thus the ratio of power to the critical power for the $\ell = 1$ mode given by Eq.4.20 is approximately the same as the Gaussian case.

Letting the beam propagate to the same time frame (634fs) as in Fig.4.4, we find that as was expected, the LG mode "pinches" as shown in Fig.4.6. The peak intensity the beam reaches is however much less than the Gaussian case with a peak electric field of $2.9 \times 10^{13} V/m \approx 1.1 \times 10^{20} Wcm^{-2}$. The reason for this reduction in peak intensity is that the intensity is distributed around the ring. In Gaussian case, the energy is all flowing towards the centre of the beam, from all directions converging on the central axis. In the LG case, the energy is essentially flowing inward, but to a different point in space around the ring. It is possible to examine Fig.4.6 to see that while the LG beam ring pinched tighter, the peak intensity radius of the ring does not appear to change in average radius by very much.

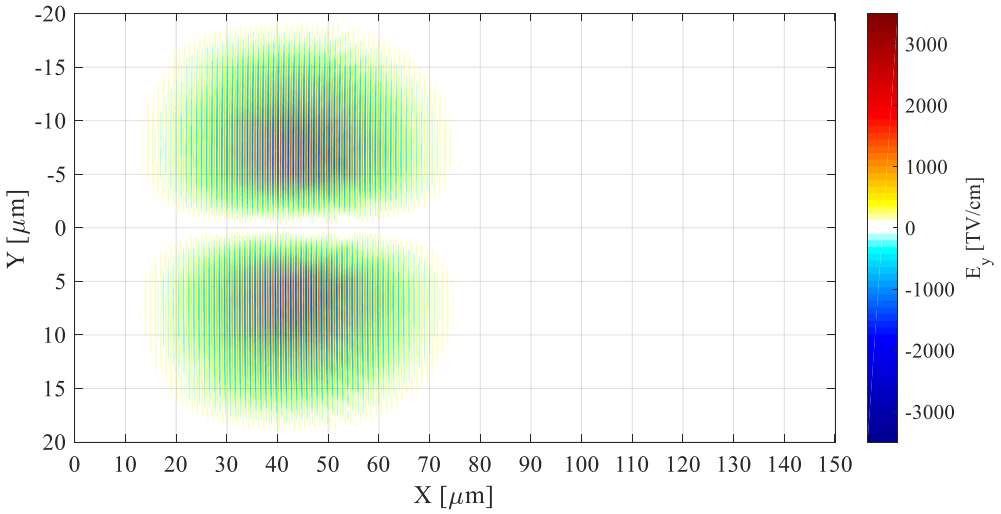

Figure 4.5: Initial electric field slice of a linearly polarized Laguerre Gaussian $\ell = 1$ laser pulse launched in a 3D PIC simulation. The time stamp for this frame is 267fs after simulation start.

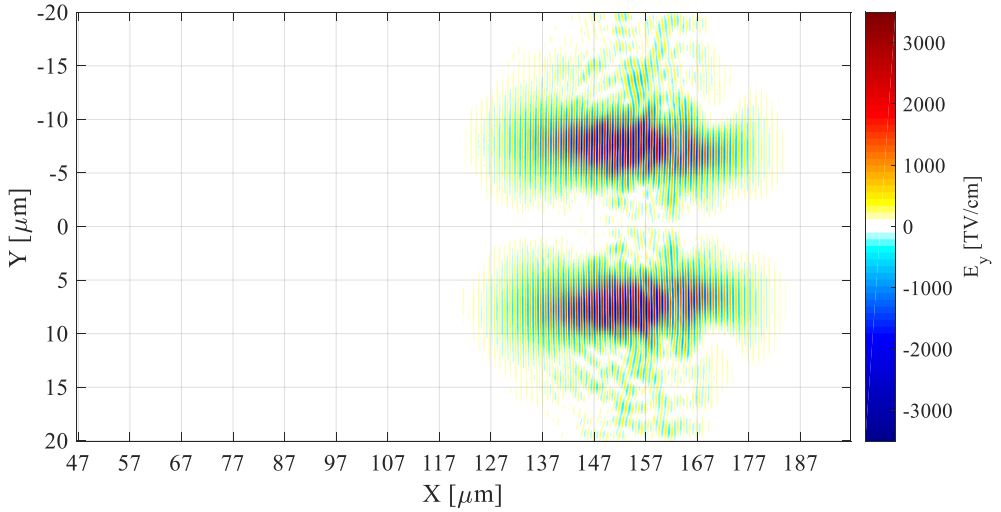

Figure 4.6: Relativistic self pinching of a linearly polarized Laguerre Gaussian $\ell = 1$ laser pulse launched in a 3D PIC simulation. The time stamp for this frame is 634fs.

Using the modified self-focussing power for the LG mode in Eq.4.24, we find $P_{c\ell} = 2.32TW$ for the $\ell = 1$ mode. The power contained within the LG mode is found to be $P \approx 97TW$ giving a predicted peak intensity from Eq.4.24 of roughly

$a_0 \approx 7$. This corresponds to a peak intensity of $6.8 \times 10^{19} Wcm^{-2}$ which is still an under-estimate of our result, but is closer.

Letting the beam propagate even further, we find that this ring collapses inwards with a decreasing average radius. We call this second mode the "ring collapse". This is shown at time 934fs in Fig.4.7 where the electric field has further increased slightly to roughly $3.1 \times 10^{13} V/m \approx 1.3 \times 10^{20} Wcm^{-2}$. This is roughly one quarter of the peak intensity of the Gaussian case. The increase in electric field is moderated by the ring spreading over a larger range of radii. Further propagation sees filamentation and break up of the beam and phase. This late time breakup, in part, may be due to boundary effects propagating into the centre of the beam.

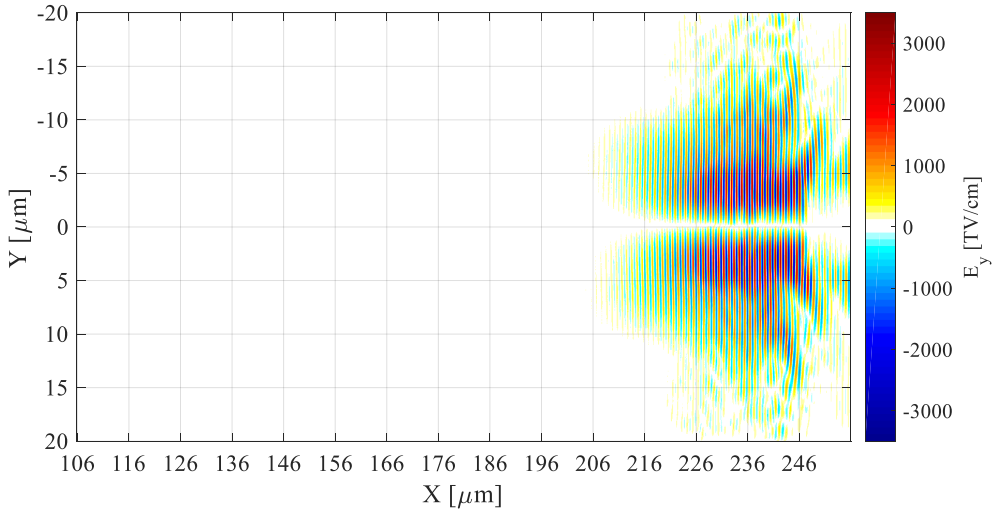

Figure 4.7: Relativistic ring collapse of a linearly polarized Laguerre Gaussian $\ell = 1$ laser pulse launched in a 3D PIC simulation. The time stamp for this frame is 934fs.

4.3.1 Plasma Channels

An interesting concept introduced to help with guiding of Gaussian beams and to further the interaction distance is through the use of a preformed plasma channel. Theoretically, this is just a plasma with a transverse parabolic plasma density profile with the lower density on axis and higher density radially outward acting as a positive lens. This corresponds to the Δn term in Eq.4.21. A parabolic plasma channel then takes the form,

$$n(r) = n_0 + \Delta n \frac{r^2}{w_0^2} \tag{4.25}$$

where in order to have stable propagation with beam radius w_0, Δn can be found to have an optimal value given by [39],

$$\Delta n = \frac{1}{\pi r_e w_0^2} \tag{4.26}$$

where r_e is the classical electron radius as described in Eq.3.87. Using this channel density profile, the Gaussian beam can propagate over many Rayleigh lengths. By extending the interaction length, the acceleration of electrons through wakefield acceleration can be enhanced reaching energies as high as 8 GeV [57].

Experimentally a plasma channel like this can be introduced using a pre-pulse from the laser (or a different laser) to pre-ionize the plasma and creating a cylindrically expanding blast wave with a density depression along the laser axis. Alternatively one could consider a discharge tube with an intense electrical discharge through gas as is done in some laboratories today [57].

If we consider the plasma channel required to extend the propagation for the Laguerre-Gaussian mode, we find that a parabolic plasma channel may not be the optimal choice in the nonlinear regime. While we don't pursue this problem in this thesis, we hypothesize that the solution could resemble a cylindrical channel with high density on axis, low density where the peak of the LG beam will be, and a high density outside of this region. Making the assumption that the optimal Gaussian solution would work for the LG beam due to its independence of laser intensity, we simply write the plasma channel density profile as,

$$n(r, \ell) = n_0 + \Delta n \frac{\left(r - w_0\sqrt{\frac{|\ell|}{2}}\right)^2}{w_0^2} \tag{4.27}$$

where $w_0\sqrt{|\ell|/2}$ is the location of the peak intensity of a $p = 0$ Laguerre-Gaussian mode. These plasma channel profiles are plotted in Fig.4.8. This plasma density profile for the LG beam could be suitable for maintaining the "ring pinch" self focussing mode and could suppress the collapse of the self focussing.

Generating such a plasma density profile in the laboratory could be done by first passing a lower powered LG mode through the plasma, similar to what is done in the

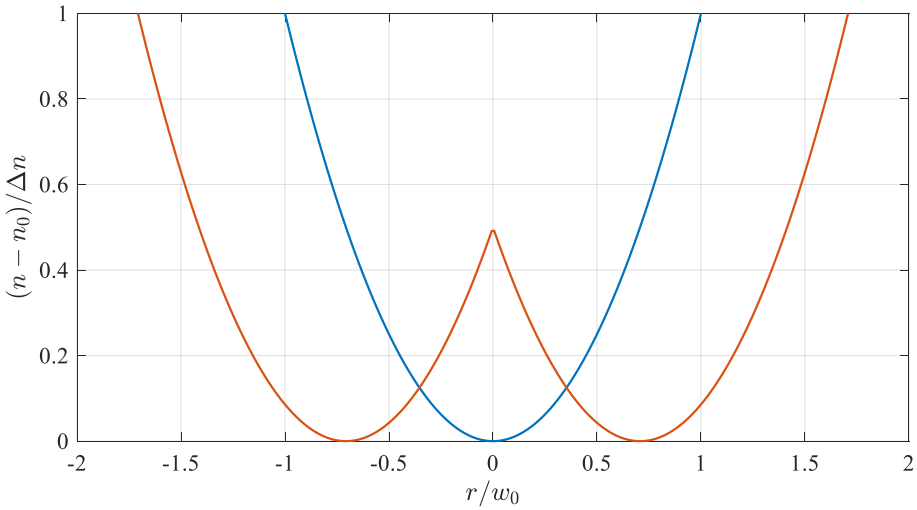

Figure 4.8: Plasma density profiles suitable for guiding a Gaussian (blue), and a Laguerre Gaussian $|\ell| = 1$ beam (red).

Gaussian case. The solution is however hypothetical and needs to be studied quite extensively using numerical solutions to the nonlinear Schrodinger equation. Creating such an optimal plasma channel profile for the LG beams experimentally could be challenging.

One issue as already mentioned is that the LG intensity profile is not symmetric about the peak intensity point in the beam, that is, the slope of the intensity on the outside radius is not the same as that of the inner radius. This is further complicated when the beam self-pinches and collapses. We do not pursue plasma channels further in this thesis, and instead indicate a route for further study as a method for extending the effects we are about to describe.

4.4 Wakefield Acceleration

Probably one of the must successful applications of underdense laser plasma interactions is the wakefield accelerator first described by Tajima and Dawson in 1979 [153]. In this scheme, a (typically) short laser pulse of pulse duration $c\tau \approx \lambda_p$ interacts with an underdense plasma driving plasma waves that have a phase velocity close to c. Electrons can be trapped (or injected) into these plasma waves accelerating to relativistic energies. If the laser is low intensity, it excites sinusoidal plasma waves

propagating along the laser axis given by,

$$\delta n_e = n_e \sin(k_p z - \omega_p t) \tag{4.28}$$

from which we use Poisson's equation to find an axial electric field,

$$\boldsymbol{E}(z,t) = \frac{n_e e}{k_p \epsilon_0} \cos(k_p z - \omega_p t)\hat{z} \tag{4.29}$$

where k_p is the plasma wavenumber, $k_p = 2\pi/\lambda_p$ and n_e is the electron density. The strength of this electric field in the linear regime is limited to E_0 as given in Eq.4.15, but can be surpassed in the nonlinear regime.

We do not intend to review the detailed theoretical analysis behind this interaction and refer the reader to some of the many works on the subject [56, 97, 39]. Instead we aim to give a review of some of the scaling laws, and the associated variations in these laws for when transitioning to higher order laser modes.

In the linear 3D regime, the plasma wakefield is often derived from the cold fluid equations; the Poisson equation,

$$\nabla \cdot \boldsymbol{E} = e\frac{\delta n_e}{\epsilon_0} \tag{4.30}$$

the continuity equation,

$$\frac{\partial n_e}{\partial t} + \nabla \cdot (n_e \boldsymbol{u}) = 0 \tag{4.31}$$

and the momentum equation,

$$m_e n_e \left[\frac{\partial \boldsymbol{u}}{\partial t} + (\boldsymbol{u} \cdot \nabla)\boldsymbol{u}\right] = -e n_e (\boldsymbol{E} + \boldsymbol{u} \times \boldsymbol{B}) - \nabla \cdot \bar{\boldsymbol{P}} \tag{4.32}$$

where $\boldsymbol{u}$ is the electron fluid velocity, and $\bar{\boldsymbol{P}}$ is the plasma pressure tensor.

From these equations, it is possible to derive an initially uniform plasma wave driven by a low intensity laser ($a^2 \ll 1$) as [39],

$$\left(\frac{\partial^2}{\partial t^2} + \omega_p^2\right)\frac{\delta n_e}{n_0} = c^2\nabla^2\left(\frac{a^2}{2}\right) \tag{4.33}$$

and,

$$\left(\frac{\partial^2}{\partial t^2} + \omega_p^2\right)\phi = \omega_p^2\frac{a^2}{2} \tag{4.34}$$

where ϕ is the electrostatic wake potential and $\delta n_e/n_0 = (n_e - n_0)/n_0$. For small density perturbations $|\delta n_e/n_0| \ll 1$, we find the electron density perturbation as,

$$\frac{\delta n_e}{n_0} = \frac{c^2}{\omega_p} \int_0^t \sin\left(\omega_p(t-t')\right) \nabla^2 \left(\frac{a^2(\boldsymbol{r}, t')}{2}\right) dt' \tag{4.35}$$

and the axial electric field as,

$$\frac{E}{E_0} = -c \int_0^t \sin\left(\omega_p(t-t')\right) \nabla \left(\frac{a^2(\boldsymbol{r}, t')}{2}\right) dt' \tag{4.36}$$

Here, E_0 represents the cold non-relativistic wave-breaking field given by $E_0 = m_e c\omega_p/e$ identical to the result given in Eq.4.15. These solutions are only valid in the linear regime where $E \ll E_0$. Upon first glance, it is clear that the plasma density perturbation and the plasma electric field are functions of a^2 which is proportional to the laser intensity. Therefore, to first order, we do not expect there to be any immediate contribution from the helical phase of an OAM beam driving a wakefield accelerator. However, we do expect that the electron density perturbation and accelerating electric field will have a different shape.

Solutions to Eq's 4.33 and 4.34 indicate that the optimal pulse length for efficiently generating wakefields occurs when the pulse duration matches the plasma wavelength, $c\tau = \lambda_p$ [39]. Due to the requirement that self-focussing occurs when $c\tau > \lambda_p$, pulse duration's are usually chosen such that self focussing can occur, but are sufficiently close to the plasma wavelength for efficient wakefield generation.

In addition to the axial electric field generated in Eq.4.36, we find that for fields with a Gaussian transverse spatial profile there are transverse fields generated in the radial and azimuthal directions, E_r and B_θ. These transverse fields are related to the axial electric field by the Panofsky-Wenzel theorem [79],

$$\frac{\partial E_z}{\partial r} = \frac{\partial(E_r - cB_\theta)}{\partial(z - ct)} \tag{4.37}$$

Therefore for a particle accelerating along the plasma axial electric field, it will experience a radial force proportional to $W_r = q(E_r - cB_\theta)$. This force can be be focussing, or defocussing and can be tailored based on the mode of the laser. For instance, it was shown that for a wakefield driven by a Laguerre-Gaussian OAM mode, a focussing force suitable for guiding positrons can be created [164]. Typically what is found for

electrons is that the force will be radially towards the axis where the laser intensity is maximal. In the case of a Gaussian laser, this is the laser axis and electrons accelerating in the laser wakefield will oscillate about the laser axis as a result of the transverse force. In the Laguerre-Gaussian case, the peak laser intensity is off axis such that the electrons still oscillate, but the oscillation takes place all around the peak intensity ring [177, 13].

Until this point, we have assumed an $a_0 \ll 1$ such that the plasma waves driven by the laser are linear. If the laser intensity becomes relativistic ($a_0 \geq 1$), then the plasma waves become nonlinear. As one might expect, the waves in the nonlinear regime are strongly dependant on the laser pulse strength and pulse duration of which many regimes have been identified [39]. For this thesis, we are concerned mostly with single pulse excitation with laser pulses on the order of the plasma wavelength ($\approx 30fs$), and as such we are mostly concerned with laser wakefield acceleration, wave-breaking, and the blow-out regime. We do not consider plasma wakefield acceleration (wakefield driven by particles as opposed to light), or self-modulated wakefield's where the laser pulse is much longer than the plasma wavelength, beat-wave accelerators driven by two overlapped pulse of frequency $\omega_0 - \omega_1 = \omega_p$, or colliding pulses [107].

4.4.1 Blow-Out Regime

Of interest to this thesis is the intensity range of $1 < a_0 < 5$ which represents intensities which are obtainable on many laser systems worldwide. In this intensity range, the linear sinusoidal wakefield steepens and the period lengthens by a factor of [96] $\lambda_{Np} \approx \sqrt{a_0}\lambda_p$, such that the plasma wave can break - much like a wave breaking on the ocean shore. In this case, the electric field of the plasma wave surpasses that of the cold wavebreaking limit E_0 and can be given through a 1D relativistic analysis as [39],

$$\frac{E_{WB}}{E_0} = \frac{a_0^2/2}{\sqrt{1 + a_0^2/2}} \tag{4.38}$$

Corrections for the 3D relativistic amplitude can be found to be approximately equal to $E_{max} \approx \sqrt{a_0}E_0$ [96].

In addition to the wave steepening, the laser ponderomotive force can become strong enough to completely expel electrons from the high intensity region while the heavy immobile ions remain in place. This expulsion creates a void of electrons in and behind the laser pulse resulting in a charge imbalance. The radius of this void

or "bubble" can be quite complex analytically depending on the plasma density and laser intensity, however it is often assumed in the intensity range we are working that the radius of the bubble can be approximated by [164, 96],

$$k_p r_B \approx 2\sqrt{a_0} \tag{4.39}$$

In the case of our example plasma of density $1 \times 10^{19} cm^{-3}$ and a laser intensity of $2.5 \times 10^{19} W cm^{-2}$, we find a bubble radius for a Gaussian drive beam of roughly $6\mu m$.

Using the same plasma density profile as in the self-focussing section and as shown in Fig.4.9, two 3D PIC simulations were run for a Gaussian beam and a Laguerre Gaussian beam of the same intensity and same pulse duration. The simulation box was reduced in longitudinal size to $100\mu m$ giving a slightly higher grid resolution in $\hat{x}$, but was widened in the transverse directions to minimize the effects of boundary conditions on the simulation.

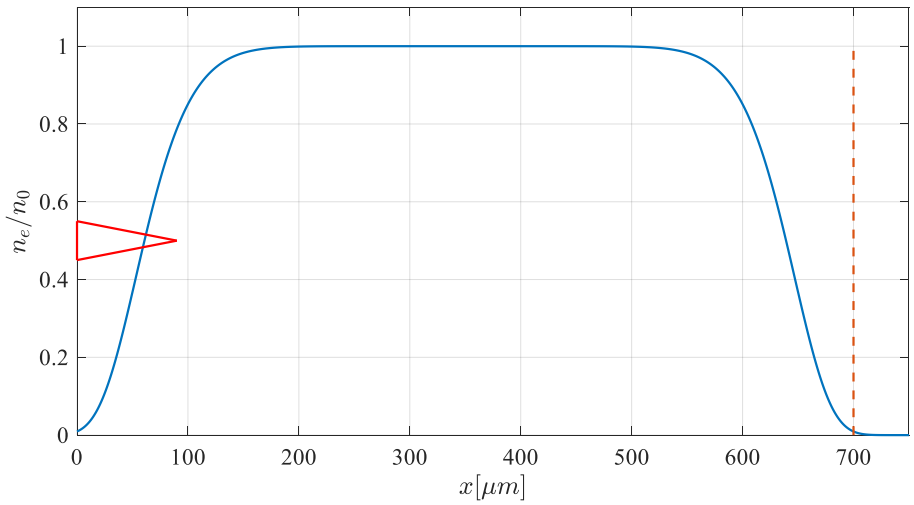

Figure 4.9: Electron density distribution used in numerical simulations of wakefield acceleration. The distribution is described by a super Gaussian shape of width $300\mu m$ and super Gaussian parameter 10. The red dotted line indicates the detection screen for the electrons and photons, while the solid red triangle represents the laser and its focal plane located at $x = 90\mu m$.

These two runs will be explored over the next few pages to identify major differences between the Gaussian and Laguerre Gaussian driven wakefields. The simulation parameters have been listed in Table. 4.2.

Table 4.2: Simulation parameters used to compare wakefields between Gaussian and Laguerre Gaussian beams.

Parameter	Gaussian Drive	Laguerre Gaussian Drive
Temporal FWHM	$30fs$	$30fs$
Peak Intensity	$2.5 \times 10^{19} Wcm^{-2}$	$2.5 \times 10^{19} Wcm^{-2}$
a_0	3.4	3.4
w_0	$8\mu m$	$9.6\mu m$
ℓ	0	1
Peak Power $[TW]$	25	97
$U[J]$	0.64	2.36
$\lambda[nm]$	800	800
n_0	$1 \times 10^{19} cm^{-3}$	$1 \times 10^{19} cm^{-3}$
$P_c[TW]$	2.7	10.9
Polarization	Linear $(\hat{y})$	Linear $(\hat{y})$

Fig.4.10 a) gives the electron density perturbed by the Gaussian pulse after the laser had propagated in the plasma for roughly $1ps$. From the figure it is clear to see the bubble behind the laser pulse, with many bubbles following behind that as the plasma wave continues to oscillate after the laser has passed. The first bubble radius appears to agree quite well with the predicted $6\mu m$. Tile b) shows the time averaged axial electric field that has been averaged over each $26.7fs$ output dump. The peak strength of accelerating field is normalized to the cold-wavebreaking limit E_0 and is found to be roughly 2.6 which is in reasonable agreement with the theoretical value of $\sqrt{a_0}E_0 \approx 1.8E_0$. Using Eq.4.38, we actually find a better agreement where $E/E_0 = 2.2$.

If instead we consider the case of the Laguerre-Gaussian pulse where $p = 0$, we find that the bubble is modified to a donut as expected. As we did with the analysis of the plasma channel, we take a 2D slice through the LG mode and find two lobes that are symmetric about the laser axis shown in Fig.4.5. To first order, we can say that each of the lobes in 2D can be approximated by a Gaussian shape and as such each will create a bubble of radius $r_B \approx 2\sqrt{a_0}/k_p$ about the peak intensity axis radius located at $r_{max} = w_{LG}\sqrt{|\ell|/2}$. We can therefore write to first order the inner and

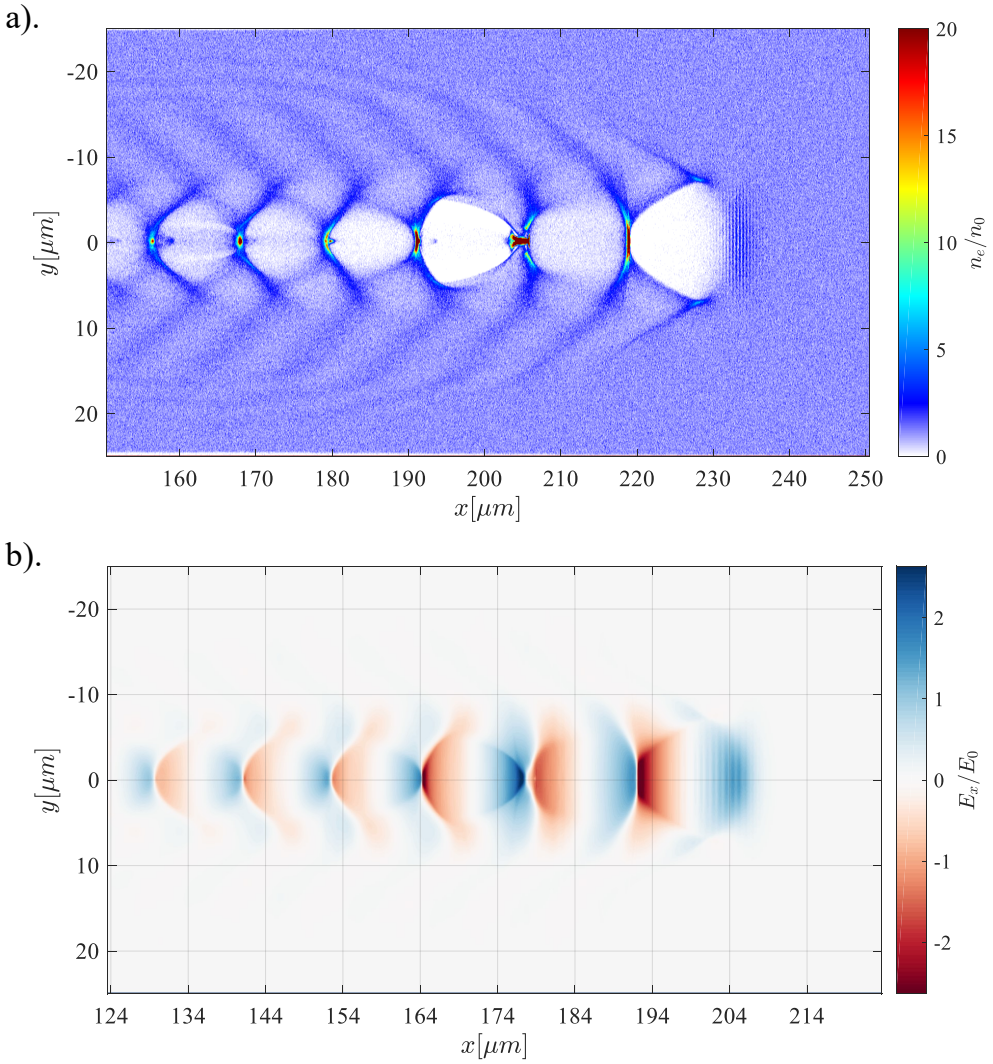

Figure 4.10: Laser wakefield acceleration with a 30fs $2.5 \times 10^{19} W cm^{-2}$ Gaussian pulse with beam waist $8\mu m$ in $1 \times 10^{19} cm^{-3}$ plasma. Tile a) shows the a 2D slice of the electron density normalized to the initial electron density of the plasma at time $t = 1ps$. Tile b) shows the a 2D slice of the axial electric field normalized to the cold wave-breaking field E_0 at time $t = 1ps$.

outer approximate bubble radii as,

$$r_{B\ell} \approx w_{LG}\sqrt{\frac{|\ell|}{2}} \pm \frac{2\sqrt{a_0}}{k_p} \tag{4.40}$$

where the + solution gives the outer radius of the bubble, while the − solution gives the bubble inner radius. In 3D this leads to a "donut bubble" from which electrons are accelerated in a ring behind the laser pulse [13]. The cross section of this donut bubble is given in Fig.4.11 a) where the electron density is normalized to the initial electron density of $n_0 = 1 \times 10^{19} cm^{-3}$. Using our model of the bubble radius, we find the predicted outer and inner bubble radii are approximately $13\mu m$ and $1\mu m$ respectively. According to Fig.4.11, we find good agreement with the outer bubble radius, but some slight discrepancy with the bubble inner radius. This could be a result of excess charge build up at the centre of the donut.

Unlike the Gaussian case, we find that the trailing donut bubbles are unstable, and tend to collapse to a single bubble on axis after 4 or 5 plasma periods. This instability has been found to be dependant on both the laser intensity and density from numerical simulations. For lower intensity lasers, where the plasma waves driven become more linear, we find the donut bubbles to be much more stable and persist for the length of the simulation box. In addition we find the interesting result in this highly nonlinear regime where there is a charge build up on the laser axis at the centre of the donut bubble in Fig.4.11 a) at $x \approx 220\mu m$. Unlike the Gaussian case, the cross-section of the donut bubble is asymmetric resulting in an asymmetric around its centre point transverse current on the rear of the bubble. This net transverse current is moving radially inward and collects on the laser axis forming a small electron bunch moving with the group velocity of the laser. Much like plasma-wakefield acceleration, these electrons are able to drive wakefields on the laser axis and if strong enough, these plasma wakefields interact with the laser wakefield donut bubble. This eventually destroys the donut ring bubble and we are left with the single bubble on axis as previously described.

While this mechanism has not been theoretically pursued in this thesis, we believe that it exists and intend to follow up with this transition from laser to plasma wakefield in further studies.

Tile b) of Fig.4.11 shows the time-averaged axial accelerating electric field generated in the wake of the LG mode. The time averaging takes place over $26.7fs$

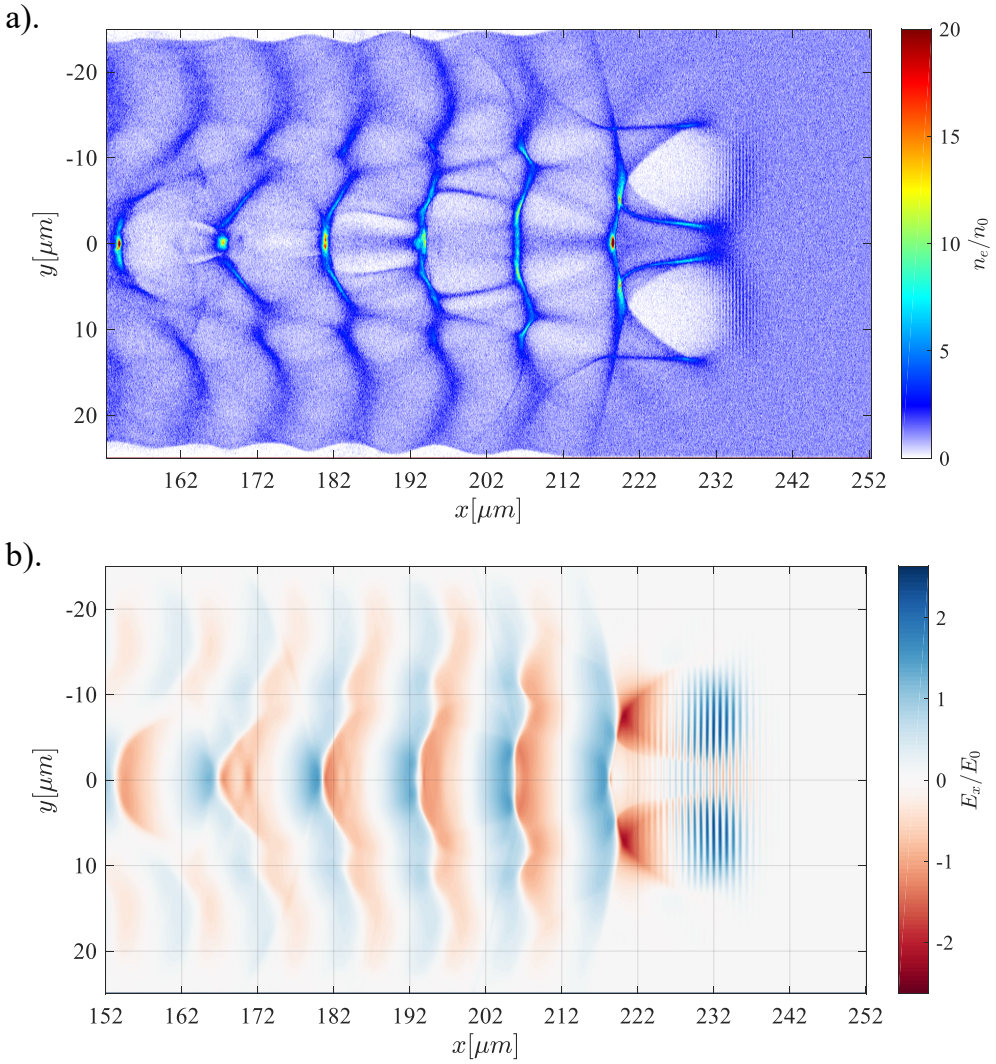

Figure 4.11: Laser wakefield acceleration with a 30fs $2.5 \times 10^{19} W cm^{-2}$ Laguerre Gaussian $\ell = 1$ pulse with beam waist $9.6 \mu m$ in $1 \times 10^{19} cm^{-3}$ plasma. Tile a) shows the a 2D slice of the electron density normalized to the initial electron density of the plasma at time $t = 1ps$. Tile b) shows the 2D slice of the axial electric field normalized to the cold wave-breaking field E_0 at time $t = 1ps$.

between each output dump. Here we see the distinct donut accelerating field following the laser pulse with a peak strength of roughly $1.8E_0$. Given the scaling law of $E_{max} \approx \sqrt{a_0}E_0$, we predict a peak accelerating field of approximately $1.8E_0$ in good agreement with the numerical simulation. Following the first bubble are plasma waves generated from the initial density perturbation. As previously described, the laser driven donut wakefield plasma is not maintained in this regime with the donut bubble collapsing to the plasma-wakefield bubble on axis. This is clearly seen in the last bubble of the axial accelerating field in tile b).

An interesting difference when using an LG mode to drive a wakefield is the focussing force as described in Eq.4.37. We re-write this equation as,

$$\frac{F_r}{q} = E_r - cB_\theta \tag{4.41}$$

where q is the charge of the particle. This highlights that the force is simply the radial component of the Lorentz force and is charge-sign dependant. The force will be focussing for positive charges when the force is negative, and de-focussing when the force is positive. Plotting the force normalized to the charge of the particle is given in Fig.4.12. Tile a) shows the focussing force for a Gaussian drive laser, where we can see the force is zero on axis, and positive towards the inside edges of the bubble. For an electron, this force is focussing inwards causing the electron to oscillate about the laser axis with an oscillation frequency of [177],

$$\omega_\beta = \frac{\omega_p}{\sqrt{2\gamma}} \tag{4.42}$$

In the case of the Laguerre-Gaussian drive beam as seen in Fig.4.12, we find a similar result, but now the centre of focussing is off axis. As a result, we find that the electrons not only oscillate about the high intensity radius, but they are free to spiral around the donut bubble. If the radius of the wakefield bubble is set to match that of the peak intensity radius, such that $2\sqrt{a_0}/k_p = w_{LG}\sqrt{|\ell|/2}$ we find that there is no longer a force-null on the axis, and positive particles are strongly focused there [164]. This mechanism has been proposed as a method to focus and collimate positron particles [164].

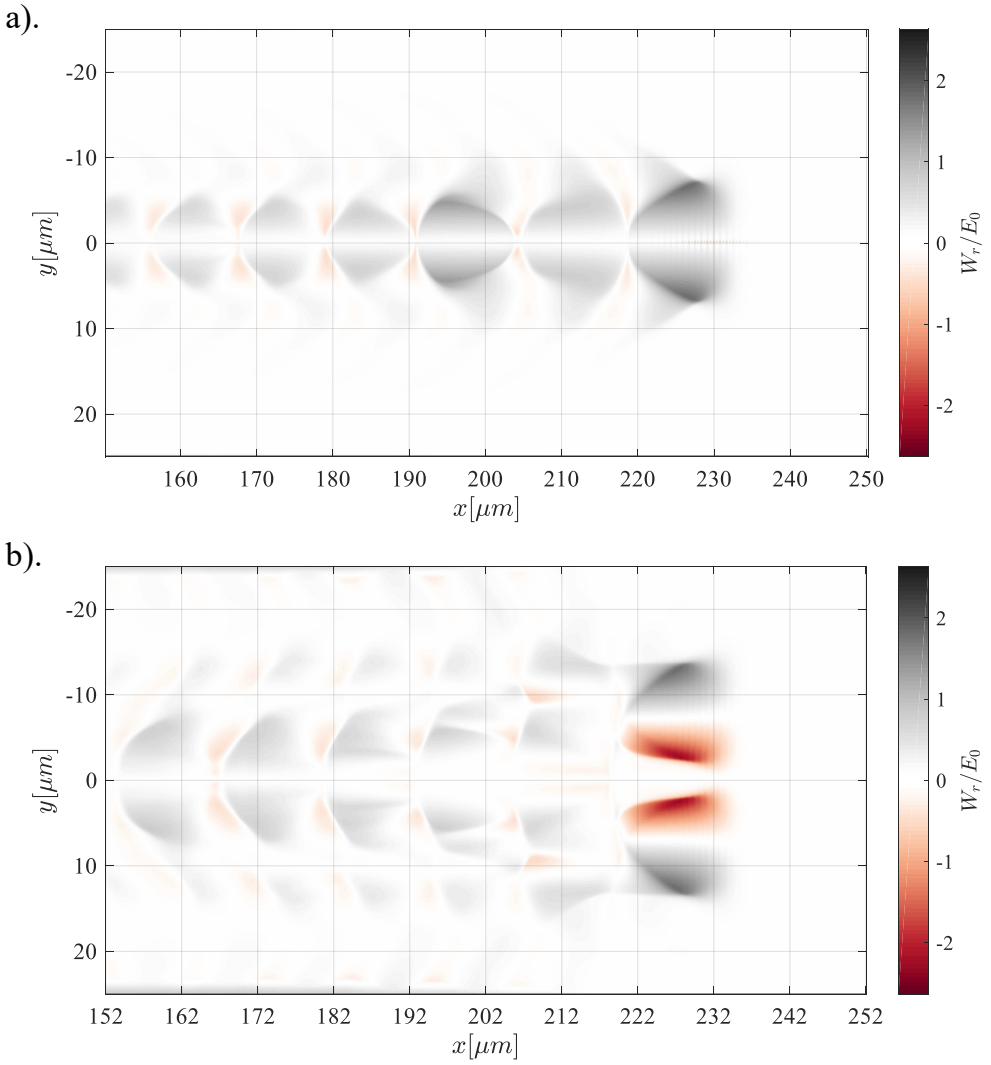

Figure 4.12: Radial forces inside the wakefield accelerator normalized to the charge of the particle. a). Radial forces found in a wakefield driven by a 30fs Gaussian laser with $a_0 = 3.4$, and $w_0 = 8\mu m$. b). Radial forces found in a wakefield driven by a 30fs Laguerre-Gaussian laser with $a_0 = 3.4$, and $w_0 = 9.6\mu m$.

4.4.2 Electron Injection and Ejection

For an electron to take advantage of these large amplitude nonlinear waves, it must be first injected into this void through some mechanism. As can be seen from Fig.4.10 and 4.11 the electrons tend to bunch up on the rear side of the bubble. If the electrons in this bunch have sufficient forward momentum, they are able to catch up with the wake and self-inject. To enable this, the bubble radius needs to be sufficiently large such that the electrons on the sheath of the bubble gain enough longitudinal momentum to move forward with a speed close to c to match the velocity of the tail of the bubble. This longitudinal momentum is obtained by the interaction of the electrons with the electric and magnetic fields on the sheath of the bubble. The crossing of the electrons on the rear of the bubble gives rise to a narrow sheath that can inject electrons into the rear of the bubble.

For this mechanism to work, the laser needs to have an a_0 of between 3 and 4 to reach the threshold required for self injection [96, 160, 53]. Plugging this into Eq.4.39 we find that the minimum bubble radius required for self injection is therefore $k_p r_B \approx 3 - 4$.

The self injection of electrons into Laguerre-Gaussian modes has been studied quite extensively [107, 177, 13, 47, 106] and can become quite complicated. One reason for this is that the donut bubble cross section is asymmetric as can be seen in Fig.4.11. This asymmetry can lead to poor electron self injection as the electrons tend to drift towards the laser axis. As we will soon see, self injection in a Laguerre Gaussian driven wakefield is not efficient, however other electron injection methods are still suitable.

The second electron injection mechanism of interest to this thesis is that of ionization injection [103, 119]. In this mechanism, electrons are ionized close to the peak intensity of the laser via barrier suppression ionization as discussed in Chapter 3. Initially the front end of the laser pulse with lower intensity ionizes and sweeps the majority of the outer shell electrons out of the way of the laser pulse before they are able to interact with the higher intensity part. However, some inner shell (k-shell) electrons could remain non-ionized depending on the laser intensity. For instance, the inner shell nitrogen electrons (6+ and 7+) do not ionize until the laser surpasses $1 \times 10^{19} W cm^{-2}$ according to Table 3.1.

If the peak laser intensity is carefully selected, and a suitable molecule is injected into the bulk ionizable material, then electrons can be injected into the laser wakefield

with intensity thresholds as low as $a_0 = 1.6$ [119, 103]. In a typical wakefield experiment, a background gas of helium is often used due to its low ionization appearance intensities of $\approx 1-10\times10^{15}Wcm^{-2}$. A second gas such as nitrogen is then introduced in small quantity, often on the order of 1% of the mixture to supply the wakefield with ionizable electrons close to the peak intensity of the laser.

As these electrons are born within the high intensity laser potential region, they are also accelerated with a large ponderomotive force and can be ejected backwards into the void of the bubble. They are born however with essentially zero initial energy through the barrier suppression mechanism, but as they slip back through the laser into the bubble, they feel the longitudinal accelerating gradient of the bubble. They can then be efficiently accelerated in the bubble to match the group velocity of the laser, and eventually surpass it.

While experimentally it is not possible to determine the source of the electrons, whether it is ionization injection or self injection, it is possible numerically. As before, we use a super-Gaussian electron distribution to accurately represent what is used in the experiment, but now we will also introduce a detection screen as shown in Fig.4.9 indicated by the red dotted line after the bulk plasma. In this figure, the electron density (blue) has been normalized to the peak density value n_0 of $1 \times 10^{19}Wcm^{-2}$.

The plasma in the simulation is composed of a mixture of helium and nitrogen. The helium has been pre-ionized to reduce computational load, while the nitrogen has been pre-ionized to the fourth electron only. The inner 3 electrons are still bound to the nucleus and must be ionized in the simulation to be injected into the wakefield. For these simulations, we use the default ADK ionization routine in the EPOCH code [7, 8].

The detection screen records the momentum and position of each electron that strikes it allowing us to estimate the energy spectrum of the electron beam, as well as the beam divergence as a function of energy and the ejected angular momentum of the electrons. Experimentally, we cannot place a detector this close to the laser-plasma interaction as it would be destroyed. Instead any electron detectors are placed sufficiently far away such that the laser diverges to a lower fluence and does not destroy them. To first order, we can assume the electrons are ballistic and take the position and momentum of each electron from the detection plane in the simulation and propagate it to a second screen 10's of centimeters away as is in the physical experiment.

Fig.4.13 a) shows the ejected energy of electrons from a wakefield acceleration driven by the Gaussian pulse used in the previous section. The bin widths were taken to be $dE = 1MeV$. The electrons that are self injected are given in blue, while the ionized electrons are shown in red. We see that both the ionized and self-injected electrons are accelerated to roughly the same energy of $450MeV$. We also note that the spectrum is quite broad and not mono-energetic as some wakefield schemes can be [161, 128, 98, 54, 43]. One of the reasons for this is the restriction in propagation distance in the simulation to $< 1mm$ for stability and numerical reasons.

Tile b) of Fig.4.13 gives the electron spectra for a wakefield driven with the Laguerre-Gaussian pulse. Here we see a clear difference in the cut-off electron energy when comparing the electrons that are self injected to those that are injected via ionization injection. This is in agreement with our previous conjecture that there is poor self injection in the Laguerre-Gaussian case due to the bubble asymmetry. We find that the peak energy of the self injected electrons is roughly half of that from the ionized electrons which are peaked at roughly $300MeV$.

In addition to the energy spectrum of the electrons, of importance is the cone angle of the ejected electron beam. A highly divergent beam would not be of use if it was highly chromatic as any attempt to refocus the electron beam would result in a large electron spot in the image plane. Fortunately, the cone angle of the electrons emitted from the wakefield accelerator is small and often refocusing is not required. Experimentally, the values of the divergence angles are often found between $1 - 10mrad$ [98, 43, 54]. The divergence of the electron beam can be complicated to estimate analytically and is often determined by numerical simulations.

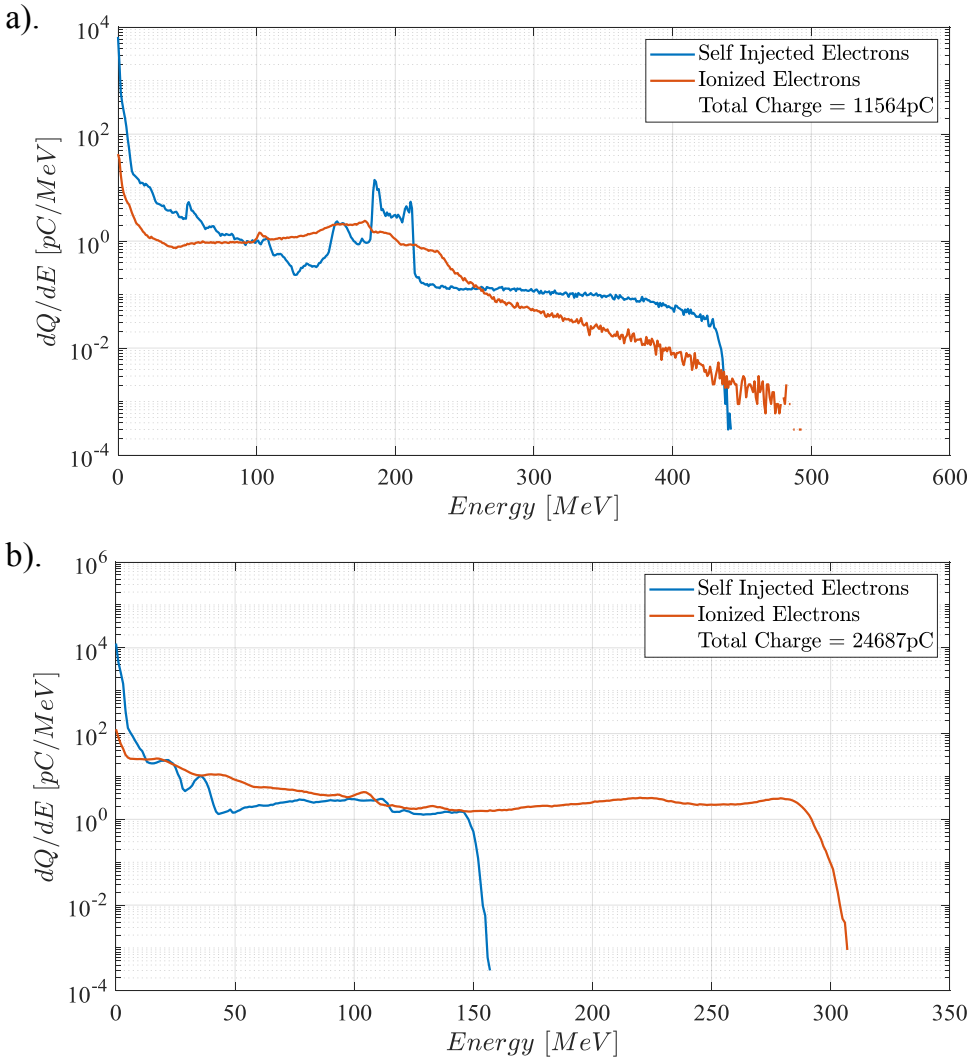

Figure 4.13: Electron spectra as detected on the detector plane. The electrons are separated into each source; the self injected electrons in blue, and the ionization injection electrons in red. Tile a) shows the results when driven by a $2.5 \times 10^{19} W cm^{-2}$ Gaussian laser pulse. Tile b) shows the results when driven by an $\ell = 1$, $2.5 \times 10^{19} W cm^{-2}$ Laguerre Gaussian laser pulse.

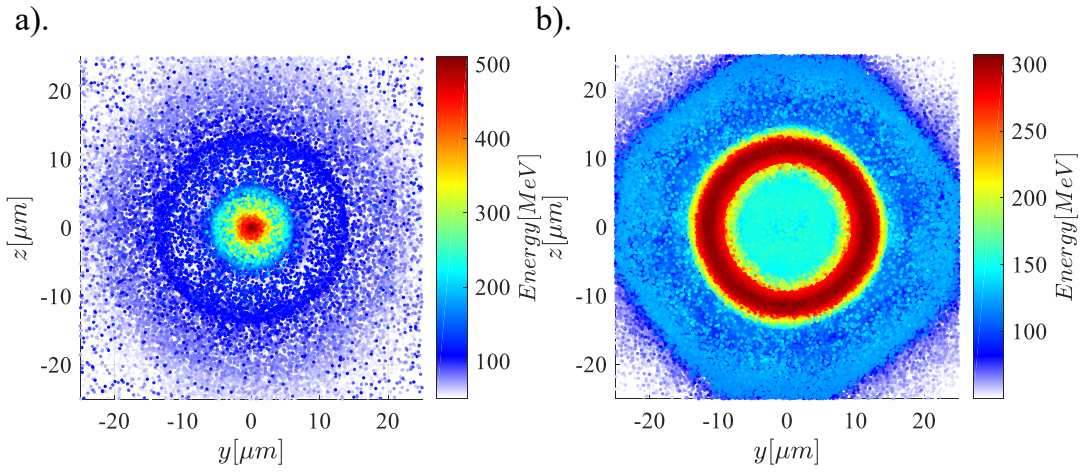

Figure 4.14: Electron spatial distributions on the near-field detector (red dotted line in Fig.4.9). The electrons are colour coded to their ejection energy according to the colourbar. a) Electron spatial distribution ejected from a Gaussian driven wakefield. b) Electron spatial distribution ejected from an $\ell = 1$ Laguerre Gaussian driven wakefield.

We begin by plotting the electron spatial distribution in Fig.4.14 in the near-field (the detector placed immediately after the plasma). Tile a) gives the near-field electron distribution when driven by the Gaussian beam, and colour coded to each electron ejection energy, while tile b) shows the near-field spatial distribution driven by the Laguerre-Gaussian beam. The difference between the two is quite clear with the electron ring generated in the Laguerre-Gaussian case. It is also clear to see the effects of the boundary conditions on the low energy electrons at larger radii producing the hard straight edges observed in Fig.4.14 b).

Taking each electron in Fig.4.14 and plotting the histogram of their divergence angles enables us to estimate the far-field spot size. Fig.4.15 shows the result for the Gaussian driven case where the self injected electrons are plotted in blue, while the ionization injection electrons are plotted in red. We find that the self injected electrons have a more collimated divergence than the ionization injection electrons. In the case of the self injected electrons, we find a peak half angle divergence of approximately $5mrad$ whereas the self injected electrons have a half angle divergence or approximately $10mrad$. Both values are in agreement with the observed values mentioned in the references above.

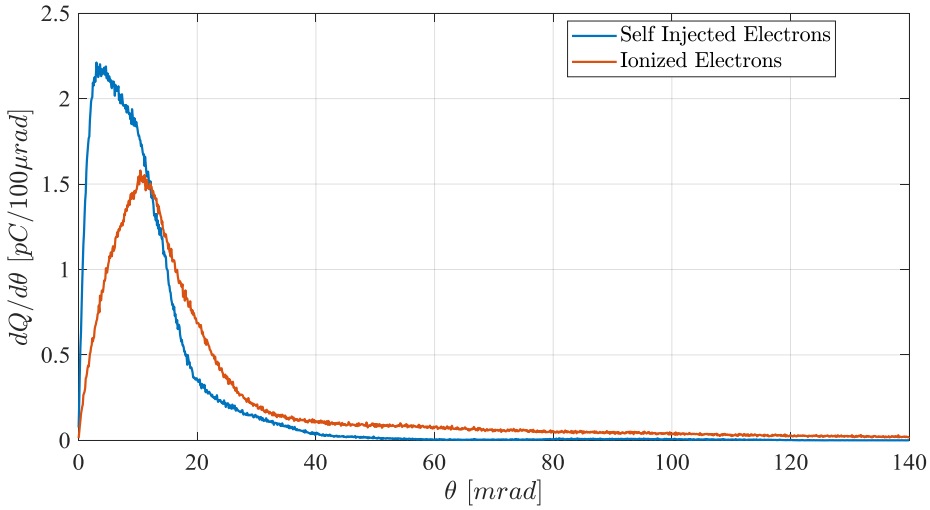

Figure 4.15: Electron divergences as found on the detector plane from a Gaussian driven wakefield acceleration. The bin-widths are found to be $d\theta = 0.1mrad$. The blue line indicates electrons that are self injected into the wake, whereas the red line indicates electrons that are injected into the wake through ionization injection.

If we instead consider the $\ell = 1$ Laguerre Gaussian driven case in Fig.4.16, we find that the divergence of the electrons is greatly increased in both cases. We first find that the smaller divergence beam is now instead the ionization injection electrons, whereas the self injected electrons now have a peak half angle divergence at roughly $40mrad$ - almost 10 times larger. The increase in the ionization injection divergence is not as drastic, but the peak of the half angle divergence is now quite broad ranging from $15 - 30mrad$. This could likely be a result of the ability for the electrons to travel azimuthally around the donut wakefield. This is not the case in the Gaussian driven case as the electrons are always focussed radially inwards to the beam axis.

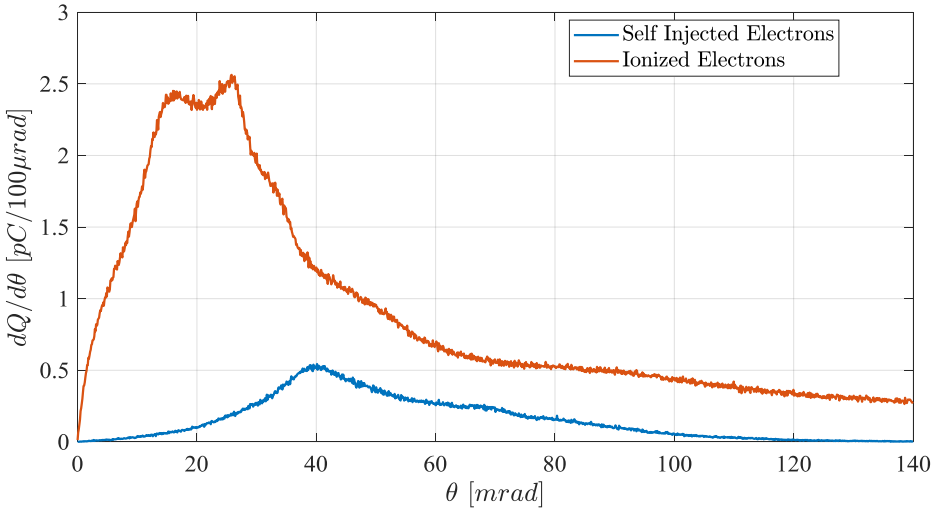

Figure 4.16: Electron divergences as found on the detector plane from a Laguerre Gaussian ($\ell = 1$) driven wakefield acceleration. The bin-widths are found to be $d\theta = 0.1mrad$. The blue line indicates electrons that are self injected into the wake, whereas the red line indicates electrons that are injected into the wake through ionization injection.

Projecting the electrons onto a far-field screen using ballistic trajectories, we can plot the spatial distribution as would be detected by a screen. The screen is placed at $287mm$ away in the $\hat{x}$ direction. The results are plotted in Fig.4.17.

Tile a) shows the far-field spatial distribution for both species electrons driven by the Gaussian pulse. Here we see a tight spot of electrons with a radius of roughly $5mm$. The high energy electrons are all located close to the axis and as the electron divergence increases, the energy decreases. Tile b) shows the results for the Laguerre-Gaussian driven case clearly showing the larger overall divergence of electrons. We do see however that the highest energy electrons are located in a ring on the screen, but there is no null on the screen axis. What we find is that there is little to no azimuthal dependence on the distribution of electrons so we are able to bin the radius of the electrons in a histogram.

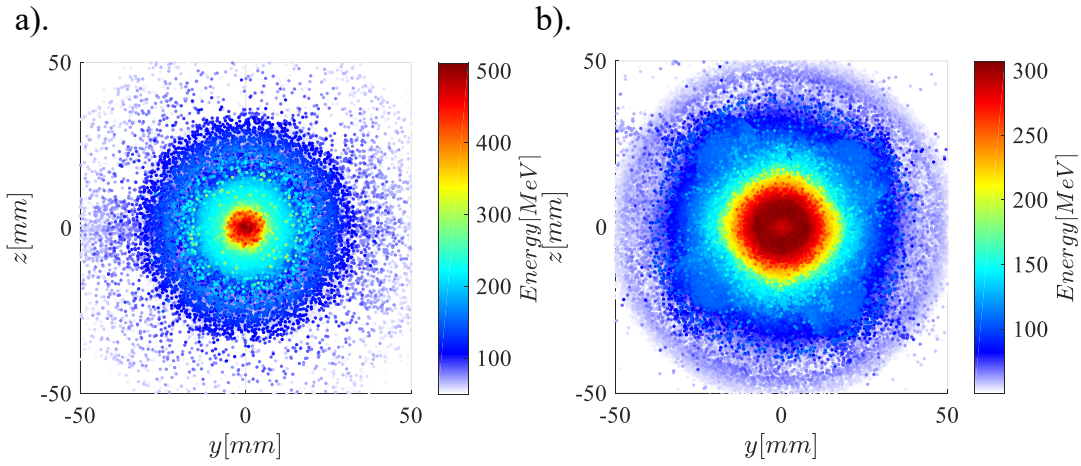

Figure 4.17: Far-field electron divergence on a screen placed $287mm$ away. Both plots are colour coordinated to the energy of the electrons striking the screen. Tile a) gives the result for the Gaussian driven case. Tile b) gives the result for an $\ell = 1$ Laguerre Gaussian driven case.

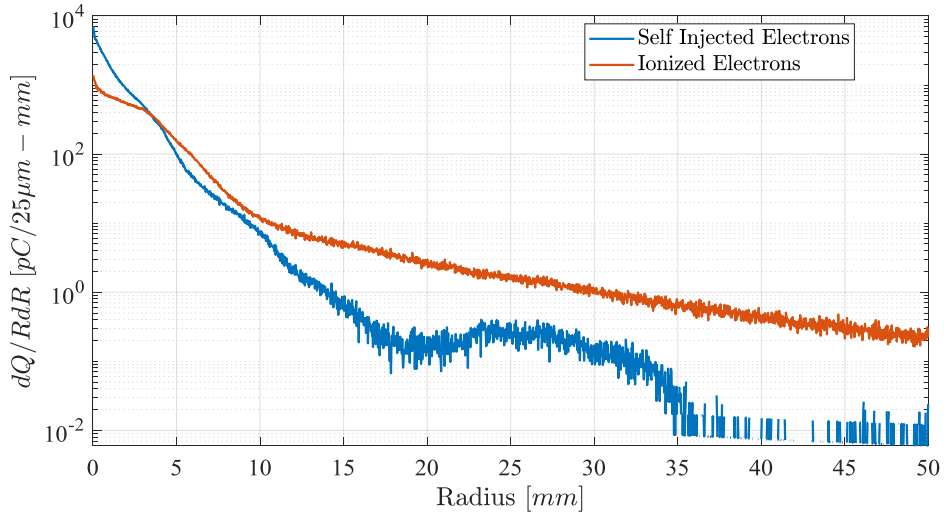

Figure 4.18: Far-field electron histogram distribution for electrons accelerated in the Gaussian driven wakefield accelerator. The bin width is taken to be $dR = 25\mu m$. The blue line indicates the self injected electrons, whereas the red line indicates the electrons injected through ionization injection.

To do this, the electrons are binned as a function of RdR to account for the

polar Jacobian. Fig.4.18 gives the radial distributions for both the self injected and ionized electrons in the Gaussian driven wakefield. Again, we see the increase in radial position of the ionization injection electrons due to their larger divergence.

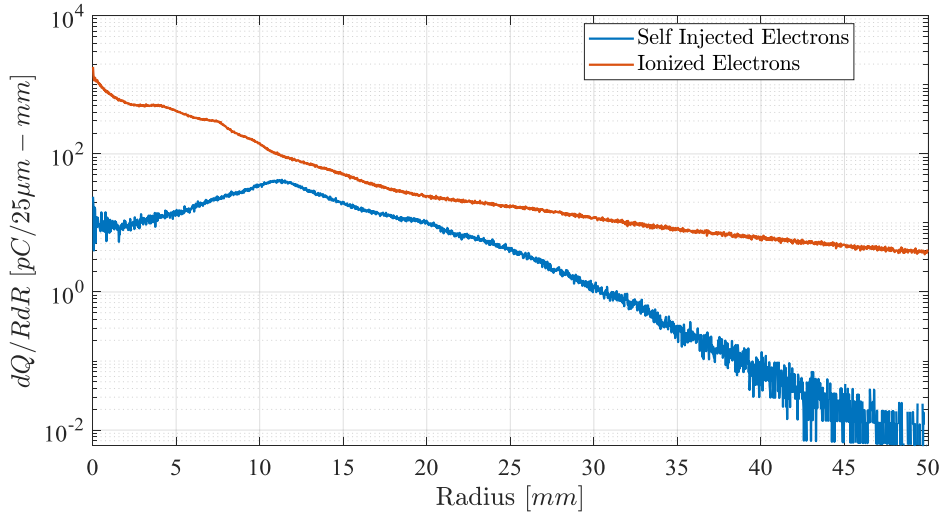

Figure 4.19: Far-field electron histogram distribution for electrons accelerated in the $\ell = 1$ Laguerre Gaussian driven wakefield accelerator. The bin width is found to be $dR = 25\mu m$. The blue line indicates the self injected electrons, whereas the red line indicates the electrons injected through ionization injection.

In the case of the Laguerre-Gaussian beam, given in Fig.4.19, we find that the distribution of self injected is peaked at roughly $12mm$ noting that the scale for the self injected electrons is 2 orders of magnitude less than the ionized electron case. The electrons injected via ionization are sharply peaked on axis, which is a surprising result given their divergence in Fig.4.16. This is in part due to the weighting of $1/R$, but also a result in the different scales used in Fig.4.16. One thing to note is that Figs.4.17 and 4.14 are scatter plots, where the highest energy electrons are placed on top of the lower energy ones. To illustrate the true detection signal, a bivariate histogram is needed.

Fig. 4.20 gives the bivariate histogram distributions of the electrons in the far-field with energies greater than $50MeV$. The bin width is selected such that $dy = dz = 100\mu m$. Tile a) gives the far-field distribution for the Gaussian driven wakefield. Due to the very limited number of electrons outside the $10mm$ radius, the axes have been cropped from those shown in Fig.4.17. Tile a) gives the electron far-field distribution

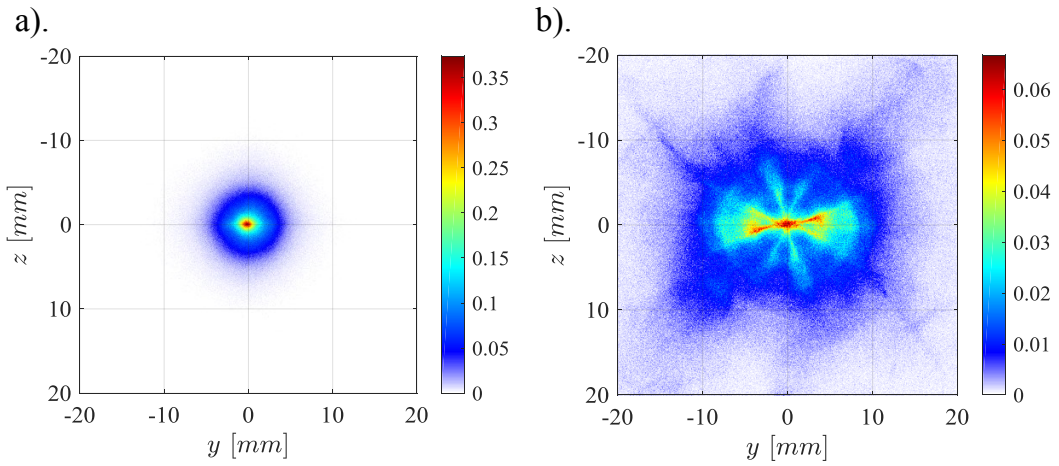

Figure 4.20: Bivariate histograms of the electron depositions on the far-field grid with energy greater than $50MeV$. The colourbars are in units of $d^2Q/dydz$ $[pC/(100\mu m)^2]$ where $dy = dz = 100\mu m$. Tile a) gives the result for the Gaussian driven wakefield. Tile b) gives the case of the Laguerre-Gaussian driven wakefield.

as driven by the Gaussian beam showing a tight, low divergence electron spot. Tile b) gives the result for the Laguerre-Gaussian case showing a much broader electron far-field distribution. We find the electrons are spread along a line orientated along the laser polarization plane with a slight twist counter-clockwise. In the next section we will show that the direction of this twist changes when the sign of ℓ is changed.

Another variable that is detected in the plane placed after the plasma in the simulation is the particle angular momentum. Given that the Gaussian beam is linearly polarized, and has no orbital angular momentum, we expect there to be no net angular momentum transferred to the plasma. Fig.4.21 gives the ejected angular momentum of each electron binned on a histogram with a logarithmic y axis. The angular momentum has been normalized to units of $\hbar$. It is clear to see the symmetry of the plot about $L_x = 0$ indicating that very little angular momentum was transferred to the electrons.

The angular momentum transferred to the electrons in the Laguerre-Gaussian beam is shown in Fig.4.22. The axis scales have been kept the same to emphasize the increase of angular momentum transfer. Starting with the self-injected electrons, we find that there is a slight asymmetry in the angular momentum absorbed. More so is the case of the ionized electrons which show a large angular momentum absorption

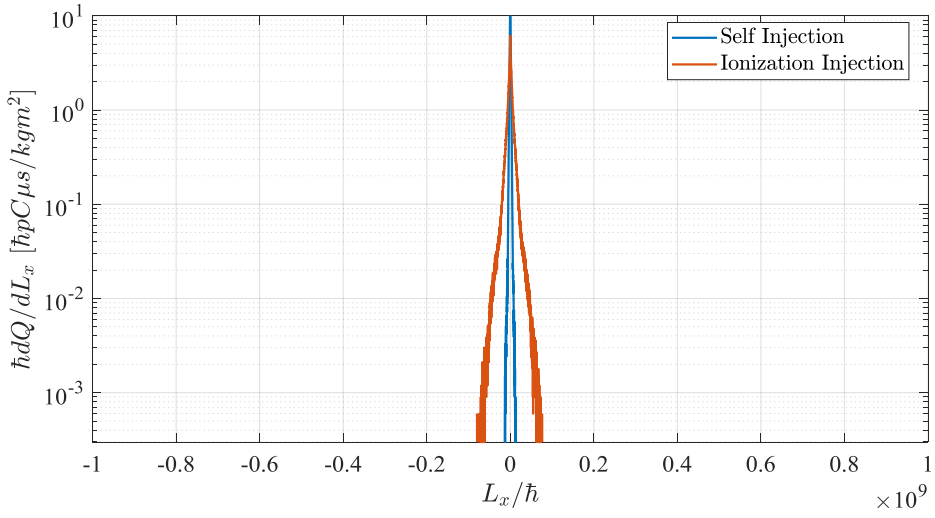

Figure 4.21: Angular momentum histogram for electrons accelerated by a linearly polarized Gaussian driven wakefield. The blue line indicates electrons that are self-injected, whereas the red line indicates electrons that were injected via ionization.

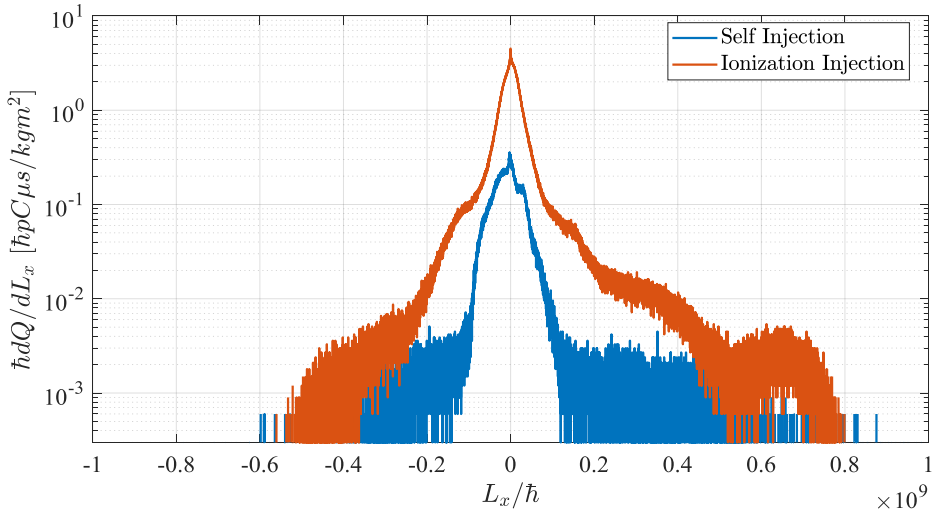

Figure 4.22: Angular momentum histogram for electrons accelerated in a wakefield driven by a linearly polarized Laguerre-Gaussian beam with $\ell = 1$. The blue line indicates electrons that are self-injected, whereas the red line indicates electrons that were injected via ionization.

peaked close to $0.7\hbar \times 10^9$.

4.4.3 Pump Depletion and Maximum Energy Gain

Once the electrons are injected into the bubble, they will accelerate due to the axial electric field. The maximum energy the electrons can gain is however limited by several factors including but not limited to, laser diffraction, electron phase detuning, pump depletion, and laser-plasma instabilities [40].

To first order, we can say that the energy gained by an electron in a wakefield is simply the product of the acceleration length, and the average electric field,

$$\Delta W \approx eL_{acc}E_x \tag{4.43}$$

At this point, we could naively take the acceleration length as the length of the plasma in the simulation $\approx 600\mu m$, and the peak accelerating fields of the Gaussian and Laguerre Gaussian fields in Figs.4.10 and 4.11. For the Gaussian case, we find a peak electric field of roughly $2.6E_0$ which gives a peak electron energy of $474MeV$ - a result that is remarkably close to the observed result in Fig.4.13. If we instead consider the Laguerre Gaussian case, we find the same scale length, but a reduced electric field of $1.8E_0$ resulting in a peak expected energy of $328MeV$ which is also very close to the observed value of the electrons injected by ionization.

One issue with the simulations above is that they are quite short in plasma length - of the order of $600\mu m$ which is considerably shorter than the $5 - 10mm$ found in the laboratory experiments. If the laser were propagating in vacuum, its acceleration length would be essentially limited to its Rayleigh range,

$$L_v = \pi z_0 = \frac{\pi k w_0^2}{2} \tag{4.44}$$

Given the parameters of our simulations, we find the resultant estimated vacuum energy gain length to be $790\mu m$. As already discussed however, this length can be greatly enhanced if the laser self focuses, and if a suitable plasma channel is used.

If we were able to simulate the plasma over longer spatial extent, we would find the maximum acceleration length would be increased from the Rayleigh range to one of two lengths, the dephasing length, and the pump depletion length.

From Fig's.4.10 and 4.11 we find that the electron is accelerated in the negative

(red) regions, however it can decelerate once the positive (blue) field gradient becomes negative. After this distance of positive acceleration, the electrons are said to dephase with the accelerator as they outrun the group velocity of the wakefield itself. This length is found to be [96],

$$L_d \approx \frac{4}{3}\frac{n_c}{n_e}\frac{\sqrt{a_0}}{k_p} \tag{4.45}$$

where a_0 is the peak intensity after self focussing.

The second scale length is the pump depletion length which is effectively the length it takes for the laser to be absorbed by the plasma. This is given as [96],

$$L_{pd} \approx \frac{n_c}{n_e}\omega_p \tau \tag{4.46}$$

where τ is the pulse duration. For our given simulation, we find the dephasing length to be roughly, $717\mu m$ and the pump depletion length to be $1406\mu m$. Clearly the pump depletion length in this case is much longer than the plasma length in the simulation indicating that a large fraction of laser energy is transmitted through the interaction region as observed in the simulation. Thus it is expected that the dephasing length will govern the maximum energy gain in the present case.

If the electron energy gain is limited purely by the dephasing length, we can calculate the maximum energy gain of the particle as [96],

$$\Delta W_{max}[GeV] \approx 1.7 \left(\frac{P[TW]}{100}\right)^{1/3} \left(\frac{10^{18}}{n_e[cm^-3]}\right)^{2/3} \left(\frac{0.8}{\lambda[\mu m]}\right)^{4/3} \tag{4.47}$$

While this form of the energy gain is useful considering experimental laser parameters, it is not useful for when considering the Laguerre-Gaussian modes which clearly have a lower electron ejection energy than the Gaussian beam. It is possible to rewrite Eq.4.47 in terms of the critical power of the beam as,

$$\Delta W[GeV] \approx 3.8 \left(\frac{P}{P_c}\right)^{-2/3} \frac{P[TW]}{100} \tag{4.48}$$

Using our previous formulas, we find the critical power for the Gaussian and Laguerre Gaussian beams to be $2.72TW$ and $10.88TW$ respectively. The corresponding laser power of each simulation was $25TW$ and $97TW$.

Plugging these values into Eq.4.48 yields the peak electrons energies as $217MeV$ and $857MeV$ for the Gaussian and Laguerre Gaussian beams respectively. Clearly

both of these values are incorrect, as we find numerically that the ejected electron energy is roughly double this in the Gaussian case. This is likely due to the fact that Eq.4.47 assumes that the laser has propagated to the point of electron dephasing which may not be the case in the simulations. In addition, the assumptions made in [96] require a plasma density that has been optimized for laser guiding, and is less than the value used in these simulations.

The result for the Laguerre-Gaussian is roughly 3 times the predicted energy ejected from the simulations. This is in part because of the increase in critical power with the LG beam. Another reason is that Eq.4.48 assumes that the LG mode self focuses in a similar manner to the Gaussian which from the previous section is clearly not the case. A more in-depth analysis into the scaling laws of electron acceleration in OAM-driven wakefields is therefore required, but is not explored in this thesis.

4.5 Betatron Radiation

Electrons accelerating through the wakefield channel feel both an accelerating force, but also a transverse focussing force according to Eq.4.37. As a result of the transverse focussing forces, the electrons will oscillate about the laser axis as they are accelerated forward. Much like in the case of a single electron emitting radiation in a laser field, the electrons oscillating in the wakefield will emit radiation. If we approximate their trajectories as circular at each instant in time with an appropriate radius of curvature, we may solve Eq's.3.85 and 3.95 analytically to obtain the radiation spatial and spectral information.

From standard electrodynamic theory, we find the spatial distribution of radiation emitted from a charge in instantaneous circular motion as [75],

$$\frac{dP(t')}{d\Omega} = \frac{e^2}{16\pi^2\epsilon_0 c^3}\frac{|\dot{\boldsymbol{v}}|^2}{(1-\beta\cos\theta)^3}\left[1-\frac{\sin^2\theta\cos^2\phi}{\gamma^2(1-\beta\cos\theta)^2}\right] \tag{4.49}$$

where θ is the angle between the observation vector and $\boldsymbol{\beta}$, while ϕ is the angle between the observation vector and $\dot{\boldsymbol{\beta}}$. Similarly, we find the emitted radiation spectra given by,

$$\frac{d^2I}{d\omega d\Omega} = \frac{e^2}{12\pi^3\epsilon_0 c}\left(\frac{\omega\rho}{c}\right)^2\left(\frac{1}{\gamma^2}+\theta^2\right)^2\left[K_{2/3}^2(\xi)+\frac{\theta^2}{(1/\gamma^2)+\theta^2}K_{1/3}^2(\xi)\right] \tag{4.50}$$

where ρ is the radius of the circular trajectory, $K_n(x)$ is the modified Bessel function of the second kind and ξ is given by,

$$\xi = \frac{\omega\rho}{3c}\left(\frac{1}{\gamma^2} + \theta^2\right)^{3/2} \tag{4.51}$$

The first term in the square bracket of Eq.4.50 corresponds to radiation polarized in the plane of the orbit, while the second term is radiation polarized perpendicular to that. From this we can define the critical frequency at which half the emitted energy is above, and half the emitted energy is below. In the direction of propagation $\theta = 0$, we define the critical frequency as $\xi = 1/2$ leading to the result [75],

$$\omega_c = \frac{3}{2}\gamma^3\left(\frac{c}{\rho}\right) \tag{4.52}$$

Integrating over all angles of Eq.4.50 we can derive the simpler result,

$$\frac{dI}{d\omega} = \frac{\sqrt{3}}{4\pi\epsilon_0}\frac{e^2}{c}\gamma\frac{\omega}{\omega_c}\int_{\omega/\omega_c}^{\infty} K_{5/3}(x)dx \tag{4.53}$$

While this form of the radiation emission is not so useful for analyzing a plasma wakefield, it is possible to convert the critical frequency to a critical energy in terms of the electron density, and the circular trajectory radius [3] assuming the strength parameter K is large,

$$E_c[keV] \approx 5 \times 10^{-24}\gamma^2 n_e[cm^{-3}]\rho[\mu m] \tag{4.54}$$

Additionally, we can derive the betatron strength parameter given by,

$$K = \frac{\gamma\rho\omega_\beta}{c} = 1.33 \times 10^{-10}\sqrt{\gamma n_e[cm^{-3}]}\rho[\mu m] \tag{4.55}$$

where ω_β is the betatron oscillation frequency $\omega_\beta = \omega_p/\sqrt{2\gamma}$. Given the critical energy of the radiation, and the betatron strength parameter allows us to characterize the radiation. For instance, the half opening of spatial distribution of the radiation is given by $\theta \approx K/\gamma$. From Eq.4.54 we can estimate for a plasma with density $1 \times 10^{19}cm^{-3}$, and estimating the electron to be accelerated to an energy of $50MeV$ such that $\gamma = 100$ and the radius to be equal to the bubble radius, we find a critical energy to be $3keV$ which is an x-ray photon. We also find the betatron parameter

for the same parameters as $K \approx 25$. Because K is larger than unity, we can treat the radiation emission to be equivalent to that of a wiggler light source similar to those found in synchrotron's.

Fig.4.23 gives the analytic spectrum of an electron in circular motion with energy $\gamma = 100$ and radius $\rho = r_B = 6\mu m$. Tile a) shows the spatial distribution leading to a "lighthouse" effect as the electron circulates about its axis. In this case, the radiation emission agrees well with the synchrotron theory in that the half angle of radiation should be $\theta \approx 1/\gamma = 0.01 rad$. The colour bar is equal to $dP/d\Omega|\dot{\boldsymbol{v}}|^2$.

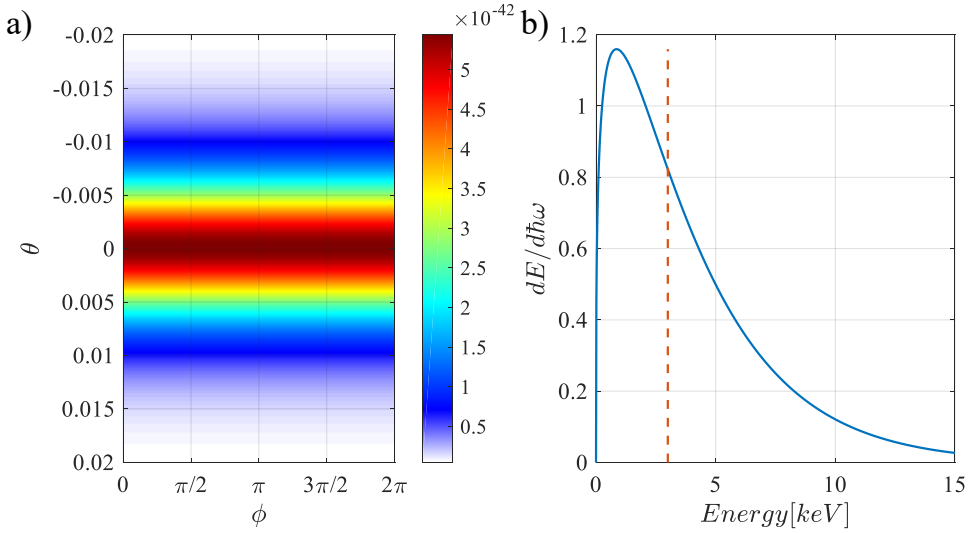

Figure 4.23: Radiation emission for an electron in instantaneous circular motion. a) Spatial radiation distribution showing the tight beam of radiation in θ. The colour bar units are $dP/d\Omega|\dot{\boldsymbol{v}}|^2$. b) Spectral distribution of radiation integrated over all angles. The red dotted line indicates the critical radiation energy. These were computed using $\gamma = 100$, $r_B = 6\mu m$.

Tile b) gives the radiation spectrum integrated over all angles normalized to $\hbar$ giving the average number of photons emitted in each frequency band. We find the critical energy, indicated by the red dotted line, is roughly $3keV$, and the radiation spectral tail extends out to photons beyond $15keV$.

As the electrons in a wakefield accelerator will not be undergoing a constant circular trajectory, we expect to find a deviation from Fig.4.23 a). Using the methods outlined in Chapter 3, we use the MATLAB single particle integrator as a radiation post-processor to EPOCH PIC simulations. In this instance, we can extract the time

history of electrons position and momentum for electrons that are above a certain cutoff energy. Given the large number of electrons and the requirement to store their time histories over a long time, we opt to just analyse electrons that have been injected through ionization injection and that have a minimum energy greater than $200MeV$. The trajectories are saved every femtosecond.

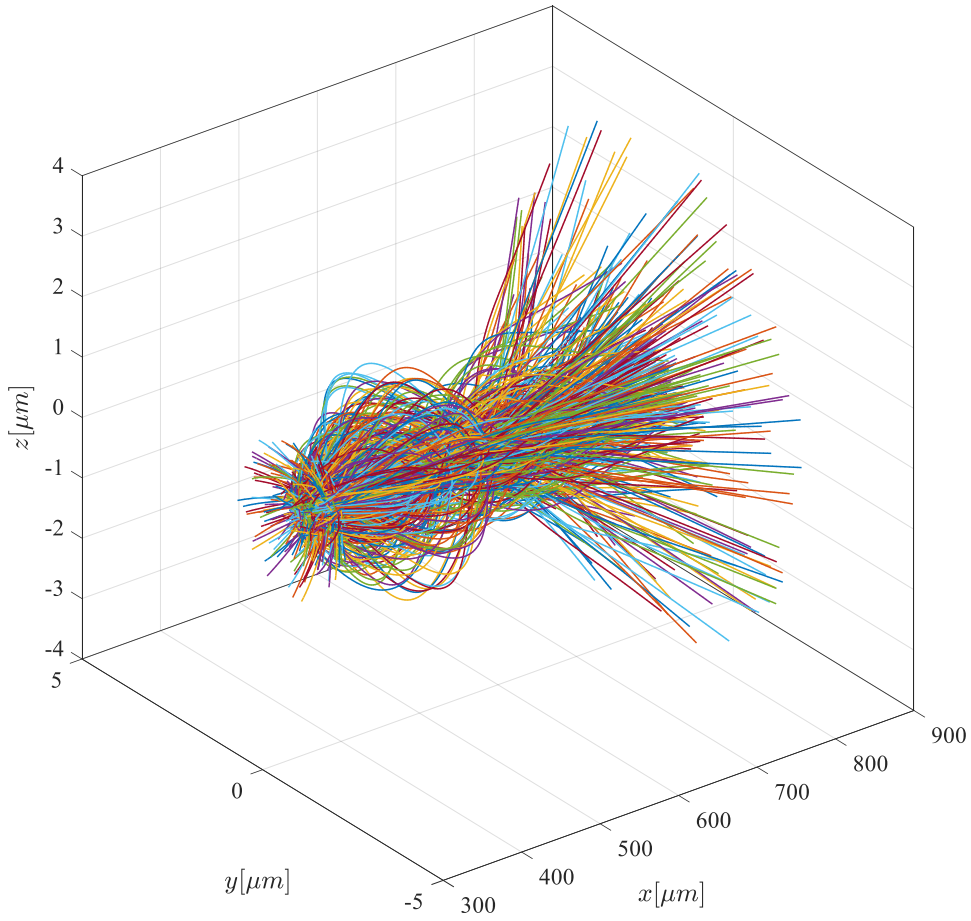

Figure 4.24: 500 sample electron trajectories injected into a Gaussian driven wakefield via ionization with energy greater than $200MeV$.

The trajectories of 500 sample electrons with energy greater than $200MeV$ in a Gaussian driven wakefield are given in Fig.4.24. Here, it is clear to see the electrons defocusing and refocusing in the wakefield bubble before being ejected out. One

should note the different relative scales of the $\hat{x}$ to the $\hat{y}$ and $\hat{z}$ axes indicating that if on the same scales, the electron beams actually appear very collimated.

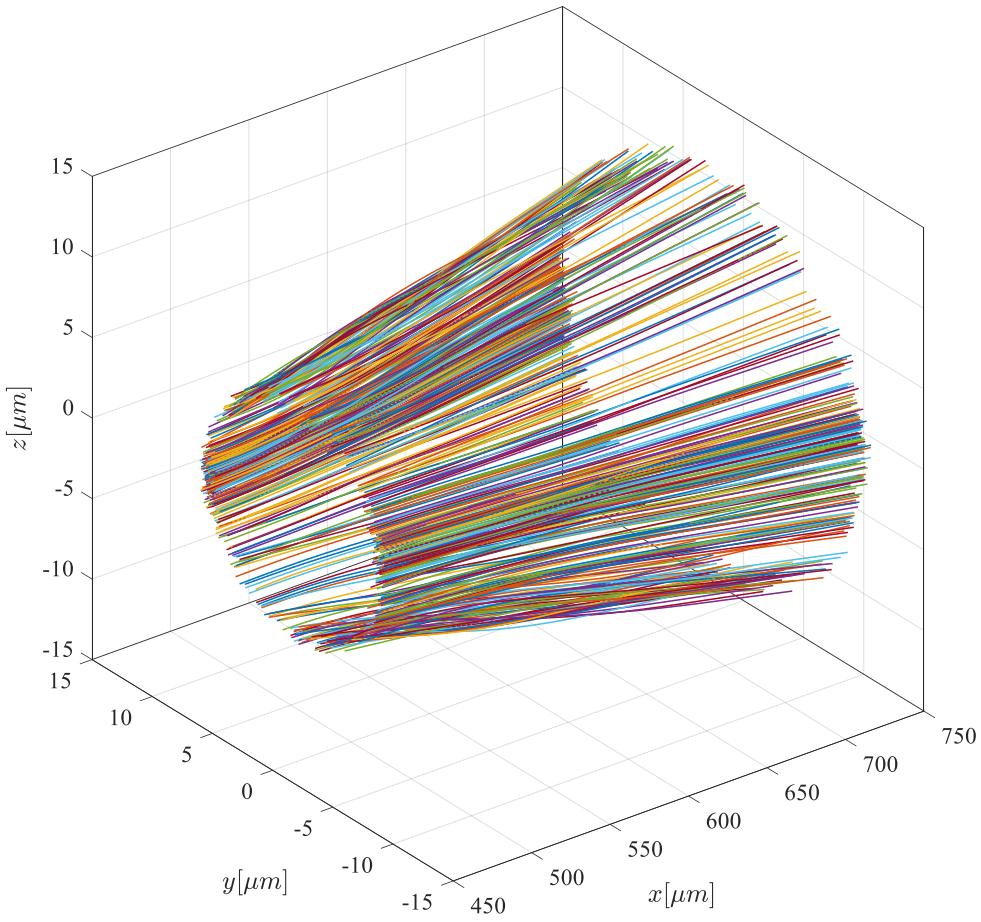

Figure 4.25: 500 sample electron trajectories injected into a Laguerre Gaussian driven wakefield via ionization with energy greater than $200 MeV$.

Considering the $\ell = 1$ Laguerre-Gaussian driven electrons, we find the expected result that the electrons are formed into a ring around the donut bubble as shown in Fig.4.25. We note that the oscillation amplitude of the electrons is smaller than the Gaussian case. We also note that while the electrons are free to move azimuthally around the donut bubble, the high energy electrons are accelerated primarily forward. Finally we remark on the divergence of the electrons which is clear in the figure. As

they propagate, the average radius of the electrons is increasing as a result of a diverging wakefield.

Taking the trajectories of 1000 random electrons from both the Gaussian and Laguerre Gaussian simulations, it is possible to project the radiation of the electrons into the far-field. This is done incoherently using Eq.3.85 at each $1fs$ timestep. The value of $\dot{\beta}$ is calculated by a simple first order backward step differential. The results are given in SI units in Fig.4.26 where the laser is polarized in the $\phi = 0°, 108°$ directions.

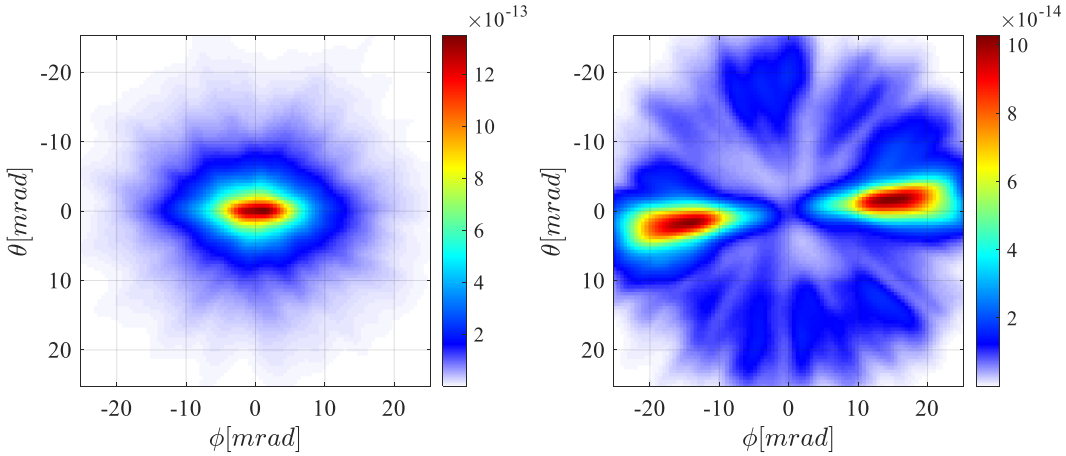

Figure 4.26: Spatial distribution of betatron radiation emitted from 1000 electrons in a wakefield accelerator driven by a) a Gaussian beam, and b) a Laguerre Gaussian beam. Both lasers are linearly polarized in the ϕ direction. The colourbar scale is in units of $W/sterad$, however is an underestimate considering the small number of electrons sampled.

Fig.4.26 a) gives the result for the Gaussian driven wakefield. Here we see the classic elliptical result [4] with the long axis aligned along the laser polarization direction. The major axis has a divergence of roughly $20mrad$, while the minor axis has a divergence of roughly $10mrad$. If we compare this to the expected divergence from the analytic model given by $\theta \approx K/\gamma$ and noting that we are only counting the contribution from electrons with energy greater than $200MeV, \gamma \approx 400$ we find an expected divergence of roughly $20mrad$. This is assuming that the radius of curvature of the electrons is roughly $1\mu m$ as observed in Fig.4.24.

If we instead consider the Laguerre-Gaussian driven case, we find the odd result that instead of the betatron forming a ring in the far-field, we instead find two-lobes. Each lobe has a similar characteristic spot divergence to the Gaussian case, and are separated along the laser polarization plane. While we do see there is a background "ring" of lower intensity, it is largely dominated by the two lobes along the polarization plane. This is due to the linear polarization of the laser and the influence of the electric field of the laser on the betatron. If the laser were circularly polarized, we might expect the radiation to be more symmetric about the ring.

Similarly to the ejected electron beam in the previous section, we notice a slight twist in the emitted radiation beam counter-clockwise about the laser axis. If we run instead the opposite handed LG mode with $\ell = -1$, we find that both the ejected electrons and the ejected radiation are twisted in the other direction. This is shown in Fig.4.27 with the radiation now twisted an equal but opposite rotation clockwise.

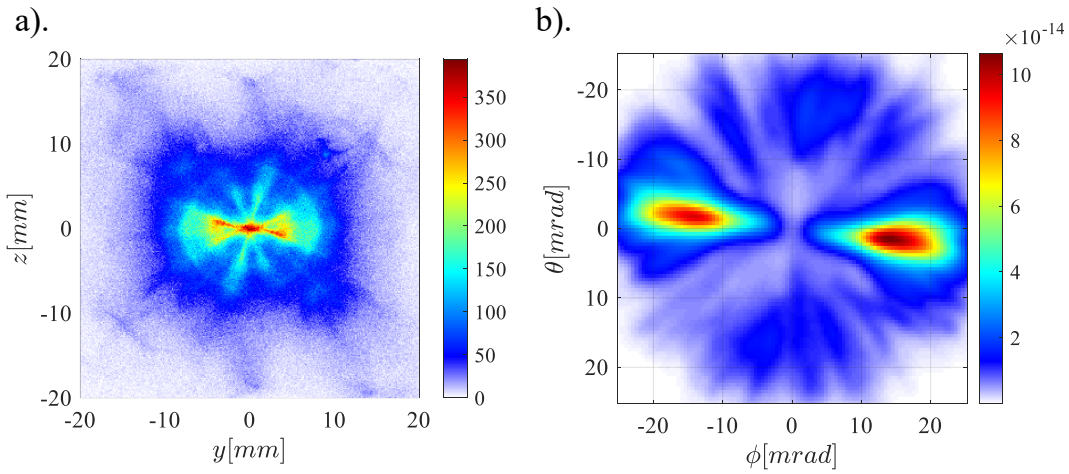

Figure 4.27: a) Bivariate histogram of electrons emitted from an $\ell = -1$ Laguerre-Gaussian driven wakefield. The colourbar scale is in $[pC/(100\mu m)^2]$ b) Spatial distribution of betatron radiation emitted from 1000 electrons in a wakefield accelerator driven by an $\ell = -1$ Laguerre Gaussian beam. The colourbar scale is in units of $W/sterad$, but again a gross underestimate due to low sampling numbers of the electrons.

The radiation emitted from an OAM driven wakefield has been studied numerically in a few cases prior [100, 168, 138], however none of these have addressed directly the

predicted far-field radiation of a linearly polarized Laguerre Gaussian wakefield, nor the phenomenon of the twisting of the emitted beam.

To calculate the radiation spectra of each drive beam becomes more challenging. While EPOCH has a built in algorithm for calculating the energy of each photon emitted when in the QED regime [37], it is not suitable for calculating photon emission from wakefield accelerators. Using the Fourier transform algorithm from Eq.3.96, we are essentially limited in an lower photon wavelength of about $600nm$ according to the Shannon-Nyquist limit using a $1fs$ timestep. We could try and interpolate the electron trajectory to a finer timestep, but would result in massive FFT's to calculate resulting in a long computation time.

We are therefore left with a gap of radiation emission that is computationally difficult to solve, from roughly $100nm$ to $0.1nm$. Some algorithms are available for computing the radiation emission in this regime using models that fit either parabolas to the electron trajectory and integrate the radiation analytically [157], or by brute force integration using super computers [101]. We are developing an algorithm to analyze this spectral emission simply by fitting the electron trajectories with piece wise circles and then integrating analytically. However it is not complete at the time of writing and is therefore not included here.

4.6 Inverse Faraday Effect

One of the primary motivations behind this thesis lies in the generation of magnetic field and the inverse Faraday effect. In this section we review the background theory of the inverse Faraday effect as outlined in [64, 5], as a basis for a numerical study in Chapter 7. While there have been many approaches on the subject [117, 116, 173, 92, 35, 69, 21, 88, 165, 105, 141, 114, 140, 68, 113], we find the work of [64, 5] to be quite straightforward and making minimal assumptions.

In essence, the Faraday effect [44] is the observed coupling between electromagnetic waves and magnetic fields in mediums with a Verdet constant [49, 32]. In the classical Faraday effect experiment, a linearly polarized laser is passed through a material, usually a glass that has a background magnetic field orientated to be aligned with the propagation direction of the laser (an axial field). The plane of polarization of the laser will rotate depending on the strength of the magnetic field B, the Verdet

constant V, and the propagation distance d [49],

$$\theta = VBd \tag{4.56}$$

Typical Verdet constants are on the order of $5 - 10 rads/T/m$ [78]. Plasmas do not have a Verdet constant but the Faraday effect can still be observed. This is a result of the change of relative index of refraction for the "R" and "L" plasma waves given by [29],

$$\tilde{\eta}_R^2 = 1 - \frac{\omega_p^2/\omega^2}{1 - \omega_c/\omega} \tag{4.57}$$

and,

$$\tilde{\eta}_L^2 = 1 - \frac{\omega_p^2/\omega^2}{1 + \omega_c/\omega} \tag{4.58}$$

respectively, where ω_p is the plasma frequency, and ω_c is the non-relativistic cyclotron frequency,

$$\omega_c = \frac{eB}{m_e} \tag{4.59}$$

The "R" and "L" solutions compose right and left circularly polarized waves respectively and can be summed together vectorally to give a linearly polarized wave. If a magnetic field is present such that "R" and "L" waves can propagate, their relative phase shift will cause a rotation in the linearly polarized beam that the sum of the two create. The phase shift, or rotation angle of the linearly polarized sum of the two can be given as [69],

$$\phi[deg] = 3.02\lambda[\mu m]^2 \int_0^d \frac{n_e[cm^{-3}]B[MG]}{10^{21}\sqrt{1 - n_e/n_c}} dx[\mu m] \tag{4.60}$$

We note that both the wavelength of the laser, and the critical density given in this equation represent the beam used to probe the magnetic field, and not necessarily the one used to drive it. We will explore further the Faraday effect in plasma in Chapter 6 when we review the experimental methods for measuring magnetic fields in plasma.

We now consider the inverse process of the Faraday effect in which the absorption of lights angular momentum can used to generate an axial magnetic field. Previously, this was thought to be due to the motion of the electrons induced by direct interaction with a laser's electric and magnetic fields [140], similar to the motion of a single electron in a circularly polarized laser as discussed in Chapter 3. However, the

process can become much more complicated and we need to consider the motion of the electrons responding to the laser, the resultant torque on the ions, and the effect of electrons opposing the change in magnetic field in the plasma. A simple method to do this is by considering the angular momentum conservation in the plasma and laser. If we assume the plasma initially has net zero angular momentum, and a laser interacts with it carrying an angular momentum density j_z as given in Eq.2.28, then at any given time, the net angular momentum of the system must be equal to that of the laser. We therefore write the electron angular momentum conservation equation as [5],

$$m_e n_e r \left(\frac{d}{dt} + \nu_{ei} \right) u_\theta = -e n_e r \left(E_\theta + u_z B_r - u_r B_z \right) - \frac{dj_z}{dt} \tag{4.61}$$

where u is the electron fluid velocity, and ν_{ei} is the electron-ion collision frequency. We recall the angular momentum density of a laser pulse of frequency ω carrying both orbital angular momentum and spin angular momentum as (Eq.2.28) [6],

$$j_z = \frac{\ell}{\omega} |\psi|^2 + \frac{\sigma_z r}{2\omega} \frac{\partial |\psi|^2}{\partial r} \tag{4.62}$$

where ψ is a solution of the Helmholtz equation.

Given the timescales of interest ($< 1ps$), and the fact the plasma of interest is underdense we can make some assumptions and simplify Eq.4.61. We first assume that the electron-ion collision frequency is zero which is often assumed in plasma of this density, and pulse duration. In this time scale, we will assume that the electrons have had time to reach steady state such that we can also assume that $d_t u_\theta = 0$. Considering the remaining terms of the axial electric field and the laser angular momentum density, we find,

$$e n_e r E_\theta \approx -\frac{dj_z}{dt} \tag{4.63}$$

Using Faraday's law (Eq.2.3), we are able to write the axial magnetic field as,

$$-\frac{1}{r} \frac{\partial}{\partial r} r E_\theta \approx \frac{\partial B_z}{\partial t} \tag{4.64}$$

allowing us to write,

$$B_z = \frac{1}{e n_e r} \frac{\partial}{\partial r} \frac{d}{dt} \left(\frac{\ell I}{\omega c} + \frac{\sigma_z r}{2\omega c} \frac{\partial I}{\partial r} \right) \tag{4.65}$$

where we have used the relation,

$$\int_0^{2\pi}\int_0^{\infty} j_z r dr d\theta = \frac{(\ell - \sigma_z)P}{\omega c} \tag{4.66}$$

with P being the total power of the laser. Integrating over time from 0 to t, we can derive the magnetic field as a function of absorbed power from the laser as [5],

$$B_z = -\frac{f_{abs}}{r e n_e \omega c}\left[\ell \frac{\partial I}{\partial r} + \frac{\sigma_z}{2}\frac{\partial}{\partial r}\left(r\frac{\partial I}{\partial r}\right)\right] \tag{4.67}$$

We remark that in this derivation, the notion of the electron density changing as a function of laser intensity has been ignored which could contribute strongly to the magnetic field generation. As we saw previously, the change in electron density as a function of laser intensity can become quite formidable in the nonlinear interaction region.

The value of f_{abs} varies depending on the laser-plasma interaction. In the paper by Ali, et. al. [5], they simply associate the fraction of absorbed laser energy with absorption due to inverse bremsstrahlung. Given that inverse bremsstrahlung is derived from the collisions in the plasma, we do not expect to see absorption by this mechanism at the densities in which we are working. There are many other mechanisms for laser absorption in low density plasmas such as stimulated Raman scattering (SRS), filamentation, and ponderomotive scattering. General formulas for these absorption mechanisms can be challenging to derive, particularly for a broad range of intensities and plasma densities. We therefore will measure the fraction of absorbed laser energy numerically in Chapter 7.

Given the intensity profile of an OAM mode in Eq.2.69 and assuming we are working with the $p = 0$ mode, we can derive the axial magnetic field as,

$$B_z = -\frac{2f_{abs}}{e n_e \omega c w_{LG}^2} I(r,\ell)\left[\ell\left(\frac{w_{LG}^2|\ell|}{r^2} - 2\right) + \sigma_z\left(\frac{|\ell|^2 w_{LG}^2}{r^2} - 2 - 4|\ell| + \frac{4r^2}{w_{LG}^2}\right)\right] \tag{4.68}$$

where we re-write for completeness,

$$I(r,\ell) = I_0 \frac{\eta\bar{\gamma}^2}{|\ell|!}\left(\frac{r\sqrt{2}}{w_{LG}}\right)^{2|\ell|} exp\left(\frac{-2r^2}{w_{LG}^2}\right) \tag{4.69}$$

The values of $\bar{\gamma}$ and η are given in table's 2.2 and 2.3.

To compute the expected magnetic field in plasmas and laser powers of relevance to this thesis, we assume the following laser and plasma parameters; All lasers will contain the same peak power of 100TW. They also will all have the same Gaussian pulse duration of FWHM $= 100fs$ and the same wavelength of $\lambda = 1\mu m$. The initial plasma density will be assumed to be $3 \times 10^{19} cm^{-3}$. For now we will assume that the laser is entirely absorbed into the plasma and as such, $f_{abs} = 1$. We will assume a Gaussian near-field in the laser and as such, we will use values of η and $\bar{\gamma}$ from column two ($n = 1$) of Tables 2.2 and 2.3. The beam waist of the fundamental Gaussian beam will be $8\mu m$ and modified by the value of $\bar{\gamma}$ in the Laguerre-Gaussian cases.

Fig. 4.28 gives the intensity profile of a circularly polarized, fundamental Gaussian beam overlaid with the corresponding axial magnetic field predicted by Eq.4.68. It is clear to see that the magnetic field shape follows from the Gaussian pulse shape and has a peak field strength of over $20kT$. We note that the magnetic field is minimum when $r = w_0$ and while it may appear that the magnetic field is not divergence-free, integrating over the disc finds that the total magnetic field generated is zero.

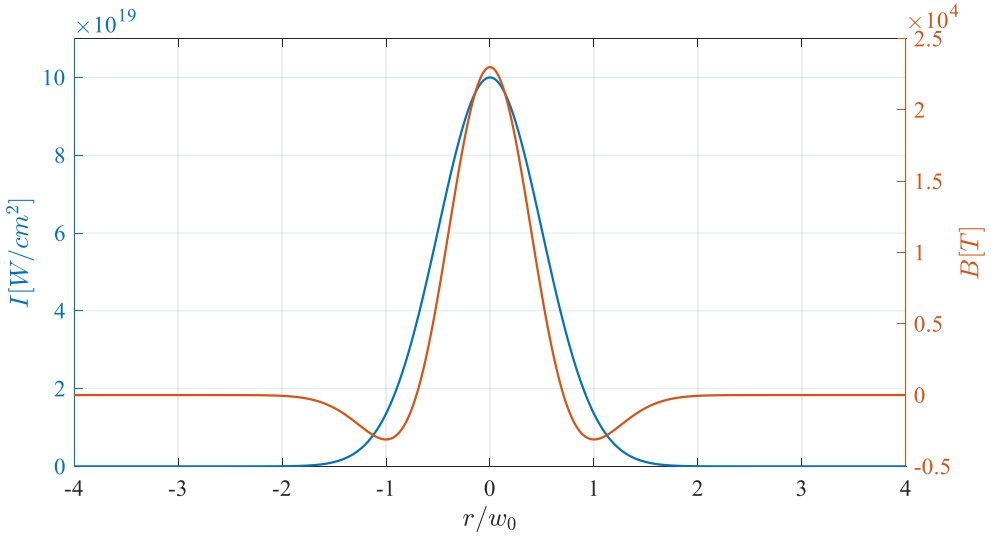

Figure 4.28: Intensity and generated magnetic field profiles of a circularly polarized ($\sigma_z = 1$) Gaussian laser exhibiting the inverse Faraday effect. The relevant plasma and laser parameters are given in the text.

If we instead consider the generated magnetic field from a linearly polarized Laguerre-Gaussian laser as shown in Fig.4.29, we find that the generated magnetic field also has a Gaussian-like shape. We find that for a laser with the same power, the

peak magnetic field strength is reduced drastically to roughly $9kT$ assuming $f_{abs} = 1$. This is due to two factors; the reduction of peak laser intensity due to the donut mode, and also due to the increase in beam waist due to the diffraction effects.

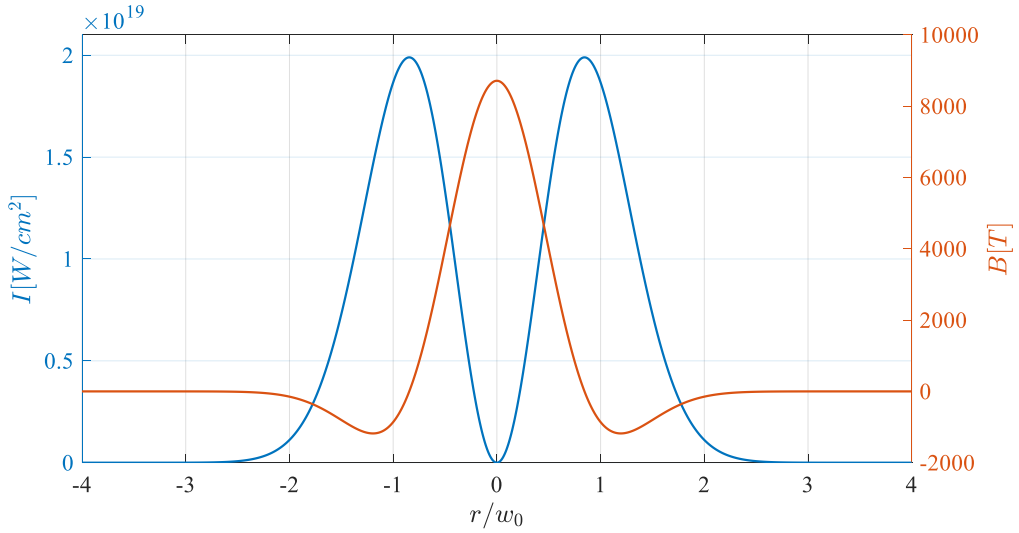

Figure 4.29: Intensity and generated magnetic field profiles of a linearly polarized ($\sigma_z = 0$) Laguerre-Gaussian laser with OAM ($\ell = -1$) exhibiting the inverse Faraday effect. The relevant plasma and laser parameters are given in the text.

Given that Eq.4.68 has ℓ^2 terms, we may be tempted to think that increasing the OAM in the beam may increase the magnetic field strength but we find this is not the case. Fig.4.30 gives the magnetic fields generated by the first five topological charges for linearly polarized beams all for the same total laser power of $P = 100TW$. The relevant beam fitting parameters and topological charges are given in the legend.

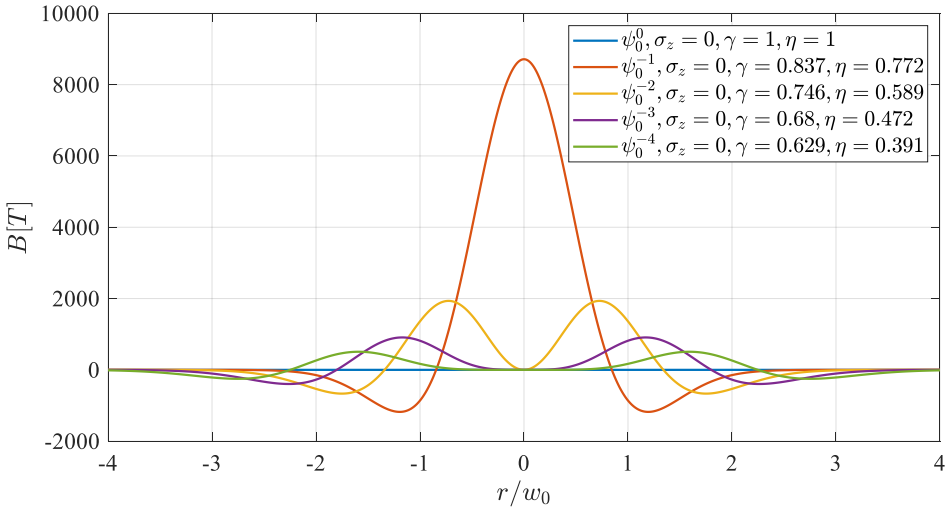

Figure 4.30: Various magnetic fields generated by the inverse Faraday effect from linearly polarized OAM beams. The topological charges $0, -1, -2, -3, -4$ are represented by the blue, red, yellow, purple, and green lines respectively. The beam fitting parameters are given in the legend.

We find that unsurprisingly the magnetic field generated by the linearly polarized $\ell = 0$ beam generates no magnetic field. The red line shows the $\ell = -1$ mode with the identical result to Fig.4.29. As the OAM of the beam is increased to $-2, -3$ and -4, we find that the peak magnetic field strength quickly decreases, while increasing its radius. We also find the interesting result that the generated magnetic field is no longer Gaussian in shape and instead follows the Laguerre-Gaussian shape. The reason for this deviation can be seen in Eq.4.68 with the $1/r^2$ terms. If $|\ell| > 2$, this divergent term is cancelled out, but it is not in the $|\ell| = 1$ case resulting in the strong magnetic field on axis.

If we instead consider the effect of having a beam with both spin and orbital angular momentum, we can see both their constructive and the destructive nature. If we recall Eq.2.31, we can see that the total integrated angular momentum of the beam can be zero if the SAM and OAM are destructive, but the two can be constructive if the signs are alike. Fig.4.31 shows the result of a destructive OAM-SAM beam where the spin has been set to $\sigma_z = 1$, and the OAM has been set to values of $\ell = 0, -1, -2, -3, -4$.

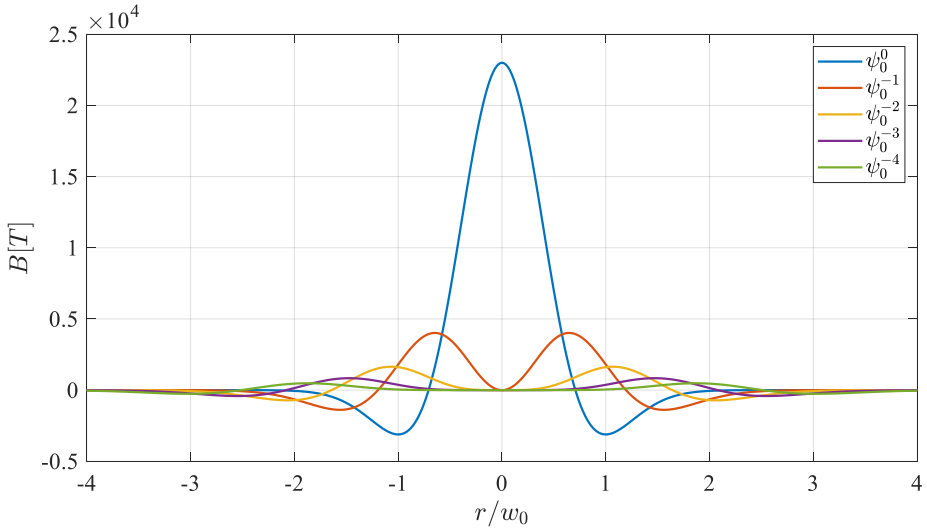

Figure 4.31: Various magnetic fields generated by the inverse Faraday effect from circularly polarized ($\sigma = 1$) OAM beams. The topological charges $0, -1, -2, -3, -4$ are represented by the blue, red, yellow, purple, and green lines respectively.

As expected, we find no change to the $\ell = 0$ case, but we find the $\ell = -1$ case has been greatly damped close to the axis. The magnetic field no longer has a peak on axis and now resembles the Laguerre-Gaussian shape that one expects according to the higher order modes. We find that the higher order ℓ modes have also been significantly damped but still retain the same shape.

Fig.4.32 gives the result for the constructive interference case where $\sigma_z = -1$ and $\ell = 0, -1, -2, -3, -4$. Here we can see the enhanced result where the $\ell = -1$ mode almost matches the peak field strength of the $\ell = 0$ driven case. What is of interest here is that the predicted directions of the fields is in opposite directions even though they are both circularly polarized in the same direction.

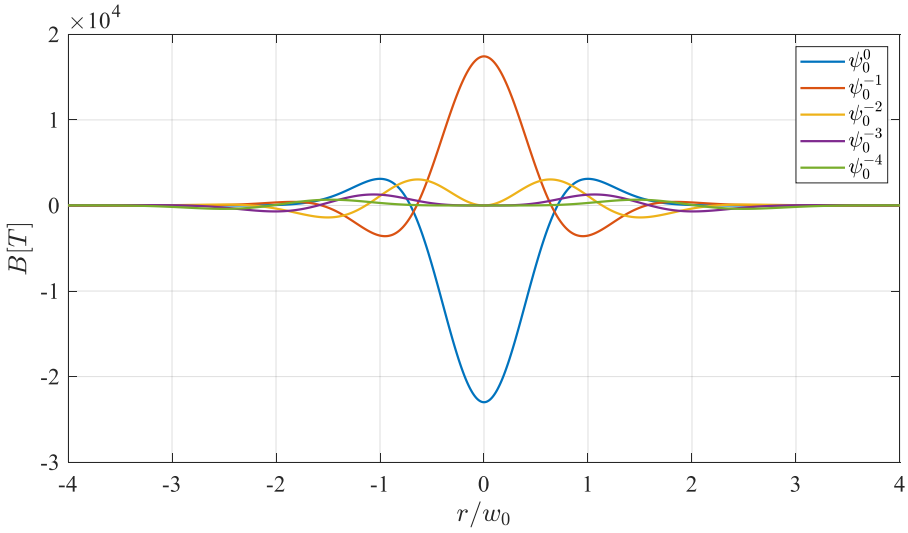

Figure 4.32: Various magnetic fields generated by the inverse Faraday effect from circularly polarized ($\sigma = -1$) OAM beams. The topological charges $0, -1, -2, -3, -4$ are represented by the blue, red, yellow, purple, and green lines respectively.

Considering the higher order ℓ modes, we find that there is some enhancement in their peak field strengths, but they retain the same shape and the corresponding null on axis. From this analytic model, it is clear that if one was to generate a magnetic field using a linearly polarized laser, then the optimal OAM beam to choose would the $|\ell| = 1$ beam. By changing the sign of ℓ, we can control in which direction the magnetic field will point.

To verify this simple analytic model, we need to utilize full 3D PIC simulations. These simulations would be able to calculate the value of f_{abs}, variations in the plasma density due to ponderomotive effects, non-steady state electron velocities and other effects that were neglected in the analysis here. In addition, we will be able to investigate the axial length of the generated magnetic field, and most importantly, its lifetime in the plasma.

4.7 Conclusions

In this chapter, we explored the interaction of LG modes with under-dense plasma utilizing the 3D PIC code EPOCH. Using the resources at ComputeCanada, we were able to study for the first time large volume interactions of paraxial OAM beams with

plasma investigating self-focussing, electron acceleration and some radiation emitted in the process.

We found that the relativistic self-focussing of an OAM beam can have complex dynamics as we identified two new self focussing phenomena, namely the ring pinch mode, and the ring collapse mode. We have yet to explore the stability and criteria of each of these modes. We further explored the use of using OAM modes to drive wakefield acceleration of electrons, and found that the energy distribution, and the spatial distribution of the ejected electrons decrease. Further study is needed to explore the interaction of the laser pulse in the plasma over much longer distances that are realistic ($\approx 5mm$), which may be difficult to do with fully 3D simulations.

The change in electron energy did not agree with the analytic models derived for Gaussian driven wakefields, even with adjusting the corresponding parameters of the interaction. This indicates a need for new analytic and empirical models for OAM driven wakefield scaling. Modelling of the betatron spatial distribution was performed, and found a splitting of the emitted radiation spots due to the linearly polarized donut ring. The modelling of the spectral distribution of the emitted x-rays is an ongoing task given the difficulty of modelling radiation emission between $100eV$ and $10keV$.

Chapter 5

Generation of High Intensity Optical Vortices

Until this point, the work presented in this thesis has been purely theoretical and numerical. In this chapter we review the experimental results of high intensity optical vortex generation at the Centros Laseres Pulsados Ultraintensos (CLPU) in Salamanca, Spain.

We begin by reviewing current technology and methods for generating OAM beams in low power laser systems. We then introduce the original concept of an off-axis spiral phase mirror developed and manufactured at the University of Alberta nanoFAB centre. We review some of the more detailed theory extending from the work we did in Chapter 2 to include manufacturing perturbations. We then review the implementation of this device in a low power system built in the University of Alberta laboratory, and also its deployment in two separate high intensity campaigns at CLPU. Finally, we discuss a more accurate modelling of more realistic asymmetric OAM beams at focus using a perturbation expansion into multiple LG modes.

The work in this chapter has resulted in two publications, [93, 95] and a two-year provisional patent was put in place while commercial interest in the off-axis spiral phase mirror was explored: A. Longman, and R. Fedosejevs, "*Off-Axis Spiral Phase Mirror*", U.S. Provisional Patent #62/508,222 (2017-2019). A further publication on the perturbation modelling methods is expected in the near future.

5.1 Low Intensity Optical Vortex Generation

To generate an optical vortex from a plane wave, the phase of the beam must be manipulated in some manner, most often in the laser near-field. There are many methods to do this of which we will review some of the most common here. We focus on linearly polarized input and output beams and omit spin-orbit coupling mechanisms as this is outside the scope of this thesis [99].

Laser Cavities

Given that the Laguerre Gaussian modes are a solution to the Helmholtz equation in cylindrical coordinates, we first look for methods of generating the higher order LG modes in the laser cavity itself. It is usually most desirable to operate a laser cavity in its fundamental Gaussian (or flat-top) mode as this allows for the amplifier crystals to be used efficiently in space, and to be efficiently cooled. It is however possible to design the laser cavity to support other modes by using curved mirrors, or by using mirrors with holes or spot-defects on them to suppress the fundamental mode [74].

To generate a Laguerre Gaussian mode using this method, the end mirrors of the cavity must be spherical, and often a hole or defect is placed on the centre of the mirror. While this mode is capable of produced high quality laser modes, it is often not of interest due to issues pumping and cooling the lasing crystals for higher order modes as previously mentioned. The degree of control of this method can be limited as there is no way to specify the handedness of the LG output mode, and as a result, both modes can be generated in the cavity.

Modification of the laser cavity can also be very-undesirable in large laser systems as it can risk damaging the amplifiers and optics in the laser system if not properly executed. Most commercial and research laser facilities do not allow modification of the laser cavity for this reason and so any mode conversion must be performed external to the laser cavity.

Cylindrical Mode Converters

One of the first methods used to convert laser modes into OAM beams was to use cylindrical lenses [6, 174, 15]. In this method, cylindrical lenses are used to transform a Hermite-Gaussian (HG) beam into a Laguerre-Gaussian beam by phase shifting one of the axes. While the Laguerre-Gaussian modes can be derived from the paraxial

Helmholtz equation using cylindrical coordinates, the Hermite-Gaussian modes are solutions when using Cartesian coordinates.

We find that the Laguerre-Gaussian solutions can be represented by Hermite-Gaussian solutions using the following [15],

$$\psi_{LG}(\ell,p)=\sum_{k=0}^{N} i^k \sqrt{\frac{(N-k)!k!}{2^N \ell! p!}} \psi_{HG}(N-k,k) \frac{1}{k!}\frac{d^k}{dt^k}\left[(1-t)^\ell (1+t)^p\right]_{t=0} \tag{5.1}$$

where the Hermite-Gaussian modes are given by,

$$\begin{aligned}\psi_{HG}(m,n)=C_{mn}\frac{1}{w(z)} exp\left(-\frac{r^2}{w^2(z)}\right) H_n\left(\frac{x\sqrt{2}}{w(z)}\right) H_m\left(\frac{y\sqrt{2}}{w(z)}\right) \\ exp\left[-i\left(\frac{kr^2}{2R}+(n+m+1)\Psi\right)\right]\end{aligned} \tag{5.2}$$

with R being the radius of curvature, Ψ being the Gouy phase (Eq.2.37), and C_{mn} being a normalization constant. We note that the the HG mode is equivalent to $m=N-k$ in Eq.5.1. We also introduce the Hermite polynomial $H_n(x)$. For example, a linearly polarized $\ell=1, p=0$ LG mode can be decomposed as [115],

$$LG_{10}\hat{x} = HG_{10}\hat{x} + iHG_{01}\hat{x} \tag{5.3}$$

where we note that the constituent HG modes are phase shifted by $\pi/2$.

If we rotate an HG_{10} mode by 45° in the transverse plane relative to the $\hat{x}$ axis, then the HG mode may be decomposed into two orthogonal HG_{10} and HG_{01} modes. Phase shifting one of these modes can be achieved using two cylindrical lenses as shown in Fig.5.1.

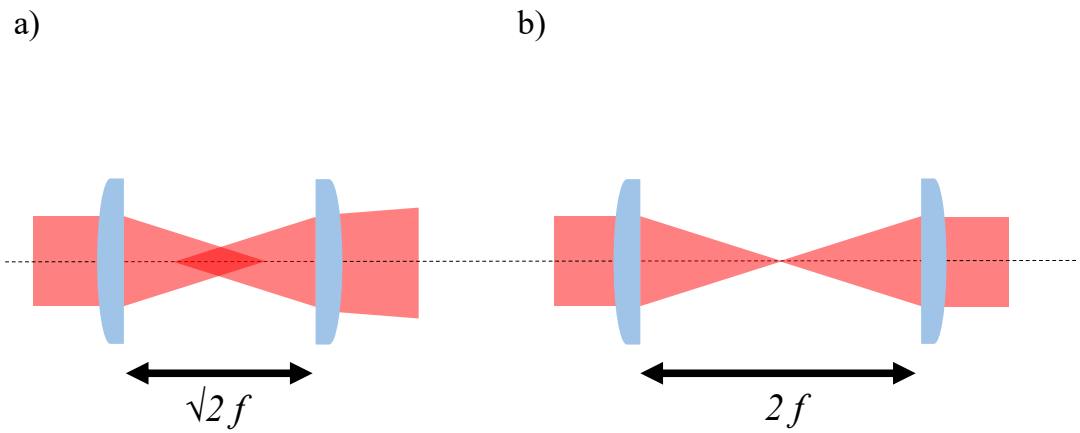

Figure 5.1: Phase shift configurations for cylindrical lenses. a) $\pi/2$ phase shift configuration. b) π phase shift configuration.

If the two cylindrical lenses are aligned such that the distance between them is $\sqrt{2}f$, the lenses will shift one mode $\pi/2$ radians relative to the other mode giving the the required i in Eq.5.3. This is illustrated in tile a) of Fig.5.1. Tile b) on the other hand shows the configuration where the lenses are placed $2f$ from each other giving a π phase shift between the ejected modes.

The cylindrical mode converter is a high efficiency converter such that the only ejected mode is the solution of Eq.5.2. It is also economical in that it can be constructed with two inexpensive cylindrical lenses. However the requirement of a high purity HG mode puts large restriction on the system as most lasers do not output a higher order HG mode. It is possible to generate HG modes in the lab using stepped phase plates, or a half mirror, but as we shall see in the next section, it is more reasonable to convert directly to an OAM mode in this case.

If we are to consider high-power, ultrafast pulses (30fs), we find that the cylindrical mode converter is further limited due to the damage threshold in the glass, and nonlinear effects on the ultrashort pulse such as group-velocity dispersion, B-integral, and self focussing in the glass [23].

Diffractive Holograms

Probably one of the most popular methods for generating OAM beams, as well as many other exotic phased beams is to use a spatial light modulator (SLM) [172]. The SLM is essentially a liquid crystal display (LCD) screen programmed to contain an image that either transmits or reflects an incoming beam. The image on an SLM can be programmed to any pattern desired, including holograms and diffraction patterns used for generating OAM beams.

The diffraction pattern on the SLM is derived by interfering a tilted planar wavefront with a helical wavefront. If we first consider a generalized tilted plane wave, we can write the electric field as,

$$E_1 = E_0 e^{i(k_x x + k_y y)} \hat{x} \tag{5.4}$$

where the wavevector k_x and k_y determine the tilt of the wavefront in the corresponding directions. This is illustrated in Fig.5.2 a) where the values of $k_x = 2$ and $k_y = 0$ have been assigned. As we have seen before, the helical wavefront can be introduced into the plane wave as,

$$E_2 = E_0 e^{i\ell\theta} \tag{5.5}$$

The result for $\ell = 1$ is given in Fig.5.2 b).

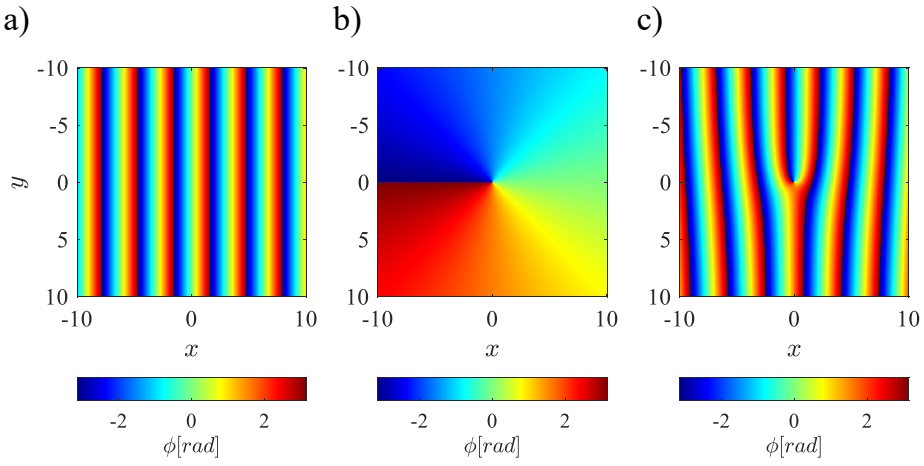

Figure 5.2: Wavefront maps for a) tilted planar wavefront, b) helical wavefront, and c) the combination of both a tilted planar wavefront and a helical wavefront.

Interfering the two wave fronts is found from their vector product [22],

$$\boldsymbol{E}_3^2 = \boldsymbol{E}_1^2 + \boldsymbol{E}_2^2 + 2\boldsymbol{E}_1 \cdot \boldsymbol{E}_2 \tag{5.6}$$

and the result is given in Fig.5.2c). From this figure, it is clear to see the "fork" structure in the interference pattern. The number of forks in this pattern is indicative of the charge of the OAM beam and is often used as a method to decode OAM beams carrying information [172].

Given that the diffraction pattern cannot imprint a specific phase into the beam, we find that instead it imprints a binary phase pattern onto the laser near-field. Examples of these binary phase masks for the first 3 OAM beams are given in Fig.5.3.

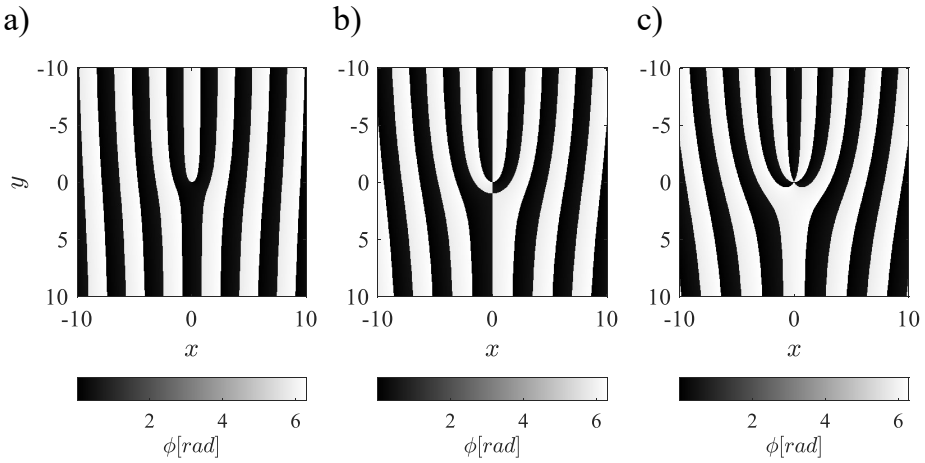

Figure 5.3: Binary diffraction masks for various OAM beams. a) $|\ell| = 1$, b) $|\ell| = 2$, and c) $|\ell| = 3$. The beam is highly absorbed where the mask is black, and transmitted where the mask is white.

We find that the case of $|\ell| = 1$ is symmetric about the x-axis, and therefore the phase mask has no preference over which state of OAM it will produce. Therefore both the $\ell = 1$ and the $\ell = -1$ mode are diffracted from the mask in opposite directions. Additionally, the $\ell = 0$ mode is produced and remains on axis to the incoming beam. Fig.5.3 tiles b) and c) show the corresponding phase masks for the $|\ell| = 2$ and $|\ell| = 3$ modes respectively.

This highlights one of the fundamental issues with diffractive optics - the efficiency is low. If we consider the transmissive phase mask above, we find that approximately

half of the light is not transmitted. the half that is transmissive is diffracted into the corresponding modes, of which there are at least 3. Therefore a standard diffractive phase mask is of the order of 16% efficient to a single ℓ mode.

We find additional problems with phase masks and SLM's in high power laser systems. High-power laser systems have large diameter beams to reduce the impact of the laser fluence on the optics, and as a result the SLM must also be large. Typical SLM's are on the order of a cm in diameter and the cost of even a small device can be very high. Scaling up to large diameter SLM's would be too costly using current technology. We also consider that if one were to simple make a static mask for the near field which has been done before [34]. We find that in this situation, significant laser fluence on the mask could damage it, and as already mentioned, there is a significant loss of energy through the diffraction process into the adjacent modes. From [34], we find that the ℓ modes are roughly 33% of the laser intensity of the diffracted $\ell = 0$ mode. With this, we estimate a mode conversion efficiency of roughly 10%.

5.2 Spiral Phase Plates

Probably the simplest, and most efficient method of converting a laser mode to an OAM mode external to the laser cavity is to use a transmissive spiral phase plate (SPP) [16, 93, 130, 131]. The spiral phase plate imprints a helix directly into the wavefront of the laser by means of a helical piece of glass. The surface of a spiral phase plate is shown in Fig.5.4 a). The helix is usually machined into the surface of a piece of glass with known index n. The height (pitch) of the spiral H is given by,

$$H(n-1) = L\lambda \tag{5.7}$$

where L is the topological charge of the spiral phase plate. In chapter 2, we explored solutions where L is an integer such that the ejected mode could be represented by a single Laguerre-Gaussian azimuthal mode number ℓ. It is possible for L to be any real number and often is mismatched to an integer value due to manufacturing defects.

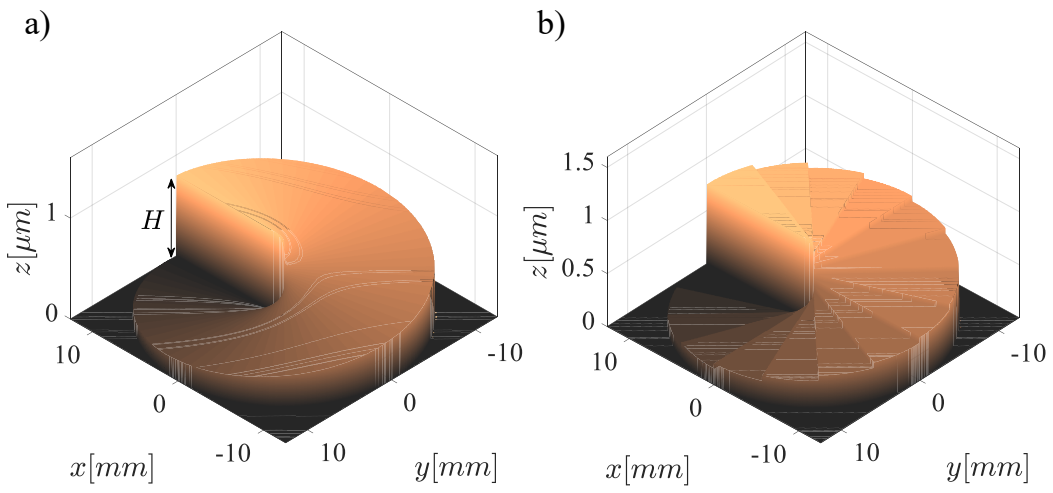

Figure 5.4: Spiral phase plates showing helical structure on the surface. a) continuous spiral phase plate. b) stepped spiral phase plate.

One issue with spiral phase plates is that the spiral can be difficult to machine into the glass surface over the size required and at the phase singularity on axis. For instance, if we consider quartz glass that has a refractive index at 800nm of $n \approx 1.45$. This gives a spiral phase plate height of approximately 1778nm. This can be difficult to manufacture, especially if the phase plate is of large diameter (> 1") making spiral phase plates very expensive.

A much simpler approach to manufacturing SPP's has since been employed [151]. In this approach, the helical surface is discretized into steps yielding a stepped spiral phase plate as shown in Fig.5.4 b). This simplifies the manufacturing of the phase plate as the steps can be deposited onto a substrate via a nano-fabrication technique such as sputtering or electron beam evaporation. There is a reduction in the mode conversion efficiency however and will be explored in section 5.3.

After the laser passes through the spiral phase plate, a helical wavefront is imprinted in the beam as shown in Fig.5.5. The helicity that is imprinted into the beam is opposite to that of the SPP due to the thicker sections of the SPP retarding the phase the most.

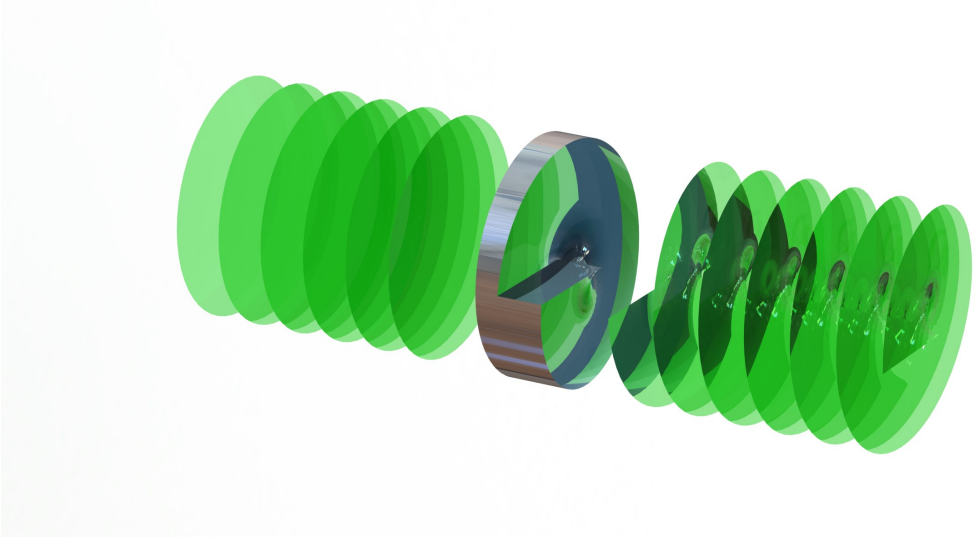

Figure 5.5: OAM mode generation illustration through a spiral phase plate. The handedness of the OAM beam is illustrated to show the opposite charge on the transmitted beam.

As the ejected beam from the spiral phase plate is not diffracted into multiple modes, we find the conversion efficiency of a SPP to be very high. From chapter 2 Eq.2.78, we find that choosing an optimal LG beam waist, the conversion efficiency for an $L = \ell = 1$ mode can be as high as 93.08% [93]. For higher order modes, we find that the conversion efficiency decreases to a single LG mode and higher order radial p modes are additionally generated.

Furthermore, we find that in a similar manner to the cylindrical mode converters, SPP and stepped-SPP have limitations for use in high-power and ultra-short beams due to damage and other non-linear effects. If we consider an ultra-short laser pulse with a significant bandwidth ($> 10nm$), we find that in most transparent media, the pulse will stretch due to group-velocity dispersion [23]. To compensate for this, the pulse can be chirped initially such that the phase plate acts a pulse-compression medium, but in doing this we find that we introduce other unwanted nonlinear effects.

If the laser pulse is of sufficient intensity in the phase plate, we can introduce self-phase modulation into the beam in which the wavefront of the laser will curve due to the intensity dependant refractive index [23],

$$n(I) = n_0 + n_2 I(r, t) \tag{5.8}$$

where n_0 is the linear refractive index, and n_2 is the second order nonlinear refractive index. This wavefront curvature can cause the laser to self focus inside the medium and reaching much higher intensities causing significant damage to the optic. Additionally, we may find the a similar effect along the propagation direction in the form of a B-integral,

$$B = \frac{2\pi}{\lambda} \int n_2 I(z) dz \tag{5.9}$$

This nonlinear effect can cause significant shift in the phase of the laser in the high intensity areas as compared to the low intensity areas. These nonlinear effects can be removed from the optic entirely if we can instead reflect the beam from the SPP instead of transmitting it through it.

5.2.1 Spiral Phase Mirrors

An extension to SPP and stepped-SPP was introduced by converting the transmission based optic to one that instead reflects in the form of a spiral phase mirror (SPM) [27, 55]. In this case, the step height H is set to,

$$H = \frac{L\lambda}{2} \tag{5.10}$$

The spiral phase mirror is capable of generating high quality OAM modes without nonlinear effects. If the SPM is used in a retro-reflecting configuration, we find that there is significant risk of laser energy being reflected back into the compressor and amplifier. This is of major concern to high-power lasers in which any laser retro-reflection could significantly damage the laser. It is possible to use optics to ensure the laser is not retro-reflected back into the laser such as Pockel's cells, and wave-plates, but these are all transmission based and will re-introduce the issues we seek to remove with the regular spiral phase plates.

While there have been a few attempts to generate high-intensity OAM beams [24, 34, 86, 162], there have been none to address the problems of generating OAM beams at high intensity without significant distortion to the laser pulse. In [24], a SPP was inserted in the front end of the laser before amplification and compression. This produced an asymmetric OAM beam at focus somewhat similar to a Hermite Gaussian mode as opposed to a Laguerre-Gaussian mode. The peak intensity was estimated to be on the order of $1 \times 10^{19} W cm^{-2}$ with a pulse duration of 650fs.

Mode converting after amplification and compression was performed in [34] using both a transmission fork grating, and a large 8-step spiral phase plate. Using this method they were able to obtain a peak intensity of approximately $1 \times 10^{19} W cm^{-2}$ in 25fs.

5.3 Mode Conversion Efficiency of Stepped Spiral Phase Plates

One could argue that introducing steps into the spiral phase optic surface could degrade the generated OAM mode significantly at focus, or that having a laser with a broad bandwidth would lead to a poor conversion efficiency. We now address these issues analytically to prove that in fact this is not the case. We start by considering a stepped spiral phase optic, with a total number of steps N. The transmission operator in Eq.2.72 is modified to give a stepped profile,

$$T = exp\left(-iL\frac{2\pi n(\theta)}{N}\right) \tag{5.11}$$

where $n(\theta)$ refers to the individual step number for a given angle. As this transmission operator is purely a function of azimuthal position, we find that Eq.2.74 remains unchanged and we instead only have to compute Φ in Eq.2.77. Including steps into the calculation of Φ, we find [93],

$$\Phi_{\ell LN} = \sum_{n=0}^{N-1} \int_{2\pi n/N}^{2\pi(n+1)/N} exp\left[i\left(\ell\theta - L\frac{2\pi n}{N}\right)\right] d\theta \tag{5.12}$$

If the topological charge is an integer, and the output mode is set to be equal to the topological charge ($\ell = L$), we find that this integral and sum can be compute analytically to give,

$$\Phi_{LN} = \frac{-iN}{L}\left[exp\left(\frac{iL2\pi}{N}\right) - 1\right] \tag{5.13}$$

If for instance we had a mirror with $N = 16$ steps, and a topological charge of one, the mode conversion efficiency is decreased from $\eta = 0.9308$ to $\eta = 0.9189$. We find that after the phase plate has been imprinted with $N = 16L$ steps, there is a negligible return in OAM mode conversion efficiency. This is illustrated for the first 3

Table 5.1: Conversion efficiencies from a TEM_{00} mode to various LG modes for given spiral phase optic (SPO) step numbers N. The $N = \infty$ case corresponds to a continuous SPO.

SPO, Waist Ratio	$L = 1, \gamma = 1/\sqrt{2}$			$L = 2, \gamma = 1/\sqrt{3}$		
$\eta_{\ell p}$	η_{10}	η_{11}	η_{12}	η_{20}	η_{21}	η_{22}
$N = 8$	0.8840	0	0.0327	0.6839	0	0.0641
$N = 16$	0.9189	0	0.0340	0.8013	0	0.0751
$N = 32$	0.9279	0	0.0344	0.8330	0	0.0781
$N = \infty$	0.9308	0	0.0345	0.8437	0	0.0791

topological charges in Fig.5.6. The conversion efficiencies to the first 3 radial modes for an $\ell = L = 1, 2$ stepped spiral phase optic is given in Table 5.1. We find that when γ is optimally chosen, there are no $p = 1$ modes generated as observed in chapter 2.

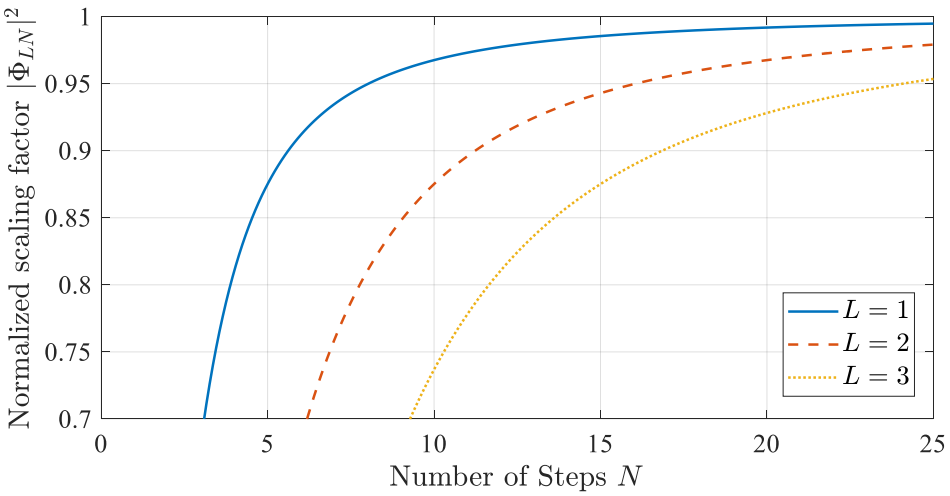

Figure 5.6: Multiplicative scaling factor $|\Phi_{LN}|^2$ as a function of the total number of stepped spiral phase optic steps N for the $\ell = L = 1, 2, 3$ cases normalized to $4\pi^2$.

If there is a mismatch in the topological charge number with the output mode number ($\ell \neq L$), we find that it is still possible to solve Eq.5.12 analytically,

$$\Phi_{\ell LN} = \frac{-i}{\ell}\left[exp\left(\frac{i\ell 2\pi}{N}\right) - 1\right]\frac{exp\left(i2\pi(\ell - L)\right) - 1}{exp\left(i2\pi(\ell - L)/N\right) - 1} \tag{5.14}$$

and if we take the limit where $N \to \infty$, we find the result,

$$\lim_{N\to\infty} \Phi_{\ell LN} = \frac{-i}{\ell - L}\left[exp(i2\pi(\ell - L)) - 1\right] \tag{5.15}$$

This allows us to estimate the sensitivity of the stepped spiral phase optic relative to manufacturing defects creating a mismatch in ℓ and L. Fig.5.7 plots the conversion efficiency scaling factor as a function of the charge of the SPO.

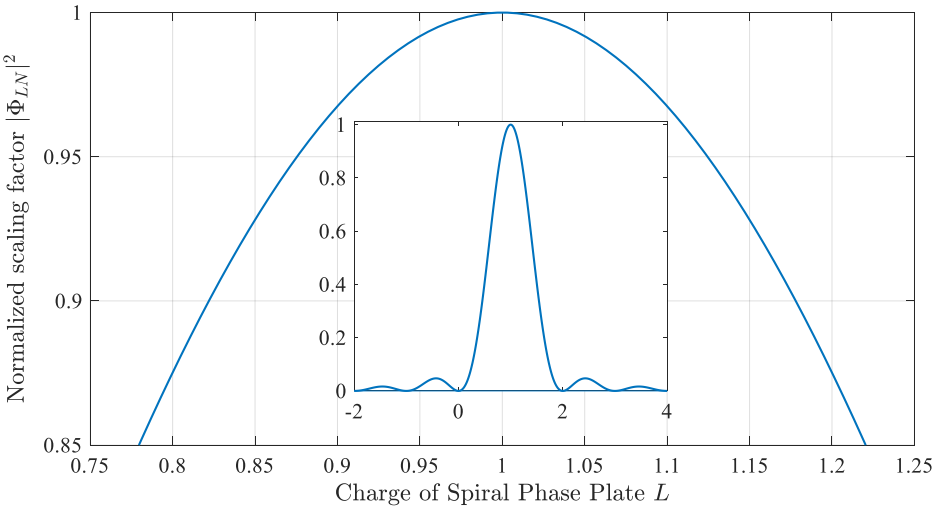

Figure 5.7: Multiplicative scaling factor $|\Phi_{LN}|^2$ as a function of intrinsic topological charge L of the spiral phase optic to the $\ell = 1$ mode. Inset into the image is a wider field of view showing the behaviour away from $(\ell = L = 1)$.

From Fig.5.7 we find that the scaling factor remains above 95% if the charge of the SPO remains within roughly 10% of the centre value of the SPO. For instance, if we have a SPO designed to operate at 800nm, and the SPO is being used in a reflective configuration such that the step height $H = 400$nm, then the step height can fluctuate as much as 40nm and still have a conversion efficiency close to 90%.

If the spiral phase optic does have a non-integer topological charge, we find that a spectrum of ℓ and p LG modes are produced. Fig.5.8 gives some of the spectral components produced from a $L = 1.2$ SPO, decomposing into modes with a beam waist ratio of $\gamma = 1/\sqrt{2}$.

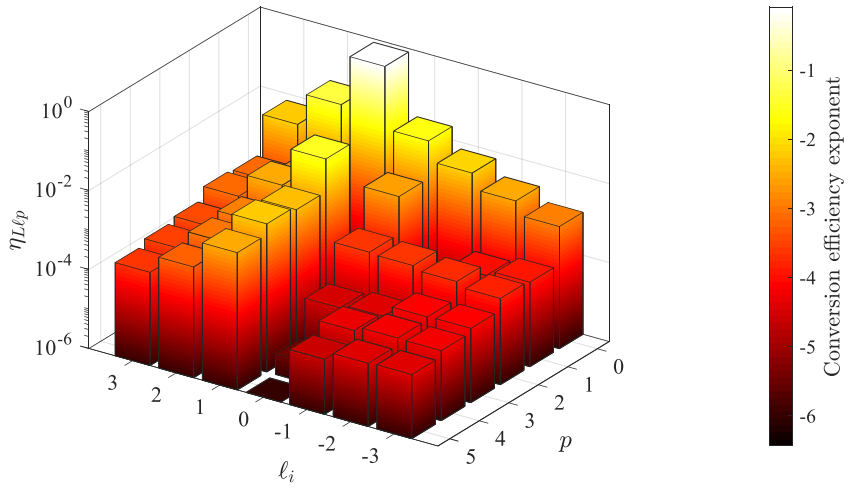

Figure 5.8: Laguerre-Gaussian mode spectrum ($\mathrm{LG}_{\ell_i,p}$) generated from a continuous $L = 1.2$ spiral phase optic.

While we have shown that it is possible to use a stepped spiral phase optic with minimal reduction in conversion efficiencies when using $N = 16L$, and we have shown that the SPO's are not very sensitive to manufacturing defects, we still have to answer the question of how laser bandwidth plays a role in mode conversion efficiency. Ultra-short laser pulses generated from titanium sapphire lasers can have significant bandwidth [9, 166]. For example, titanium sapphire has a bandwidth of almost 200nm and laser pulses generated in titanium sapphire laser systems can have bandwidths in excess of 100nm. The VEGA 2 laser in CLPU in Spain which produces 30fs pulses for instance has a bandwidth of approximately 80nm [166].

To model the laser bandwidth in the conversion efficiency calculations, we introduce a new frequency dependant transmission operator as,

$$T = exp\left[-iL\left(\frac{2\pi n\nu}{N\nu_0}\right)\right] \tag{5.16}$$

where ν is the frequency of interest and ν_0 is the central laser frequency. Using this transmission function, we can convolve it with a Gaussian distribution of frequencies

of standard deviation σ. This give the following formula [93],

$$|\Phi_{\ell LN\nu}|^2 = \int_{-\infty}^{\infty} \frac{1}{\sigma\sqrt{2\pi}} exp\left[-\frac{1}{2}\left(\frac{\nu-\nu_0}{\sigma}\right)^2\right] \left|\sum_{n=0}^{N-1}\int_{2\pi n/N}^{2\pi(n+1)/N} exp\left[i\left(\ell\theta - L\frac{2\pi n\nu}{N\nu_0}\right)\right]d\theta\right|^2 d\nu \tag{5.17}$$

As before, we are able to solve the sum and inner integral analytically, but the integral over frequency space must be computed numerically,

$$|\Phi_{\ell LN\nu}|^2 = \int_{-\infty}^{\infty} \frac{1}{\sigma\sqrt{2\pi}} exp\left[-\frac{1}{2}\left(\frac{\nu-\nu_0}{\sigma}\right)^2\right] \left|\frac{-i}{\ell}\left[exp\left(\frac{i\ell 2\pi}{N}\right)-1\right]\frac{exp\left(i2\pi(\ell - L\frac{\nu}{\nu_0})\right)-1}{exp\left(i2\pi(\ell - L\frac{\nu}{\nu_0})/N\right)-1}\right|^2 d\nu \tag{5.18}$$

We can relate the standard deviation of the frequency bandwidth to the full-width half maximum (FWHM) through the relation, $FWHM = 2\sqrt{2\ln 2}\sigma$.

The mode conversion efficiency was calculated for a broad range of value of bandwidths for 4 laser wavelengths that are often found in the laboratory are given in Fig.5.9. If we consider the case of the CLPU laser with 80nm of bandwidth at 800nm, we find the mode conversion scaling factor is roughly 0.99 indicating that the bandwidth plays very little role in the mode conversion.

This surprising result can be interpreted as such; given that the we assumed the bandwidth of the laser has a Gaussian shape, the strongest components are close to the central wavelength of the laser and contribute the most to the output mode. Given that the bandwidth of the laser is roughly 10% of the central wavelength, we expect the topological charge of the SPO will be modified by roughly a factor of 0.1 for the wavelengths far from the central wavelength. From Fig.5.7, we found that even a 10% error in the topological charge still leads to a very high conversion efficiency $|\Phi|^2 \approx 0.96$.

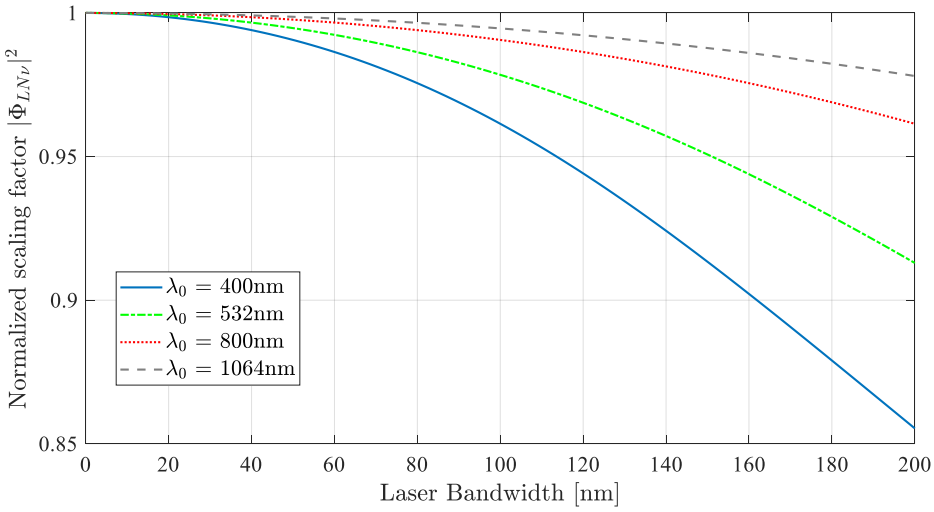

Figure 5.9: Multiplicative scaling factor $|\Phi_{LN}|^2$ as a function of laser bandwidth in nanometers for the case of $L = 1$ and $N = \infty$. Four central laser wavelengths are plotted from top to bottom: 1064nm, 800nm, 532nm, and 400nm in dashed grey, dotted red, dash-dot green and solid blue respectively.

5.4 Off-Axis Spiral Phase Mirrors

As was previously discussed, an optimal solution for generating ultrafast, high-power OAM modes is to use the spiral phase mirror due to its mitigation of nonlinear effects introduced by transmitting the beam through a transparent media. The problem with spiral phase mirrors is that the can only be used in a retro-reflecting configuration risking damage to the laser amplifier and compressor. In this section, we introduce the concept of an off-axis (or oblique-axis) spiral phase mirror (OASPM).

5.4.1 Theory

To convert a spiral phase mirror to the off-axis case, we utilize the example of a stepped spiral phase mirror (SSPM) as illustrated in Fig.5.10 a) and c). In tile a) we see a laser beam being retro-reflected from a 16 step SSPM from the top view while tile c) shows the SSPM face on. From tile c we see the circular imprint of the laser in red with an equal area of the beam on each step face. The angle of each step is

given by the simple formula,

$$\Delta\phi = \frac{2\pi}{N} rad \tag{5.19}$$

The values of the step angles measured from the horizontal axis is given in the Figure. The area shaded by the laser on each step is the same such that the reflected beam carries a 16-fold symmetric wavefront. If the laser is not well centred in the mirror such that some steps reflect more light than others, the resultant beam at focus could be an asymmetric OAM focal spot.

If we instead consider the oblique angle of incidence as shown in Fig.5.10 b) and d), we find that the laser spot imprinted in the mirror is now stretched along the incidence plane into an ellipse. As we still require that the beam is equally divided into N steps, the laser beam area imprinted onto each step must remain the same.

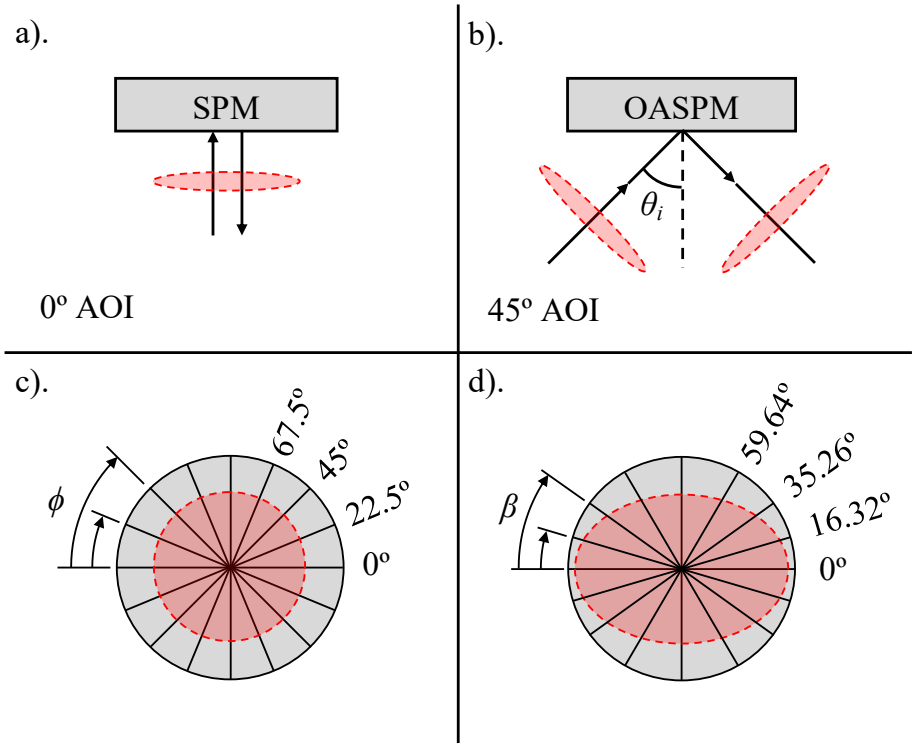

Figure 5.10: a) Retro-reflecting configuration of a normal incidence SPM; b) oblique angle of incidence to an OASPM shown here at 45°; c) front view of a stepped SPM indicating the step angle ϕ from horizontal and the circular laser beam outline in red; d) front view of a stepped OASPM indicating the step angle β relative to the horizontal plane and the elliptical laser beam outline in red.

By integrating over each sector area on the OASPM in tile d), we find that the sector angle relative to the incident plane can be related to the incidence angle of the laser θ_i by [95],

$$\beta = \arctan\left(\cos(\theta_i)\tan(\phi)\right) \tag{5.20}$$

where ϕ is the angle of each step relative to incidence plane in the normal incidence case, and θ_i is the incidence angle of the oblique case. Example values of β are given in Fig.5.10 d) for an incidence angle of 45°. Implementation of a variable step angle can be employed straight-forwardly when manufacturing stepped spiral phase mirrors, but may become more challenging when manufacturing continuous spiral phase mirrors as will be discussed in the next section.

In the normal incidence case, we find that each individual step height is given by H/N such that,

$$h = \frac{H}{N} = \frac{\lambda L}{2N} \tag{5.21}$$

where the factor of 2 represents the fact that the laser is retro-reflected and essentially double passes the helical surface. Considering instead the off-axis case, we find that Eq.5.20 must be modified to incorporate the wavefront shift according to the Bragg condition,

$$h = \frac{\lambda L}{2N\cos(\theta_i)} \tag{5.22}$$

Fig.5.11 shows the azimuthal cross-section of an OASPM with $N = 12$, in polar coordinates. Here, a continuous OASPM is indicated by the green dotted line, and the red dotted line indicates an incident laser. The figure allows us to identify a region where the incident beam is shadowed from interacting with the step adjacent to the 2π phase step. This can be mitigated by manufacturing the OASPM such that the 2π phase step is parallel to the plane of incidence. The maximum shadowing is expected to then be from the individual steps that are on the order of λ/N in height. At $\theta_i = 45°$, we expect the shadowed area to be equal to the step height and is therefore negligible compared to the wavelength.

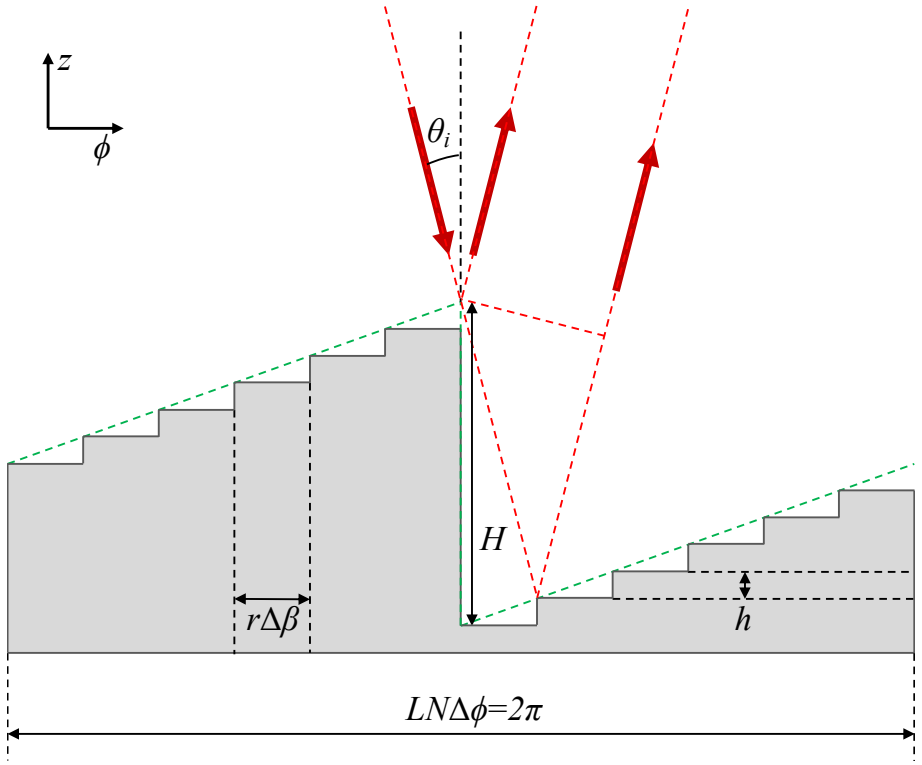

Figure 5.11: Illustration of an $L = 1, N = 12$ stepped OASPM in $\phi - z$ coordinates. The green dotted line represents a continuous OASPM ($N \to \infty$), and the red lines indicate light rays at a given incidence angle θ.

An additional limitation of the stepped OASPM is diffraction from the step edges depending on the manufacturing technique and the step edge width. Through fabrication of the OASPM via electron beam evaporation, we found the step edge width to be on the order of $100\mu m$ primarily as a result of mask position uncertainty as masks are interchanged. The corresponding area of the step edges relative to the total surface area of a large diameter beam ($> 100mm$) is around 1% and assumed to have a negligible effect on the focal spot. Much sharper edges could be produced using microelectronic lithographic techniques and would be required for microscale OASPM's. Sharp step edges may, however, generate high local electric fields that can either heat or damage the OAPSM surface with higher laser fluences. This could be mitigated through the use of high-reflectivity dielectric coatings or by grading the step edges over several wavelengths reducing any sharp electric field spikes while still contributing to only very small diffraction losses at the steps. An illustration of the OASPM in use is given in Fig.5.12

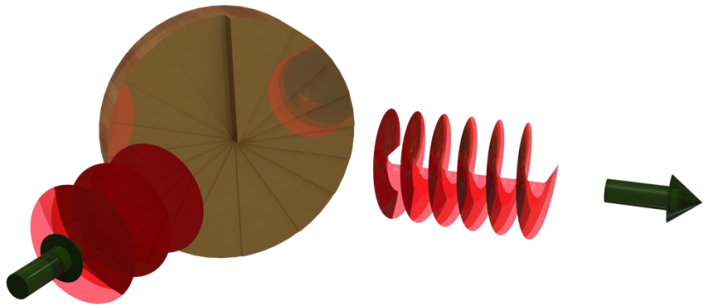

Figure 5.12: Illustration of the OASPM mode converting an off-axis beam. Unlike an SPP, the handedness of the ejected beam matches the handedness of the OASPM helix.

5.4.2 Manufacturing

Several prototype OASPM's were manufactured at the University of Alberta's nanoFAB centre using electron-beam evaporation techniques. This included 2 inch diameter mirrors for use in the low power laser systems, as well as 5 inch mirrors for use in the CLPU laser system. The processes and measurements of manufacturing are described in the appendix.

5.5 Experimental Implementation

To test the capability of the 2" OASPM's, a small scale setup was developed at the University of Alberta for low power OAM beam generation. Following successful tests of the OASPM at low power, three 5" OASPM's were fabricated and used at the CLPU VEGA2 laser which will be reviewed here.

5.5.1 Low Power OAM Generation

A bench-top setup was developed at the University of Alberta for generating and diagnosing OAM beams using low power lasers of various wavelengths. It was designed such that a variety of beams and wavelengths can be introduced and analyzed

through near-field and far-field imaging diagnostics, as well as interferometry. The experimental setup is illustrated in Fig.5.13.

In this setup, a laser is introduced and aligned to the setup axis using the first three alignment mirrors m. The beam is then expanded into a collimated beam of diameter $\approx 25mm$. This then passes through 2 lenses f_1 separated by distance $2f_1$, the focal plane of which is cleaned by a spatial filter pinhole of diameter $100\mu m$. This converts the incoming laser mode to an Airy ring in the near-field with a central lobe diameter of roughly $1cm$. The outer Airy rings are then removed in the near-field using the near-field aperture i.

After cleaning the near-field at i, the beam is split in two using a 50:50 beam-splitter b. The laser that passes through the beam-splitter interacts with the OASPM a with an incidence angle $\theta_i = 45°$. The beam is then reflected from a flat aluminum mirror m before passing the second beam-splitter and being focused by f_2 to the far-field camera. The focal spot of the laser is then re-imaged by the 4x microscope objective into the CCD.

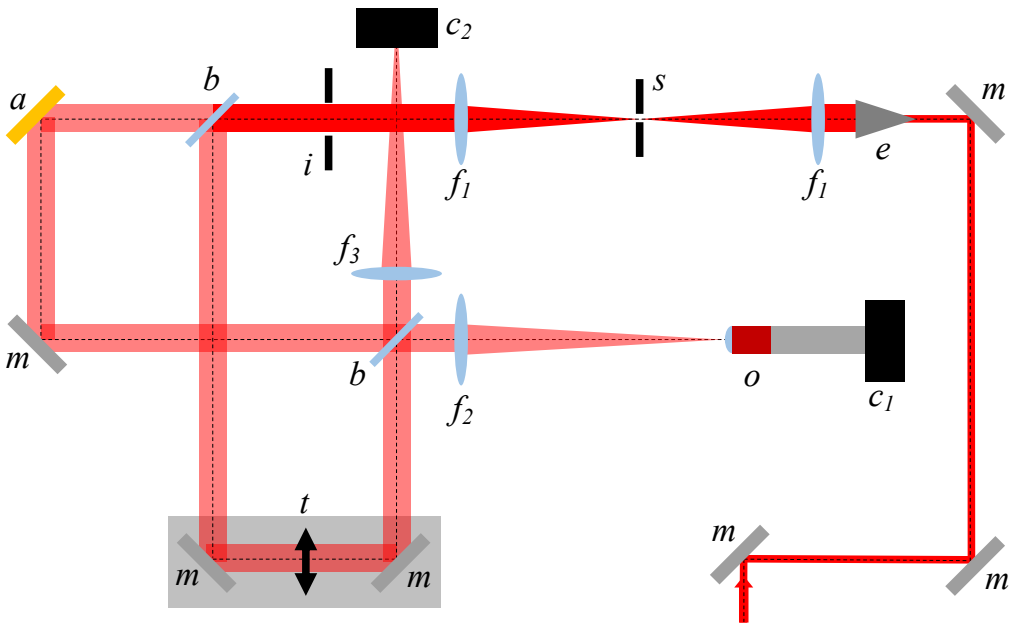

Figure 5.13: Low power OAM beam experimental setup. Key: a - OASPM, b - 50:50 beamsplitter, c_1 - far-field CCD, c_2 - near-field/interferometry CCD, e - 10x variable beam expander, f_1 - $1m$ plano-convex lens, f_2 - $750mm$ plano-convex lens, f_3 - $300mm$ plano-convex lens, i - near-field aperture, m - $\lambda/10$ aluminum mirror, o - 4x microscope objective, s - spatial filter, t - Mach-Zehnder interferometer delay translation stage.

We find that the expected intensity distribution at focus is best represented in the near-field with a Gaussian beam with a waist of $R_0 = 4.5mm$. This is a good approximation to the apertured Airy focal spot in the experiment. From chapter 2, we find the expected intensity distribution to have the following profile,

$$I(r,\ell) = I_0 \frac{\pi}{4} \xi^2 e^{-\xi^2} \left| I_{\frac{|\ell|-1}{2}}\left(\frac{\xi^2}{2}\right) - I_{\frac{|\ell|+1}{2}}\left(\frac{\xi^2}{2}\right) \right|^2 \tag{5.23}$$

where $\xi = r/w_0$ and $I_n(X)$ is the modified Bessel function of the first kind. Considering a helium-neon (HeNe) gas laser of wavelength $632.8nm$, and a Gaussian near-field waist of $r_0 = 4.5mm$, we find the expected far-field intensity distributions in Fig.5.14 a) and c) for the $\ell = 0$ and $\ell = 1$ beams respectively. Tiles b) and d) show the experimental results for both cases where we see good general agreement between spot size, shape, and intensity.

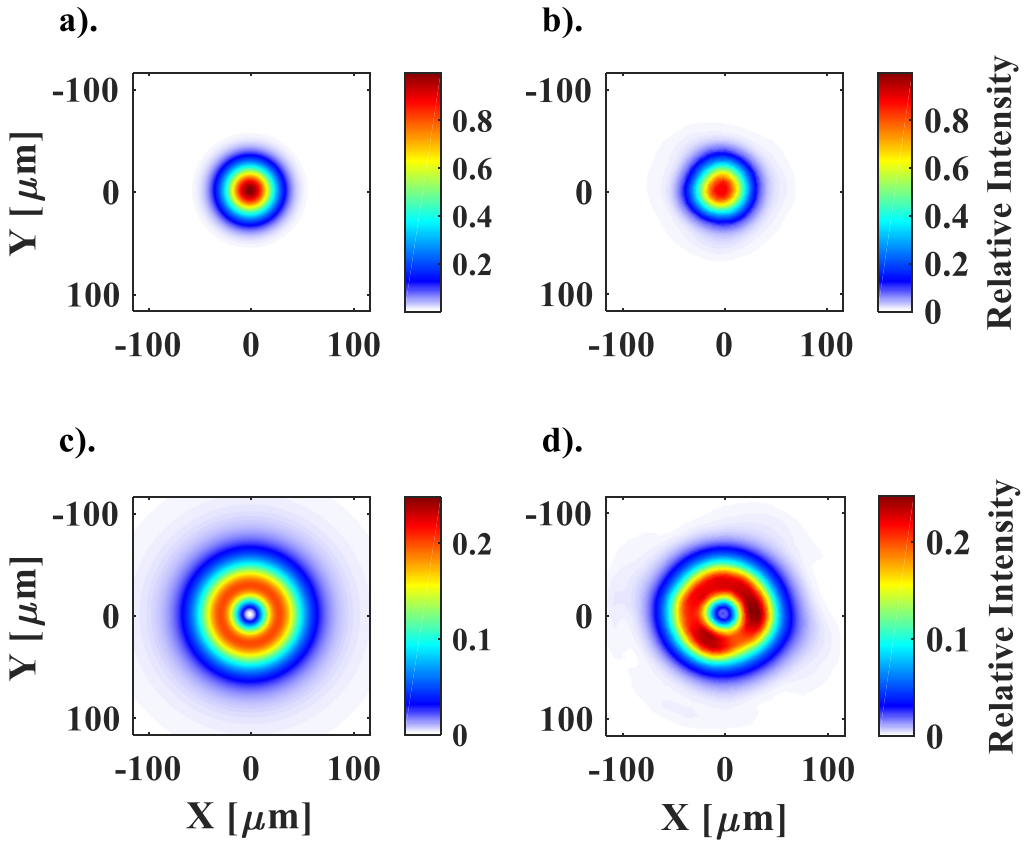

Figure 5.14: Focal spots of a Gaussian $L = 0$, and an $L = 1$ OAM beam generated from a collimated $R_0 = 4.5mm$ Gaussian near field HeNe beam with a $750mm$ focal length lens. The theoretical spots are given in tiles a) and c) for the $\ell = 0$ and $\ell = 1$ modes respectively. The experimental results are given in tiles b) and d) with $L = 0$, and $L = 1$ respectively.

The focal spot images were processed using an algorithm that removes the background, and removes any hot pixels in the image. An adaptive Wiener filter is then used to minimize any remaining noise in the image with its parameters set to minimize the standard deviation of the image whilst maintaining the pixel mean value [170]. The intensity is then calculated by summing over all pixels in the image and normalizing the sum to the theoretical result. This is equivalent to setting the laser power to the same value in both images and is of arbitrary units as the laser is continuous. Finally, the image is up-scaled to a higher resolution using a cubic spline interpolation method.

If we consider the Mach-Zehnder beam path in Fig.5.13, in which the delay arm t is used to match the path lengths of the interferometer arms, we can find the beam's angular momentum content. As the delay arm is only reflecting from flat mirrors, we expect to find an interference pattern between the OAM beam and the flat wavefront beam to be similar to what was found in Fig.5.2. To produce the tilted planar wavefront, the final turning mirror of the delay arm is finely adjusted until an interference pattern with suitable fringe widths is found.

An imaging lens (f_3) is used to image the OASPM onto the near-field camera c_2. This allows us to see the surface of the OASPM overlapped with the interference pattern as shown in Fig.5.15. The final turning mirror on the delay line was adjusted in both the θ and ϕ tilts such that both vertical and horizontal patterns were found in tiles a) and b) respectively. In tile a) we find the classic vertical fork pattern as shown in Fig.5.2. We note that there is only one split in the fork indicating that there is ± 1 OAM charge in the beam. This is made more clear in tile b) where the fringes have been rotated to be horizontal and shows the 2π phase discontinuity on the upper vertical step resulting in a phase shift of the fringe by exactly one wavelength. This is clear as the interference line "jumps" down the step edge and lines up perfectly with the next interference line.

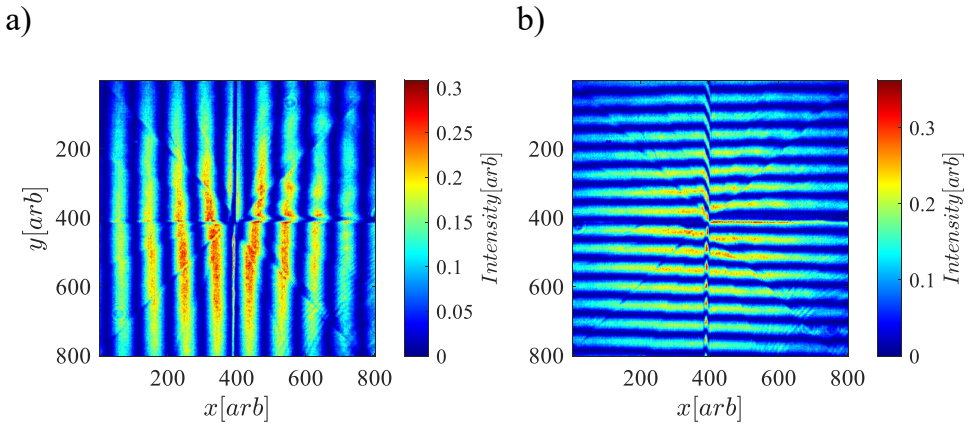

Figure 5.15: Interference patterns of an $L = 1$ OAM beam with a tilted plane wave. a) interference with a plane wave tilted in the horizontal plane, b) interference with a plane wave tilted in the vertical plane.

We note that the because we are imaging the OASPM directly, we are able to see some of the step edges directly on the camera, particularly the vertical, horizontal, and two 45° edges. There are 16 steps in the OASPM but the imaging system cannot resolve the smaller step edges as easily.

5.5.2 High Power OAM Generation

Testing of the OASPM at high power and high intensity was performed at the CLPU VEGA2 laser in Salamanca, Spain. This was done in two separate experimental campaigns in 2018 and 2019 utilizing the longer $f/13$ off-axis parabola and the short $f/4$ off axis parabola respectively.

The VEGA2 laser at CLPU is a titanium sapphire laser capable of amplifying laser pulses to 6J of energy [166]. The pulses are compressed to a Gaussian shaped pulse with a full width half maximum of approximately 30fs. The laser is centred at 800nm with a bandwidth of approximately 80nm. The compressed laser pulse has a near-field width of roughly 100mm and is characterized by a super-Gaussian shape with $n = 4$ according to Eq.2.68. After compression and beam transport, we find that typically 50% of the beam energy makes it to the focal spot in the target chamber. For intensity estimates used in the following figures, we assume that the laser has a total energy of $3J$ at focus and is compressed to $30fs$.

The beam is reflected from multiple mirrors for transport with a mix of dielectric and gold mirrors in the beam line before finally being focused by an off axis parabola. In a 2018 campaign, we opted to use the $f/13$ off axis parabola to maximize the Rayleigh range of the laser for wakefield interaction. The layout of the mirror arrangement and general geometries of the parabola chamber is given in Fig.5.16. The main beam is injected from the top of the figure and reflected from a gold mirror, where leakage light is then collected and focused through a $2m$ lens (f_1) onto a far-field imaging camera c_1. This is primarily used for alignment purposes. The reflected light from the mirror is then reflected from the OASPM (a) with an incidence angle of $\theta_i = 17.8°$. The beam reflected from the OASPM is then focused using a 30° off-axis parabola to a point 1300mm away.

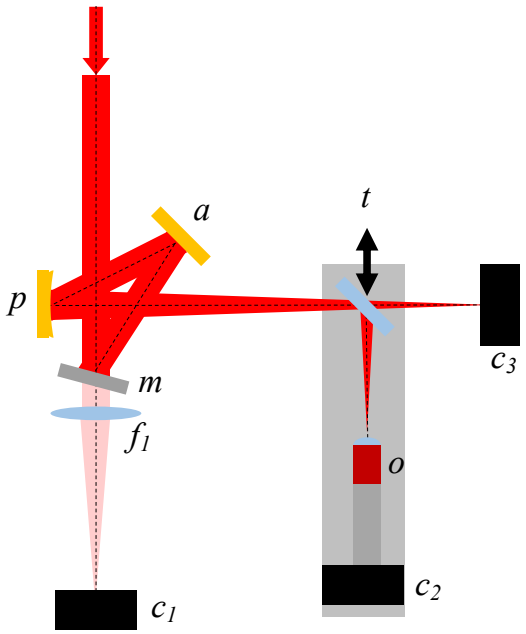

Figure 5.16: $f/13$ focus layout using the VEGA2 laser at CLPU. a - off-axis spiral phase mirror designed for use at $\theta_i = 17.8°$, c_1 - alignment CCD, c_2 - magnified focal spot CCD, c_3 - direct focal spot imaging CCD, f_1 - 2000mm lens, m - gold mirror, o - 10x infrared microscope objective, p - 30° 1300mm off-axis parabola, t - translation stage

Using a pick off mirror for imaging was necessary to reduce the intensity such that the objective would not get damaged. The on axis CCD c_3 was used to calibrate the focal spot size of the laser and was heavily attenuated to avoid damage. A total of three OASPM's were used in the experiment giving rise to four topological charges - $L = 0, \pm 1$, and $+2$. The results of these are compared to the theoretical spots as shown in Fig.5.17.

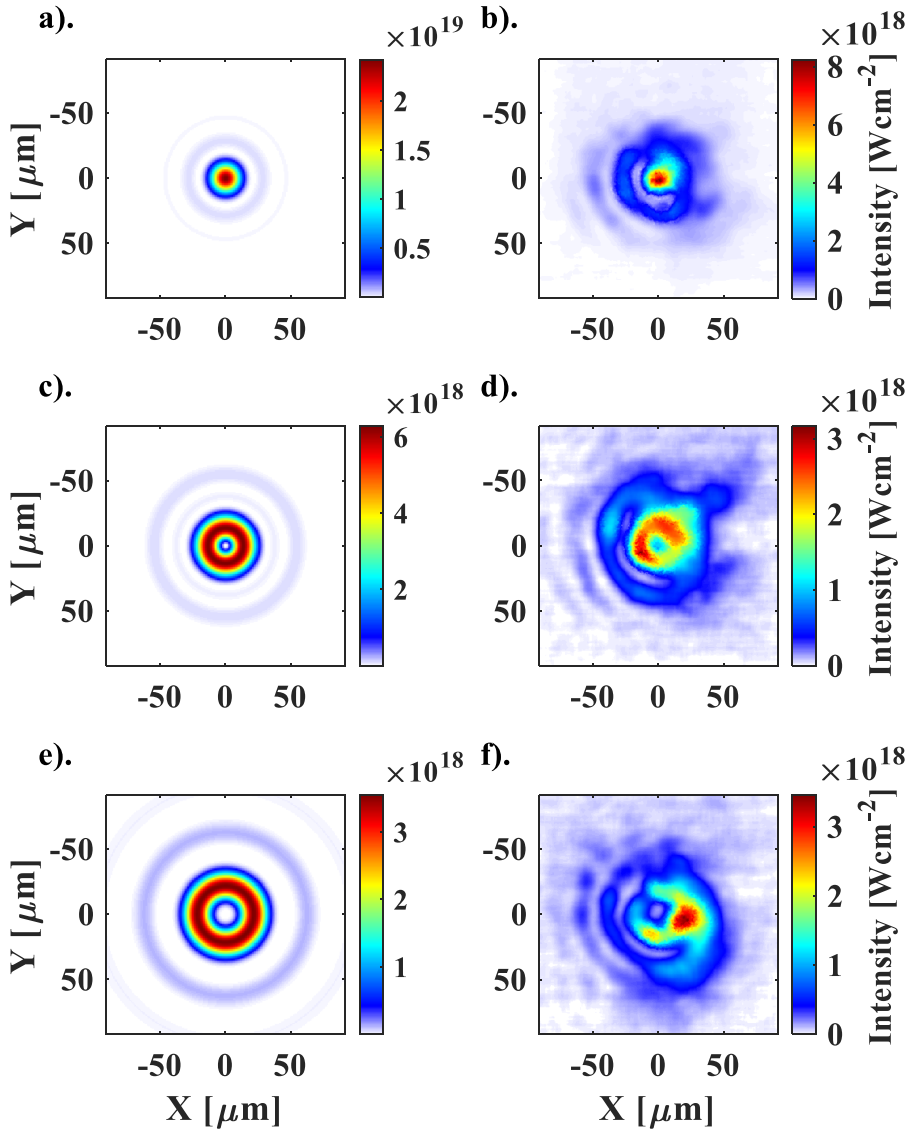

Figure 5.17: Focal spots generated using an $f/13$ off-axis parabola. Theoretical spots are given, a) $\ell = 0$, c) $\ell = 1$, e) $\ell = 2$. Experimental spots generated with OASPM's of topological charge b) $L = 0$, d) $L = 1$, f) $L = 2$.

To calculate the theoretical focal spot size, a near-field beam radius of $R_0 = 3cm$ was used as this was found to best represent the results. This was then used in our

previous far-field OAM focal spot formula from Eq.2.67 given as,

$$I_F(r,\ell) = \frac{I_0}{2}\left|\frac{\xi^{|\ell|}}{|\ell|!\left(\frac{|\ell|}{2}+1\right)}{}_1F_2\left(\frac{|\ell|}{2}+1;|\ell|+1,\frac{|\ell|}{2}+2;-\xi^2\right)\right|^2 \tag{5.24}$$

where ${}_1F_2(a;b,c;d)$ is the generalized hypergeometric function. In reality, the beam is bigger with an R_0 closer to $5cm$, however due to beam aberrations and focussing aberrations, it is difficult to obtain a diffraction limited result.

In Fig.5.17 a), we find the expected peak intensity of the spot should be on the order of $2.5 \times 10^{19} Wcm^{-2}$ if $3J$ of energy in 30fs is delivered to the focal spot. In reality as we find in tile b), this is not the case an our peak intensity for the $L = 0$ case is approximately $8 \times 10^{18} Wcm^{-2}$. This is due primarily to the large amount of energy outside of the central Airy lobe. We also find significant aberration in the focal spot as a result of astigmatism, coma, and trefoil [118]. Increasing the OAM in the beam to $L = 1$, we find the experimental result forms a ring that is modulated azimuthally, with the peak to trough ratio of roughly 3:2. This asymmetry is likely from the aberrations mentioned above, but also due to partial misalignment of the OASPM - perhaps it was not correctly centred on the beam. Given the physical setup of the mirror, it was not possible to adjust the height of the mirror in the beam restricting true centring on the mirror.

The $L = 2$ result is given in tiles e) and f) of Fig.5.17, where we find a very asymmetric focal spot. As the $L = 2$ mirror only had $N = 16$ steps, it yielded a poorer conversion efficiency as $N/L = 8$ instead of the preferred $N/L = 16$. According to Fig.5.6, this will cause a reduction in conversion efficiency to the $\ell = 2$ mode by at least 5%. As we will see in the next section, a 5% reduction in conversion efficiency can cause a significant reduction in mode quality at focus. However it is observed that for the larger size $L = 1$ and $L = 2$ modes the peak intensities are closer to the theoretical values due to the incorporation of more energy from outside the original central spot.

Taking what was learnt from the 2018 campaign, a second campaign in 2019 looked to improve the OAM focal spots as one of its goals while also using a shorter focal length $f/4$ off axis parabola. The schematic of this layout is given in Fig.5.18.

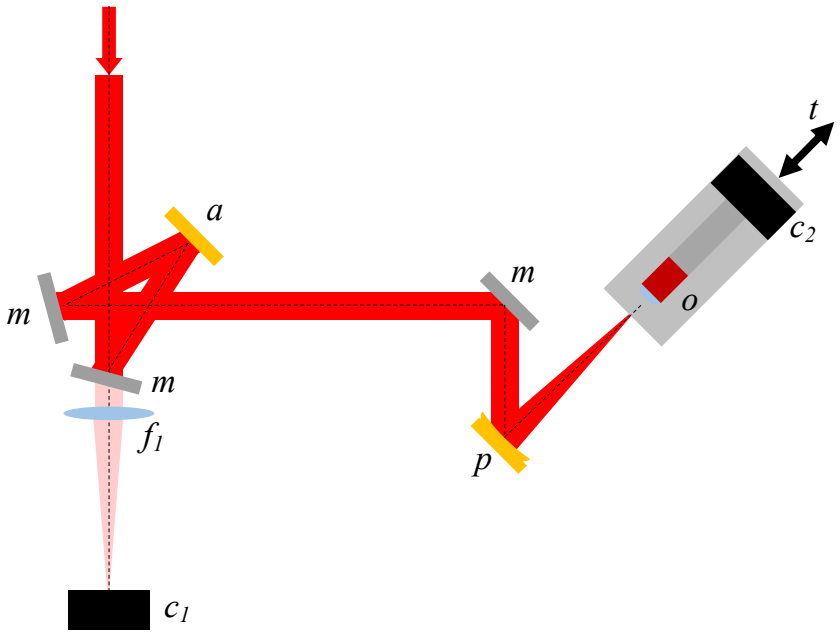

Figure 5.18: $f/4$ focus layout using the VEGA2 laser at CLPU. a - off-axis spiral phase mirror designed for use at $\theta_i = 17.8°$, c_1 - alignment CCD, c_2 - magnified focal spot CCD, f_1 - 2000mm lens, m - gold mirror, o - 20x infrared microscope objective, p - 40° 400mm off-axis parabola, t - translation stage

The setup is similar to that of the $f/13$ campaign, however given the short focal length of the off axis parabola $f = 400mm$, the OAP is now located in the main target interaction chamber. Given the shorter Rayleigh length of the parabola, it was possible to directly image the focal spot through the 20x infrared microscope objective using some neutral density filters. As the same OASPM's were used from 2018 in the 2019 experiment, the configuration was left as before.

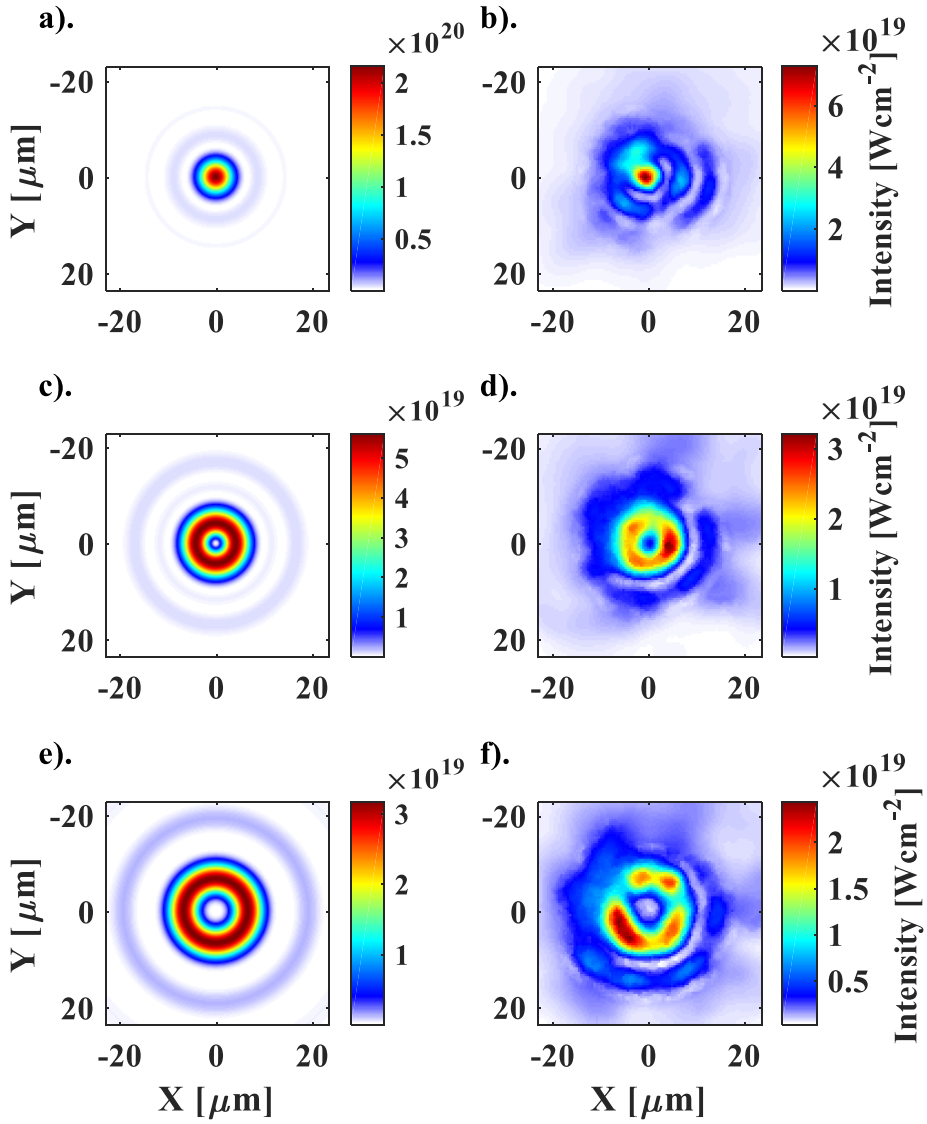

Figure 5.19: Focal spots generated using an $f/4$ off-axis parabola. Theoretical spots are given, a) $\ell = 0$, c) $\ell = 1$, e) $\ell = 2$. Experimental spots generated with OASPM's of topological charge b) $L = 0$, d) $L = 1$, f) $L = 2$.

The results are given in Fig.5.19 where we find much improved donut modes and much higher intensities. For the $L = 0$ mode, we still find in tile b) that a significant amount of energy lies outside of the central Airy spot, thus reducing the peak intensity from a theoretical value of $\approx 2 \times 10^{20} Wcm^{-2}$ to around $7 \times 10^{19} Wcm^{-2}$. The beam

aberrations however have been improved in the second campaign resulting in a much more symmetric focal spot. If we consider the $L = 1$ beam in tile d), we find that the beam is now much more symmetric and donut-like. The resulting peak intensity of the OAM focal spot is found to be $\approx 3 \times 10^{19} W cm^{-2}$ which is at least 3 times higher than any previous OAM generated in the literature [24, 34]. The $L = 2$ focal spot has been significantly improved now resembling a donut ring as opposed to a single spot before. There is still some azimuthal modulation in the beam, likely a result of trefoil, and a result of $N/L = 8$. The peak intensity of the $L = 2$ mode is quite close to the theoretical value of $3 \times 10^{19} W cm^{-2}$. This is a result of the OAM mode overlapping the aberrations in the focal spot, but also due to intensity modulations in the ring. There have been no high intensity $L = 2$ beams in the literature to date, indicating that this is the first relativistic $\ell = 2$ LG mode ever produced in the lab.

5.6 Numerical Modelling of Asymmetric Vortices

It is clear from the experimental results above that generating a perfect donut mode at high intensity is no easy task and is often degraded due to beam inhomogeneities, beam aberrations, focussing aberrations, and manufacturing defects in the OASPM. It is therefore necessary to study the effects of such aberrations and to model the beams that we can produce in the lab. Currently, almost the entirety of the literature investigating high intensity OAM-plasma interactions uses perfectly symmetric OAM donut modes, leading to results that may not be properly representative if an asymmetric beam is actually generated.

In this section, we seek to model asymmetric OAM beams similar to those found in the experimental results. To do this, we first take a standard LG mode with $p = 0$, and perturb it by an azimuthally varying amplitude transmission function,

$$T = 1 + \delta \cos(m\theta) \tag{5.25}$$

where δ is a small perturbation parameter, and m is the order of the azimuthal perturbation we want to apply. If we multiply this perturbation with a simplified LG mode, we get a perturbed wavefunction,

$$\psi(r, L)_P = \frac{2}{\sqrt{\alpha |L|!}} \frac{1}{w_0} \left(\frac{r\sqrt{2}}{w_0} \right)^{|L|} e^{iL\theta} exp\left(-\frac{r^2}{w_0^2} \right) (1 + \delta \cos(m\theta)) \tag{5.26}$$

where the P subscript indicates that it is the perturbed wavefunction. We normalize the mode such that,

$$1 = \langle \psi_P | \psi_P \rangle \tag{5.27}$$

and find the normalization factor to be given by,

$$\alpha = 2\pi + \pi\delta^2 + \frac{\delta}{2m}\sin(2\pi m)\left[\delta\cos(2\pi m) + 4\right] \tag{5.28}$$

It is clear from the normalization constant that if m is an integer, the constant becomes much simpler. While in principle m could be any value, we restrict it to be an integer for reasons discussed shortly.

Fig.5.20 gives some example focal spot distributions of the wavefunction for various value of L, δ, and m. By varying the parameters of δ and m, it is possible to generate a large variety of focal spots that can be used to represent the focus found in the experiment realistically. For instance, if we consider tile a) in Fig.5.20, we find that this qualitatively represents the result found in tile d) of Fig.5.17.

We find suitable perturbation parameters for ψ_P for each of the experimental focal spots in Fig.5.17. These are given in Fig.5.21, and although not a perfect model, it is a first order approximation to modelling the beam asymmetries. We find that the model for the $f/13$ result in tiles a) and b) works well and utilizes a small perturbation strength of $\delta = 0.1$ and an azimuthal variation of $m = 1$. We find that the same perturbation parameters are also suitable for modelling the $f/4$ focused $L = -1$ beam as shown in tiles c) and d).

The beam asymmetries in the $f/4$, $L = 2$ focal spots has a 3-fold symmetry so we opt to set $m = 3$. To obtain the azimuthal modulation, we set $\delta = 0.15$ as shown in tiles e) and f). We find the perturbed solution resembles the experimental result remarkably well, and now examine on how to implement these into simulations.

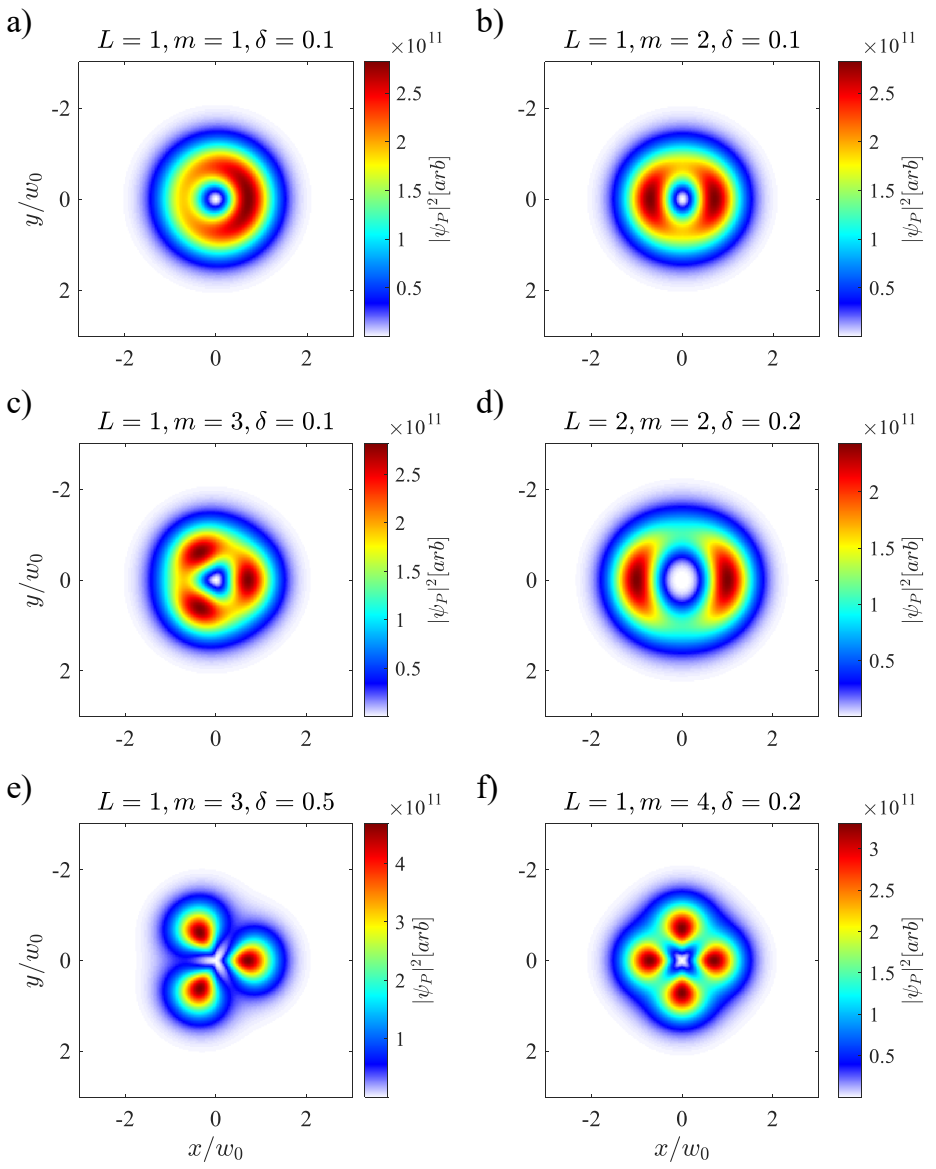

Figure 5.20: Perturbed Laguerre-Gaussian modes by the function $T = 1 + \delta\cos(m\theta)$. The relevant beam parameters are given in the title of each tile.

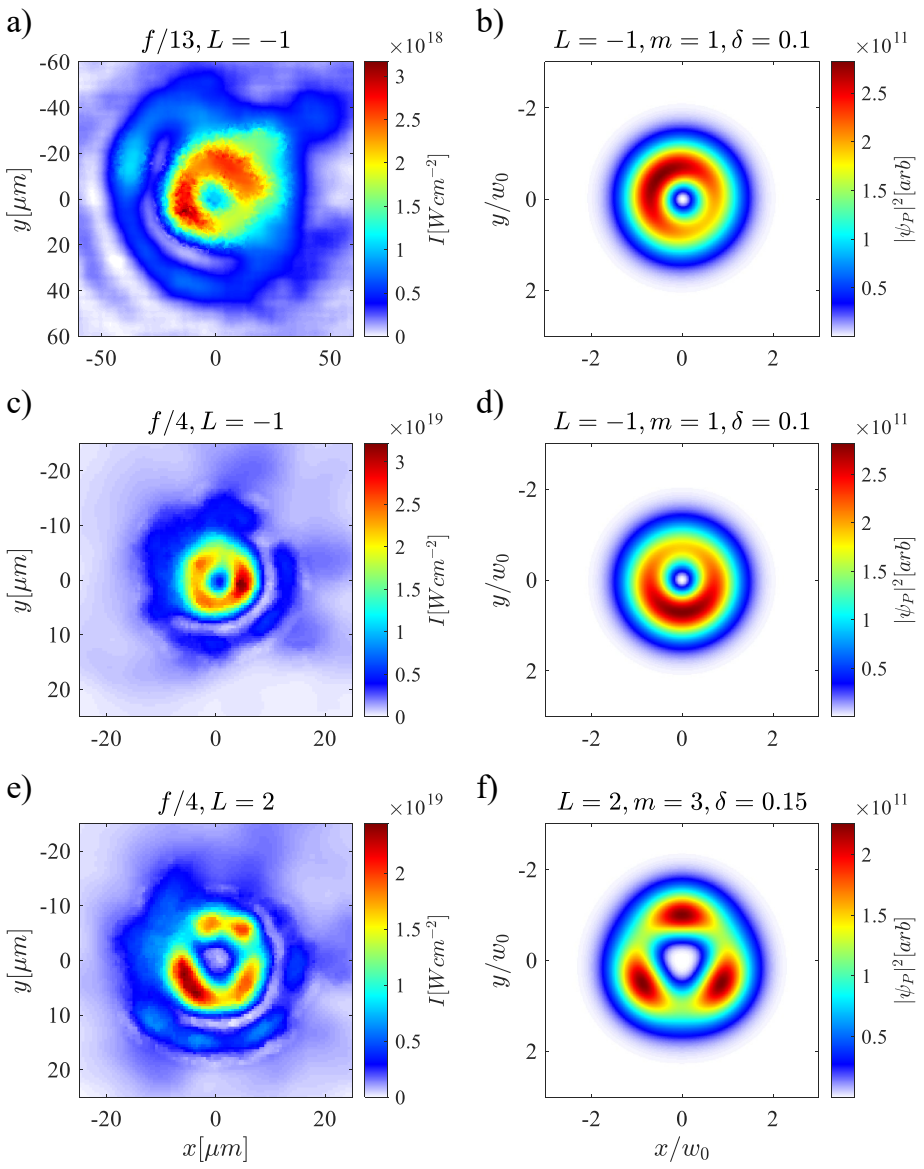

Figure 5.21: Experimental OAM focal spots (a,c,e) and suitable perturbed Laguerre-Gaussian modes (b,d,f) for modelling the focal spot. The relevant experimental and perturbation parameters are listed above each tile.

Clearly, if $\delta \neq 0$ and $m \neq 0$, the wavefunction ψ_P is not a valid solution to the Helmholtz equation and do not represent modes that preserve their shape as they propagate in free space. We therefore must decompose the perturbed wavefunction

into a linear superposition of modes that do satisfy the Helmholtz equation. To do this, we use a similar method to that in chapter 2 and decompose the perturbed wavefunction into adjacent Laguerre Gaussian ℓ modes. The mode conversion efficiency of each adjacent mode is then given by,

$$\eta = |\langle \psi_\ell | \psi_P \rangle|^2 \tag{5.29}$$

As before, we separate the integral into two components: the radial integral and the azimuthal integral. The radial integral is similar to that in Eq.2.74, but the azimuthal integral is slightly more complicated. As we are decomposing a perturbed Laguerre Gaussian mode into normal Laguerre Gaussian, we find that it is most efficient to match the beam waists of the LG modes from the perturbed wavefunction into the regular LG modes. In other words $w_{in} = w_{out}$ and we omit the need of an optimal beam waist ratio.

The conversion efficiency to the ℓ^{th} mode is then given by,

$$\sqrt{\eta} = \frac{\Gamma(\mu)}{\sqrt{2\pi|\ell|!|L|!\alpha}} \int_0^{2\pi} (1 + \delta\cos(m\theta))\, e^{i(L-\ell)\theta} d\theta \tag{5.30}$$

where μ is given by,

$$\mu = \frac{|\ell|}{2} + \frac{|L|}{2} + 1 \tag{5.31}$$

If we substitute the value of $H = L - \ell$, we find that the azimuthal integral can be solved analytically,

$$\begin{aligned} &\int_0^{2\pi} (1 + \delta\cos(m\theta))\, e^{i(L-\ell)\theta} d\theta = \\ &\qquad \frac{i\delta\left[H + e^{i2\pi H}(-H\cos(2\pi m) + im\sin(2\pi m))\right]}{(H-m)(H+m)} + \frac{i}{H}\left(1 - e^{i2\pi H}\right) \end{aligned} \tag{5.32}$$

We find that there are an infinite number of solutions if $m, L \notin \mathbb{Z}$, but if we confine our perturbation such that $L, m \in \mathbb{Z}$, then there are only 3 non-trivial solutions to the integral.

If $H = L - \ell = 0$, then the mode conversion efficiency can be given as,

$$\eta_{H=0} = \left(1 + \frac{\delta^2}{2}\right)^{-1} \tag{5.33}$$

Table 5.2: Mode conversion efficiencies to Laguerre Gaussian modes from a perturbed Laguerre Gaussian function with perturbation $(1 + \delta\cos(m\theta))$

L, m, δ	ℓ_1, η_1	ℓ_2, η_2	ℓ_3, η_3	$\sum \eta$
$1, 1, 0.1$	$1, 0.995$	$0, 0.002$	$2, 0.002$	0.999
$2, 3, 0.15$	$2, 0.989$	$-1, 0.005$	$5, 0.003$	0.997
$1, 3, 0.25$	$1, 0.970$	$-2, 0.013$	$4, 0.007$	0.990
$1, 5, 0.5$	$1, 0.889$	$-4, 0.026$	$6, 0.010$	0.925
$4, 4, 0.2$	$4, 0.980$	$0, 0.002$	$8, 0.005$	0.987

where as if $|H| = |m|$, we find,

$$\eta_{|H|=|m|} = \frac{\Gamma^2(\mu)}{2|L|!|\ell|!}\left(1 + \frac{2}{\delta^2}\right)^{-1} \tag{5.34}$$

and $\eta = 0$ if the above conditions on H are not met.

Therefore, if $m = 1$ and $L = 1$, we find the 3 LG modes required to model the focal spot are $\ell = 0, 1, 2$. It is interesting to note that the conversion efficiency is independent of m. Table 5.2 gives some example conversion efficiencies for small δ and m values. Column 1 gives the perturbation values, while columns 2-4 give the required modes to compose the perturbed solution. The fifth column gives the sum of the conversion efficiencies.

Although we have been able to convert to just 3 ℓ modes, the sum of the modes energy does not equate one as seen in column 5. This is due to energy lost to higher order p modes not included in the calculation. If δ is small ($\lessapprox 0.5$), we find that the 90% of the energy is accounted for in the 3 ℓ modes which should be sufficient for modelling. From Fig.5.21, we find that the value of δ needed to model the beams is typically small ≈ 0.15, so almost all the energy is accounted for.

To construct the modes, they are summed together, and then squared to find the intensity profile of the beam. This is shown in Fig.5.22 where the left tiles show the perturbed LG mode, and the right panels show the constructed LG mode representations. In tiles a) and b) we find an almost exact representation of the focal spot with the summed LG modes, and the peak intensity is well matched between the two.

However as we increase either m or δ, we find that the the discrepancy between the perturbed wavefunction and the summed LG modes gets worse. Tiles c) and d) show the perturbed wavefunction and summed wavefunction for the model of the

$L = 2$ experimental result. While we find a good recreation of the focal spot, its clear that it is not exactly the same and there is a significant decrease in the peak intensity of the beam. Tiles e) and f) show the extreme case of $\delta = 0.25$ and $m = 3$ were we see the perturbed wavefunction gives a lobed focal spot. The LG reconstruction of this focal spot is slightly different and has a significantly weaker peak intensity.

Given the 3 LG modes required to mode an asymmetric focus, it is possible to import the wavefunctions into PIC code simulations like EPOCH and model how the asymmetry affects laser-plasma interactions and the coupling of angular momentum. Given that the $m = 1, \delta = 0.1, L = 1$ case can be represented by an LG mode with 99.5% of its original energy, we dont expect there to be a significant change to the interaction. However, things like self-focussing and electron self injection into a wakefield may be enhanced due to the asymmetry. We will explore the effect of asymmetric OAM modes numerically when analyzing experimental results in the next 2 chapters.

5.7 Conclusions

In this chapter, we introduced the concept of the off-axis spiral phase mirror, our solution to the problem of generating high intensity OAM beams with ultra-fast lasers. We demonstrated that the OASPM was a cost effective optic producing high quality OAM beams, and yielded the highest intensity OAM focal spots to date for the both the $\ell = 1$ and $\ell = 2$ modes.

Like previous results in generating high-intensity OAM modes, the modes are not perfectly symmetric around the ring, and instead often have one or more hot-spots. These hot-spots are thought to be a result of spatial inhomogeneities in the laser near-field wavefront and intensity profile, defects in the mirror from manufacturing, and due to focussing aberrations such as astigmatism, coma, and trefoil.

To model the asymmetric donut modes, a perturbative model was developed. This model decomposes an asymmetric donut mode into three constituent LG modes, which can be easily implemented into numerical modelling.

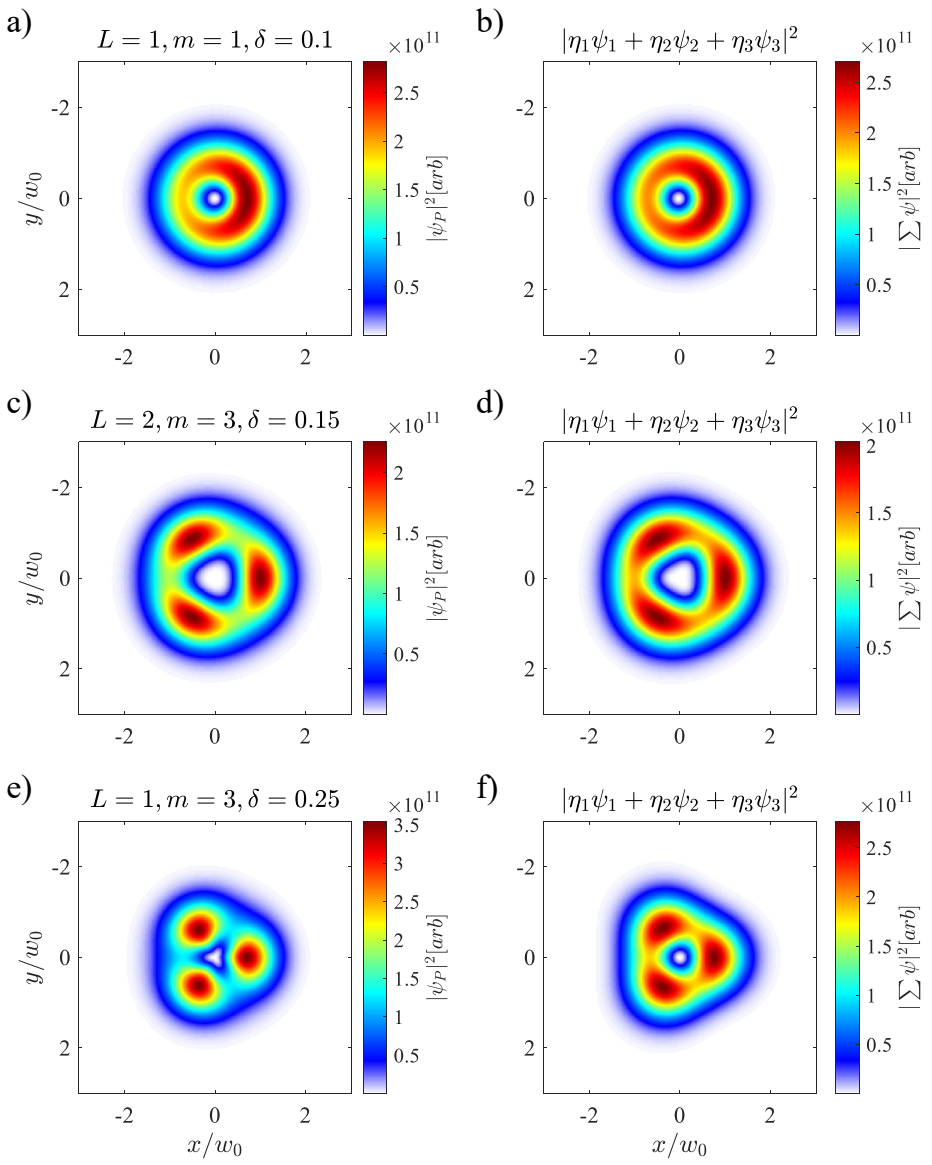

Figure 5.22: a) c) and e), perturbed wavefunctions with perturbation parameters given in the title. b) d) and f), composed Laguerre Gaussian modes to represent the perturbed wavefunctions.

Chapter 6

Wakefield Acceleration with Optical Vortices

Now that we have been able to demonstrate the successful generation of OAM modes at high power, we seek to investigate how they can be used experimentally and numerically to possibly enhance laser plasma interactions over the next two chapters. In a 2018 campaign at CLPU using the VEGA2 200TW laser [166], we used various OAM modes to drive wakefield accelerated electrons observing changes in the electron spectrum and divergence, and the betatron spectrum and divergence. To our knowledge, this was the first time OAM modes had been used to drive wakefield acceleration.

In this chapter, we first discuss the experimental setup and diagnostics used in the experiment. We then give some results of the experiment and compare to simulation predictions. Given that this was the first experiment of its kind performed, a second follow up experiment with improved diagnostics is required to confirm the observations made.

The work in this chapter has not yet been published in a peer reviewed journal, however it has been presented at multiple international conferences including the American Physical Society Division of Plasma Physics conference in 2018, the Conference on the Frontiers of Plasma Physics and Technology in 2019, and the Conference on Laser Interaction with Matter in 2018. Results of the betatron radiation and the numerical simulations are planned to be published in the near future.

6.1 Introduction

As discussed in chapter 4, wakefield acceleration of electrons from high intensity, ultrafast lasers is an area of intense research given the potential applications of the generated electron beams and betatron radiation [4]. Many schemes have been introduced to enhance the electron energies, for example by extending the interaction length using plasma channels [57]. Alternatively the interaction could be enhanced by modifying the wakefield regime from the previously discussed blow-out regime to self-modulated wakefields [90] or using direct laser acceleration schemes [137] which have been shown to enhance the brightness and energy spectrum of the emitted x-ray pulses. As the x-ray pulses are ultrafast, they can be used for many applications such as probing of warm-dense matter [109, 110, 108], or high resolution imaging [14, 72], to name a few.

Using OAM modes to drive the interaction can have some advantages over driving wakefields with Gaussian and Airy beams, such as focussing and guiding positrons [164], and for the generation of twisted radiation [177, 106]. To quantitatively verify that an OAM beam can generate stable wakefield donut bubbles and propagate in a plasma without breakup can be difficult experimentally given the spatial scales and duration of the interaction. We can however look to use diagnostics that can be used to infer processes taking place in the interaction. To do this, we have implemented an electron spectrometer that doubles as a device to measure electron far-field divergence. We also used an x-ray CCD camera with a stepped x-ray attenuation filter to estimate the x-ray brightness and its critical energy. A low noise CCD imaging a lanex screen was used to measure the x-ray divergence in addition to a second x-ray CCD with a larger CCD chip to observe off-axis x-ray emission. A Faraday probe was also used utilizing the second harmonic of the VEGA2 probe beam on a delay line to measure any axial magnetic field generated.

6.2 Experimental Setup

6.2.1 VEGA2 Laser System

The VEGA2 laser at the CLPU is a 200TW titanium sapphire laser producing 6J laser pulses before compression with a diameter of approximately 100mm. The beam has an 80nm bandwidth allowing for it to be compressed to approximately 30fs in

duration. After compression the beam is transported to the main interaction chamber where we find that approximately 42% of the laser energy is delivered to the focus of the laser. These energy losses can be attributed to the compressor efficiency ($\approx 70\%$), 10% lost in the probe beam splitter, and losses on the gold coated optics which vary in reflectivity due to various incidence angles, that are of order 98% reflective each. The energy at the focal spot of the laser was measured using a Standa $11QE95$ laser energy detector and compared to various other points in the laser beam line. These measurements were done at a reduced laser power level for safety precautions.

The primary interaction chamber used in the VEGA2 laser system at CLPU has a diameter of 1200mm with various ports for access in the laser plane and above the laser plane looking to the target chamber center. A $f = 1300mm$ off-axis parabola is used to focus the laser with an $f/\#$ of approximately 13. This results in a long Rayleigh range ($\approx mm$) suitable for wakefield acceleration. Self focussing and guiding of the laser pulse extends this interaction length over many millimeters enhancing the electron energy gain. An illustration of the laser geometry, and the diagnostics is given in Fig.6.1. Additional details like the beam splitter for the probe, and vacuum chambers have been omitted for clarity. It is noted that the vacuum chamber housing the OASPM, and the off-axis parabola can be isolated from the main interaction chamber allowing it to be pumped and vented separately. This was necessary so that the OASPM could be interchanged quickly during the day and only causing a 30-60 minute downtime of the system.

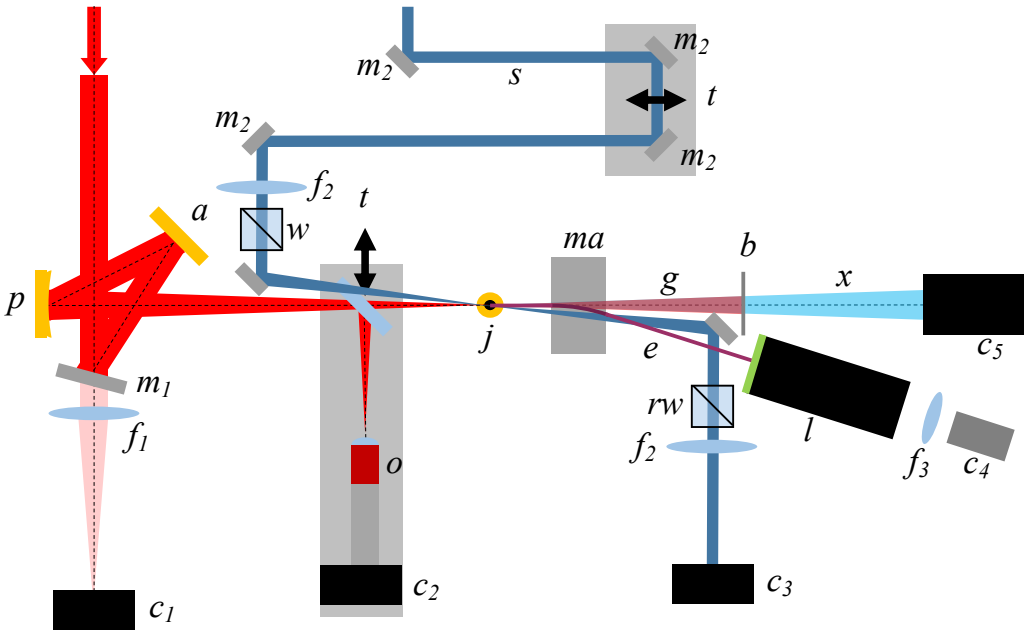

Figure 6.1: Wakefield experimental setup: a) OASPM mirror on fast exchange mount, b) laser block, c_1) alignment camera, c_2) focal spot imaging camera, c_3) Faraday rotation imaging camera, c_4) electron spectrometer imaging, c_5) Greateyes X-ray CCD and filter stack, e) electron beam, f_1) 2000mm lens, f_2) 1000mm lens, f_3) 50mm, $f/2.8$ camera objective, g) ejected laser/x-ray beam, j) gas jet on 3 axis translation stage, l) light-tight electron spectrometer housing with lanex screen attached at the front (indicated in green), m_1) gold mirror, m_2) 400nm dielectric mirror, ma) 1.2T magnet, o) 10x microscope objective, p) $f/13, 30^\circ$ off-axis parabola, rw) Wollaston prism in rotational mount, s) second harmonic probe beam, t) translation mount, w) Wollaston prism, x) betatron X-ray beam

Fig.6.1 is an extension to Fig.5.17, but now the laser is focussing into a gas jet instead of an imaging camera. The gas jet injects high pressure bursts of helium mixed with traces of nitrogen from which the laser can generate plasma with electron densities up to approximately $1 \times 10^{19} cm^{-3}$. The mixture ratio of the helium and nitrogen is set at roughly 99:1. This allows for some electrons to be injected through ionization injection via the inner shell electrons in nitrogen. Any laser light not absorbed in the interaction is absorbed or reflected from an aluminum foil beam block b as shown in Fig.6.1. The accelerated electrons are separated from the betatron x-rays by using a 1.2 Tesla permanent magnet that spectrally disperses them onto a

lanex fluorescence screen, which is then imaged by a low noise sCMOS Andor Zyla camera.

The probe line of the VEGA2 uses approximately 10% of the main beam energy via a beamsplitter, reduced in spot size to roughly 1cm and frequency doubled using a beta-barium borate (BBO) crystal. The temporal overlap of the probe with the main laser pulse at focus is adjusted using the retro-reflecting mirrors on the translation stage. The probe is orientated such that its k-vector is as close to a collinear with main beam as possible with a crossing angle of $\approx 1^{\circ}$.

6.2.2 Gas Nozzles

Gas was injected into the vacuum chamber using a Parker solenoid valve fitted with a conical nozzle machined from brass. The conical nozzle is machined with a conical expansion section and a throat diameter of $800\mu m$ expanding to $5mm$ allowing for the gas flow to become supersonic. This supersonic flow gives the advantage of producing a hard density edge in vacuum for regions close to the nozzle exit.

Using a simple model, we can estimate the Mach number of the flow inside and outside of the nozzle given the heat capacity ratio of the gas being injected γ_c. For a supersonic nozzle of throat area A^*, we find the Mach number M can be determined by,

$$\frac{A}{A^*} = \frac{1}{M}\left[\frac{2+(\gamma_c-1)M^2}{\gamma_c+1}\right]^{\frac{\gamma_c+1}{2(\gamma_c-1)}} \tag{6.1}$$

where A is the cross sectional area in the plane of interest. If we want to consider the gas flow outside of the nozzle into the vacuum, we can estimate the cross-sectional area by assuming the gas will expand into a cone of half-angle,

$$\sin(\alpha) = \frac{1}{M} \tag{6.2}$$

Knowing the Mach number for regions close to the nozzle exit allows us to estimate the density by the formula,

$$\frac{\rho}{\rho_0} = \left[1+\frac{\gamma_c-1}{2}M^2\right]^{-\frac{1}{\gamma_c-1}} \tag{6.3}$$

where the initial density is calculated at the nozzle throat using the ideal gas law,

$$\rho_0 = \frac{P_0}{k_B T_0} \tag{6.4}$$

where we assume the gas is initially at room temperature ($T_0 \approx 300K$), k_B is Boltzmann's constant and P_0 is the pressure of the gas in the valve. Depending on the gas, we find that the density and Mach number as it expands into vacuum can vary. This is due to the ratio of specific heats changing from monatomic gases to diatomic gasses. In the experiment at CLPU, a mixture of helium and nitrogen was used with a mix ratio of approximately 99:1 respectively. The ratio of specific heats for helium is found to be $\gamma_c = 5/3$, while for nitrogen molecules it is found to be $\gamma_c = 7/5$.

The nozzles used in the experiment had a nozzle conical half angle of 11.31° and an exit diameter of 5mm. Using these values, and a range of backing pressures used in the experiment from 5-50Bar, we are able to estimate the gas density in the interaction region of interest. Figure 6.2 shows the estimated gas number density profile for a pressure of 50Bar at room temperature in the nozzle throat, and the predicted electron number density as a function of height above the gas nozzle for a mixture of 99:1 helium and nitrogen.

From an experimental imaging system, the laser was determined to be interacting with gas approximately 1.7mm above the nozzle exit. Fig. 6.3 gives the estimated electron density as a function of nozzle throat pressure at 1.7mm above the nozzle exit.

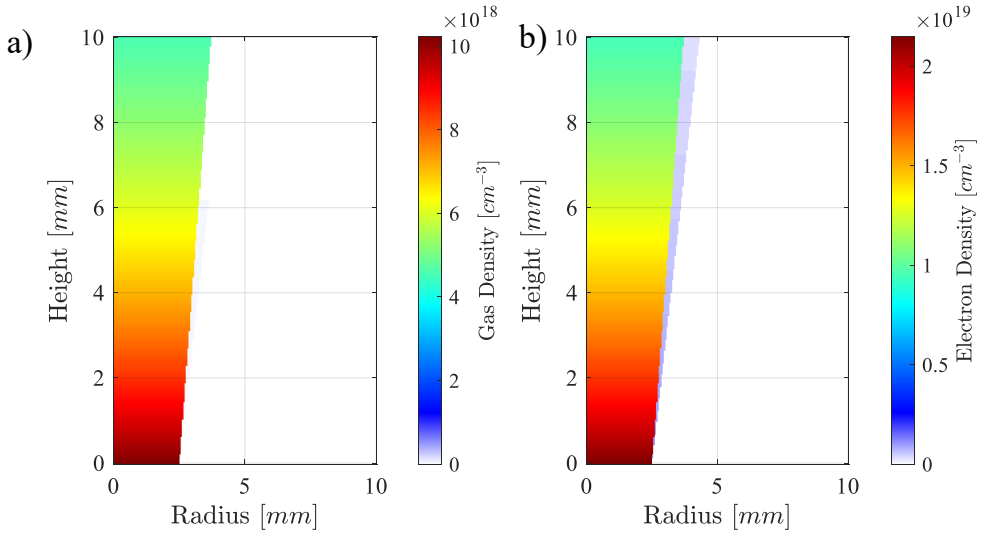

Figure 6.2: Analytic estimates for a) molecular gas density, and b) the total electron density from the gas jet assuming complete ionization of both helium and nitrogen for a backing pressure of 50Bar.

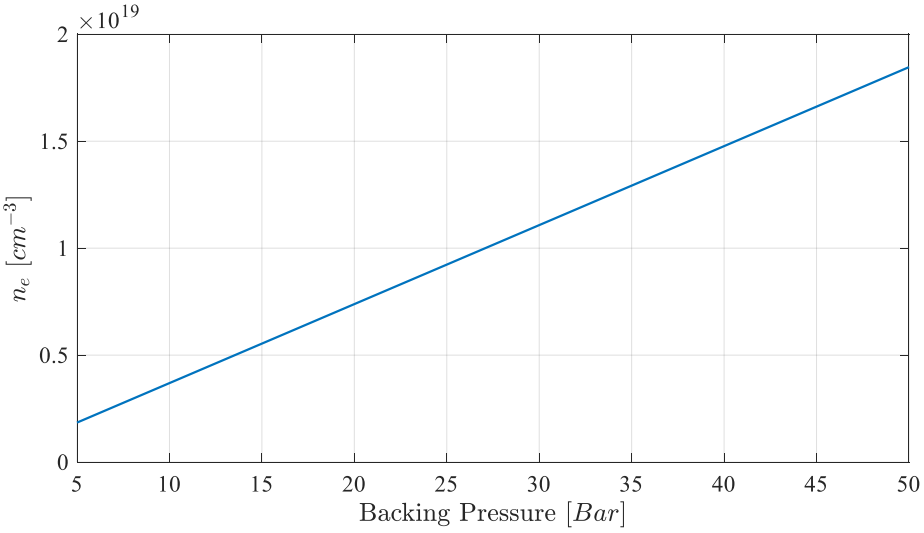

Figure 6.3: Estimated electron density 1.7mm above the gas nozzle exit as a function of backing pressure.

The assumptions made in the model requires knowing the actual pressure at the nozzle throat, and assumes a perfectly smooth surface inside the nozzle which is not the case for the real nozzle. We must therefore look to compare the analytic model

to measurements in the lab. Measurements of the gas density were made using a Mach-Zehnder interferometer using pure nitrogen given its higher refractive index. The density of the gas is then inferred using an Abel transform [59] performed by C. Salgado at CLPU. Assuming the gas jet to be axially symmetric, we can use a radial Abel inversion to predict the refractive index of the gas given by,

$$\Phi(x) = \frac{4\pi}{\lambda_0} \int_x^{r_0} \frac{(\eta_r(r) - 1) r dr}{(x^2 - r^2)^{1/2}} \tag{6.5}$$

where $\Phi(x)$ is the phase shift, x is the transverse coordinate, and $\eta_r(r)$ is the refractive index of the gas as a function of pressure (radius). From the refractive index, it is possible to infer the molecular density using measured values [18]. Measurements were made for a range of backing pressures for nitrogen gas, with an example density map given in Fig.6.4 a). Here we find the gas density to be vertically stratified due to the uncertainty of the density from the Abel inversion. As the uncertainty of the Abel inversion is inversely proportional to the radius, we are mostly concerned with the density gradient towards the edge of the gas plume. There are high density gas regions at the outer edges of image and are thought to be due to aberrations in the imaging system.

A lineout of the gas density at $y = 1.7mm$ (red dashed line in tile a) is taken and plotted in blue in tile b) of Fig.6.4. A super Gaussian density profile is fitted to this lineout weighted as a function of radius, this ensures that the fit is weighted to the areas of higher precision. We find that for 30Bar of backing pressure, the gas plume is suitably described by the equation,

$$n = n_0 exp\left(-\frac{x^{14}}{[2700\mu m]^{14}}\right) \tag{6.6}$$

where n_0 is the maximum gas density, found to be $1.3 \times 10^{18} cm^{-3}$ for a 30Bar backing pressure.

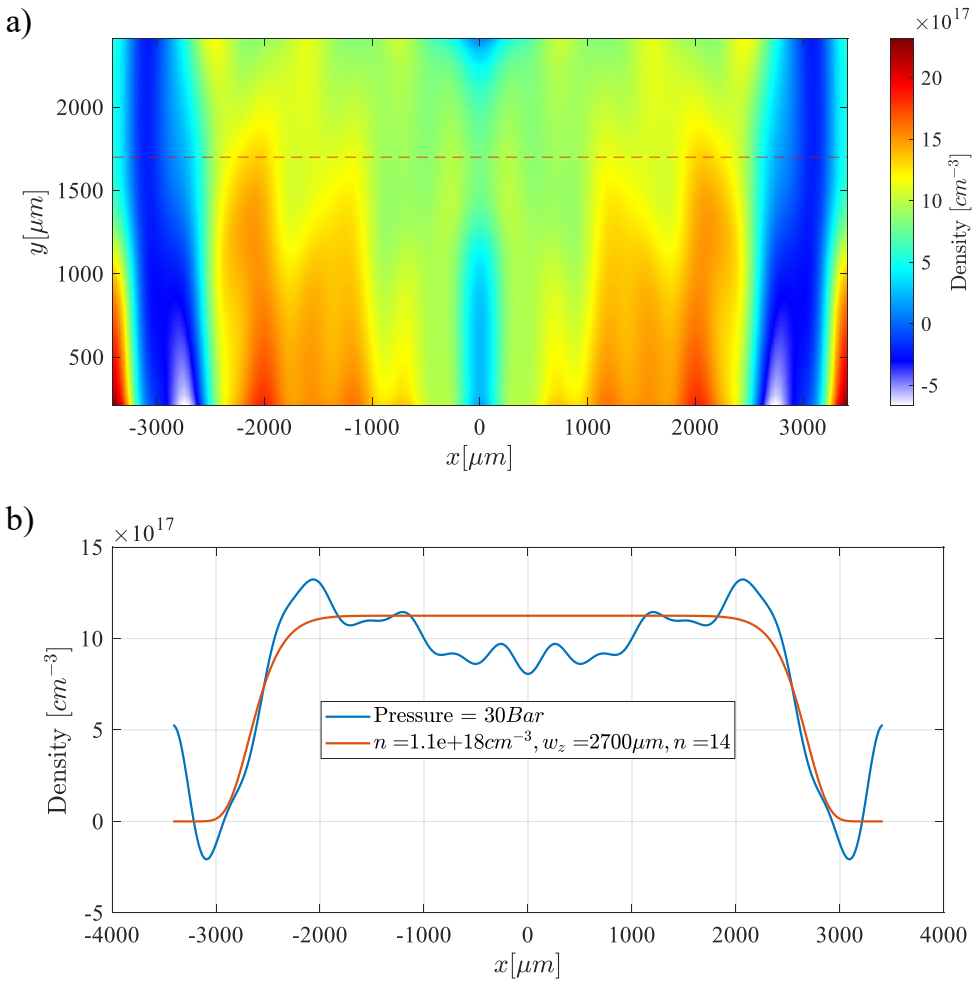

Figure 6.4: a) Measured nitrogen density with 30Bar backing pressure. Density is measured from the top of the nozzle. b) Lineout of gas density (blue) located at 1.7mm (red dashed line in a). The red line represents a weighted fit to the data using a super-Gaussian.

Using pure nitrogen molecules in our analytic model, we find that for the same backing pressure of 30Bar, the estimated gas pressure is much higher - about $4.0 \times 10^{18} cm^{-3}$ which is roughly 3 times higher than that measured. The reason for this discrepancy is due to assuming the nozzle throat pressure is equal to the backing pressure, uncertainties in the orifice diameter, and surface roughness inside the nozzle walls. We therefore assume that the density of helium is also roughly 3 times less

than the analytic model, although this has not been confirmed experimentally yet.

Assuming that after self focussing the laser intensity surpasses $1 \times 10^{19} cm^{-3}$, we can estimate the electron density to be 2.12 times greater than the molecular density of a mixture of 99:1 helium-nitrogen. Using the values of the peak gas density in the measured profiles, we plot the electron density as a function of backing pressure in Fig.6.5. Here we find a linear increase in electron density as a function of backing pressure as predicted in Fig.6.3. The estimated electron density in the interaction region $1.7mm$ above the nozzle is then found to be,

$$n_e[cm^{-3}] = P[Bar] \cdot 8.112 \times 10^{16} + 5.783 \times 10^{17} \tag{6.7}$$

This is then combined with Eq.6.6 to give a first order estimate of the electron density in the interaction.

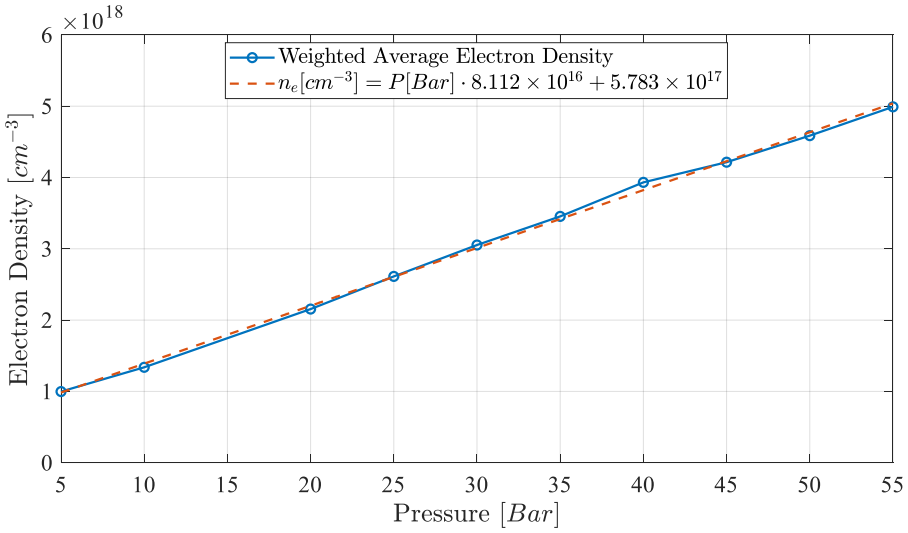

Figure 6.5: Estimated electron density as a function of backing pressure for a 99:1 helium-nitrogen mixture. The red dashed line gives a linear fit with parameters given in legend.

6.2.3 Focal Spots

The focal spots obtained by the 10x objective have been given previously in Fig.5.18. While we do not show the spots again here, we plot the cumulative energy distribution as a function of radius given in Fig.6.7. Here the diffraction limited spots are plotted with dashes, while the experimental data is plotted as solid lines. All profiles have

assumed the same total power (100TW) reaches focus, and hence all tend to the same value as $r \to \infty$. The solid red line indicates the 50% energy point radius. The values of the 50% energy radius are given in Table 6.1

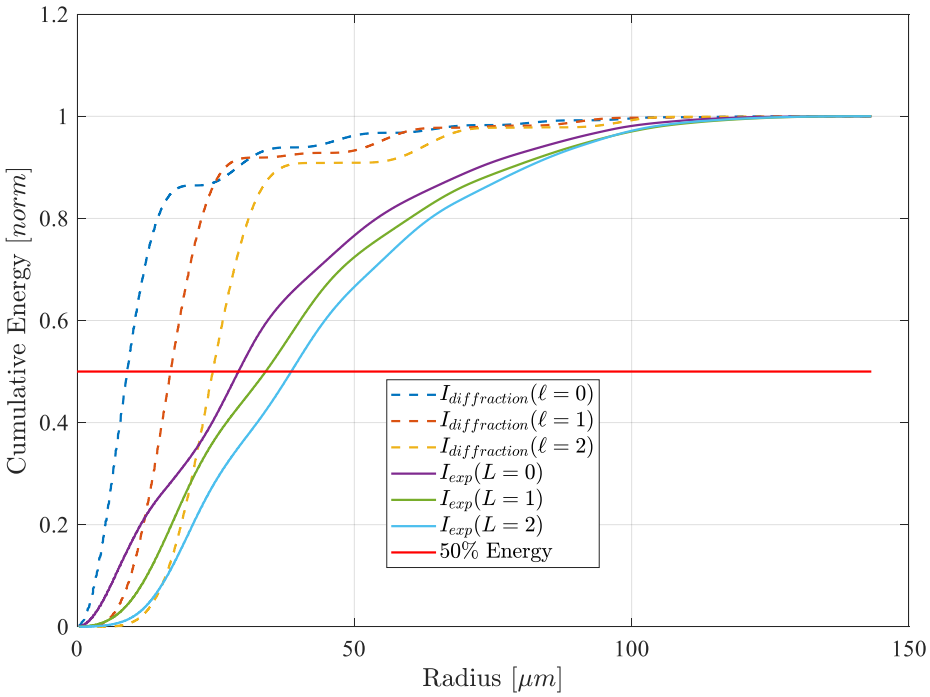

Figure 6.6: Cumulative energy distributions for the focal spots found in Fig.5.18. The dashed lines indicate the diffraction limited spots, while the solid lines give the experimental results. The solid red line represents the 50% energy cutoff.

Given the vacuum parameters in Table 6.1, and assuming the only power that contributes to self-focussing comes from within the first Airy null, it is possible to estimate the peak intensity, and beam waist of the laser after self focussing in plasma. If we assume a plasma density of $3.5 \times 10^{18} cm^{-3}$, slightly more than estimated from Fig.6.5, we can calculate the critical power for self focussing in the plasma using Eq.4.20. The peak intensity of the beam is then estimated using Eq.4.23 and converted to Wcm^{-2}. These values are given in Table 6.1.

Assuming the beams are generated by Gaussian near-field beams, we can use the values of $\bar{\gamma}$ and η from Table's 2.2 and 2.3 to calculate the beam waist that would ensure that both the peak intensity is maintained, and the radius ensures the correct amount of energy in the beam according to Table 6.1. We note that given

Table 6.1: Vacuum and self-focussed parameters of the beams given in Fig.5.18.

Parameter	$L = 0$	$L = 1$	$L = 2$
Peak Intensity (Vacuum) $[Wcm^{-2}]$	8×10^{18}	2.5×10^{18}	1.5×10^{18}
50% Energy Radius $[\mu m]$	29	34	38.5
1^{st} Airy Null Radius $[\mu m]$	16.5	28	29
Laser Power within First Null $[TW]$	29	41	35
Critical power (@$3.5 \times 10^{18} cm^{-3}$) $[TW]$	7.77	31.07	62.14
a_0 (self-focussed)	3.10	2.19	1.65
I_{sf} $[Wcm^{-2}]$	2.08×10^{19}	1.04×10^{19}	5.89×10^{18}
w_{0-sf} $[\mu m]$	9.4	9.4	10.1
m, δ	$0, 0$	$1, 0.1$	$1, 0.3$
ℓ_1, η_1	$0, 1$	$1, 0.995$	$2, 0.957$
ℓ_2, η_2	N/A	$0, 0.002$	$1, 0.019$
ℓ_3, η_3	N/A	$2, 0.002$	$3, 0.019$

the parameters of beam waist in Table 6.1, it is possible to simulate the $L = 0$ mode and the $L = 1$ mode using the EPOCH simulation deck that we have been previously using. However we find that with the increased beam radius and the increase in ring size due to additional OAM, simulating the $L = 2$ mode becomes difficult due to strong interactions of the OAM mode with the boundary conditions.

To simulate asymmetric OAM beams, we estimate the perturbation parameters δ, m, as given in Table 6.1, similar to what was found in Fig.5.21. The modal decomposition of the perturbed LG modes is performed and given at the end of Table 6.1. Simulations using both perturbed and non-perturbed LG_{10} modes were performed using a shortened super Gaussian electron density profile with peak density of $3.5 \times 10^{18} cm^{-3}$ and width $700 \mu m$. The simulations results will be presented and compared to the experimental results in the results section of this chapter.

6.3 Diagnostics

6.3.1 Electron Spectrometer

After the electrons are accelerated through the wakefield within the gas jet plume, they are ejected with the laser beam and the betatron X-rays. To measure the electron energy, we utilize a simple 1.2T permanent dipole magnet with the magnetic field oriented perpendicular to the electron beam velocity vector. The magnetic field disperses the electrons according to their energy, after which they strike a Kodak

medium grade Lanex screen which is activated by the electrons and fluoresces at 546nm, as illustrated in Fig.6.1. The Lanex screen has been previously calibrated by another group using a known electron source allowing for the conversion of the emission brightness of the film to electron charge per unit area [26]. The 546nm light is then re-imaged onto a high sensitivity sCMOS camera through which the losses due to vacuum chamber windows, imaging systems, and the camera quantum efficiency are accounted for.

Modelling of the electron trajectories through a magnetic field can be calculated to first order assuming a constant, homogeneous magnetic field throughout the magnet and assuming no fringing fields at the magnet edges. While this is useful to compute as a first order approximation, a detailed analysis including magnetic field gradients, and fringing fields outside of the magnet should be carried out for an accurate estimate of the spectrometer dispersion relation, and the corresponding resolution.

The magnetic field of the permanent magnet is scanned using a Hall probe, and tabulated into a 2D map, as shown in Fig.6.7. To account for an electron passing through a magnetic field gradient, it is necessary to integrate its trajectory numerically, similar to what was done with the single particle integrator in Chapter 3. This also allows for more complex, and divergent trajectories to be simulated through the spectrometer allowing estimates to be made on the spectrometer resolution.

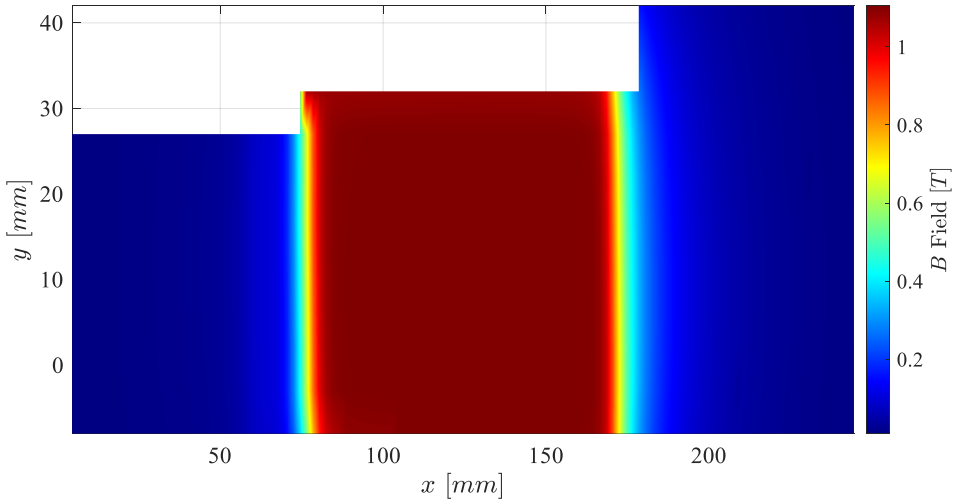

Figure 6.7: Magnetic field map of the magnetic electron spectrometer at CLPU. The electron enters from the left at position (0,0).

The magnet was eventually rotated 30 degrees about the laser axis to deflect electrons downwards towards the ground rather than into the walls to reduce bremsstrahlung radiation and neutron generation. This rotation turned the essentially 2D spectrometer mapping problem into a 3D problem. Additionally, the lanex detection screen was mounted 22.5degrees relative to the perpendicular of the laser axis as shown in Fig.6.1 and Fig.6.8. Accounting for these geometries, the electron trajectories can be computed, and their displacement from the laser axis on the lanex screen determines their energy. The 2D geometries are plotted in Fig.6.8 with the dipole magnet placement in yellow and the lanex shown in green.

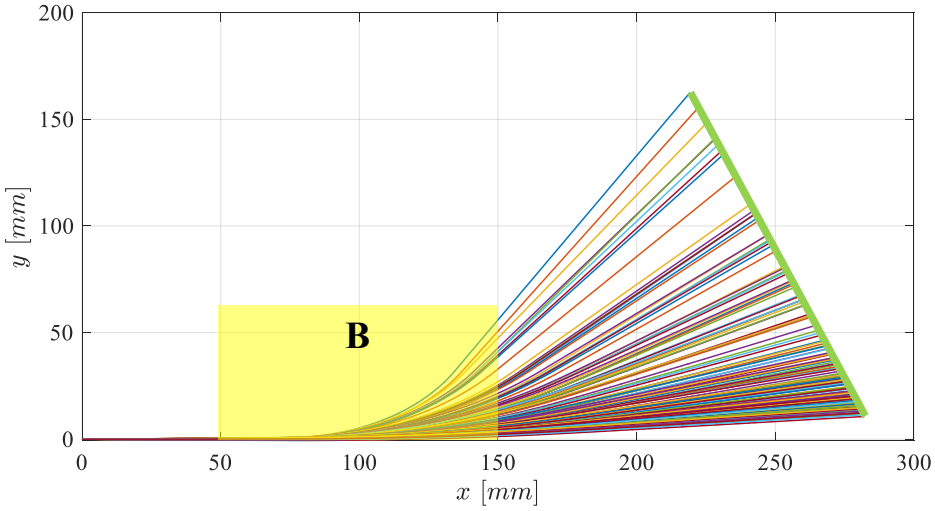

Figure 6.8: Sample trajectories of electrons with half angle divergences up to $10mrad$ passing through the magnetic spectrometer and striking the green lanex screen on the right.

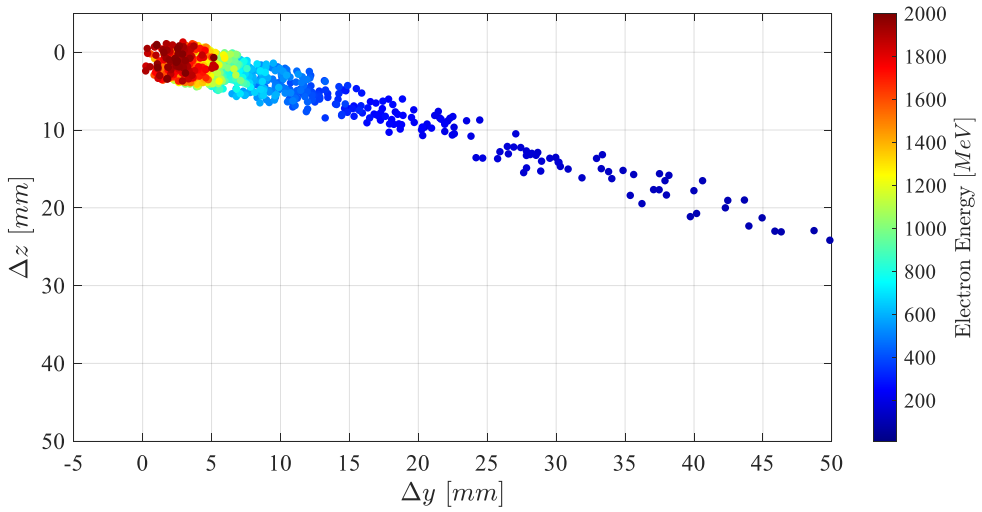

Figure 6.9: Electron displacement maps as seen by the Lanex screen. 1000 electrons are randomly assigned energies within a divergence angle cone of half angle $10mrad$. The colorbar indicates the initial energy of each electron.

If instead we plot the lanex screen as seen by the camera, we can see the electrons scattered as a function of their energy as shown in Fig.6.9. Here, 1000 electrons are injected into the simulation with a random energy, and a random divergence within a cone of half angle $10mrad$. It is clear to see some of the limitations of the resolution of the spectrometer, particularly for high energy electrons. To model the electron energy, several simulations were run for various divergence angles. The dispersion relation was found for the electrons with zero initial divergence, while upper and lower bounds on the dispersion relation were found for $10mrad$ divergence electrons. Theses results are summarized in Fig.6.10.

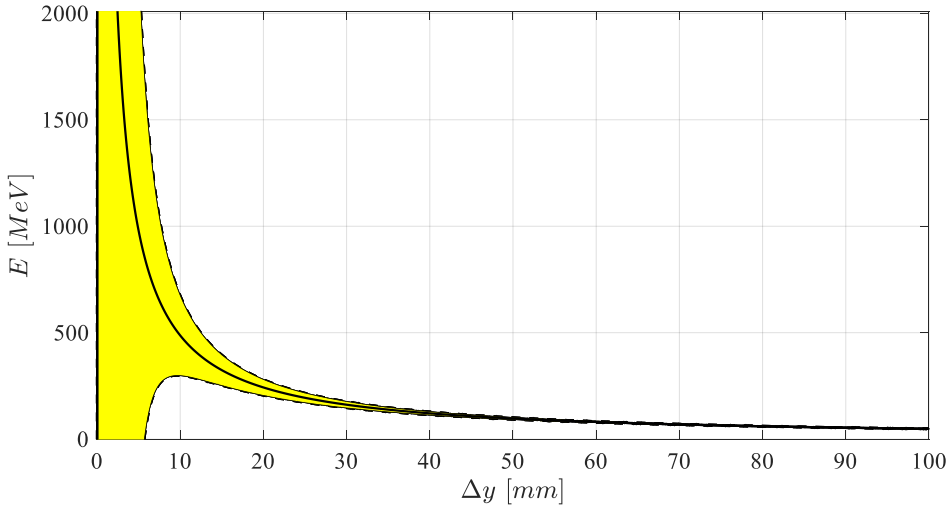

Figure 6.10: Electron spectrometer dispersion relation, with resolution indicated in yellow for a $10mrad$ divergence beam.

The dispersion relation was found to be,

$$E[MeV] = \frac{4846}{\Delta y[mm] - 0.049} \tag{6.8}$$

while the resolution for a $10mrad$ beam is given by,

$$\delta E[MeV] = \frac{4846}{\Delta y[mm] - 0.049} - \frac{4797}{\Delta y[mm] - 2.900} \tag{6.9}$$

This resolution is indicated in Fig.6.10 by the yellow shaded area. Further corrections can be made to resolution if one was to include the energy dependence on divergence, but here we assume the divergence is independent of electron energy.

In order to determine the uncertainty in energies determined by the electron spectrometer, we must determine the shot to shot variations in the electron beam pointing. This is estimated from the standard deviation of the mean of the centre point of electron beams driven by a TEM mode. Experimentally, it was found that the electron beam pointing variation of roughly $\delta y = 2.4mm$, yielding the uncertainty of the electron energy,

$$\delta E[MeV] = \frac{11630}{(\Delta y[mm] - 0.049)^2} \tag{6.10}$$

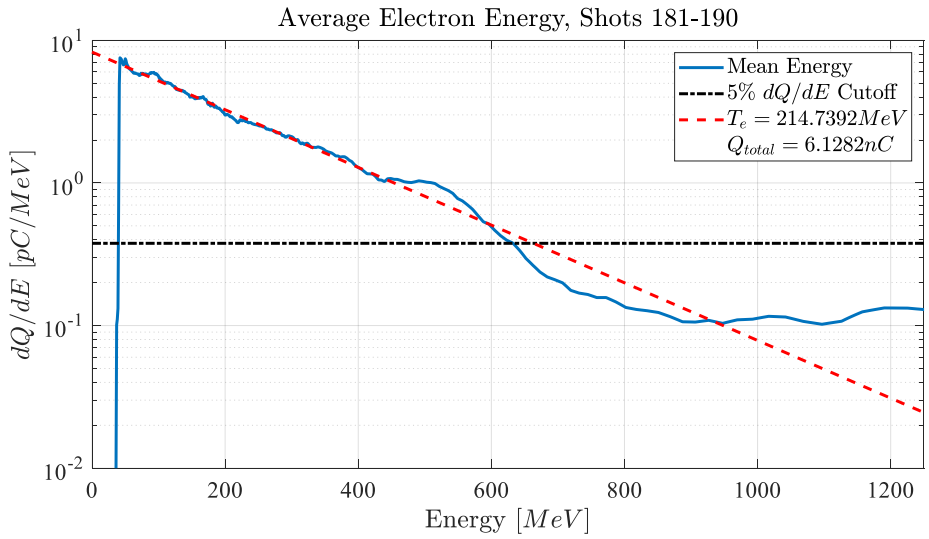

Figure 6.11: Example electron spectra for 10 shots from an LG10 drive beam. The red dotted line indicates the electron temperature, and the black dash-dot represents the 5% of max dQ/dE cutoff. The total charge detected is given in the legend.

To measure the electron energy from the spectral plots, the image is post processed to remove background and x-ray noise, and then interpolated using Eq.6.8. An example electron spectrum driven by an LG10 mode with electron density $n_e \approx 1 \times 10^{18} cm^{-3}$ averaged over 10 shots is given in Fig. 6.11. Here, an electron temperature has been fitted to the spectra using the formula,

$$\frac{dQ}{dE} \propto e^{-\frac{E}{k_B T}} \tag{6.11}$$

We find for the shots in Fig.6.11, the average electron temperature is $\approx 215 MeV$. The total charge from the shot is estimated by integrating over the spectrum, in which we find the estimated charge is approximately $6.13nC$. The error in the charge is found from the lanex calibration [26], the lanex imaging system errors and background subtraction uncertainty which are estimated to be on the order of 35%. To estimate the peak electron energy, the electron energy is taken at the point where it is found to be roughly 5% of the peak electron dQ/dE. For Fig.6.11, this is found to be $633 \pm 198 MeV$. The cutoff energy for various operating conditions is found and compared in the results section.

6.3.2 Electron Divergence

The electron divergence is measured using the same system as the electron spectrometer, except the spectrometer magnet is removed and the lanex is moved into the direct path of the laser using a remote control translation stage. The imaging system onto the lanex screen, and hence the relative calibrations remain the same. To compare the electron divergence to simulations, we are interested in measuring several components - this includes the electron beam spot size, the spot shape, and how many electron spots are present on the detection screen.

We can do this in one of two ways, the first of which is to overlap consecutive shots without modification. This gives a good estimate of the electron beam pointing stability, and overall divergence. The second is to overlap shots by aligning the peaks of electron spots over the top of each other. While this method removes the true nature of the shot to shot divergence, it allows us to estimate an average spot size and shape for the electron beam which may be more comparable to simulations.

Fig.6.12 shows the results for 10 shots driven by an LG_{-10} drive beam with an electron density of approximately $1 \times 10^{18} cm^{-3}$. The raw overlap of several spots is shown in tile a). Here we find multiple electron spots spread out in space, both from shot to shot pointing variation, but also from multiple electron spots arising from the interaction - likely due to filamentation and break up of the laser wakefield into smaller beamlets. By selecting the centre point of each electron spot, or the centroid of multiple electron spots, we can overlap them. This removes any shot to shot variation in the electron spots and makes them more suitable for a quantitative analysis. This can be seen in tile b) where we have been able to reduce the electron spot to a single spot with some outside noise as opposed to three spots.

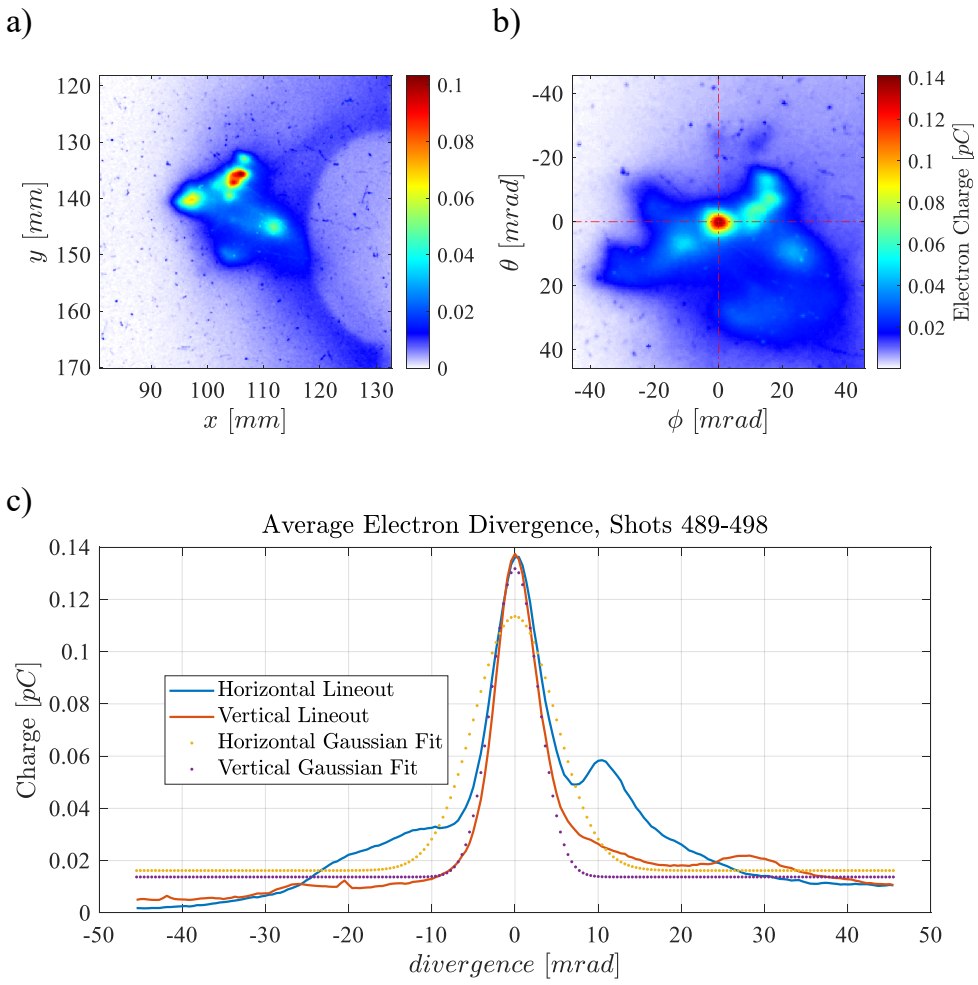

Figure 6.12: Example electron spot measurements. a) Raw output spots from 10 shots. b) Overlapped spot centroids, the red dash-dot lines indicate the lineout positions. c) Horizontal and vertical line-outs of b) fitted with Gaussian profiles.

Line-outs are then taken in both the vertical and horizontal directions of the electron spot as indicated by the red dash-dot lines in tile b). These are then plotted in tile c) in the solid lines and identified in the legend. Gaussian profiles are then fitted to each of the line-outs in order to estimate the full-width-half-maximum (FWHM) in each direction. For the Gaussian fits in Fig.6.12, we find FWHM values of $11.52mrad$ and $6.55mrad$ for the horizontal and vertical directions respectively. Also computed for each set of shots is the average number of electron spots observed, standard

deviation of the mean of the position of the electron spot centroid, and any rotation angle observed in the matched centroid spot. This is achieved by fitting an elliptical Gaussian to tile b).

6.3.3 X-ray detection

The betatron x-rays generated were measured using several diagnostics included x-ray CCD's and a lanex screen being imaged by an intensified CCD camera. However the only diagnostic to yield results with a good signal-to-noise ratio was the Greateyes x-ray CCD camera with a stepped filter. This diagnostic allowed for the determination of the betatron brightness, and the x-ray critical energy.

From chapter 4.5, we discussed the theory of betatron radiation emission and described the critical energy given by Eq's 4.52 and 4.54. The textbook synchrotron spectrum was plotted in Fig.4.23 b) showing the critical energy point in the emitted spectrum. Measuring an x-ray spectrum can be done in multiple ways including reimaging the x-rays onto a Bragg-crystal using a Kirkpatrick-Baez microscope [176, 52, 81], using zonal plates[76], or by using its transmission value through various thicknesses of a material such as aluminum.

In this experiment we use the latter technique using sheets of aluminum shielding of varying thickness. This is shown in Fig.6.13 tiles a) and b). Here, tile a) gives an exploded view of the filter stack placed in front of the x-ray CCD chip χ. The outermost layer, namely layer α is a $25\mu m$ sheet of aluminum mounted on a $4\mu m$ sheet of mylar, it covers the entire CCD and ensures no laser-light can reach the chip. The second layer β is a $180\mu m$ thick aluminum sheet and covers the left half of the chip. The third layer γ is made of vertical strips of aluminum of thickness $180\mu m$. The last layer δ is a horizontal strip of aluminum of thickness $90\mu m$. The layers stacked on top of one another creates a filter stack with 6 unique channels. This can be seen in tile b) of Fig.6.13. The corresponding layers as indexed in the figure are found to be $4\mu m$ of mylar plus the following thicknesses of aluminum: $1 = 385\mu m$, $2 = 205\mu m$, $3 = 475\mu m$, $4 = 295\mu m$, $5 = 205\mu m$, $6 = 25\mu m$, $7 = 295\mu m$, $8 = 115\mu m$.

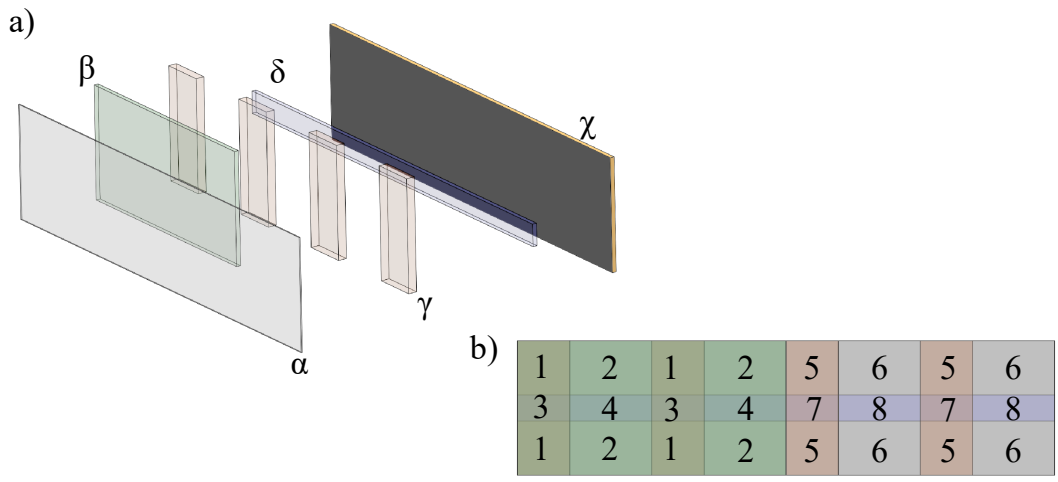

Figure 6.13: X-ray CCD filter stack diagram. a) Exploded diagram showing various layers of the filter: $\alpha = 25\mu m Al + 4\mu m$ Mylar, $\beta = 180\mu m$ Al, $\gamma = 180\mu m$ Al, $\delta = 90\mu m$ Al, and χ is the x-ray CCD. Tile b) gives the front view of the filter showing the different regions of thickness, each area thickness is given in the text.

The transmission of the betatron through each thickness of aluminum and Mylar is computed using Beer's law [49] and using the mass attenuation coefficient of aluminium [148]. Convolving the transmission spectra of aluminum with the transmission spectra of Mylar and the response function of the x-ray CCD allows us to derive a response curve for a given critical energy of the x-rays, and for the thickness of aluminum. For a given critical energy, the ratio of the mean signal in one channel in the filter to a reference channel (say the $25\mu m$ channel) is well defined and unique. Given that we have 6 channels on the filter, we can estimate the critical energy of a bunch of x-ray photons by comparing the mean signals in each channel to a reference channel and then comparing it to an analytic spectrum. Details of this method are given in the appendix.

From the critical energy of the x-ray beam and the number of counts in a given channel, it is possible to estimate the peak brightness of the beam. Typical units of brightness of a synchrotron x-ray source is given by,

$$brightness = \left(\frac{photons}{0.1\% BW \cdot srad} \right)_{peak} \tag{6.12}$$

where $0.1\%BW$ indicates the number of photons within a bandwidth of 0.1% of the critical x-ray energy.

6.3.4 Faraday Rotation

As shown in Fig.6.1, a second harmonic probe beam was used to measure any axial magnetic fields generated within the interaction via Faraday rotation. The probe was injected close to collinear to the main beam using a small mirror to ensure that it measured the axial magnetic field. The probe was focussed using two long focal length lenses ensuring a large focal spot. A fixed Wollaston prism was used upstream from the interaction area, while one in a remote controlled rotational mount as indicated by rw in Fig. 6.1. The prism in the rotational mount is adjusted such that the probe beam is maximally extinguished.

If the probe passes through a magnetic field within the plasma, the plane of polarization will rotate according to Eq. 4.60 that we will restate here,

$$\phi\,[deg] = 3.02\lambda[\mu m]^2 \int_0^d \frac{n_e[cm^{-3}]B[MG]}{10^{21}\sqrt{1-n_e/n_c}} dx[\mu m] \tag{6.13}$$

We can estimate the rotation of the probe by using a few estimated numbers. For example, we can use the laser wavelength of $800nm$, a plasma density of $3.5\times10^{18}cm^{-3}$, and an interaction length of approximately $1mm$. Using the model of the inverse Faraday effect from chapter 4, we can estimate the magnetic field generated by the laser of peak intensity $1\times10^{19}Wcm^{-2}$ and $\ell = 1$ with a self focussed beam waist of $9.4\mu m$ as given in Table 6.1. If we assume that the laser energy absorbed is on the order of 4%, we find a peak magnetic field strength of $160T$ on the laser axis. Plugging this into Eq.6.13, we find a polarization rotation angle of approximately $11deg$ per mm of interaction length. As the polarization is rotated by the Faraday effect, light can now be transmitted through the second Wollatson prism and be imaged into a camera.

While this polarization rotation angle is quite easy to measure, it assumes a constant magnetic field and a constant electron density throughout the interaction which is a poor assumption given dynamics of the laser wakefield. For a more suitable measurement, precise details of the interaction length, plasma density in the generated magnetic field regions, and good knowledge of the magnetic field shape are required. The plasma density and interaction length could be estimated using a high resolution interferometer imaging the plasma density. In reality the crossing angle of approxi-

mately 50 $mrad$ between the Faraday probe and the wakefield plasma would limit the interaction length with a 20 μm diameter magnetic field column to approximately 400 μm. The actual magnetic field shape and length would need to be estimated using simulation data, and likely a second diagnostic such as a spectrometer looking for splitting of the spectral lines from the Zeeman effect might be useful [124].

Alternatively, the probe could be made to be less collinear with the main drive laser - perhaps at a $45deg$ angle of incidence. This has the advantage of having a smaller sampling range in the propagation direction so may be less susceptible to chaotic magnetic fields as the plasma density ramps up and down, and in regions where the wakefield is unstable. However, the probe will sample both the axial magnetic field, and the radial/azimuthal magnetic fields in the plasma which would need to be de-convolved to obtain just the axial field. As the radial and azimuthal magnetic fields are typically asymmetric about the laser axis, this could be done by simply looking for a DC component of the polarization rotation.

While the Faraday probe was set up in the experiment, it did not result in any data in the end due to technical difficulties with the probe - mostly alignment and timing overlap issues.

6.3.5 Pulse Duration

A commercial second harmonic autocorrelator [159], was used to adjust the laser compressor to best compress and measure the laser pulse once in the morning and once in the afternoon before shots were taken. Ideally, the adjustment in the laser compressor between morning and afternoon should be small, however a drift was found day-to-day in the optimal compression position of the gratings. This drift is likely due to variations in temperature, humidity, and air pressure in the lab.

While we were able to measure and compress the laser optimally once in the morning and once in the afternoon, the optimal grating position was adjusted throughout the day based on the inferred drift direction, and the observed electron energies and total charge. The pulse duration was then estimated based on the relative distance between the gratings compared to the optimal separation. The optimal position of the gratings was estimated based on a linear fit of the best grating position as a function of time based on the morning and afternoon data points. The error in pulse duration using this method is estimated to be on the order of 30%.

6.4 Results

6.4.1 Electron Spectrum

Electron spectra was measured for a variety of backing pressures for four different OAM modes throughout the course of the experimental campaign. It was found that the results of the $L = -1$ mirror were not useful due to a defect in the mirror causing issues with the focal spot and the corresponding data. Given the size of the error bars, they will be omitted from the following plots as they obstruct information.

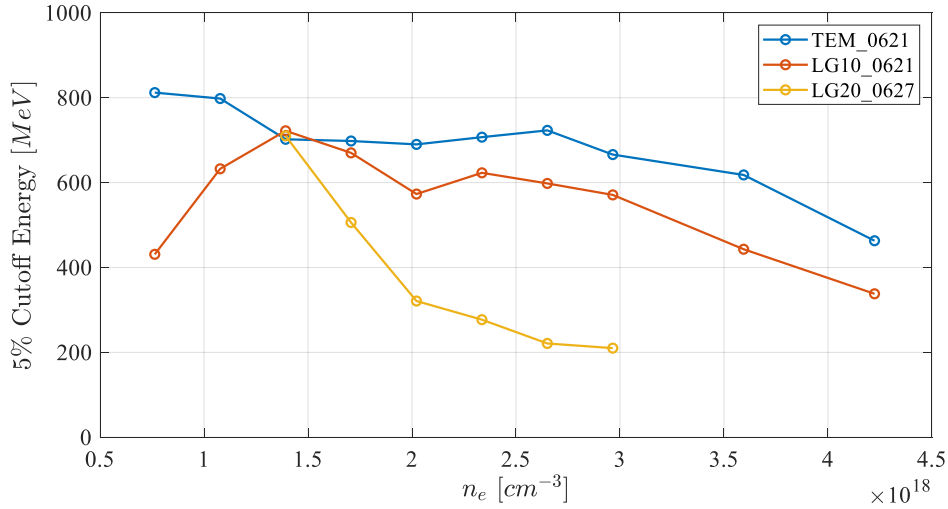

Figure 6.14: Peak electron ejection energies as a function of electron density for the Gaussian mode (blue), the Laguerre-Gaussian $\ell = 1$ mode (red), and the $\ell = 2$ mode (yellow). Error bars have been removed for clarity.

Fig.6.14 gives the results of the peak electron energy as defined in Fig.6.11 as a function of electron density for the $L = 0, 1$ and 2 modes. Here we find a consistent decrease of peak electron energy as the OAM of the beam is increased at densities above $1.5 \times 10^{18} cm^{-3}$. When the density is approximately $1.4 \times 10^{18} cm^{-3}$ we find the same cutoff electron energy for each of the modes. It is not clear at this stage why they all have an equivalent peak ejection energy at this density, but we could speculate that this density is the optimal density for laser guiding in the plasma for all the modes. In other words, it is likely due to extended propagation distances where we find a good balance between laser diffraction, and self-focussing in the plasma.

An issue with plotting the ejection energy as a function of density alone is that it ignores the fluctuations in the laser pulse duration and peak intensity. If we take the peak vacuum intensity of the laser from Table 6.1, and incorporate fluctuations in the laser pulse duration, and laser energy, we can estimate the peak intensity of the laser from shot to shot. Plotting the peak electron ejection energy as a function of the product of electron density and intensity shows a linear relationship for the three modes as shown in Fig.6.15. The lines of best fit to each of the electron ejection energies can be given by,

$$E[MeV]_{TEM} = -1.2213 \times 10^{-35} n_e I_{pk}[Wcm^{-5}] + 856.72 \tag{6.14}$$

$$E[MeV]_{LG10} = -6.1809 \times 10^{-35} n_e I_{pk}[Wcm^{-5}] + 869.02 \tag{6.15}$$

$$E[MeV]_{LG20} = -2.1029 \times 10^{-34} n_e I_{pk}[Wcm^{-5}] + 1135.7 \tag{6.16}$$

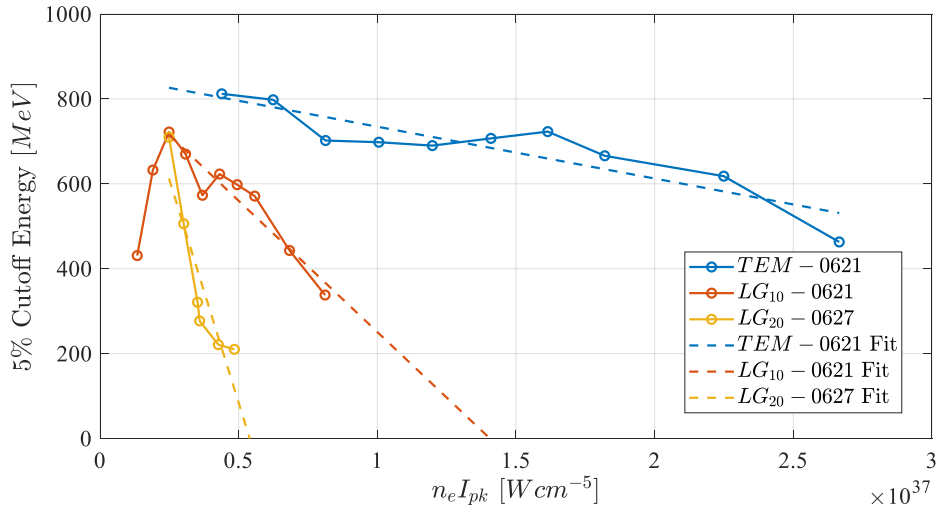

Figure 6.15: Peak electron ejection energies as a function of the product of electron density and peak laser intensity for the Gaussian mode (blue), the Laguerre-Gaussian $\ell = 1$ mode (red), and the $\ell = 2$ mode (yellow).

While these linear fits made to the peak electron energy are useful to estimate the scaling of electron energy for the various LG modes, they are only valid for a small region, and for the intensities used in this experiment. If the intensity is drastically changed from the values in Table 6.1, the operating regime of the wakefield accelerator

will change and the scaling laws will no longer be valid. Similarly, we notice there is a sharp drop off of peak electron energy as the density is further decreased past the optimal value of $1.4 \times 10^{18} cm^{-3}$. This is likely due to the laser no longer self focussing effectively in the plasma and diffracting quickly.

We can estimate the critical power for self focussing in plasma at $1.4 \times 10^{18} cm^{-3}$ using,

$$P_c = 17 \left(\frac{n_c}{n_e} \right) 4^{|\ell|} \frac{|\ell|!(|\ell|+1)!}{(2|\ell|)!} [GW] \tag{6.17}$$

From this we find the critical power for the $\ell = 0, 1, 2$ modes as 19, 76, and 151TW respectively. It is clear to see that while the estimated power available for self focussing is met for the $\ell = 0$ mode with the available power in the first Airy ring according to Table 6.1, we fall drastically short for the $\ell = 1$ and 2 modes, yet we are still able to accelerate electrons to the same energy as the $\ell = 0$ mode.

One possible explanation for this is that the asymmetry in the OAM modes is causing the threshold for self focussing to change from that estimate by Eq.6.17. To explore this further, three 3D simulations were run using the EPOCH PIC code and the parameters in Table 6.1 at a density of $3.5 \times 10^{18} cm^{-3}$. The simulations are very similar to those in Chapter 4 with a super-Gaussian plasma density to emulate the gas jet profile, albeit much shorter to reduce computational time. Additionally, the laser beam waist w_0 and the peak laser intensity have been set to the estimated self focussed value in Table 6.1.

Fig.6.16 gives a comparison between the simulated and measured spectra for electron densities at $3.5 \times 10^{18} cm^{-3}$ when driven by a Gaussian laser. Here we find an experimental electron energy cutoff of $723 \pm 259 MeV$ (as defined in Fig.6.11 as the 5% of peak dQ/dE), while the numerical estimate for the cutoff is approximately $300 MeV$. The simulation value disagrees within the error of the experimental result, likely as an underestimate from the simulation. The total charge is calculated by integrating under each curve and is found to be $6.8 \pm 2.2 nC$ for the experimental value, and $3.9 nC$ for the simulated value. While these values are slightly outside of the errorbars of each other, we argue that the simulation is likely an underestimate in both electron energy and flux due to the limited spatial length of the simulation. 2D simulations could be run over much longer interaction lengths resulting in better estimates of the electron energy and flux, but these cannot be done for the OAM modes as the helical wavefront will not be resolved in 2D.

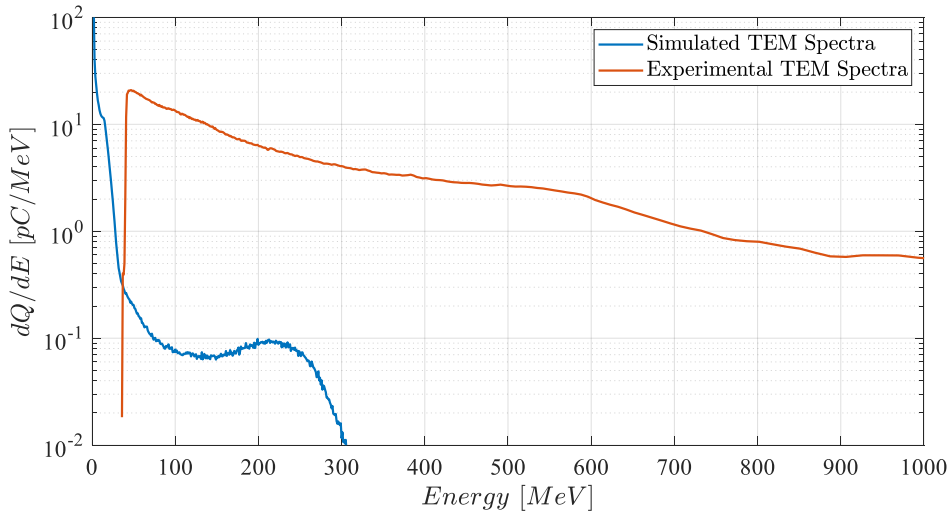

Figure 6.16: Simulated (blue) and experimental (red) electron spectra driven by a TEM Gaussian beam in a plasma density of $3.5 \times 10^{18} cm^{-3}$.

If we compare these electron energy values to the estimate found in Lu et.al. [96], we find an estimate for the peak electron energy of $737MeV$ assuming $100TW$ at focus, almost perfect agreement with the experimental result. If we consider the total power at focus available for self focussing to be $29TW$ as suggested in Table 6.1, we find an estimate of peak electron energy to be $488MeV$, closer to the simulated estimate. We conclude that a peak measured electron energy of $723 \pm 259MeV$ is therefore not unreasonable and in good agreement with analytic estimate, the simulated value of $300MeV$ is likely an underestimate. Larger 3D simulations are therefore needed to effectively simulate the TEM driven wakefield and to encapsulate all the 100TW of power at focus. Alternatively, 2.5D simulations [89] could be used that can effectively represent both the TEM and LG10 modes in a less computationally expensive simulation.

If we instead consider the comparison between experiment and simulation for the LG driven wakefield, we find a larger deviation as shown in Fig.6.17. Here we find the experimental electron cutoff energy to be $623 \pm 192MeV$, while the simulated spectra cuts off at approximately $80MeV$. Clearly this is a large discrepancy, and given the results from the TEM mode, we can infer that it is likely the simulations causing the discrepancy rather than the experimental data. If we instead consider the total charge in the electron beam, we find that the experimental value is found to be $5.3 \pm 1.7nC$ while the simulation value is found to be $2.7nC$.

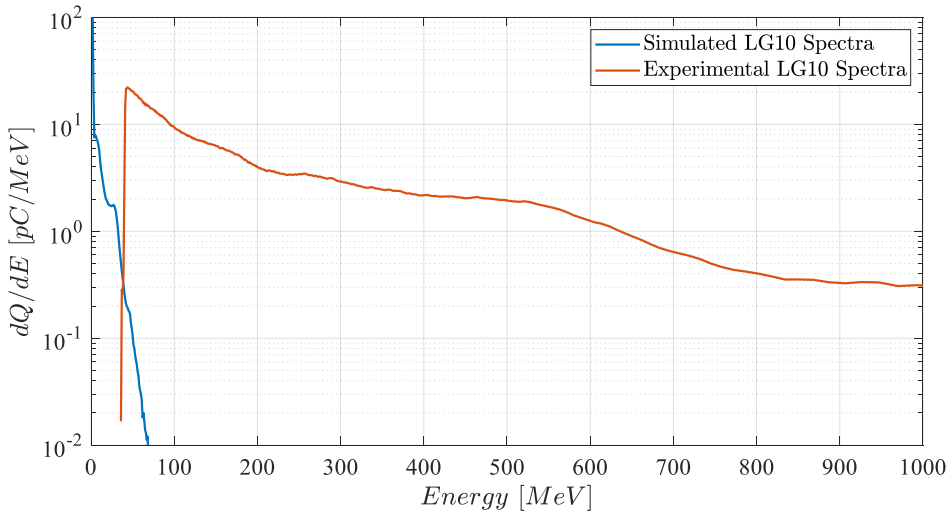

Figure 6.17: Simulated (blue) and experimental (red) electron spectra driven by a LG10 Laguerre Gaussian beam in a plasma density of $3.5 \times 10^{18} cm^{-3}$.

One reason for this discrepancy could be that the OAM mode is asymmetric as can be seen in Fig.5.17. A third simulation was run that emulated an asymmetric LG beam using the perturbation parameters given in Fig.5.21 tile b). The electron spectra from the symmetric and asymmetric OAM beams is given in Fig.6.18. Here we find a slight enhancement in the ejected electron energy for the asymmetric case increasing the ejected energy to roughly $90 MeV$. While this is still a fraction of the measured electron energy, it does indicate that if the beam is asymmetric, the electron energy can be enhanced.

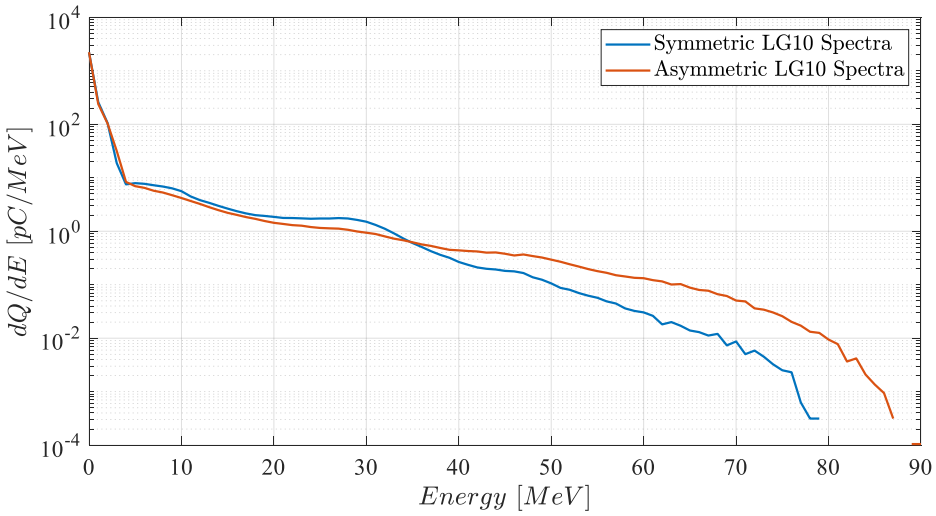

Figure 6.18: Comparison of electron spectra between a symmetric OAM beam (blue) and an asymmetric OAM beam (red) with perturbation parameters $\delta = 0.1, m = 1$.

The primary issue that we currently face with modelling how OAM beams can drive wakefield acceleration and other phenomena is how they relativistically self-focus, particularly if they are asymmetric. If the resultant self-focussed asymmetric beam is highly asymmetric it may be more suitable to describe it locally as a Gaussian beam near the hot spot.

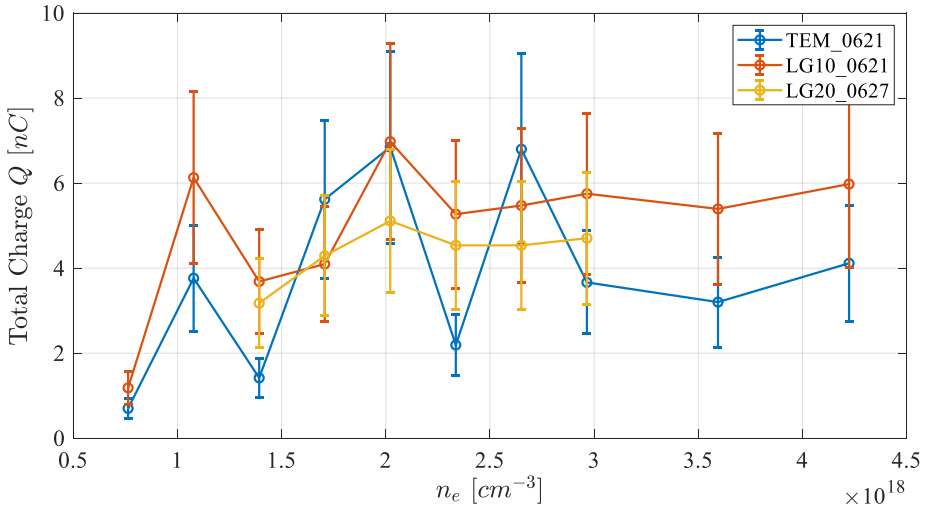

Figure 6.19: Total ejected charge from the wakefield as a function of electron density. The charge ejected from the Gaussian TEM mode are indicated in blue, while the charge ejected from the $L = 1$ and $L = 2$ modes are shown in red and yellow respectively.

If we consider the total charge ejected from the experimental wakefields as a function of density as found in Fig.6.19, we find that generally there is more charge ejected from the wakefield for the $L = 1$ beam as compared to the $L = 0$ beam. This is likely the result of having a larger accelerating cross sectional area for the OAM mode, while the asymmetry in the beam aids with injection into the wakefield bubble. The results from the $L = 2$ are not enhanced however, likely due to a lower intensity and a greater asymmetry than the $L = 1$ beam.

6.4.2 Betatron Spectrum

While we were unable to measure the betatron divergence during the campaign due to a poor signal-to-noise ratio and larger beam size than the on axis x-ray camera, we were able to measure the betatron brightness and critical energy of the spectrum. Fig.6.20 shows the critical betatron energy plotted as a function of the product of electron density and peak laser intensity.

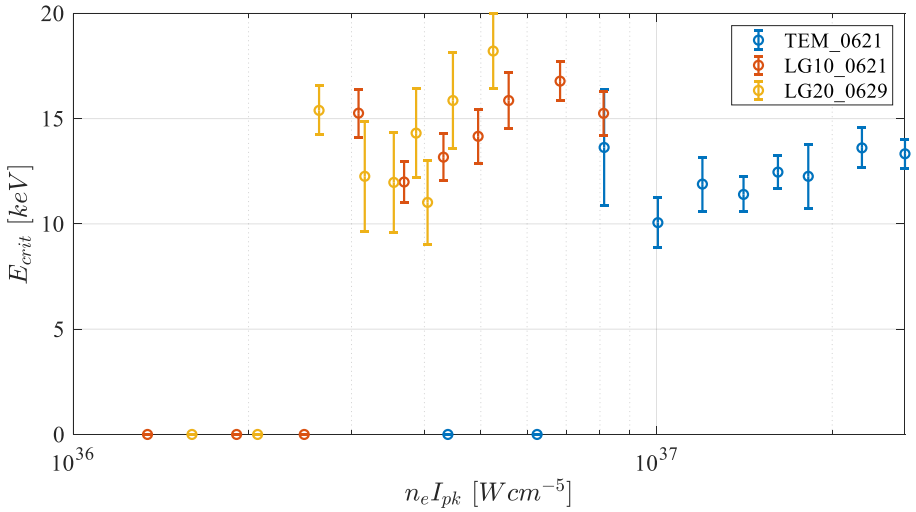

Figure 6.20: Betatron critical energy as a function of the product of the electron density and peak laser intensity. The Gaussian TEM driven betatron is shown in blue, while the betatron driven by the $L = 1$ and $L = 2$ beam are shown in red and yellow respectively.

Here we see a clear enhancement of betatron critical energy as the OAM of the laser is increased. The reasons for this increase in betatron critical energy is currently unknown, but is likely due to the presence of a background magnetic field generated by the inverse Faraday effect, or additional azimuthal magnetic fields in the ring bubble. As estimated in section 6.3.4, a background magnetic field of approximately $160T$ may have been generated from the $L = 1$ beam. According to the basic formula for the critical frequency of the synchrotron spectrum given in Eq.4.52 and [75],

$$\omega_c = \frac{3}{2}\gamma^3 \left(\frac{c}{\rho}\right) \tag{6.18}$$

the critical energy is inversely proportional to the electron orbit radius ρ, which in turn is inversely proportional to the magnetic field. Therefore the critical frequency is proportional to the magnetic field within bubble $\omega_c \propto B$ [104]. It is clear that the enhancement in critical energy must be a result of additional magnetic field, as we know that the average particle energy γ is overall lower for the OAM modes as observed in Fig.6.14.

While we find that the spectrum of the betatron is enhanced, we find that the total brightness of x-ray photons are reduced as the OAM in the beam is increased.

This is shown in Fig. 6.21 where the y-axis units are given as number of photons per 0.1% bandwidth per unit steradian. while the total charge is relatively comparable from each electron bunch according to Fig.6.19, we estimate that the total number of electrons available for betatron oscillations, and the total length for the electrons to oscillate may be decreased. Additionally, it could also be that the total divergence of the betatron emission increases with the OAM modes.

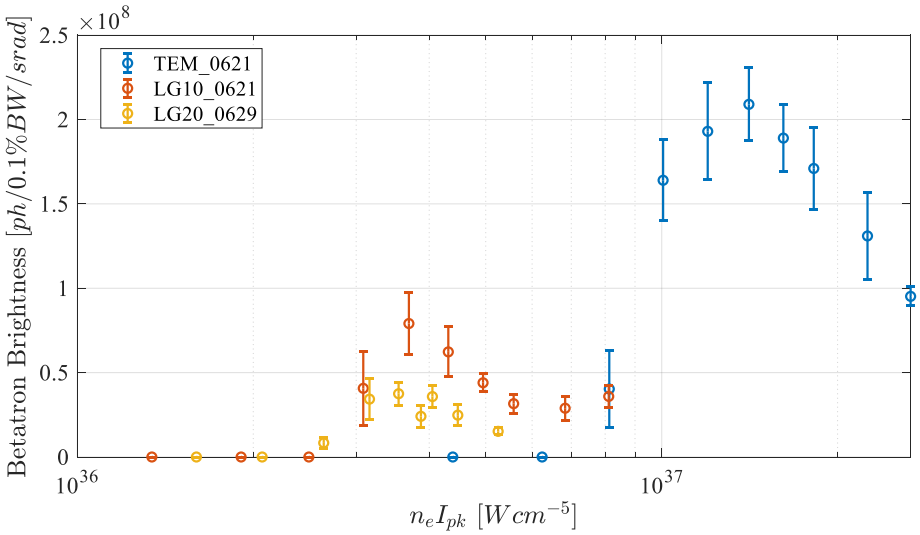

Figure 6.21: Peak betatron brightness as a function of the product of electron density and peak laser intensity. The Gaussian TEM driven betatron is shown in blue, while the betatron driven by the $L = 1$ and $L = 2$ beam are shown in red and yellow respectively.

The total number of photons emitted in a Gaussian driven wakefield can be estimated to be [82],

$$N_{ph} \approx N_e \frac{2\pi}{9} \frac{e^2}{\hbar c} N_0 \tag{6.19}$$

where N_e is the total number of electrons available for betatron oscillations and N_0 is the number of betatron oscillations each electron will undergo. In the 3D bubble regime, this can be estimated to be [111],

$$N_0 \approx \frac{\sqrt{2a_0}}{3\pi\sqrt{\gamma}} \left(\frac{n_c}{n_e}\right) \tag{6.20}$$

Here we find that the total number of betatron oscillations is proportional to the

peak laser intensity, $\sqrt{a_0}$. This implies that the number of x-ray photons scales as $N_{ph} \propto I^{1/4}$. In vacuum, we find that the peak intensity of the laser for an $L = 1$ beam is approximately 20% of a Gaussian beam and 9% for the $L = 2$ beam. This corresponds to a reduction in brightness of 67% and 55% respectively. After self focussing, the ratios of laser intensity may be different.

We find from Fig.6.21 that the peak brightness of the $L = 1$ beam and the $L = 2$ beam compared to the $L = 0$ beam is approximately 38% and 18% respectively. In addition to the reduction in betatron brightness from the reduced number of betatron oscillations N_0, the total number of electrons was likely reduced due to asymmetries in the beam. In this case, electrons on one side of the OAM ring may perform betatron oscillations where the laser intensity is larger, whereas on the opposite side, the bubble may be weaker and the corresponding number of electrons injected into the bubble may be less. While we did observe that the charge ejected from the wakefield was similar for the three modes, the average electron energy of each of the beams was different as indicated by Fig.6.14.

6.4.3 Electron Divergence

From the simulations in Chapter 4, we predicted that the ejected electron beam from the Gaussian drive beam should be a single electron spot with a narrow divergence. The electron beam from the $L = 1$ mode was slightly more complicated as shown in Fig.4.20b) with multiple spots and a very divergent beam in comparison to the Gaussian driven result. Experimentally, this was not always the case with the Gaussian driven wakefield often producing multiple electron spots and sometimes the OAM driven wakefield only producing a single electron spot.

Fig.6.22 gives the average number of electron spots found for each set of shots with error bars determined by the standard deviation of the mean of the number of spots. Here, we find that the $L = 2$ beam produced on average the most electron spots, while on average, the $L = 1$ beam produced a similar number of electron spots to the $L = 0$ drive. This was likely the result of beam filamentation and breakup in the plasma causing multiple electron spots in the $L = 0$ case and beam asymmetries in the OAM driven cases. The filamentation is primarily a result of a laser power significantly greater than the critical power in the plasma, but also as a result of inhomogeneities in the laser wavefront. These wavefront inhomogeneities can be a result of aberrations of the incoming laser wavefront after amplification and

compression, as well as focussing aberrations such as astigmatism and coma in the beam.

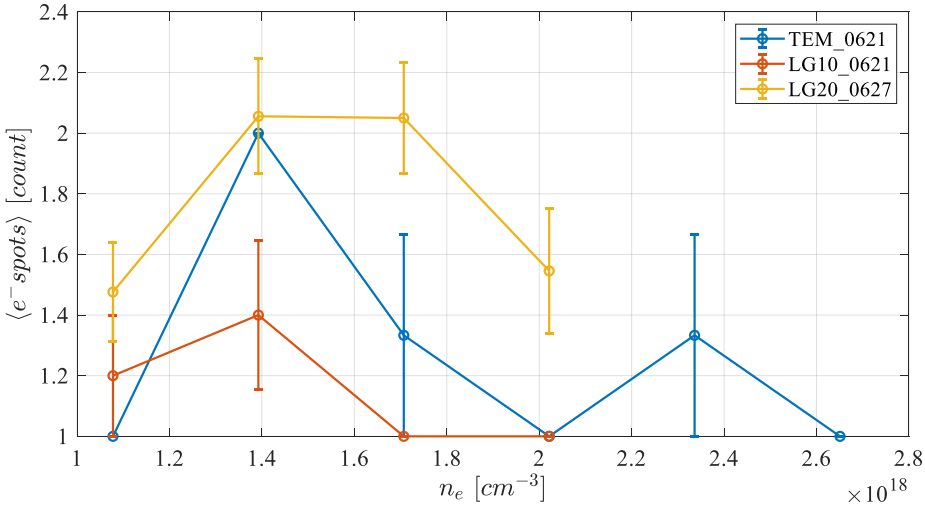

Figure 6.22: Averaged number of ejected electron spots as a function of electron density. The Gaussian TEM driven wakefield is shown in blue, while the wakefield driven by the $L = 1$ and $L = 2$ beam are shown in red and yellow respectively.

Given the multiple electron spots produced in each shot, and shot to shot electron pointing variation, it is possible to estimate the divergence of the spots relative to one another and give an root-mean-square (RMS) spread of the spots. This is useful for determining the repeatability of the wakefield, but doesn't give us information about the change in divergence and the distribution of the electron beams that results from the presence of OAM. While this shot to shot variation is of interest for a high repetition laser wakefield accelerator, it is not so useful in determining major differences in the electron divergence between Gaussian and OAM modes.

To try and better understand the divergence of the spots produced, we can overlap the centroids of each set of electron spots, which in theory could tell us the change in divergence of each set of electron spots as a result of OAM in the beam. We find that overlapping the electron centroids, as shown in Fig.6.12 b), can result in single electron spots, or multiple spots. We take both a horizontal or a vertical lineout of the spots and fit it with a Gaussian function. We opt however to primarily use the vertical Gaussian as it was found there was a significant electron tail to the right of the electron spot as a result of a fringing magnetic field from the spectrometer

magnet.

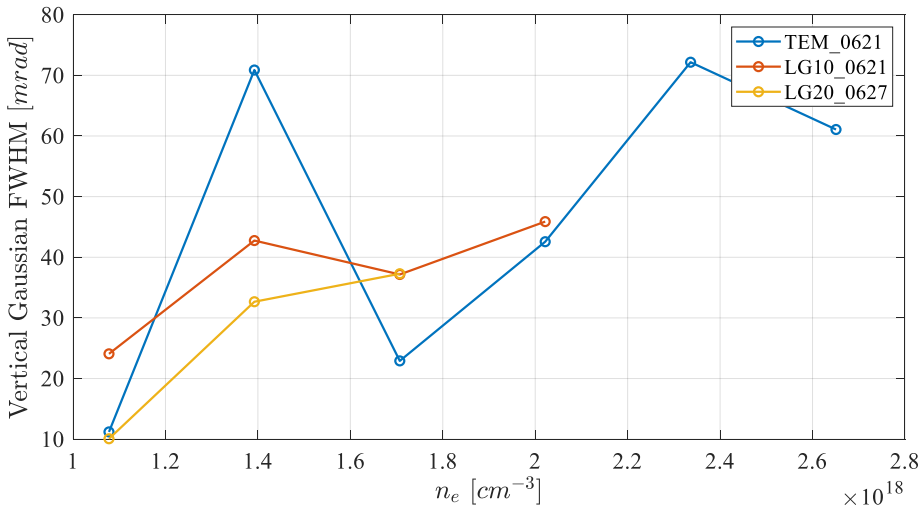

Figure 6.23: Full-Width-Half-Maximums (FWHM) of vertical lineouts of electron spots. The Gaussian TEM driven wakefield is shown in blue, while the wakefield driven by the $L = 1$ and $L = 2$ beam are shown in red and yellow respectively.

The full-width-half maximum (FWHM) values from the vertical lineouts are plotted in Fig.6.23. If we consider the TEM driven wakefield where filamentation was not observed according to Fig.6.22, ie. at $2 \times 10^{18} cm^{-3}$, we find the average FWHM to be on the order of $40 mrad$. This is in good agreement with the result found the simulations with an electron density of $3.5 \times 10^{18} cm^{-3}$ as shown in Fig.6.24. The simulations of a Gaussian driven wakefield did not produce multiple spots as the wavefront used in the simulation was perfectly flat. The breakup and filamentation of the Gaussian beam is in agreement with other observations [91, 70].

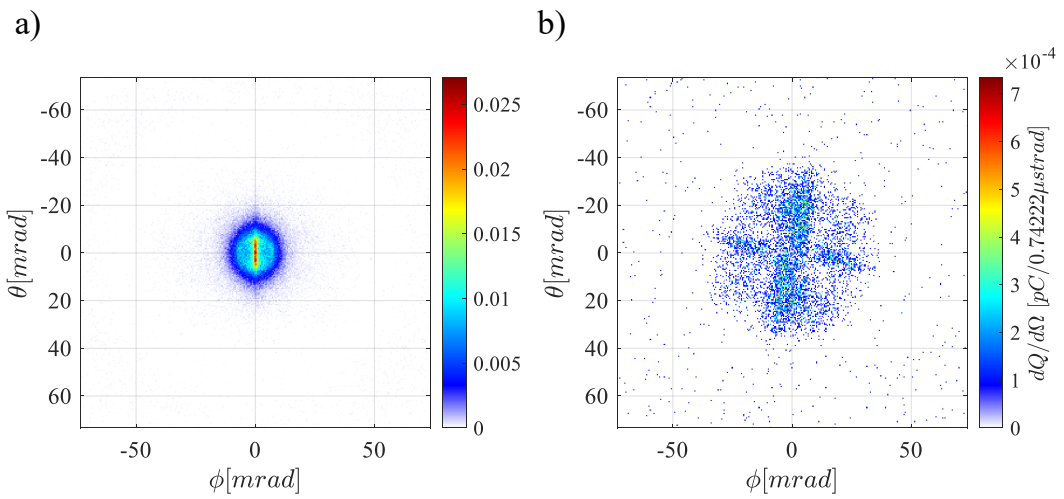

Figure 6.24: a) Simulated electron divergence driven by a Gaussian laser. b) Simulated electron divergence driven by a symmetric LG_{10} laser. Both simulations were run at an electron density of $3.5 \times 10^{18} cm^{-3}$ using the parameters in table 6.1.

The simulation result of a symmetric $L = 1$ driven wakefield is given in Fig.6.24 b). Here we see that the overall divergence of the beam is on the order of $60-70mrad$. This spot was not observed experimentally however, as the average FWHM of each electron spot observed was on the order of 20 - $40mrad$. To simulate this, two further simulations were run using asymmetric LG beams with perturbation parameters $\delta = 0.1$ and $m = 1$. The results for the asymmetric LG_{10} and LG_{-10} are given in Fig.6.25 a) and b) respectively.

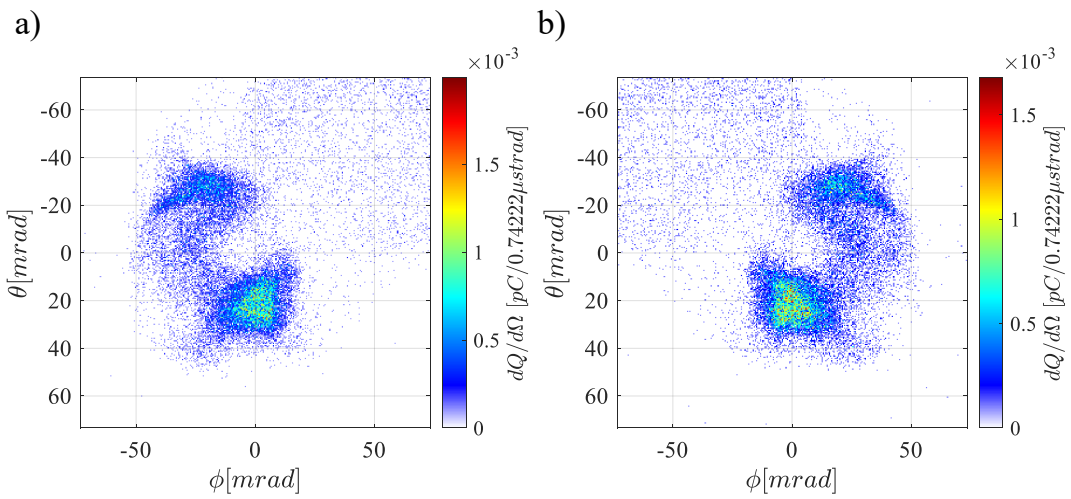

Figure 6.25: a) Simulated electron divergence driven by an asymmetric LG_{10} beam. b) Simulated electron divergence driven by an asymmetric LG_{-10} laser. Both simulations were run at an electron density of $3.5 \times 10^{18} cm^{-3}$ using the parameters in table 6.1.

Here we find that the large divergent spot from the symmetric driven wakefield breaks into two smaller spots, rotated one way or the other depending on the handedness of the OAM beam. This indicates two phenomena - clearly there is some coupling of OAM to the plasma as the rotation of the spot changes with the handedness of the beam, but also that the beam filaments due to the asymmetry in the intensity of the beam. We find that the divergence of the larger electron spot is on the order of $30 - 40 mrad$, in agreement with the result found in Fig.6.23.

While in the simulations we found that the asymmetry in the OAM beam only broke the electron beam into two spots, it indicates that a beam with a larger modulation parameter in the perturbation ($m \geq 2$) could result in more electron spots being generated as seen in the experiment.

6.5 Conclusions

In conclusion to the experimental investigation of OAM driven wakefield, we have found that overall electron ejection energy and divergence are not improved when increasing the OAM in a laser beam as expected from the PIC simulations in chapter 4. We did find however that the betatron critical energy was enhanced in the interaction

when increasing OAM content. We find this to be likely a result of an increased background magnetic field in the wakefield bubble. While we have not been able to show this increase in critical energy in simulations yet, we plan to pursue exploring the mechanism behind this enhancement in future work. This could possibly be done by implementing a new post processing routine for the radiation where the trajectory of electron is treated as either a set of circles, or as a set of parabolic arcs [157]. The radiation integrals could then be carried out analytically for each time step of the electron trajectory.

Although there was a slight increase in the critical energy of the betatron radiation, the overall flux of photons was however decreased possibly due to the reduction in intensity of the LG beams, an increase in betatron divergence, and due to the decrease of electrons contributing to the betatron radiation.

Chapter 7

Linearly Polarized Optical Vortices and the Inverse Faraday Effect

In this final chapter, we explore numerically one of the most interesting applications of OAM driven plasmas - the so called inverse Faraday effect. While we have briefly discussed the analytic model in Chapter 4, numerical simulations are required to verify the existence of an OAM driven axial magnetic field, and to characterize its spatial extent and temporal persistence.

We carry out some of the largest scale 3D PIC simulations to date to investigate the generation of large axial magnetic fields in the interaction of linearly polarized OAM modes with underdense plasma. It is shown that indeed large fields up to the order of 800T can be generated under suitable interaction conditions.

The material in this chapter has not yet been published, but has been presented in a seminar at Lawrence Livermore National Laboratory, as well as the upcoming American Physical Society Division of Plasma Physics Conference in 2020. A peer reviewed publication of the findings is expected shortly after completion of the thesis.

7.1 Introduction

While it has been studied in some detail analytically [5, 64, 88], and in the case of a circularly polarized beam experimentally [113], the inverse Faraday effect has yet to be demonstrated numerically or experimentally with linearly polarized laser pulses. It has been numerically studied for some exotic polarization OAM states (azimuthal and radial polarization) [117, 116, 21], with multiple overlapped OAM modes [141,

165], and with seeded magnetic fields [173] to name a few examples.

The primary reason for a lack of numerical verification of linearly polarized light driving the inverse Faraday effect is that the simulations need to be 3D, and have large spatial extents to effectively estimate interaction lengths, and persistence of the magnetic field. Another reason for this lack of observation is that in the equation derived in chapter 4 (Eq.4.68),

$$B_z = -\frac{2\bar{\gamma}^2 f_{abs}}{e n_e \omega c w_0^2} I(r,\ell) \left[\ell \left(\frac{w_0^2 |\ell|}{\bar{\gamma}^2 r^2} - 2 \right) + \sigma_z \left(\frac{|\ell|^2 w_0^2}{\bar{\gamma}^2 r^2} - 2 - 4|\ell| + \frac{4\bar{\gamma}^2 r^2}{w_0^2} \right) \right] \quad (7.1)$$

is a function of the fraction of the laser intensity absorbed per unit length f_{abs}.

It has been shown to first order that the a linearly polarized beam can transfer OAM to electrons, but when integrating over one laser cycle, the net angular momentum of the electrons is zero [116]. However, if the equations of motion are integrated numerically, it was shown in Chapter 3 that the absorption of OAM scales linearly with the energy absorbed by an electron via the ponderomotive scattering potential (Eq.3.19),

$$U = \frac{a_0^2}{2} m_e c^2 \quad (7.2)$$

This infers that the OAM absorption should scale as a function of a_0^2 and become a dominant mechanism of OAM absorption at relativistic intensities, independent of polarization state. This has been recently remarked by others [158].

There are many scaling laws to explore, including investigating OAM absorption both as a function of laser intensity and density, the scaling of magnetic field strength as a function of beam waist and OAM content, and to explore the extent and persistence of the magnetic field for each case. We are limiting ourselves at this point however to investigating the magnetic field spatial extent and persistence to a single density and single intensity for three linearly polarized OAM modes; the $\ell = 0, 1$ and 2 cases. Future work will explore the validity of Eq.7.1 as functions of the laser intensity and plasma density.

To explore the magnetic field generation, several sets of simulations were run using the EPOCH PIC code [8]. The simulation parameters having been summarized in Table 7.1 and are identical to the self-focussing simulations run in Chapter 4 and in Table 4.1. The simulation used a Lagrangian tracking box with a total length of $150\mu m$, and transverse size $40\mu m \times 40\mu m$. This ensured that interaction between the laser and the boundary conditions was minimal. The grid resolution was $37.5nm$ in

Table 7.1: Simulation parameters used for inverse Faraday effect.

Parameter	Value
Peak Intensity $[Wcm^{-2}]$	2.5×10^{19}
$n_e\ cm^{-3}$	3×10^{19}
$t_{FWHM}\ [fs]$	100
$w_{LG}\ [\mu m]$	9.6
$\lambda\ [\mu m]$	1
$T_e\ [keV]$	2.6

the propagation direction and $80nm$ in the transverse directions. The bulk helium electron temperature was then set to $2.6keV$ such that the Debye length would be $70nm$. While this is slightly lower than the transverse grid resolution, once the electrons interact with the laser pulse they will heat and the Debye length should be resolved. Tests of increasing the electron temperature found little change to the simulation result. It was found however that not resolving the Debye length in the simulation resulted in a reduction of the generated magnetic field. 2 particles per cell were used in the simulations resulting in a total number of 2 billion particles in the simulation.

Two sets of simulations were run, one with symmetric OAM modes, and the other with an asymmetric mode to test the stability of magnetic field generation in the presence of a realistic laser pulse.

7.2 Symmetric Drive Beams

To explore the validity of Eq.7.1, we have run two simulations using the parameters in Table 7.1 and Table 4.1 using linearly polarized beams with charges $\ell = 1, 2$. Simulations for $\ell = 0$ were run, but yielded no axial magnetic field as expected. Given the parameters in Table 7.1 we are able to compute the generated magnetic field if we know the laser energy absorbed per unit length. This variable can vary greatly depending on the electron density, intensity and OAM content in the beam. Fig.7.1 gives the laser absorption as a function of time, from which the absorption per unit length can be estimated for the symmetric $\ell = 1$ and $\ell = 2$ modes.

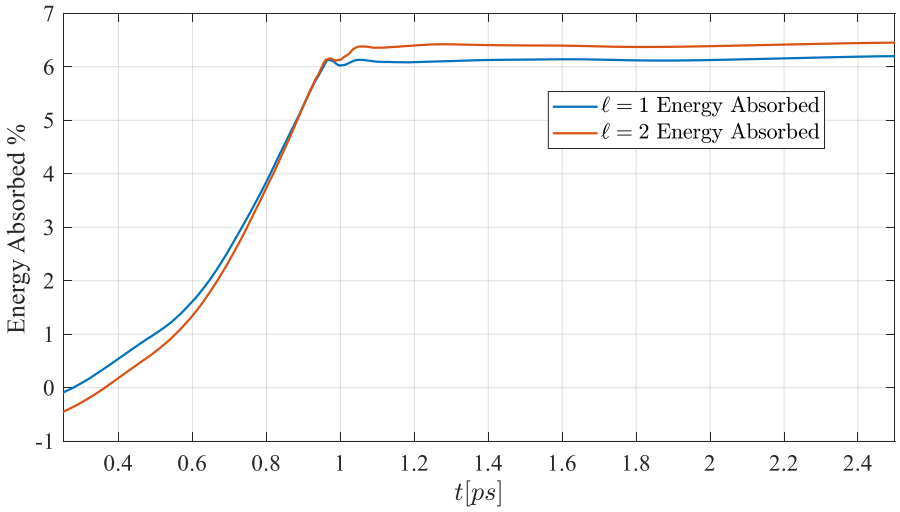

Figure 7.1: Fraction of laser energy absorbed verses time for the symmetric $\ell = 1$ (blue) OAM beam and the $\ell = 2$ (red) OAM beam

The simulation is set up such that the Lagrangian window tracks the laser pulse for $850fs$, after $850fs$ the Lagrangian window is frozen and the laser leaves the tracking box. The evolution of the magnetic field in the plasma and its subsequent decay can then be observed at that position. From Fig.7.1, we find that for the $\ell = 1$ mode, 6% of the laser energy was absorbed by the plasma until the laser left the simulation window, while for the $\ell = 2$ mode, 6.4% of the energy is absorbed. The length of the box was $150\mu m$ giving a temporal window of $500fs$ for laser absorption. Given that the time of laser absorption starts at approximately $300fs$, we assume that the 6% of absorbed laser energy accounts for the entirety of the magnetic field generated within the Lagrangian box.

Fig.7.2 shows the generated magnetic field from the $\ell = 1$ mode at $1ps$ of simulation time, almost immediately after the laser pulse left the simulation window. Here we see a long cylindrical magnetic field with an average peak strength upwards of $1000T$. Remarkably, the length of the magnetic field is on the order of $100\mu m$, at least 10 times that found in previous simulations [88, 173, 141, 117] and in good agreement with that found in the experimental findings of circular polarization driven inverse Faraday effect [113]. If we follow the laser in the Lagrangian window, instead of stopping to see the magnetic field evolve as in Fig.7.2, we find that the magnetic field generation slows and stops after the laser propagates further and starts to

diffract.

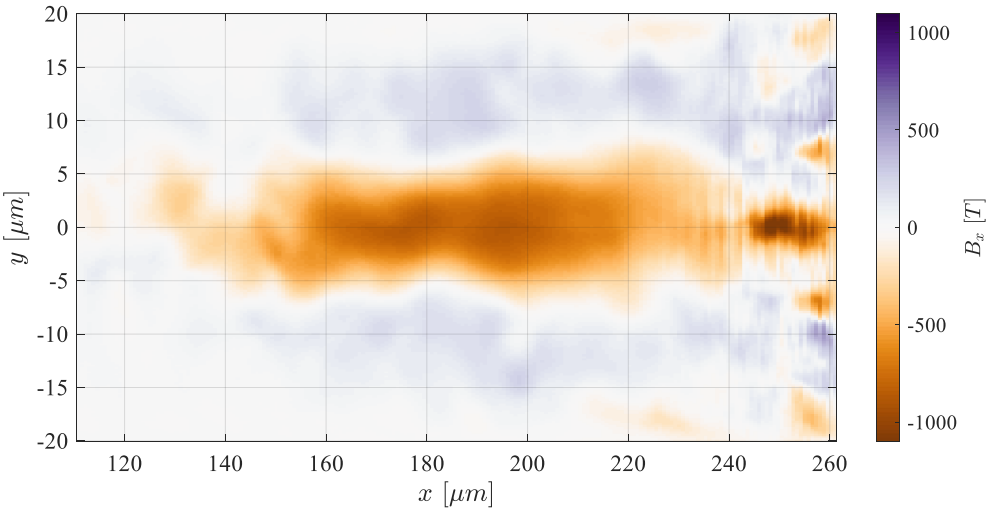

Figure 7.2: 2D slice of the axial magnetic field generated from the inverse Faraday effect while driven by an $\ell = 1$ OAM mode at time $1ps$.

We find that the Rayleigh length, given by $z_0 = kw_0^2/2$ is on the order of $200\mu m$ for a wavelength of $1\mu m$ and a beam waist of $8\mu m$ as given as the starting parameter for the entering laser beam in the simulation. This length is similar to the range over which the magnetic field was formed within the plasma. This indicates that the length of magnetic field may be limited to the range of self-focussing in the plasma, and may be extended using a plasma channel, or by fine tuning of the plasma density such that the laser self-guides over longer distances.

If we instead use a 3D isosurface to visualize the magnetic field, we can infer its overall shape and any features that may be present. Fig.7.3 gives the $-300T$ isosurface of the axial magnetic field at time $1ps$. It is clear to see the cylindrical structure of the field, but now we can see a slight twisting of the field due to a forward drift of the electrons as they orbit behind the laser pulse.

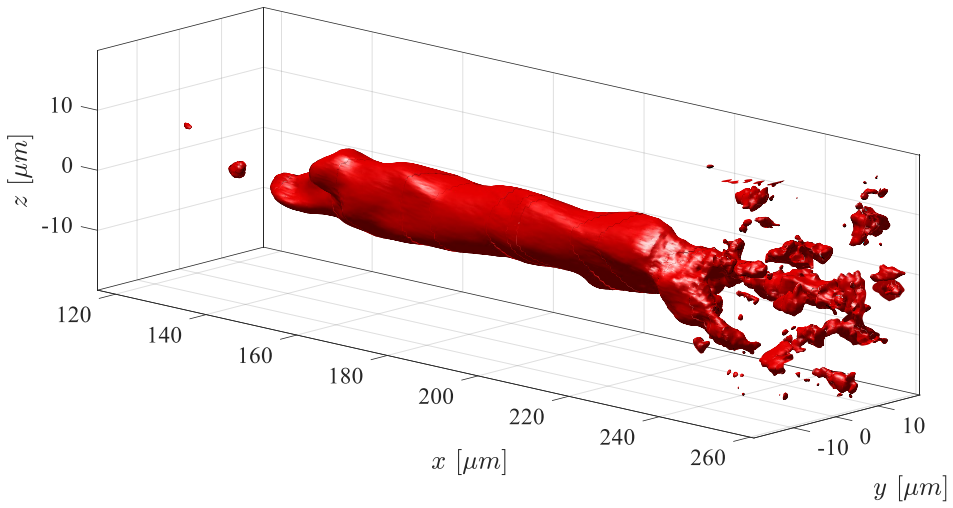

Figure 7.3: Axial magnetic field isosurface of value $-300T$ driven by an $\ell = 1$ mode at $1ps$.

The motion of the electrons to cause this corkscrew magnetic field must have both an azimuthal current density J_θ and a forward current density J_x. The J_θ component is clearly due to the OAM transfer to the electrons, while the J_x component likely comes from the laser ponderomotive force and wakefield acceleration. This corkscrew motion of the electrons and the magnetic field generation can lead to a screw pinch instability [51]. The screw pinch is essentially a hybrid of combining both the θ pinch and Z pinch configurations. Further work is needed to characterize this pinch generation in a laser driven plasma, and determine its dependence on OAM mode charge, plasma density, and laser intensity.

To compare the magnetic field strength to analytic calculations, we need to take radial line-outs of the magnetic field. Given the asymmetries in the magnetic field, we chose to average azimuthally each point along the radius, and then take the longitudinal average of the field between $x = 156\mu m$ and $x = 206\mu m$. Plotting the magnetic field profile as a function of radius over this range is given in Fig.7.4 in blue. Here we find good agreement between the theory shown by a red dashed line, and numerical result with the analytic result being a slight underestimate of the simulation.

This discrepancy is likely due to several factors, the first being the assumption that the electron density is not modified during the interaction in the analytic model. It is found from the simulations that often the electron density can be reduced by more than 50% due to the ponderomotive force sweeping the electrons away from the

interaction. Another reason is that the laser intensity likely self focussed to a higher intensity in the plasma. Both of these mechanisms would account for a stronger magnetic field according to Eq.7.1.

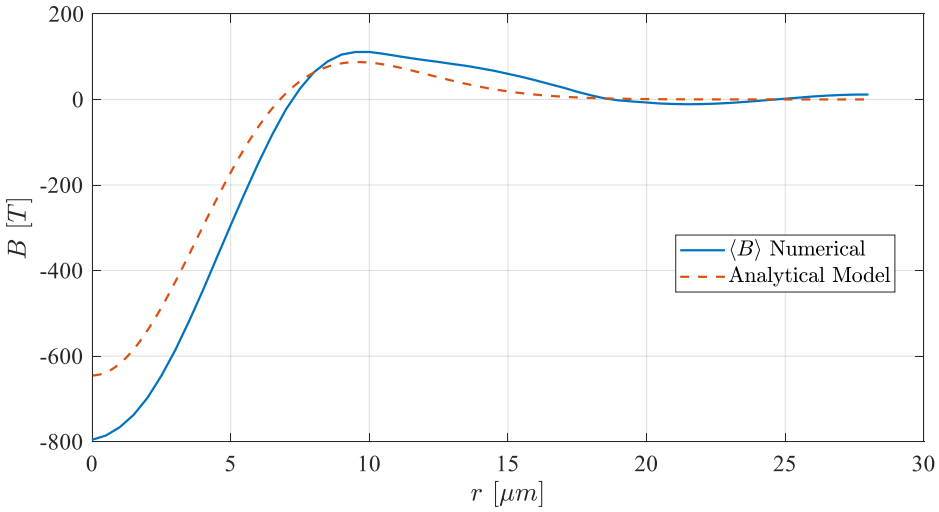

Figure 7.4: Comparison between the analytic and numerical model for the inverse Faraday effect driven by an $\ell = 1$ OAM mode at $1ps$. The numerical magnetic field is azimuthally averaged over 2π radians and longitudinally averaged between $156\mu m$ and $206\mu m$ according to Fig.7.2.

After the laser has left the simulation box, the magnetic field evolves in time. Fig.7.5 gives the magnetic field measured at $2.34ps$ in the simulation time. Here we see the magnetic field has lost significant strength compared to the values shown in Fig.7.2. Additionally, we find that the magnetic field now has kinks in it, likely a result from an instability in the screw pinch.

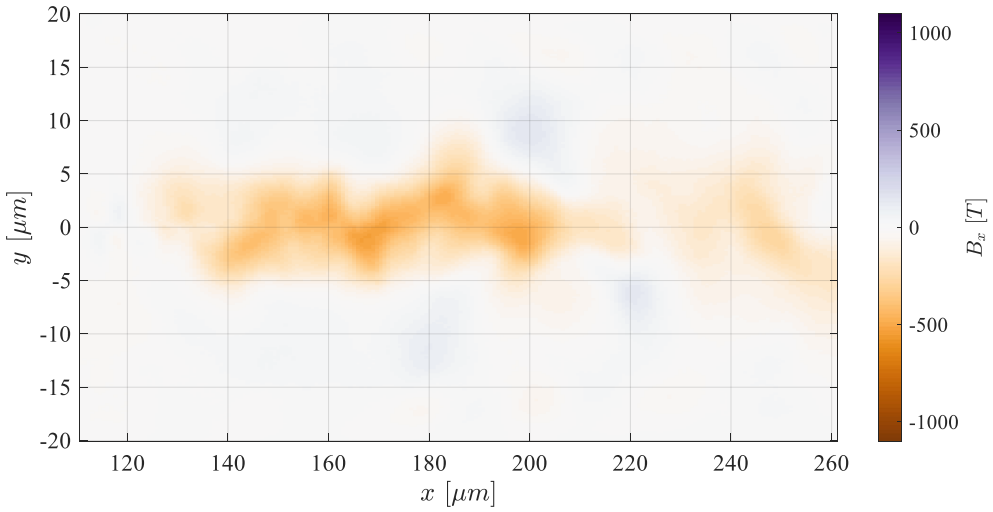

Figure 7.5: 2D slice of the axial magnetic field generated from the inverse Faraday effect while driven by an $\ell = 1$ OAM mode at time 2.34ps.

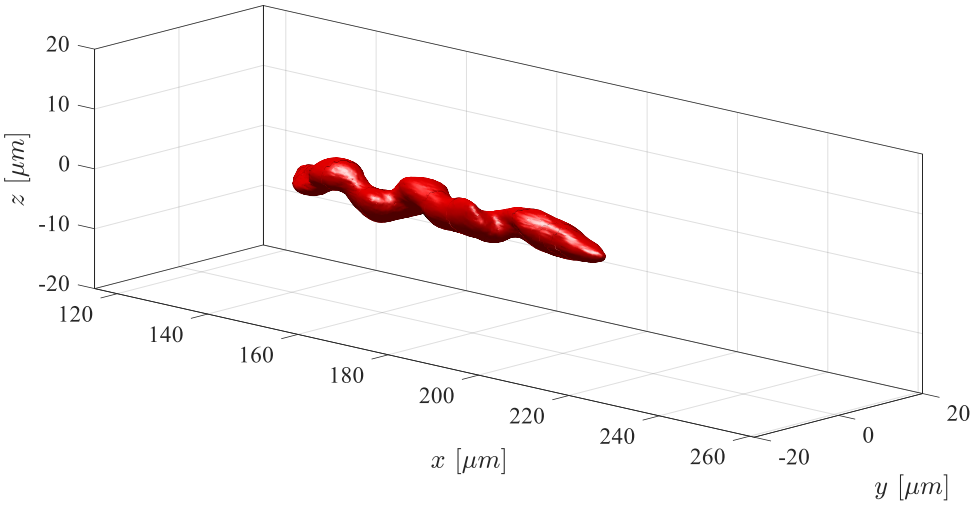

Figure 7.6: Axial magnetic field isosurface of value $-300T$ driven by an $\ell = 1$ mode at 2.34ps.

Imaging the isosurface of the magnetic field at 2.34ps is shown in Fig.7.6 and highlights the corkscrew kinking in the fields. Taking the average radial lineout of the magnetic field as before, and plotted in Fig.7.7, we find that the average peak magnetic field strength has decayed from a peak strength of $-800T$ to $-400T$ in a

time of 1.34ps.

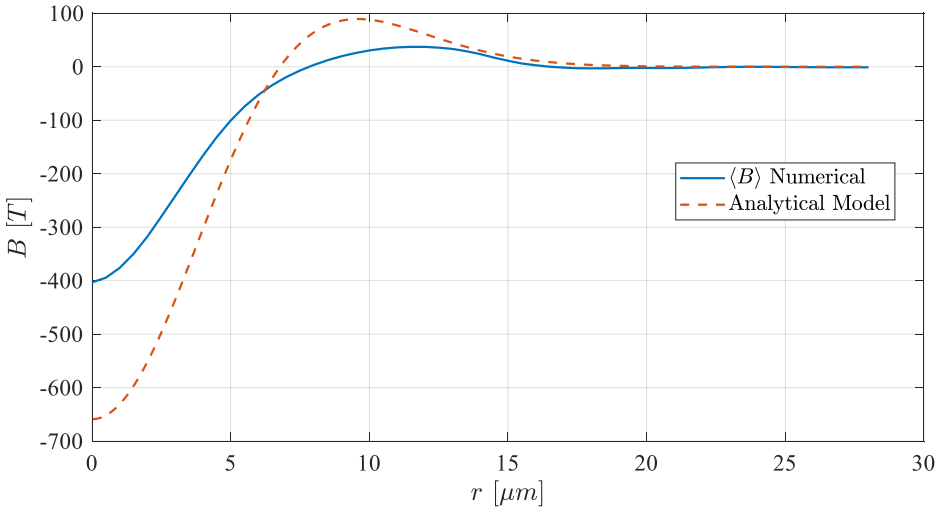

Figure 7.7: Comparison between the analytic and numerical model for the inverse Faraday effect driven by an $\ell = 1$ OAM mode at 2.34ps. The numerical magnetic field is azimuthally averaged over 2π radians and longitudinally averaged between 156μm and 206μm according to Fig.7.2.

Plotting the peak average magnetic field strength on axis as a function of time is given in Fig.7.8. We note that the peak field strength does not decay following a smooth curve but rather a noisy curve, likely a result of the magnetic field kinking from an instability. We have fitted an exponential decay curve to the peak field strength, and found a decay time on the order of 1.25ps.

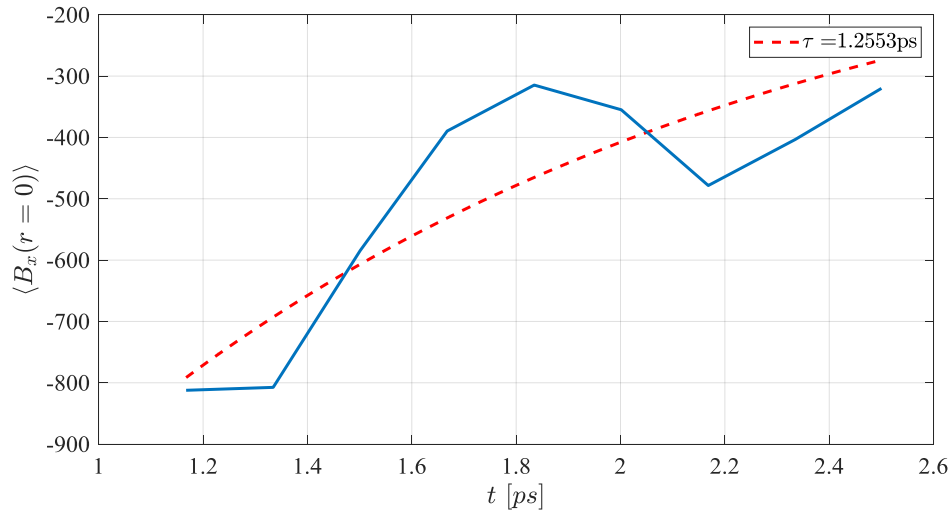

Figure 7.8: Peak average magnetic field at $r = 0$ as a function of time after the laser has left the simulation box. The red dotted line indicates the exponential decay fit with the constant given in the legend.

To explore the source of the magnetic field decay, we calculate the magnetic field diffusion time scale in the plasma using a simple first order estimate. Taking the magnetic field diffusion in the plasma [29],

$$\frac{\partial \mathbf{B}}{\partial t} = \frac{\eta}{\mu_0}\nabla^2\mathbf{B} \tag{7.3}$$

where η is the resistivity of the plasma. Approximating the Laplacian operator as a length scale squared L^2, we can rewrite Eq.7.3,

$$\frac{\partial \mathbf{B}}{\partial t} \approx \frac{\eta}{\mu_0 L^2}\mathbf{B} \tag{7.4}$$

Integration of Eq.7.3 is then trivial giving an exponential decay of the magnetic field strength given by,

$$\mathbf{B} = \mathbf{B}_0 e^{\pm t/\tau} \tag{7.5}$$

where τ is the decay time given by,

$$\tau = \frac{\mu_0 L^2}{\eta} \tag{7.6}$$

We can estimate the resistivity using the Spitzer model [29],

$$\eta \approx \frac{\pi e^2 \sqrt{m_e}}{(4\pi\epsilon_0)^2 (k_b T)^{3/2}} \ln \Lambda \tag{7.7}$$

where $\ln \Lambda \approx 10$ is the Coulomb logarithm and assuming a starting temperature of $2.6keV$. Using the scale length $L \approx w_0$, we find the decay time to be on the order of $10ns$. If we compare this to the value found in the simulation given in Fig.7.8, we find the numerical decay time is roughly 4 orders of magnitude faster than that of the magnetic field diffusion time. This could be due to several reasons, primarily that the electrons in orbital motion are extremely energetic with relativistic velocities and are not governed by normal thermal diffusion. The decay of the field could thus be accelerated as the electrons leave the simulation boundary. The screw instability may also cause of faster decay of the magnetic field through mixing and dissipation of the magnetic fields.

A simple way to explore this decay could be through plotting the energy stored in the magnetic fields as a function of time instead of using the peak field on axis. To estimate the energy stored in the magnetic field, we sum the square of the magnetic field in each cell in the simulation, and multiply it by necessary constants,

$$U_B = \sum_{i,j,k} \frac{B_{i,j,k}^2}{2\mu_0} \Delta x_i \Delta y_j \Delta z_k \tag{7.8}$$

This formula can only be used to estimate the magnetic field energy generated after the laser has left the simulation, and so is plotted from $1ps$ on in Fig.7.9. Here we find a much smoother decay in the magnetic field energy in the simulation, with a decay constant of slightly under $1ps$. Additionally we can estimate what fraction of the laser energy was converted into magnetic field energy. In this given simulation, approximately $9J$ was injected into the simulation of which slightly more than 0.1% is converted into magnetic field energy.

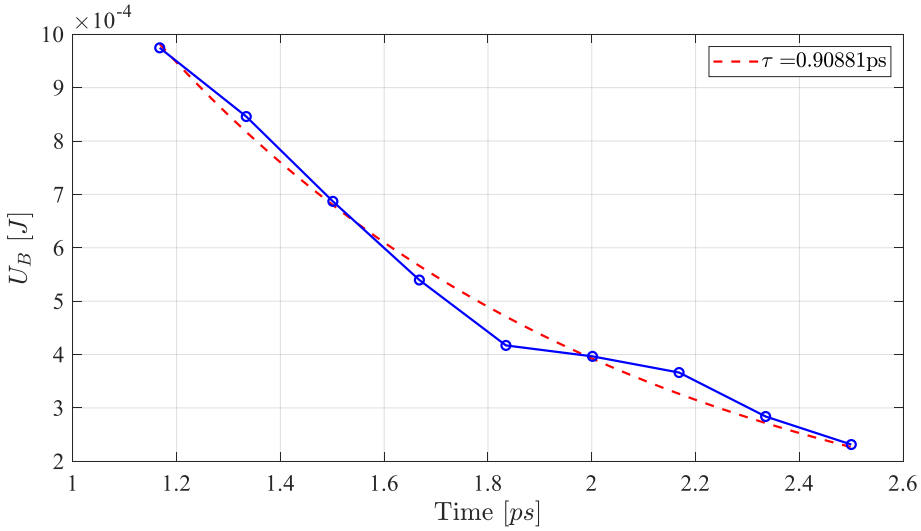

Figure 7.9: Total magnetic field energy in the simulation as a function of time driven by the $\ell = 1$ OAM beam.

We recall that only 6% of the laser energy was absorbed by the plasma in this given situation. Therefore, of the laser energy absorbed, roughly 1.7% was converted into magnetic field energy.

If we instead consider the case where the laser has twice the angular momentum, namely the $\ell = 2$ case, we find as expected, that for the same peak intensity the strength of the field is decreased. Fig.7.10 gives the 2D slice of the magnetic field driven by a $\ell = 2$ beam with peak intensity $2.5 \times 10^{19} W cm^{-2}$. We note that even though the total laser energy is higher ($12J$) to account for the decreased relative intensity of the $\ell = 2$ mode, the peak magnetic field is not as strong as that found in Fig.7.2.

Imaging the initial magnetic field at $1ps$ using a 3D isosurface is given in Fig.7.11. We again see the twisting of the magnetic field, but we do not see twice the number of twists per unit length from the topological charge of the laser as one might expect.

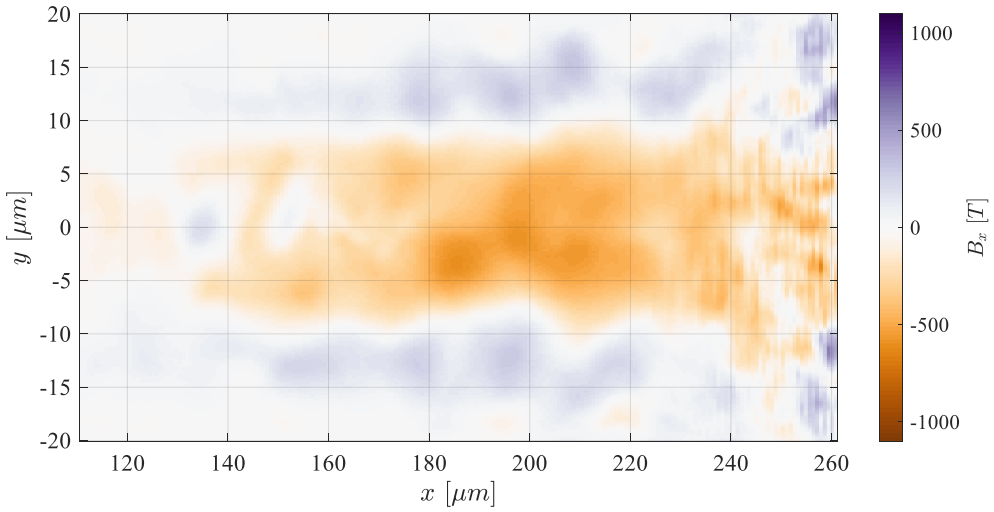

Figure 7.10: 2D slice of the axial magnetic field generated from the inverse Faraday effect while driven by an $\ell = 2$ OAM mode at time $1p$

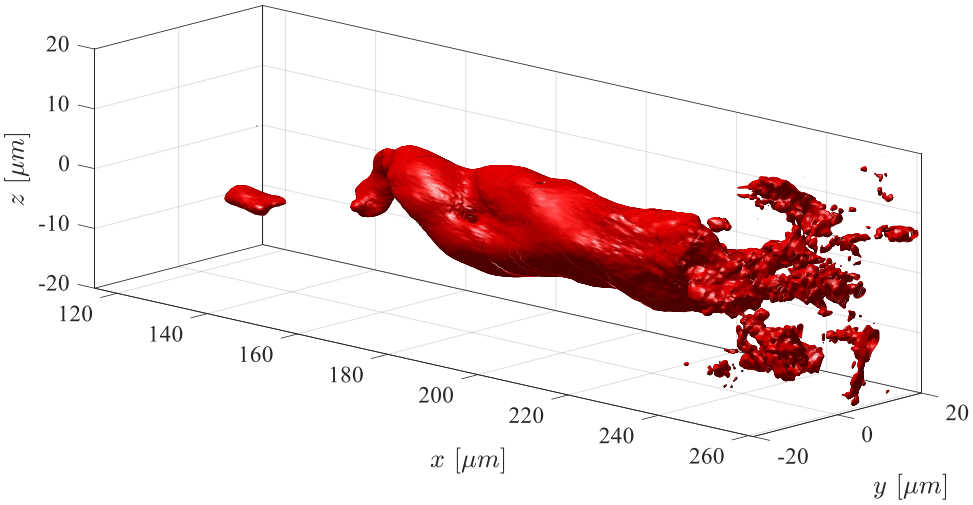

Figure 7.11: Axial magnetic field isosurface of value $-300T$ driven by an $\ell = 2$ mode at $1ps$.

Plotting average lineouts of the magnetic field as discussed previously from $x = 156\mu m$ to $x = 206\mu m$ and comparing to theory for the initial field at $1ps$ is given in Fig.7.12. Here we see good agreement between the theory and the simulations for radii larger than $10\mu m$. The theory predicts that for $r = 0\mu m$, the magnetic field

should be zero, however this was not found in the simulations. It was found that the magnetic field is reduced on axis, but does not go exactly to zero. The reason for this is likely due to the magnetic field evolving in space and time after its creation, essentially washing out some of the expected features. If one looks at Fig.7.10 between $x = 140\mu m$ and $x = 160\mu m$, we find the field does go to zero on axis, but in regions where the field is stronger, the null is not as prominent.

We also find that the peak magnetic field strength at roughly $r = 5\mu m$ is not as strong as theory would suggest. This is also likely due to some washing out the fields towards the axis, possible driven by an inward radial current as a result of charge separation from the ponderomotive sweeping out of the electrons.

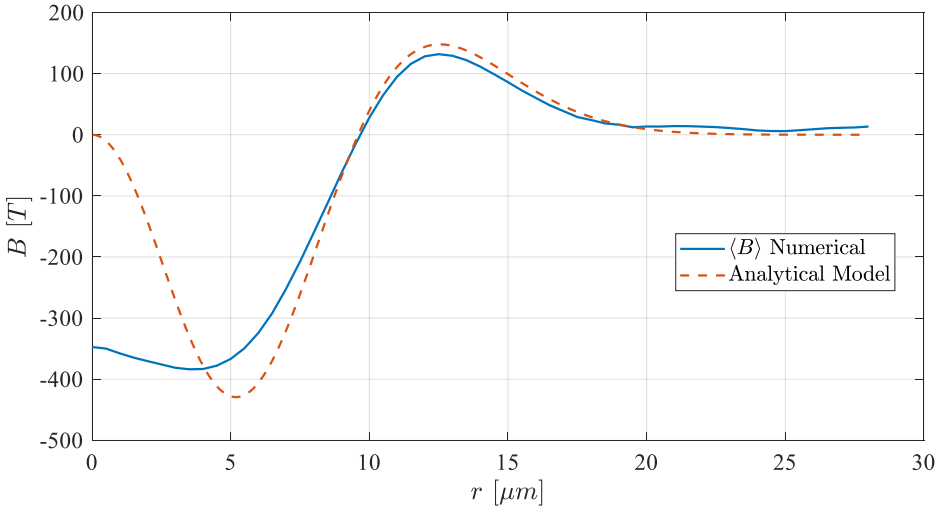

Figure 7.12: Comparison between the analytic and numerical model for the inverse Faraday effect driven by an $\ell = 2$ OAM mode at $1ps$. The numerical magnetic field is azimuthally averaged over 2π radians and longitudinally averaged between $156\mu m$ and $206\mu m$ according to Fig.7.10.

Progressing the simulation in time to $2.34ps$, we again plot the 2D slice of the magnetic field in Fig.7.13. We find as before, the magnetic field has decayed, but this time the relative decay has been much less than for the $\ell = 1$ case.

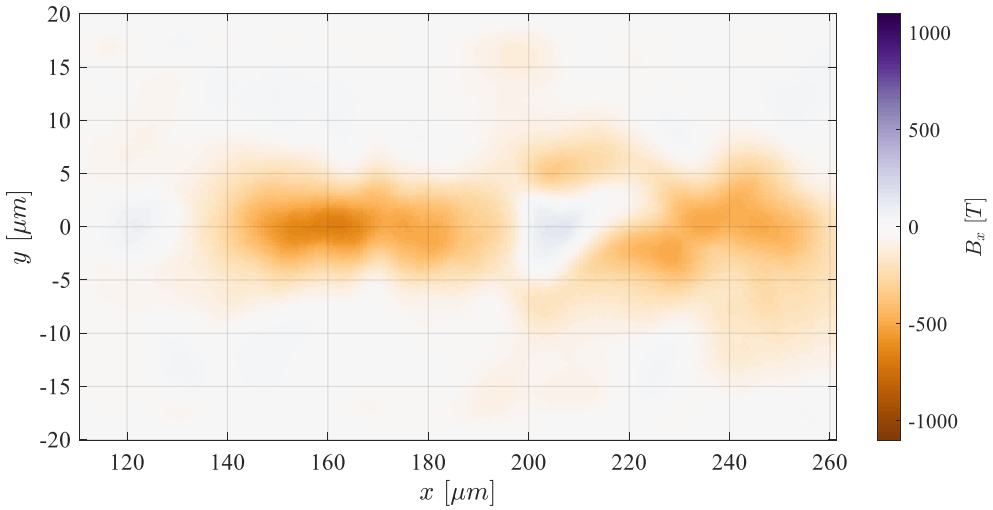

Figure 7.13: 2D slice of the axial magnetic field generated from the inverse Faraday effect while driven by an $\ell = 2$ OAM mode at time $2.34ps$

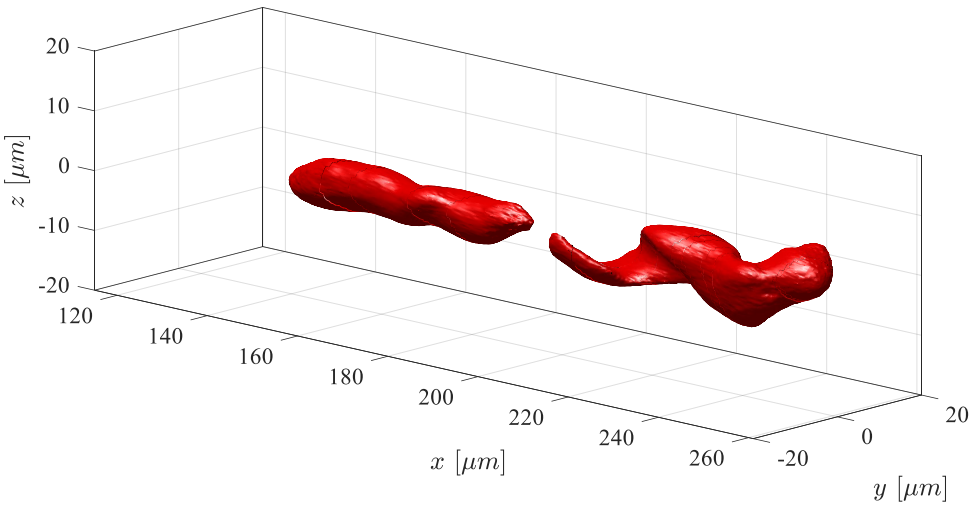

Figure 7.14: Axial magnetic field isosurface of value $-300T$ driven by an $\ell = 2$ mode at $2.34ps$.

The isosurface of the magnetic field in Fig.7.14 at $2.34ps$ shows the breaking up of the magnetic field, and some twisting of the field towards the front. Plotting the average radial lineouts of the magnetic field again from $156\mu m$ to $206\mu m$ can be seen in Fig.7.15. It is quite clear that the magnetic field has smoothed out considerably

with any features predicted by the model now washed out, and we are essentially left the result expected from an $\ell = 1$ driven magnetic field.

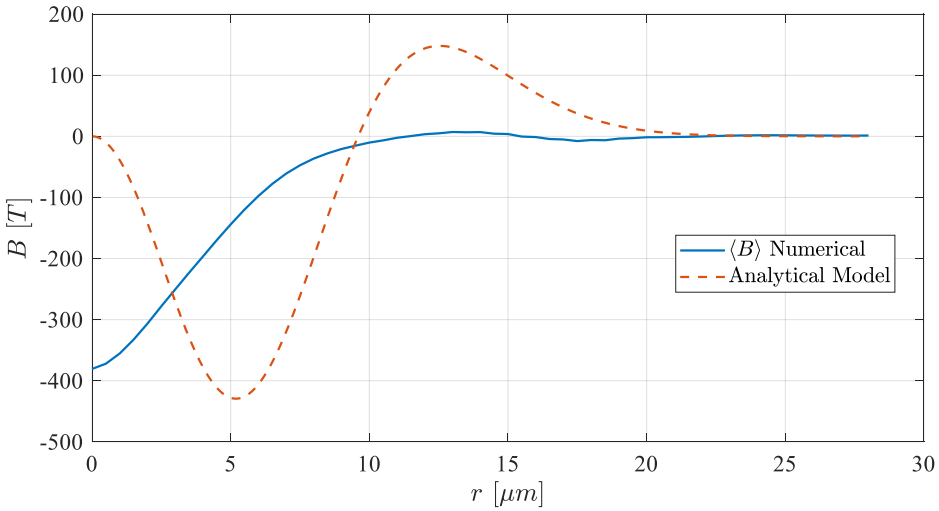

Figure 7.15: Comparison between the analytic and numerical model for the inverse Faraday effect driven by an $\ell = 2$ OAM mode at $2.34ps$. The numerical magnetic field is azimuthally averaged over 2π radians and longitudinally averaged between $156\mu m$ and $206\mu m$ according to Fig.7.13.

Interestingly, the peak strength of the magnetic field has not decayed at all, but rather translated and confined itself to the axis. While the peak magnetic field strength has remained almost constant as time has progressed, the energy within the magnetic field must have decreased as the effective area of the field has shrunk as the radius gets smaller. While we could plot the peak magnetic field strength as a function of time, this may not be the best variable to track as the peak field may not be changing over some periods of time, however the total energy in the fields is continuously decaying.

We therefore plot the total magnetic field energy in the simulation as a function of time in Fig.7.16. Fitting the decay using a exponential as we did in Fig.7.9, we find the decay time has been more than doubled from $0.91ps$ for the $\ell = 1$ case to $2.31ps$ for the $\ell = 2$ case. The reason for this increase in magnetic field persistence is not currently clear, but likely could be related to less kinking from the screw type instability reducing the scattering of electrons and mixing of the field components.

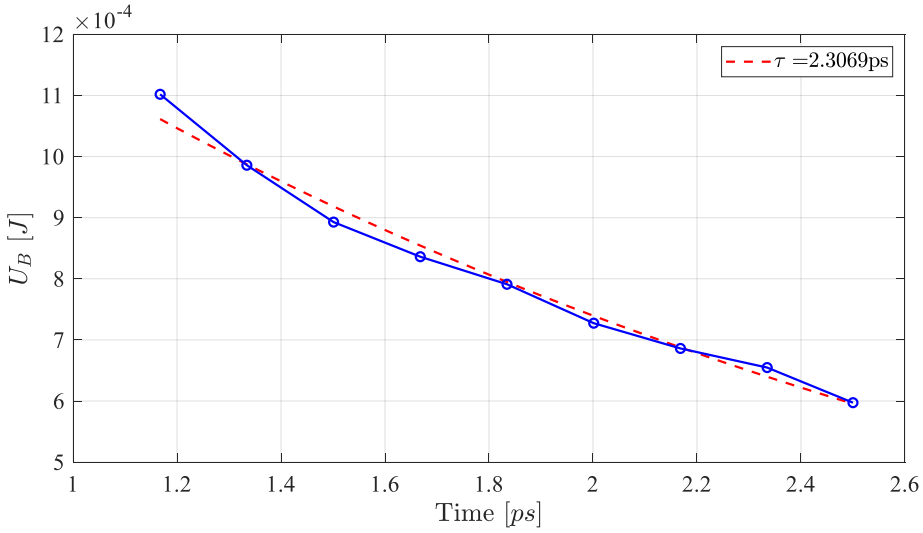

Figure 7.16: Total magnetic field energy in the simulation as a function of time driven by the $\ell = 2$ OAM beam.

It has been shown previously that in θ-pinch configurations, an increase in the azimuthal mode number leads to an increase in the instability threshold [50]. In this work, the $\ell = 1$ wobble instability is observed in the θ pinch configuration, but appears to be more suppressed for $\ell = 2$. In this case, using an $\ell = 2$ mode to drive magnetic fields may be more suitable if longer lived fields are desired, even though the peak magnetic field strength is weaker.

7.3 Asymmetric Drive Beams

Another important question regarding magnetic field generation driven by donut OAM modes is if the mechanism still works for real, asymmetric beams like those generated in Chapter 5. To do this, a single simulation using a perturbed LG_{10} beam was used with perturbation parameters $\delta = 0.1, m = 1$. Decomposing this perturbed OAM mode into 3 LG modes, we find the constituent modes are composed of an $\ell = 1$ mode comprising 99.5% of the energy, an $\ell = 2$ mode accounting for 0.2% of the energy and an $\ell = 0$ mode also accounting for 0.2% of the energy. The missing 0.1% is accounted for from rounding errors and additional LG p modes.

To first order, we can assume that each of the constituent modes couple to the plasma independently of each other and each generate their own independent mag-

netic field. In this sense, we expect the reduction of the magnetic field generated in Fig.7.4 to only be reduced by 0.5%. Considering the null contribution from the $\ell = 0$ mode and the zero magnetic field on axis from the $\ell = 2$ mode, there should essentially be no change to the magnetic field. This assumption may be valid if the perturbation is small, but for larger values of δ and m, we may expect more drastic modification of the magnetic field.

Fig.7.17 gives the laser energy absorbed by the plasma as a function of time for the symmetric $\ell = 1$ (blue) and asymmetric $\ell = 1$ (red) modes. We see a slight difference between the two, with the energy absorbed by the plasma from the asymmetric mode about ($\approx 0.05\%$) less than the symmetric case.

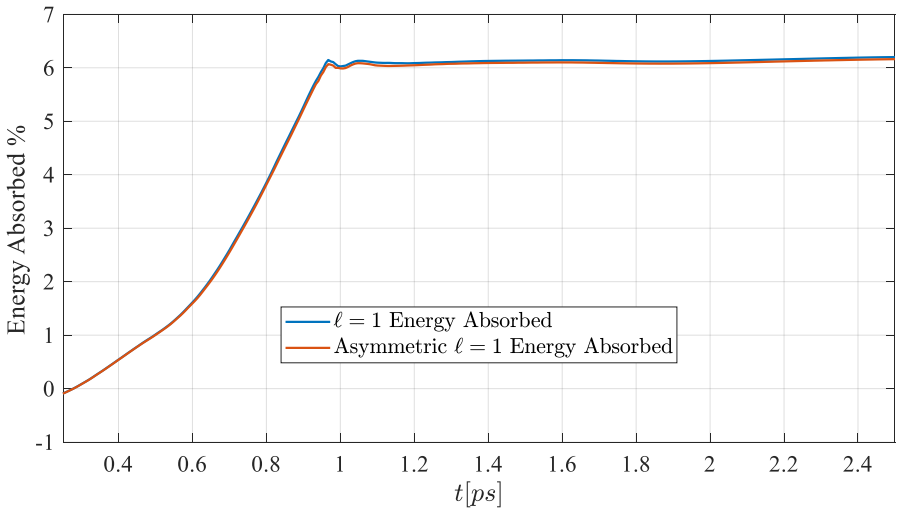

Figure 7.17: Fraction of laser energy absorbed per unit time for the symmetric $\ell = 1$ (blue) OAM beam and the asymmetric $\ell = 1$ (red) OAM beam

Plotting the 2D slice of the magnetic field at $1ps$ highlights a slight bend downwards of the magnetic field not present in Fig.7.2. We do however note the the peak magnetic field strength looks similar, if not the same as the symmetric driven case.

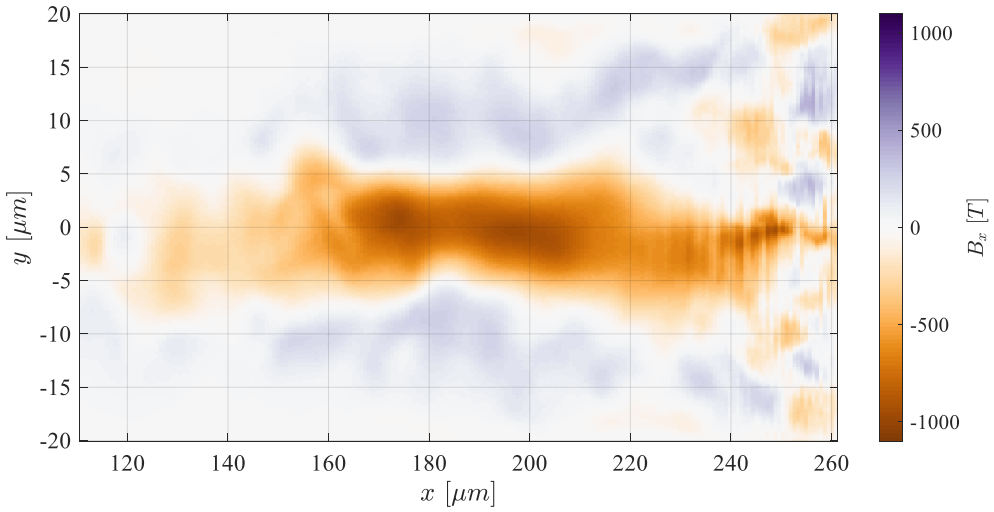

Figure 7.18: 2D slice of the axial magnetic field generated from the inverse Faraday effect while driven by an asymmetric $\ell = 1$ OAM mode at time $1ps$.

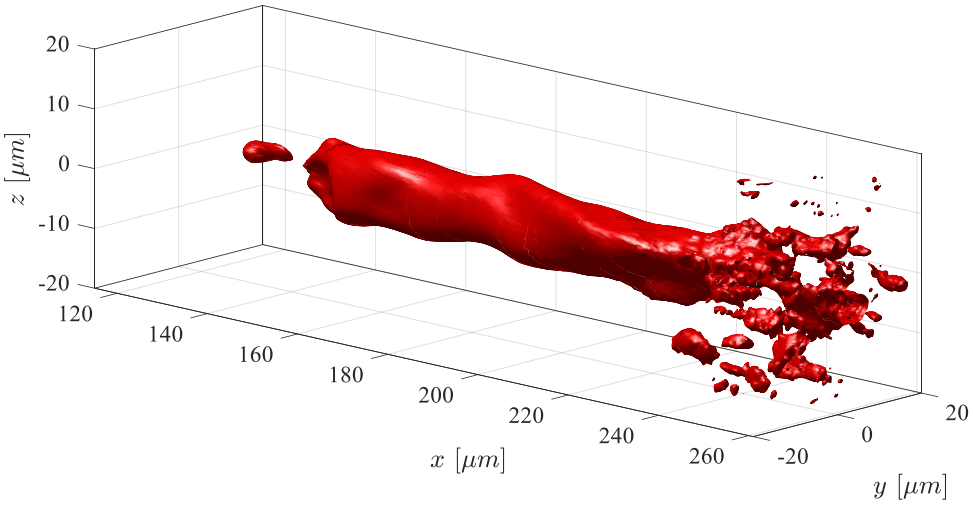

Figure 7.19: Axial magnetic field isosurface of value $-300T$ driven by an asymmetric $\ell = 1$ mode at $1ps$.

The isosurface of the $-300T$ magnetic field at $1ps$ is plotted in Fig.7.19 yielding an almost identical result to that in Fig.7.3. Plotting the average radial lineout is given in Fig.7.20 and compared to the symmetric case. Here, the blue line represents the magnetic field lineout of the symmetric case, the red is the asymmetric case and

the yellow dashed line is the analytic model.

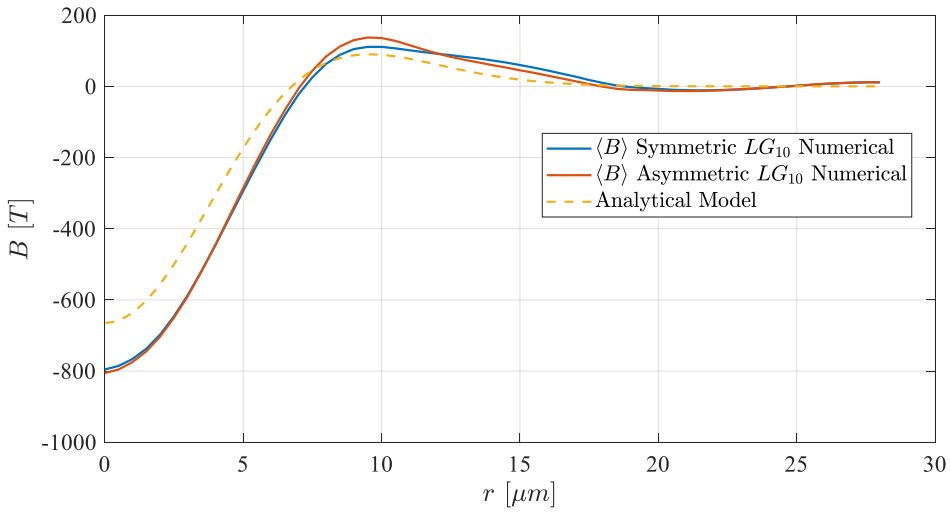

Figure 7.20: Comparison between the analytic and numerical models for the inverse Faraday effect driven by a symmetric $\ell = 1$ OAM mode (blue), and an asymmetric $\ell = 1$ OAM mode (red) at $1ps$. The numerical magnetic field is azimuthally averaged over 2π radians and longitudinally averaged between $156\mu m$ and $206\mu m$ according to Fig.7.18.

We find that the two numerical magnetic field lineouts overlap almost exactly with the asymmetric case being slightly stronger on axis. This is a good verification that to first order, the asymmetric beams created in the lab can create strong magnetic fields with little to no hindrance to the field.

While it was found that increasing the ℓ number of the OAM beam increases its decay time, we do not expect a significant change in the magnetic field decay time when using an asymmetric mode. Fig.7.21 gives the decay curve of the field and has been fitted with an exponential fit. Here, we find the field has a decay time of $1.14ps$, slightly shorter than the fit of $1.26ps$ found in Fig.7.8. We do however find that the decay of the field in the simulation is much less noisy as compared to the symmetric driven case. This could be a reason for the discrepancy in the decay times, and is likely due to less severe pinching from the wobble instability [50], which may be suppressed by the asymmetric mode.

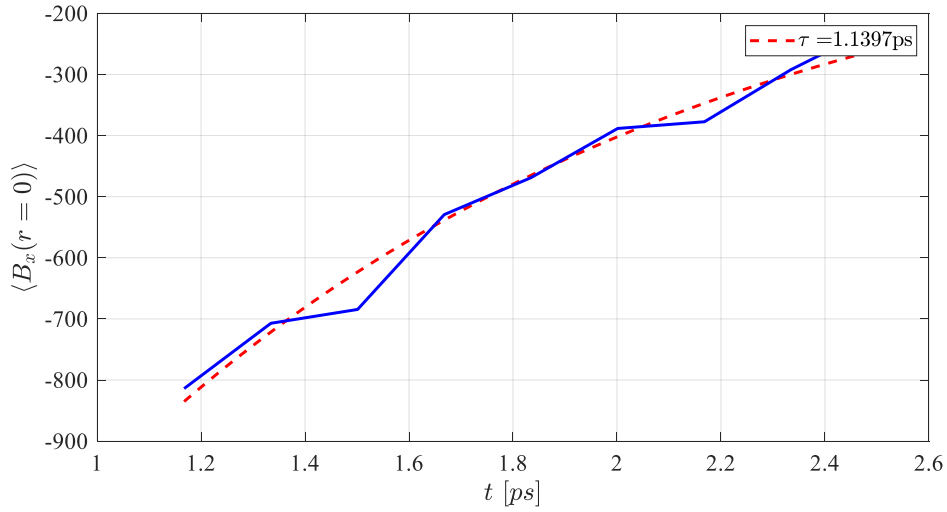

Figure 7.21: Peak average magnetic field at $r = 0$ as a function of time after the laser has left the simulation box for an asymmetric driven OAM mode. The red dotted line indicates the exponential decay fit with constant in the legend.

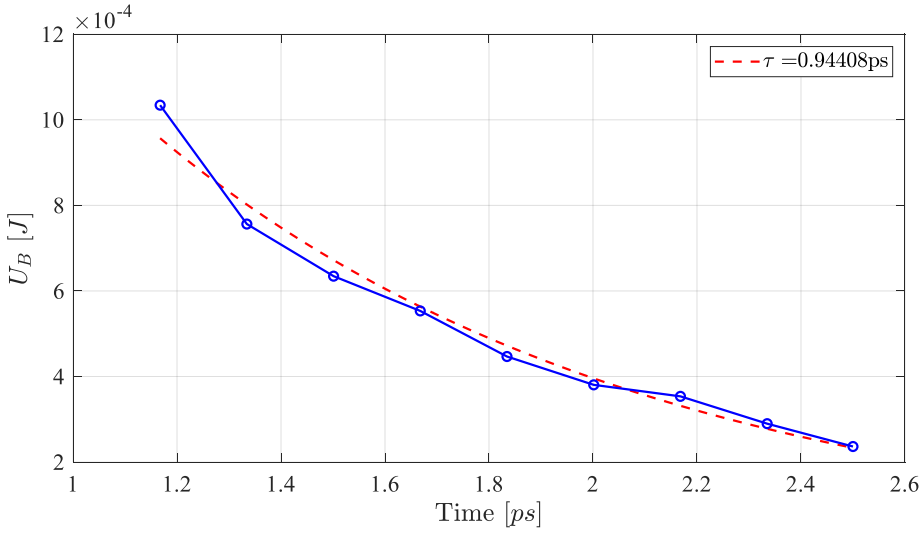

Figure 7.22: Total magnetic field energy in the simulation as a function of time driven by the asymmetric $\ell = 1$ OAM beam.

If we instead compare the decay time found from the magnetic field energy in the simulation as shown in Fig.7.22, we find a much smaller discrepancy between the two with the asymmetric time found at $0.94ps$ and the symmetric case being slightly

shorter at $0.91ps$. This value is in good agreement with value found using the value of peak magnetic field strength.

7.4 Conclusions

In this Chapter, we have shown that the analytic models found in Haines [64], and Ali et al, [5], are in good agreement with the results found from PIC simulations. This is the first time that the analytical models have been verified by a full 3D simulation.

In addition to demonstrating the validity of the analytical models, we have also shown that the spatial extent can be long - at least on the order of $100\mu m$ and likely extending out to the mm scale if plasma channels can be utilized to guide the laser pulse. The extent of these fields is at least an order of magnitude greater than that shown in other works [88, 116, 117], in which tightly focussed laser pulses were used with very short pulse duration's.

It was found that the magnetic fields do not decay by diffusion into plasma alone, and decays much faster due to hot electrons with a radial component to their current density. The decay time was found to roughly double when increasing the OAM mode number from $\ell = 1$ to $\ell = 2$. A possible explanation for the increase in decay time is the mitigation of the wobble instability due to the corkscrew pinch.

While these are significant findings in the dynamics of magnetic fields generated by linearly polarized lasers, there is still some work to be done. In particular, we are interested in the role of laser pulse duration as shorter laser pulses ($\approx 30fs$) have been found in the simulations to not produce significant magnetic fields. Additionally, verifying the inverse relationship of the electron density, and linear relationship of laser intensity would provide even stronger verification of the magnetic field generation model.

Chapter 8

Conclusions and Future Work

8.1 Conclusions

The goal of the thesis was to explore the coupling of linearly polarized orbital angular momentum (OAM) beams to underdense plasma theoretically, numerically, and experimentally. To successfully achieve this, the generation and characterization of OAM beams in high-power and high-intensity laser systems was investigated. This resulted in the publication of two peer-reviewed papers on the diffraction theory of OAM beams, and a third paper on the experimental demonstration of the highest intensity OAM beams for both the $\ell = 1$ and $\ell = 2$ modes to date.

The off-axis-spiral phase mirror (OASPM) was the key tool developed for mode converting high power laser systems, and since its introduction has gained large interest from major universities and research facilities. Until the introduction of the OASPM, mode conversion of high-power lasers was difficult requiring expensive optics, and typically could not be done with ultrafast laser systems. We demonstrated that the OASPM was a cost effective optic producing high quality OAM beams yielding the highest intensity OAM focal spots to date. The OASPM has now unlocked a new area of research into experimental OAM-plasma interactions at high intensities, and as such, the OASPM could become a standard optic in high-power laser facilities.

The diffraction of OAM beams generated by high power laser systems, and formulas for the far-field intensity distributions produced by these various near-field beams were developed. Given the complex formulas to describe the far-fields, we explored two methods of fitting Laguerre-Gaussian (LG) modes to these results. LG modes offer a simpler alternative to the exact far-field diffraction result and can be used for

analytic and numerical modelling purposes. The fitting parameters of low-order LG modes to the far-field diffraction results for Gaussian, super-Gaussian and flat top lasers have been developed. In addition, to model more realistic asymmetric OAM modes, a perturbative model was developed. This model decomposes an asymmetric OAM mode into three constituent modes, which can be easily implemented into numerical modelling.

In addition to developing high intensity OAM modes in the lab, we explored the interaction of high intensity OAM modes with single particles and a plasma.

The electrodynamics of free electron motion in LG modes was explored using a newly-derived paraxial equation based on the model of Erikson and Singh [38]. From this model, we were able to show that in addition to the energy gained by a scattering electron from the ponderomotive force, an angular momentum is also gained with a direct scaling to the ponderomotive scattering. The trapping of electrons for energy gain within the optical vortex was also investigated indicating that electrons may be optimally accelerated from a wide variety of initial radii within the peak intensity ring of the OAM ring.

Using the 3D PIC code EPOCH, we found that the relativistic self-focussing of an OAM beam can have complex dynamics as we identified two new self focussing phenomena, namely the ring pinch mode, and the ring collapse mode. We have yet to explore the stability and criteria of each of these modes. We further explored using OAM modes to drive wakefield acceleration of electrons, and found that the peak energy of the electrons decreases and the divergence increases using OAM modes. Further study is needed to explore the interaction of the laser pulse in the plasma over much longer distances ($\approx 5mm$) that currently are difficult to do with fully 3D simulations.

The change in ejected electron energy from OAM driven LWFA did not agree with the analytic models derived for Gaussian driven wakefields with simple adjusting of the corresponding parameters of the interaction. This indicates a need for new analytic and empirical models specifically for OAM driven wakefield scaling. Modelling of the betatron spatial distribution was performed, and a splitting of the emitted radiation spots was found due to the linearly polarized OAM ring with a slight twist from the polarization axis depending on the handedness of the OAM mode. The modelling of the spectral distribution of the emitted x-rays is an ongoing task given the difficulty of accurate modelling of radiation emission between $100eV$ and $10keV$.

By showing that the angular momentum transferred from the laser to the electrons scaled as a_0^2, much like the ponderomotive force, we were able to justify OAM transfer to the plasma in high intensity interactions. OAM beams of charge $\ell = 1$ and $\ell = 2$ were simulated and the axial magnetic fields found agreed almost exactly with the analytic results that give the radial distribution of the magnetic field and the corresponding strength.

In addition, we found decay times of the magnetic fields to be on the order of $1ps$ for the $\ell = 1$ mode, and roughly $2ps$ for the $\ell = 2$ mode. We also were able to show that the magnetic fields produced were at least on the order of $100\mu m$, suitable for fast ignition related use. It is likely that the magnetic field length could be increased through the use of a plasma channel so that the laser self guides, but requires further work in understanding the self focussing properties of LG modes in under dense plasma.

To verify the generation and application of OAM modes experimentally, a 4 week campaign at the CLPU in Salamanca, Spain utilized the 200TW VEGA 2 laser to drive wakefield acceleration with varying OAM modes. Generation of $\ell = 0, 1$ and 2 modes was successful using the OASPM, and we were able to accelerate electrons successfully. While there was no significant enhancement in electron energy or divergence due to an increase in beam OAM, the fact that similar electron energies could be obtained at the significantly lower peak intensities is in itself remarkable. There was also an increase in betatron x-ray critical energy, perhaps due to the presence of additional magnetic fields.

In the near future we plan to publish the work done on single particle electrodynamics in OAM modes and the scattering of electrons from pulses, the experimental results from the CLPU campaign showing the enhancement of betatron critical energy, and the numerical verification of the inverse Faraday effect with linearly polarized OAM modes.

8.2 Forward

The work performed in this thesis has opened up the way to generate high intensity OAM laser pulses and apply them to the study of laser plasma interactions. While the present thesis carries out a preliminary study of such interactions, there is much work to be done in all areas of study.

Probably the first area is the understanding and modelling of self-focussing in underdense plasma. Without this, understanding of wakefield energy scaling, magnetic field generation and laser propagation will be difficult to move forward. This could also lead to a better understanding of the necessary shape of plasma channels required for longer propagation of the OAM modes for enhanced magnetic field generation and electron energy gain.

To do this, larger simulations over longer duration's are required which will be difficult using a fully 3D code given the massive output files (currently $\approx 30TB$). Instead one could look to using a 2.5D code that uses cylindrical coordinates and decomposes the azimuthal coordinate into adjacent modes of a Bessel function [89]. Larger scale simulations would also allow a more complete and accurate simulation of the LWFA of electrons and perhaps help address the differences between the current simulation and experimental results in terms of electron energy spectra observed. In addition work in modelling the spectrum of the emitted betatron radiation is also required and is currently underway.

The generation of axial magnetic fields using OAM pulses and scaling with pulse duration and plasma conditions is a major area of future exploration both with numerical simulations and experimental measurements. Such fields could potentially be measured by a variety of techniques such as Faraday rotation, Zeeman spectroscopy and proton radiography.

The actual exploitation of the hollow centre channel of OAM modes is another future area of investigation both for enhanced trapping, acceleration, and guiding of electrons but also for the wakefield acceleration of positrons as predicted in published simulations.

While not included in this thesis, a second campaign using OAM beams at the CLPU in Salamanca was conducted in 2019 interacting with solid targets. In this campaign, high-intensity OAM beams were used to drive target-normal-sheath-acceleration (TNSA) in solid aluminium targets producing proton and ion beams. Work is still underway in the analysis of the results with the generation of magnetic fields and potential enhanced guiding of electrons and protons is yet another major area of application of OAM pulses.

Overall the present work is a first step towards a whole new regime of high intensity interaction physics employing the new tool of orbital angular momentum.

Bibliography

[1] U.S. Energy Information Administration. *Annual Energy Outlook 2020*. 2020. URL: https://www.eia.gov/outlooks/aeo/ (visited on 09/09/2020).

[2] National Aeronautics and Space Administration. *Global Climate Change - Carbon Dioxide Levels*. 2020. URL: https://climate.nasa.gov/vital-signs/carbon-dioxide/ (visited on 09/09/2020).

[3] Félicie Albert et al. "Betatron oscillations of electrons accelerated in laser wakefields characterized by spectral x-ray analysis". In: *Phys. Rev. E* 77 (5 May 2008), p. 056402.

[4] F Albert et al. "Laser wakefield accelerator based light sources: potential applications and requirements". In: *Plasma Physics and Controlled Fusion* 56.8 (July 2014), p. 084015.

[5] S. Ali, J. R. Davies, and J. T. Mendonça. "Inverse Faraday Effect with Linearly Polarized Laser Pulses". In: *Phys. Rev. Lett.* 105 (3 July 2010), p. 035001.

[6] L. Allen et al. "Orbital angular momentum of light and the transformation of Laguerre-Gaussian laser modes". In: *Phys. Rev. A* 45 (11 June 1992), pp. 8185–8189.

[7] M.V. Ammosov, N.B. Delone, and V.P. Krainov. "Tunnel ionization of complex atoms and of atomic ions in an alternating electromagnetic field". In: *Sov. Phys. JETP* 64 (6 Dec. 1986), pp. 1191–1194.

[8] T D Arber et al. "Contemporary particle-in-cell approach to laser-plasma modelling". In: *Plasma Physics and Controlled Fusion* 57.11 (Sept. 2015).

[9] Sterling Backus et al. "High power ultrafast lasers". In: *Review of Scientific Instruments* 69.3 (1998), pp. 1207–1223.

[10] Stephen M. Barnett. "Relativistic Electron Vortices". In: *Phys. Rev. Lett.* 118 (11 Mar. 2017), p. 114802.

[11] Stephen M. Barnett and L. Allen. "Orbital angular momentum and nonparaxial light beams". In: *Optics Communications* 110.5 (1994), pp. 670–678.

[12] Stephen M Barnett et al. "On the natures of the spin and orbital parts of optical angular momentum". In: *Journal of Optics* 18.6 (Apr. 2016), p. 064004.

[13] C. Baumann and A. Pukhov. "Electron dynamics in twisted light modes of relativistic intensity". In: *Physics of Plasmas* 25.8 (2018), p. 083114.

[14] K. Behm et al. "Demonstration of femtosecond broadband X-rays from laser wakefield acceleration as a source for pump-probe X-ray absorption studies". In: *High Energy Density Physics* 35 (2020), p. 100729.

[15] M.W. Beijersbergen et al. "Astigmatic laser mode converters and transfer of orbital angular momentum". In: *Optics Communications* 96.1 (1993), pp. 123–132.

[16] M.W. Beijersbergen et al. "Helical-wavefront laser beams produced with a spiral phaseplate". In: *Optics Communications* 112.5 (1994), pp. 321–327.

[17] C. Bellei et al. "Fast ignition: Dependence of the ignition energy on source and target parameters for particle-in-cell-modelled energy and angular distributions of the fast electrons". In: *Physics of Plasmas* 20.5 (2013), p. 052704.

[18] Clarence E. Bennett. "Dispersion and Refractive Index of Nitrogen Measured as Functions of Pressure by Displacement Interferometry". In: *Phys. Rev.* 37 (3 Feb. 1931), pp. 263–275.

[19] J. Bialek. "Tracing the flow of electricity". In: *IEE Proceedings - Generation, Transmission and Distribution* 143.4 (1996), pp. 313–320.

[20] Iwo Bialynicki-Birula and Zofia Bialynicka-Birula. "Relativistic Electron Wave Packets Carrying Angular Momentum". In: *Phys. Rev. Lett.* 118 (11 Mar. 2017), p. 114801.

[21] D. R. Blackman et al. "Kinetic plasma waves carrying orbital angular momentum". In: *Phys. Rev. E* 100 (1 July 2019), p. 013204.

[22] Max Born and Emil Wolf. *Principles of Optics*. 7th. Cambridge University Press, 1999.

[23] Robert W. Boyd. *Nonlinear Optics*. 3rd. Academic Press, Inc., 2008.

[24] C. Brabetz et al. "Laser-driven ion acceleration with hollow laser beams". In: *Physics of Plasmas* 22.1 (2015), p. 013105.

[25] B. H. Bransden and C. J. Joachain. *Quantum Mechanics*. 2nd. Pearson Prentice Hall, 2000.

[26] A. Buck et al. "Absolute charge calibration of scintillating screens for relativistic electron detection". In: *Review of Scientific Instruments* 81.3 (2010), p. 033301.

[27] Geoff Campbell et al. "Generation of high-order optical vortices using directly machined spiral phase mirrors". In: *Appl. Opt.* 51.7 (Mar. 2012), pp. 873–876.

[28] Government of Canada. *The economics of solar power in Canada*. 2020. URL: `https://www.cer-rec.gc.ca/nrg/sttstc/lctrct/rprt/cnmcsfslrpwr/index-eng.html` (visited on 09/09/2020).

[29] Francis F. Chen. *Introduction to Plasma Physics And Controlled Fusion, Volume 1*. 2nd. Plenum Press, 1984.

[30] Hank Childs et al. "VisIt: An End-User Tool For Visualizing and Analyzing Very Large Data". In: *High Performance Visualization–Enabling Extreme-Scale Scientific Insight*. Oct. 2012, pp. 357–372.

[31] W. N. Cottingham and D. A. Greenwood. *An Introduction to Nuclear Physics*. 2nd. Cambridge University Press, 2001.

[32] A. Dalgarno and A. E. Kingston. "The refractive indicies and Verdet constants of the inert gases". In: *Proceedings of the Royal Society of London. Series A, Mathematical and Physical Sciences* 259 (1298 Dec. 1960), pp. 424–431.

[33] Carlos A. De Moura and Carlos S. Kubrsly. *The Courant–Friedrichs–Lewy (CFL) Condition - 80 Years After Its Discovery*. 1st. Birkhauser Basel, 2013.

[34] A. Denoeud et al. "Interaction of Ultraintense Laser Vortices with Plasma Mirrors". In: *Phys. Rev. Lett.* 118 (3 Jan. 2017), p. 033902.

[35] J. Deschamps, M. Fitaire, and M. Lagoutte. "Inverse Faraday Effect in a Plasma". In: *Physical Review Letters* 25.19 (Nov. 1970), pp. 1330–1332.

[36] T. R. Dittrich et al. "Design of a High-Foot High-Adiabat ICF Capsule for the National Ignition Facility". In: *Phys. Rev. Lett.* 112 (5 Feb. 2014), p. 055002.

[37] R Duclous, J G Kirk, and A R Bell. “Monte Carlo calculations of pair production in high-intensity laser–plasma interactions”. In: *Plasma Physics and Controlled Fusion* 53.1 (Nov. 2010), p. 015009.

[38] W. L. Erikson and Surendra Singh. “Polarization properties of Maxwell-Gaussian laser beams”. In: *Phys. Rev. E* 49 (6 June 1994), pp. 5778–5786.

[39] E. Esarey, C. B. Schroeder, and W. P. Leemans. “Physics of laser-driven plasma-based electron accelerators”. In: *Rev. Mod. Phys.* 81 (3 2009), pp. 1229–1285.

[40] E. Esarey et al. “Overview of plasma-based accelerator concepts”. In: *IEEE Transactions on Plasma Science* 24.2 (1996), pp. 252–288.

[41] Eric Esarey, Phillip Sprangle, and Jonathan Krall. “Laser acceleration of electrons in vacuum”. In: *Phys. Rev. E* 52 (5 Nov. 1995), pp. 5443–5453.

[42] E. Ezcurra et al. “A natural experiment reveals the impact of hydroelectric dams on the estuaries of tropical rivers”. In: *Science Advances* 5.3 (2019).

[43] J. Faure et al. “A laser–plasma accelerator producing monoenergetic electron beams”. In: *Nature* 431 (Sept. 2004), pp. 541–544.

[44] A. Ferguson. “Faraday’s Diary: being the various Philosophical Notes of Experimental Investigation made by Michael Faraday, DCL, FRS, during the years 1820-1862 and bequeathed by him to the Royal Institution of Great Britain”. In: *Nature* 130 (1932), pp. 828–830.

[45] Richard P Feynman, Robert B Leighton, and Matthew L Sands. *The Feynman Lectures on Physics*. 2nd. Addison-Wesley, 1965.

[46] Robert Fickler et al. “Quantum entanglement of angular momentum states with quantum numbers up to 10,010”. In: *Proceedings of the National Academy of Sciences* 113.48 (2016), pp. 13642–13647.

[47] Ali Shekari Firouzjaei and Babak Shokri. “Analysis of radial and longitudinal field of plasma wakefield generated by a Laguerre-Gauss laser pulse”. In: *Physics of Plasmas* 23.6 (2016), p. 063102.

[48] R. A. Fonseca et al. “OSIRIS: A Three-Dimensional, Fully Relativistic Particle in Cell Code for Modeling Plasma Based Accelerators”. In: *Computational Science — ICCS 2002*. Ed. by Peter M. A. Sloot et al. Berlin, Heidelberg: Springer Berlin Heidelberg, 2002, pp. 342–351.

[49] Mark Fox. *Optical Properties of Solids*. 2nd. Oxford University Press, 2010.

[50] J. P. Freidberg and L. D. Pearlstein. "Rotational instabilities in a theta pinch". In: *The Physics of Fluids* 21.7 (1978), pp. 1207–1217.

[51] Jeffrey Freidberg. *Ideal MHD*. 1st. Cambridge University Press, 2014.

[52] H. Friesen et al. "Kirkpatrick-Baez microscope for hard X-ray imaging of fast ignition experiments". In: *Review of Scientific Instruments* 84.2 (2013), p. 023704.

[53] D. H. Froula et al. "Measurements of the Critical Power for Self-Injection of Electrons in a Laser Wakefield Accelerator". In: *Phys. Rev. Lett.* 103 (21 Nov. 2009), p. 215006.

[54] C. G. Geddes et al. "High-quality electron beams from a laser wakefield accelerator using plasma-channel guiding". In: *Nature* 431 (Sept. 2004), pp. 538–541.

[55] Devinder Pal Ghai. "Generation of optical vortices with an adaptive helical mirror". In: *Appl. Opt.* 50.10 (Apr. 2011), pp. 1374–1381.

[56] Paul Gibbon. *Short Pulse Laser Interactions with Matter*. 1st. Imperial College Press, 2005.

[57] A. J. Gonsalves et al. "Petawatt Laser Guiding and Electron Beam Acceleration to 8 GeV in a Laser-Heated Capillary Discharge Waveguide". In: *Phys. Rev. Lett.* 122 (8 Feb. 2019), p. 084801.

[58] Joseph W Goodman. *Introduction to Fourier Optics*. 3rd. Roberts and Co. Publishers, 2005.

[59] N. Gottardi. "Evaluation of electron density profiles in plasmas from integrated measurements". In: *Journal of Applied Physics* 50.4 (1979), pp. 2647–2651.

[60] I. S. Gradshteyn and I. M. Ryzhik. *Table of Integrals, Series, and Products*. 7th. Elsevier/Academic Press, Amsterdam, 2007.

[61] David J Griffiths. *Introduction to Electrodynamics*. 4th. Re-published by Cambridge University Press in 2017. Pearson, 2013.

[62] David J Griffiths and Darrell F Schroeter. *Introduction to Quantum Mechanics*. 3rd. Cambridge University Press, 2018.

[63] E. Gschwendtner et al. “AWAKE, The Advanced Proton Driven Plasma Wakefield Acceleration Experiment at CERN”. In: *Nuclear Instruments and Methods in Physics Research Section A: Accelerators, Spectrometers, Detectors and Associated Equipment* 829 (2016). 2nd European Advanced Accelerator Concepts Workshop - EAAC 2015, pp. 76–82.

[64] M. G. Haines. “Generation of an Axial Magnetic Field from Photon Spin”. In: *Phys. Rev. Lett.* 87 (13 Sept. 2001), p. 135005.

[65] A. A. Harms et al. *Principles of Fusion Energy*. 1st. World Scientific Publishing, 2000.

[66] Hermann A. Haus. *Waves and Fields in Optoelectronics*. 1st. Englewood Cliffs, NJ: Prentice-Hall, 1984.

[67] C. Z. He et al. “Towards an in situ, full-power gauge of the focal-volume intensity of petawatt-class lasers”. In: *Opt. Express* 27.21 (Oct. 2019), pp. 30020–30030.

[68] Y. Horovitz et al. “Measurements of Inverse Faraday Effect and Absorption of Circularly Polarized Laser Light in Plasmas”. In: *Phys. Rev. Lett.* 78 (9 Mar. 1997), pp. 1707–1710.

[69] Y. Horovitz et al. “The inverse Faraday effect in plasma produced by circularly polarized laser light in the range of intensities 109–1014 W/cm2”. In: *Physics Letters A* 246.3 (1998), pp. 329–334.

[70] C. M. Huntington et al. “Current Filamentation Instability in Laser Wakefield Accelerators”. In: *Phys. Rev. Lett.* 106 (10 Mar. 2011), p. 105001.

[71] O. A. Hurricane et al. “Fuel gain exceeding unity in an inertially confined fusion implosion”. In: *Nature* 506 (2014), pp. 343–348.

[72] A. E. Hussein et al. “Laser-wakefield accelerators for high-resolution X-ray imaging of complex microstructures”. In: *Scientific Reports* 9.3249 (2019).

[73] ITER. *ITER Research Plan*. 2020. URL: `https://www.iter.org/newsline/-/3121` (visited on 09/09/2020).

[74] Akihiko Ito, Yuichi Kozawa, and Shunichi Sato. “Generation of hollow scalar and vector beams using a spot-defect mirror”. In: *J. Opt. Soc. Am. A* 27.9 (Sept. 2010), pp. 2072–2077.

[75] John David Jackson. *Classical Electrodynamics*. 3rd. Wiley, 1999.

[76] Chris Jacobsen, Malcolm Howells, and Tony Warwick. "Zone-Plate X-Ray Microscopy". In: *Springer Handbook of Microscopy*. Ed. by Peter W. Hawkes and John C. H. Spence. 2019, pp. 1145–1204.

[77] Mikkel Jørgensen, Kion Norrman, and Frederik C. Krebs. "Stability/degradation of polymer solar cells". In: *Solar Energy Materials and Solar Cells* 92.7 (2008), pp. 686–714.

[78] G. W. C. Kaye and T.H. Laby. *Tables of physical and chemical constants*. 15th. Longman Scientific, 1986.

[79] Rhon Keinigs and Michael E. Jones. "Two-dimensional dynamics of the plasma wakefield accelerator". In: *The Physics of Fluids* 30.1 (1987), pp. 252–263.

[80] M. H. Key et al. "Fast ignition relevant study of the flux of high intensity laser-generated electrons via a hollow cone into a laser-imploded plasma". In: *Physics of Plasmas* 15.2 (2008), p. 022701.

[81] Paul Kirkpatrick and A. V. Baez. "Formation of Optical Images by X-Rays". In: *J. Opt. Soc. Am.* 38.9 (Sept. 1948), pp. 766–774.

[82] I. Kostyukov, S. Kiselev, and A. Pukhov. "X-ray generation in an ion channel". In: *Physics of Plasmas* 10.12 (2003), pp. 4818–4828.

[83] V.I. Kruglov, Yu.A. Logvin, and V.M. Volkov. "The Theory of Spiral Laser Beams in Nonlinear Media". In: *Journal of Modern Optics* 39.11 (1992), pp. 2277–2291.

[84] Lev Landau and Evgeny Lifshitz. *The Classical Theory of Fields*. 4th. Butterworth-Heinemann, 1975.

[85] J. D. Lawson. "Lasers and Accelerators". In: *IEEE Transactions on Nuclear Science* 26.3 (1979), pp. 4217–4219.

[86] A. Leblanc et al. "Plasma holograms for ultrahigh-intensity optics". In: *Nature Physics* 13 (2017), pp. 440–443.

[87] David LeBlanc. "Molten salt reactors: A new beginning for an old idea". In: *Nuclear Engineering and Design* 240.6 (2010), pp. 1644–1656.

[88] Z. Lécz, A. Andreev, and A. Seryi. "Plasma rotation with circularly polarized laser pulse". In: *Laser and Particle Beams* 34.1 (2016), pp. 31–42.

[89] Rémi Lehe et al. “A spectral, quasi-cylindrical and dispersion-free Particle-In-Cell algorithm”. In: *Computer Physics Communications* 203 (2016), pp. 66–82.

[90] N Lemos et al. “Self-modulated laser wakefield accelerators as x-ray sources”. In: *Plasma Physics and Controlled Fusion* 58.3 (Feb. 2016), p. 034018.

[91] Wentao Li et al. “Observation of laser multiple filamentation process and multiple electron beams acceleration in a laser wakefield accelerator”. In: *Physics of Plasmas* 20.11 (2013), p. 113106.

[92] T V Liseykina, S V Popruzhenko, and A Macchi. “Inverse Faraday effect driven by radiation friction”. In: *New Journal of Physics* 18.7 (July 2016), p. 072001.

[93] Andrew Longman and Robert Fedosejevs. “Mode conversion efficiency to Laguerre-Gaussian OAM modes using spiral phase optics”. In: *Opt. Express* 25.15 (July 2017), pp. 17382–17392.

[94] Andrew Longman and Robert Fedosejevs. “Optimal Laguerre–Gaussian modes for high-intensity optical vortices”. In: *J. Opt. Soc. Am. A* 37.5 (May 2020), pp. 841–848.

[95] Andrew Longman et al. “Off-axis spiral phase mirrors for generating high-intensity optical vortices”. In: *Opt. Lett.* 45.8 (Apr. 2020), pp. 2187–2190.

[96] W. Lu et al. “Generating multi-GeV electron bunches using single stage laser wakefield acceleration in a 3D nonlinear regime”. In: *Phys. Rev. ST Accel. Beams* 10 (6 June 2007), p. 061301.

[97] Andrea Macchi. *A Superintense Laser-Plasma Interaction Theory Primer*. 1st ed. Springer Netherlands, 2013.

[98] S. P. D. Mangles et al. “Monoenergetic beams of relativistic electrons from intense laser–plasma interactions”. In: *Nature* 431 (Sept. 2004), pp. 535–538.

[99] L. Marrucci et al. “Spin-to-orbit conversion of the angular momentum of light and its classical and quantum applications”. In: *J. Opt.* 13 (2011), p. 164001.

[100] J. L. Martins et al. “Radiation emission in laser wakefields driven by structured laser pulses with orbital angular momentum”. In: *Scientific Reports* 9.9840 (2019).

[101] J. L. Martins et al. “Radiation post-processing in PIC codes”. In: *Harnessing Relativistic Plasma Waves as Novel Radiation Sources from Terahertz to X-Rays and Beyond*. Vol. 7359. 2009, pp. 214–221.

[102] D N Maywar et al. “OMEGA EP high-energy petawatt laser: progress and prospects”. In: *Journal of Physics: Conference Series* 112.3 (May 2008), p. 032007.

[103] C. McGuffey et al. “Ionization Induced Trapping in a Laser Wakefield Accelerator”. In: *Phys. Rev. Lett.* 104 (2 Jan. 2010), p. 025004.

[104] Fulvio Melia. *Electrodynamics*. 1st. The University of Chicago Press, 2001.

[105] J. T. Mendonça. “Kinetic description of electron plasma waves with orbital angular momentum”. In: *Physics of Plasmas* 19.11 (2012), p. 112113.

[106] J. T. Mendonça and J. Vieira. “Donut wakefields generated by intense laser pulses with orbital angular momentum”. In: *Physics of Plasmas* 21.3 (2014), p. 033107.

[107] P. Michel et al. “Efficient electron injection into plasma waves using higher-order laser modes”. In: *Physics of Plasmas* 13.11 (2006), p. 113112.

[108] M. Z. Mo et al. “Characterization of laser wakefield generated betatron X-ray radiation using grazing incidence mirror reflection”. In: *Eur. Phys. J. D* 68.301 (2014).

[109] M. Z. Mo et al. “Laser wakefield generated X-ray probe for femtosecond time-resolved measurements of ionization states of warm dense aluminum”. In: *Review of Scientific Instruments* 84.12 (2013), p. 123106.

[110] M. Z. Mo et al. “Measurements of ionization states in warm dense aluminum with betatron radiation”. In: *Phys. Rev. E* 95 (5 May 2017), p. 053208.

[111] Mianzhen. Mo. “Study of Relativistic Electrons Generated from Ultra-intense Laser-Plasma Interaction relevant to Laser Wakefield Acceleration and Fast Ignition Laser Fusion”. PhD thesis. University of Alberta, 2015.

[112] S. M. Mohammadi et al. “Orbital Angular Momentum in Radio—A System Study”. In: *IEEE Transactions on Antennas and Propagation* 58.2 (2010), pp. 565–572.

[113] Z. Najmudin et al. “Measurements of the Inverse Faraday Effect from Relativistic Laser Interactions with an Underdense Plasma”. In: *Phys. Rev. Lett.* 87 (21 Nov. 2001), p. 215004.

[114] N. Naseri, V. Yu. Bychenkov, and W. Rozmus. "Axial magnetic field generation by intense circularly polarized laser pulses in underdense plasmas". In: *Physics of Plasmas* 17.8 (2010), p. 083109.

[115] Lukas Novotny and Bert Hecht. *Principles of Nano-Optics*. 2nd. Cambridge, UK: Cambridge University Press, 2012.

[116] R. Nuter et al. "Gain of electron orbital angular momentum in a direct laser acceleration process". In: *Phys. Rev. E* 101 (5 May 2020), p. 053202.

[117] R. Nuter et al. "Plasma solenoid driven by a laser beam carrying an orbital angular momentum". In: *Phys. Rev. E* 98 (3 Sept. 2018), p. 033211.

[118] J. B. Ohland et al. "A study on the effects and visibility of low-order aberrations on laser beams with orbital angular momentum". In: *Appl. Phys. B* 125.202 (2019).

[119] A. Pak et al. "Injection and Trapping of Tunnel-Ionized Electrons into Laser-Produced Wakes". In: *Phys. Rev. Lett.* 104 (2 Jan. 2010), p. 025003.

[120] R. K. Pathria and Paul D Beale. *Statistical Mechanics*. 3rd. Elsevier, 2011.

[121] Justin Peatross and Michael Ware. *Physics of Light and Optics*. 2015.

[122] Justin Peatross et al. "Vector fields in a tight laser focus: comparison of models". In: *Opt. Express* 25.13 (June 2017), pp. 13990–14007.

[123] A. Picón et al. "Photoionization with orbital angular momentum beams". In: *Opt. Express* 18.4 (Feb. 2010), pp. 3660–3671.

[124] B. B. Pollock et al. "High magnetic field generation for laser-plasma experiments". In: *Review of Scientific Instruments* 77.11 (2006), p. 114703.

[125] Nuscale Power. *Nuscale Small Modular Reactors*. 2020. URL: `https://www.nuscalepower.com/` (visited on 09/09/2020).

[126] Brice Quesnel and Patrick Mora. "Theory and simulation of the interaction of ultraintense laser pulses with electrons in vacuum". In: *Phys. Rev. E* 58 (3 Sept. 1998), pp. 3719–3732.

[127] Aleksandar D. Rakić et al. "Optical properties of metallic films for vertical-cavity optoelectronic devices". In: *Appl. Opt.* 37.22 (Aug. 1998), pp. 5271–5283.

[128] C. Ren et al. “Global Simulation for Laser-Driven MeV Electrons in Fast Ignition”. In: *Phys. Rev. Lett.* 93 (18 Oct. 2004), p. 185004.

[129] A. Rousse et al. “Scaling of betatron X-ray radiation”. In: *Eur. Phys. J. D* 45 (2007), pp. 391–398.

[130] G. Ruffato, M. Massari, and F. Romanato. “Generation of high-order Laguerre Gaussian modes by means of spiral phase plates”. In: *Opt. Lett.* 39.17 (Sept. 2014), pp. 5094–5097.

[131] Gianluca Ruffato et al. “Spiral phase plates with radial discontinuities for the generation of multiring orbital angular momentum beams: fabrication, characterization, and application”. In: *Optical Engineering* 54.11 (2015), pp. 1–8.

[132] B. Rus et al. “ELI-beamlines: progress in development of next generation short-pulse laser systems”. In: *Research Using Extreme Light: Entering New Frontiers with Petawatt-Class Lasers III*. Ed. by Georg Korn and Luis O. Silva. Vol. 10241. 2017, pp. 14–21.

[133] Lucas Sá and Jorge Vieira. “Self-focussing of multiple interacting Laguerre-Gauss beams in Kerr media”. In: *Physical Review A* 100.013836 (July 2019).

[134] Carlo Salvetti. “The birth of nuclear energy: Fermi’s pile”. In: *Enrico Fermi: His Work and Legacy*. Ed. by Carlo Bernardini and Luisa Bonolis. Berlin, Heidelberg: Springer Berlin Heidelberg, 2004, pp. 177–203.

[135] E. S. Sarachik and G. T. Schappert. “Classical Theory of the Scattering of Intense Laser Radiation by Free Electrons”. In: *Phys. Rev. D* 1 (10 May 1970), pp. 2738–2753.

[136] Andrei Seryi. *Unifying Physics of Accelerators, Lasers, and Plasma*. 1st. CRC Press, 2016.

[137] J. L. Shaw et al. “Role of Direct Laser Acceleration of Electrons in a Laser Wakefield Accelerator with Ionization Injection”. In: *Phys. Rev. Lett.* 118 (6 Feb. 2017), p. 064801.

[138] Zhong-Chen Shen et al. “Acceleration and radiation of externally injected electrons in laser plasma wakefield driven by a Laguerre–Gaussian pulse”. In: *Chinese Physics B* 26.11 (Oct. 2017), p. 115204.

[139] Z. -M. Sheng et al. "Angular Distributions of Fast Electrons, Ions, and Bremsstrahlung x/ γ-Rays in Intense Laser Interaction with Solid Targets". In: *Phys. Rev. Lett.* 85 (25 Dec. 2000), pp. 5340–5343.

[140] Z. M. Sheng and J. Meyer-ter-Vehn. "Inverse Faraday effect and propagation of circularly polarized intense laser beams in plasmas". In: *Phys. Rev. E* 54 (2 Aug. 1996), pp. 1833–1842.

[141] Y. Shi et al. "Magnetic Field Generation in Plasma Waves Driven by Co-propagating Intense Twisted Lasers". In: *Phys. Rev. Lett.* 121 (14 Oct. 2018), p. 145002.

[142] F. Shinsuke et al. "Kilotesla Magnetic Field due to a Capacitor-Coil Target Driven by High Power Laser". In: *Scientific Reports* 3 (Jan. 2013), p. 1170.

[143] H Shiraga et al. "Fast ignition integrated experiments with Gekko and LFEX lasers". In: *Plasma Physics and Controlled Fusion* 53.12 (Nov. 2011), p. 124029.

[144] A. E. Siegman. "Quasi fast Hankel transform". In: *Opt. Lett.* 1.1 (July 1977), pp. 13–15.

[145] E. Siegman Anthony. *Lasers*. 1st. University Science Books, 1986.

[146] Stephen A. Slutz and Roger A. Vesey. "High-Gain Magnetized Inertial Fusion". In: *Phys. Rev. Lett.* 108 (2 Jan. 2012), p. 025003.

[147] National Institute of Standards and Technology. *Atomic Spectra Database Ionization Energies*. 2020. URL: `https://physics.nist.gov/PhysRefData/ASD/ionEnergy.html` (visited on 05/10/2020).

[148] National Institute of Standards and Technology. *X-Ray Mass Attenuation Coefficients*. 2020. URL: `https://physics.nist.gov/PhysRefData/XrayMassCoef/tab3.html` (visited on 08/20/2020).

[149] R. B. Stephens et al. "K_α fluorescence measurement of relativistic electron transport in the context of fast ignition". In: *Phys. Rev. E* 69 (6 June 2004), p. 066414.

[150] Donna Strickland and Gerard Mourou. "Compression of amplified chirped optical pulses". In: *Optics Communications* 56.3 (1985), pp. 219–221.

[151] K. Sueda et al. "Laguerre-Gaussian beam generated with a multilevel spiral phase plate for high intensity laser pulses". In: *Opt. Express* 12.15 (July 2004), pp. 3548–3553.

[152] Max Tabak et al. “Ignition and high gain with ultrapowerful lasers”. In: *Physics of Plasmas* 1.5 (1994), pp. 1626–1634.

[153] T. Tajima and J. M. Dawson. “Laser Electron Accelerator”. In: *Phys. Rev. Lett.* 43 (4 July 1979), pp. 267–270.

[154] Tesla. *Tesla Powerwall*. 2020. URL: `https://www.tesla.com/en_ca/powerwall` (visited on 09/09/2020).

[155] W. Theobald et al. “Initial cone-in-shell fast-ignition experiments on OMEGA”. In: *Physics of Plasmas* 18.5 (2011), p. 056305.

[156] M. Thévenet et al. “Vacuum laser acceleration of relativistic electrons using plasma mirror injectors”. In: *Nature Physics* 12 (Dec. 2016), pp. 355–360.

[157] A. G. R. Thomas. “Algorithm for calculating spectral intensity due to charged particles in arbitrary motion”. In: *Phys. Rev. ST Accel. Beams* 13 (2 Feb. 2010), p. 020702.

[158] V.T. Tikhonchuk et al. “Numerical study of momentum and energy transfer in the interaction of a laser pulse carrying orbital angular momentum with electrons”. In: *High Energy Density Physics* 37 (2020), p. 100863.

[159] Rick Trebino. *Frequency-Resolved Optical Gating: The Measurement of Ultrashort Laser Pulses*. 1st. Springer, 2000.

[160] F. S. Tsung et al. “Near-GeV-Energy Laser-Wakefield Acceleration of Self-Injected Electrons in a Centimeter-Scale Plasma Channel”. In: *Phys. Rev. Lett.* 93 (18 Oct. 2004), p. 185002.

[161] F. S. Tsung et al. “Simulation of monoenergetic electron generation via laser wakefield accelerators for 5–25TW lasers”. In: *Physics of Plasmas* 13.5 (2006), p. 056708.

[162] Charles Varin et al. “Direct Electron Acceleration with Radially Polarized Laser Beams”. In: *Applied Sciences* 3.1 (2013), pp. 70–93.

[163] J.-L. Vay et al. “Modeling of 10 GeV-1 TeV laser-plasma accelerators using Lorentz boosted simulations”. In: *Physics of Plasmas* 18.12 (2011), p. 123103.

[164] J. Vieira and J. T. Mendonça. “Nonlinear laser driven donut wakefields for positron and electron acceleration”. In: *Physical Review Letters* 112 (2014), p. 215001.

[165] J. Vieira, J. T. Mendonça, and F. Quéré. "Optical Control of the Topology of Laser-Plasma Accelerators". In: *Phys. Rev. Lett.* 121 (5 July 2018), p. 054801.

[166] L. Volpe et al. "Generation of high energy laser-driven electron and proton sources with the 200 TW system VEGA 2 at the Centro de Laseres Pulsados". In: *High Power Laser Science and Engineering* 7.E25 (2019).

[167] M. Vranic et al. "Classical radiation reaction in particle-in-cell simulations". In: *Computer Physics Communications* 204 (2016), pp. 141–151.

[168] J. W. Wang et al. "Plasma channel undulator excited by high-order laser modes". In: *Scientific Reports* 7.16884 (2017).

[169] W.-M. Wang et al. "Magnetically Assisted Fast Ignition". In: *Phys. Rev. Lett.* 114 (1 Jan. 2015), p. 015001.

[170] Norbert Wiener. *Extrapolation, Interpolation, and Smoothing of Stationary Time Series: With Engineering Applications*. 1st. MIT Press, 1964.

[171] G. J. Williams et al. "Laser intensity scaling of the magnetic field from a laser-driven coil target". In: *Journal of Applied Physics* 127.8 (2020), p. 083302.

[172] A. E. Willner et al. "Optical communications using orbital angular momentum beams". In: *Adv. Opt. Photon.* 7.1 (Mar. 2015), pp. 66–106.

[173] D Wu and J W Wang. "Magetostatic amplifier with tunable maximum by twisted-light plasma interactions". In: *Plasma Physics and Controlled Fusion* 59.9 (Aug. 2017), p. 095010.

[174] Alison M. Yao and Miles J. Padgett. "Orbital angular momentum: origins, behavior and applications". In: *Adv. Opt. Photon.* 3.2 (June 2011), pp. 161–204.

[175] Erik Zeek et al. "Pulse compression by use of deformable mirrors". In: *Opt. Lett.* 24.7 (Apr. 1999), pp. 493–495.

[176] G. Zeraouli et al. "Development of an adjustable Kirkpatrick-Baez microscope for laser driven x-ray sources". In: *Review of Scientific Instruments* 90.6 (2019), p. 063704.

[177] Guo-Bo Zhang et al. "Acceleration and evolution of a hollow electron beam in wakefields driven by a Laguerre-Gaussian laser pulse". In: *Physics of Plasmas* 23.3 (2016), p. 033114.

Appendix A

Single Particle Integration in MATLAB

Ionization and Particle Evolution

To solve the equations of motion of an electron in general electric and magnetic fields that are functions of both space and time, we used an algorithm developed in MATLAB. In this algorithm, we utilize the MATLAB ODE113 function which utilizes a variable-step, variable-order Adams-Bashforth-Moulton solver of orders 1 to 13.

The equations of motion are solved using the relativistic momentum of the particle using normalized values given by, $\boldsymbol{p} = \boldsymbol{p}/\boldsymbol{m_e c}$, $\boldsymbol{v} = \boldsymbol{v}/c$, $\boldsymbol{x} = k\boldsymbol{x}$, $t = \omega t$, $\boldsymbol{E} = e\boldsymbol{E}/m_e c\omega$, and $\boldsymbol{B} = e\boldsymbol{B}/m_e\omega$. This allows us to write the equations in a reduced form as,

$$\gamma = \sqrt{1 + \boldsymbol{p}^2} \tag{A.1}$$

$$\boldsymbol{p} = \boldsymbol{v}/\gamma \tag{A.2}$$

$$\begin{aligned}\frac{d\boldsymbol{p}}{dt} = \left(\boldsymbol{E} + \frac{\boldsymbol{p}}{\gamma} \times \boldsymbol{B}\right) + \alpha \left[\boldsymbol{E} \times \boldsymbol{B} + \boldsymbol{B} \times \left(\boldsymbol{B} \times \frac{\boldsymbol{p}}{\gamma}\right) + \boldsymbol{E}\left(\boldsymbol{E} \cdot \frac{\boldsymbol{p}}{\gamma}\right)\right] - \\ \alpha\gamma\boldsymbol{p}\left[\left(\boldsymbol{E} + \frac{\boldsymbol{p}}{\gamma} \times \boldsymbol{B}\right)^2 - \left(\frac{\boldsymbol{p}}{\gamma} \cdot \boldsymbol{E}\right)^2\right]\end{aligned} \tag{A.3}$$

where,

$$\alpha = \frac{1}{4\pi\epsilon_0}\frac{2e^2\omega}{3c^3 m_e} \tag{A.4}$$

The electric and magnetic fields of the lasers are used from the modified version of

the Erikson-Singh model as described in chapter 3.

Before the motion of the electron can be computed, its initial space-time coordinate is calculated. Each electron is initialized in space either as a free standing electron or as an electron bound to an atom. Typically this is done by assuming some volume and randomly distributing electrons or atoms within the volume, but in theory can be done in any number of ways. If the electrons are ionized from atoms or ions, their position in space and time of where and when they will appear in the laser pulse is calculated using the ionization routine discussed in chapter 3.

Once the initial coordinates of the electron are chosen, the evolution of the electron is computed using the ODE113 function. This is written using MATLAB's parallel processing toolbox to take advantage of multiple processors, and is in theory saleable to super computers. The code outputs for each electron its position and momentum vectors as a function of time in the rest laboratory frame.

Radiation

From the particle motion as a function of time, we are interested in the scattered radiation from the electron - both its power and spectrum in any given direction. We start by specifying a grid in which the radiation will be calculated, the grid is set by a number of grid points N, and a surface area defining the position of each grid point.

The power emitted in any given direction at any given time by the particle is given by [75],

$$\frac{dP(t')}{d\Omega} = \frac{e^2}{16\pi^2\epsilon_0 c}\frac{\left|\boldsymbol{n}\times\left((\boldsymbol{n}-\boldsymbol{\beta})\times\dot{\boldsymbol{\beta}}\right)\right|^2}{(1-\boldsymbol{n}\cdot\boldsymbol{\beta})^5} \tag{A.5}$$

where $\boldsymbol{n}$ is the unit vector between the position of the particle and the detector grid point coordinate. $\boldsymbol{\beta}$ is found directly from the integrator output, and $\dot{\boldsymbol{\beta}}$ is calculated using a first order backward differentiator,

$$\dot{\beta}_i(t_j) \approx \frac{\beta_i(t_j)-\beta_i(t_{j-1})}{t_j - t_{j-1}} \tag{A.6}$$

While a first order differentiator may seem insufficient for the problem, we remark that this estimate is not being used to advance the timesteps in the code, and only used an approximate in the radiation calculation. We also note that given the dynamic steps in the integrator which are finer in areas of where $\dot{\beta}$ is large. Given that Eq.A.5 can all be calculated in the lab frame, we can calculate Eq.A.5 directly from the results

of the integrator. Examples of the radiation emitted from this equation are given in Fig's.3.14,3.15, and 3.16.

Typically, the calculation of power radiated per unit steradian is fast, and can be computed with a resolution of 100x100 pixels reasonably quickly for a single electron ($\approx$ 100 seconds), and so many electrons can be used to calculate the radiation.

The calculation of radiation spectrum is however much more challenging computationally. From Eq.3.96, we find the radiation emitted from the electron over a given time t,

$$\frac{d^2I}{d\lambda d\Omega} = \frac{e^2}{8\pi^2\epsilon_0\lambda^2}\left|\int e^{i2\pi ct/\lambda}\frac{\boldsymbol{n}\times\left[(\boldsymbol{n}-\boldsymbol{\beta})\times\dot{\boldsymbol{\beta}}\right]}{(1-\boldsymbol{\beta}\cdot\boldsymbol{n})^3}dt\right|^2_{ret} \tag{A.7}$$

As discussed in chapter 3, using Eq.3.93 is challenging, despite working in the laboratory frame. We therefore opt to use Eq.A.7, but now have to transform the lab time of the particle to its retarded time. To do this, we interpolate the position of the particle in the lab time with the position of the particle in the retarded time,

$$t_{ret} = interp\left(t' + \frac{R(t')}{c}, t'\right) \tag{A.8}$$

This is done using a constant time step dt such that the maximum frequency resolved can be set according to the Shannon-Nyquist theorem. Fig.A.1 gives a simple relation between the retarded observer time, and the particle time for a highly relativistic electron in circular motion.

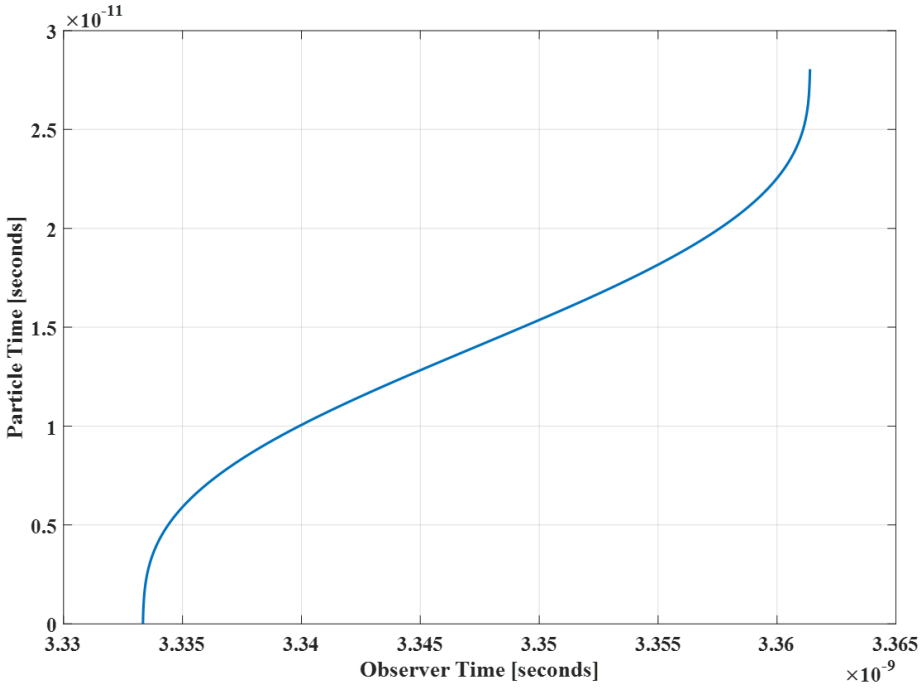

Figure A.1: Particle time as a function of the retarded observer time

By using the retarded time of the particle, we can then interpolate its position and momentum into the retarded time also for calculations. The reason we use the retarded time is that Eq.A.7 is a direct Fourier transform and we can therefore utilize the fast Fourier transform algorithm (FFT). This has proven to be extremely fast and accurate. Calculating the FFT of a typical electron trajectory in a laser field, we find that each grid point takes on the order of 20 seconds to compute per electron. While not as fast as the power calculation, we remark that this is still very fast and accurate typically up to 100nm wavelengths. Beyond this, the FFT takes longer to compute (scales as $\mathcal{O}(NlogN)$).

Visualizing the accuracy of the FFT, we find that it is accurate all the way up to the 17th laser harmonic for a simple electron oscillating in a relativistic laser pulse. This is shown in Fig.A.2. This also indicates the dynamic range of the FFT which in this particular case is roughly 8 orders of magnitude.

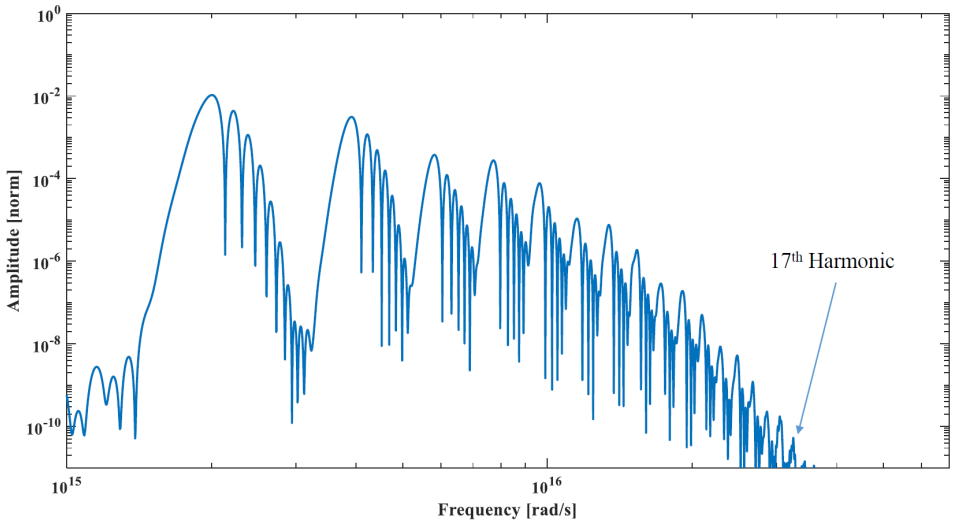

Figure A.2: Frequency spectrum emitted from a single electron in a relativistic laser pulse. The first harmonic is the peak on the left.

A separate package for visualizing the data was also written using MATLAB. This was able to run locally given the output files from the electrons were typically small as certain values were averaged over the ensemble.

Appendix B

Particle in Cell (PIC) Codes

The particle-in-cell (PIC) method is a powerful tool for modelling laser-plasma interactions, particularly in regions where the density is close to or less than the critical density. Given the complexity of PIC codes, and the need for optimized programming, we opt to use the already available open source code EPOCH developed by the team at the University of Warwick in the UK [8].

The PIC code basically works by the discretization of space into a grid at which the electric and magnetic fields are computed at each grid point using the finite difference time domain solver, although some new PIC codes take advantage of spectral solutions [89]. The current density at each point is computed from electrons and ions on the grid, from which the electric and magnetic fields can also be computed. The electrons and ions are free to move about the grid under the constraints of the electric and magnetic fields at each point they pass. It is important that the electrons and ions interact with each grid point they pass, otherwise the solutions become non-physical and so the timestep of the simulation is usually determined via the Courant-Friedrichs-Lewy condition [33].

Due to the density of plasmas typically being high ($> 10^{16} cm^{-3}$), we find that it is often too computationally expensive to represent electrons and ions as individual particles. Instead, they are typically weighted into macro-particles that represent 10000 or so real particles. These macro particles maintain the same charge-mass ratio and as thus, their dynamics in the Lorentz force is unchanged. Things get more complicated however when calculating the effects of radiation reaction which scales as e^2/m_e.

Physics can be turned on or off for various needs, usually at the cost of compu-

tational time. Often we use ionization routines to model ionization injection into the wakefield, or if the plasma is sufficiently dense, we may want to enable collisions. These additional physics packages usually add great complexity to the code, requiring many hours of work to ensure they are properly implemented.

Injection of a laser field into the simulation can be done in many ways, of which EPOCH utilizes an antenna model for the generation of EM waves into the simulation and so laser parameters must be specified on the boundary condition. This can become complicated for Laguerre-Gaussian modes due to the helical phase, and as such, a custom version of EPOCH was written in which I implement new diagnostic functions (field angular momentum, and particle angular momentum diagnostics), and new math functions ($atan2$).

In addition, the outputting of data, and visualization of data can be cumbersome given the multi terabyte files the are written in 3D simulations. The majority of visualization was performed using the VisIt package developed at LLNL [30]. For more detailed plots, the EPOCH output was down-sampled and visualized using custom MATLAB routines.

While we do not review the details of PIC codes here, we instead summarize the parameters used for the simulations in this thesis. Further details on the EPOCH code can be found in the user and developers manuals [8].

Self focussing and inverse Faraday simulations

For these simulations, we opted to use a longer, narrower box that resolved the Debye length. Most physics was switched off including ionization and collision routines. A moving window was employed to track the laser pulse, but was stopped at 850fs - the time at which the magnetic field generated was most collimated and cylindrical. After this time the laser was found to diffract and filament in the simulation such that no magnetic field was generated.

The output of the simulation was typically divided into two files, the first of which contained all the axial magnetic field information. This was then down-sampled using MATLAB and then visualized. The other output contained information on the absorption, angular momentum, and current densities in the plasma.

Some example simulation parameters are given below in Table B.1. Parameters not mentioned here are given in the main text in Tables 4.1 and 7.1.

Table B.1: Simulation parameters used for self focussing and the inverse Faraday effect.

Parameter	Value
n_x, n_y, n_z	$4000, 500, 500$
n_{part}	$2 * n_x * n_y * n_z$
Field Ionization	F
T_{end}	$2.5ps$
x, y, z $[\mu m]$	$150, 40, 40$
Solver	Second Order Maxwell
Boundaries	Open
Species 1,fraction	Electrons,2/3
Species 2,fraction	Helium 2+,1/3

Wakefield acceleration simulations

In the wakefield simulations, a slightly different setup was used. We opted for a shorter box as the laser pulse was a third of the duration of that in the previous simulations. We opted for field ionization to be switched on allowing for the ionization injection of nitrogen 5,6, and 7 electrons into the wakefield simulations. In addition, the EPOCH quantum electrodynamics package was turned on allowing for high energy photon emission from electron oscillations.

To account for direct laser acceleration of electrons, the field solver in EPOCH was switched to use the Lehe solver [89], in which the magnetic field is interpolated onto particle position. It was shown previously that not accounting for this magnetic field interpolation, electron energies can be over estimated [137].

The outputs used in this simulation featured a detector plane at the end of the super-Gaussian plasma distribution which registered electrons with energies greater than $1MeV$, and X-ray photons generated from the betatron. The detector recorded both the ejected position of the particle, and its corresponding momentum. A second output recorded the time history of electron position and momentum every femtosecond for electrons with energy greater than $50MeV$. Additionally, the electron density, field information, and angular momentum information was also captured at 30fs time intervals.

Some example simulation parameters are given below in Table B.2. Parameters not mentioned here are given in the main text in Table 6.1.

Table B.2: Simulation parameters used for wakefield acceleration.

Parameter	Value
n_x, n_y, n_z	$4000, 500, 500$
n_{part}	$2 * n_x * n_y * n_z$
Field Ionization	T
T_{end}	$2.75ps$
x, y, z $[\mu m]$	$100, 50, 50$
Solver	Lehe, 0.96 dt multiplier
Boundaries	Open
Species 1,fraction	electrons,101/151
Species 2,fraction	Helium 2+,99/302
Species 3,fraction	Nitrogen 4+,1/302
Species 4,fraction	Ionizable Electrons,0
Species 5,fraction	QED Photons,0
QED, Radiation Reaction	T, T
QED Start time	$100fs$

Appendix C

Manufacturing Techniques of an OASPM

Several prototype OASPM's were manufactured at the University of Alberta's nanoFAB centre using electron-beam evaporation techniques. Originally, sputtering deposition was used but it was later found that this was not suitable as the sputtering process is not directional enough leading to bleeding under manufacturing mask edges.

Using the electron-beam evaporation method, the spiral staircase is built up in layers by using a set of masks. To first order, if we have 16 steps in our staircase, we would think that we would need 16 masks to build the staircase. However, using a method similar to that in Sueda [151], a 16 step staircase can be constructed using as few as 5 deposition layers. To illustrate this, we show 5 example masks used to construct a 16 step staircase in Fig. C.1.

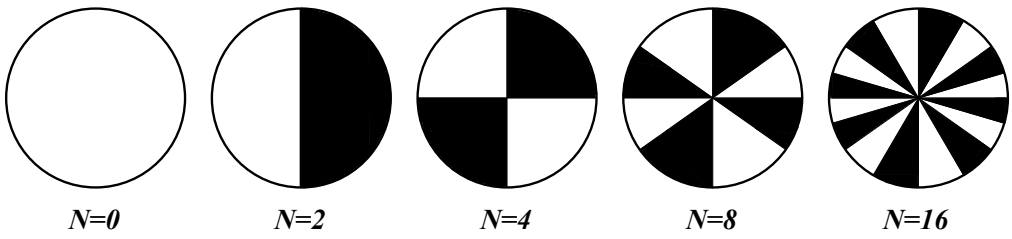

Figure C.1: Consecutive mask layers for manufacturing a 16 step OASPM.

The process occurs in 5 stages from left to right in Fig.C.1. The first layer, namely $N = 0$ is used to create a highly reflective surface across the mirror substrate to ensure

a good reflectivity throughout, however this may not be necessary depending on the substrate. Through our development, two substrates were used, the first was a 2 inch Thorlabs unprotected gold mirror with flatness $\lambda/10$ (PF20-03-M03). As the mirror was pre-coated with a thick layer of gold, it was unnecessary to deposit the $N = 0$ layer. The second substrate was a 5 inch CVI mirror blank with $\lambda/10$ flatness. As this mirror blank was un-coated, a 25nm layer of titanium was first deposited onto the substrate as an adhesion layer, followed by approximately 200nm of gold. It is important that the thickness of gold deposited is many times the thickness of the optical penetration depth of gold at the laser wavelength.

The optical penetration depth δ_p through a material can be calculated by the Beer-Lambert law [49],

$$I(z) = I_0 e^{-z/\delta_p} \tag{C.1}$$

where $I(z)$ is the intensity of the laser after propagating a distance z through the material, and initial intensity I_0. The optical penetration depth is related to the wavelength of the laser and the complex index of refraction κ of the material by,

$$\delta_p = \frac{\lambda}{4\pi\kappa} \tag{C.2}$$

For gold at 800nm, we find $\kappa = 4.705$ [127], thus the penetration depth is approximately $13.5nm$. Coating the mirror with $200nm$ as a base layer ensures that the mirror is then only limited by the reflectivity of gold at 800nm ($R = 96.8\%$).

The second mask labelled $N = 2$ in Fig.C.1, creates the first 2 steps on the OASPM. The deposition thickness of gold on this mask is computed from Eq.5.22 using $N = 2$. For instance, if we are using an 800nm laser, with an incidence angle of 45° and a topological charge of $L = 1$, we find that the first mask thickness needs to be 282.8nm. If we were to use a higher topological charge, this mask would not be necessary. We find that the masks are only necessary if $L < N$ for each mask.

As previously found, it is not necessary for the deposition thickness to be exact and the tolerance in this deposition is on the order of 1%. However, if a high precision deposition can be made onto the substrate, then this is preferable as it will minimize any asymmetry in the focal spot. To monitor the deposition thickness of gold during electron beam evaporation, a piezo crystal monitor was used and calibrated using a Zygo white-light profilometer.

Subsequent mask layers are added including the $N = 4, 8, 16$ masks, with depo-

sition thicknesses (for an 800nm, $L = 1, \theta_i = 45°$) beam as 141.4nm, 70.7nm, and 35.4nm respectively. One issue with the masks was found that as the number of steps increases, the inside angle of the mask becomes sharper. This is problematic as it becomes difficult to manufacture small angles in the masks. The masks used were cut from aluminum sheet using a CNC waterjet with a kerf of approximately 1mm. To overcome this restraint, for the $N = 8, 16$ masks, two masks were aligned on top of each other, each with half the mask spokes missing at the centre. This is illustrated in Fig.C.2.

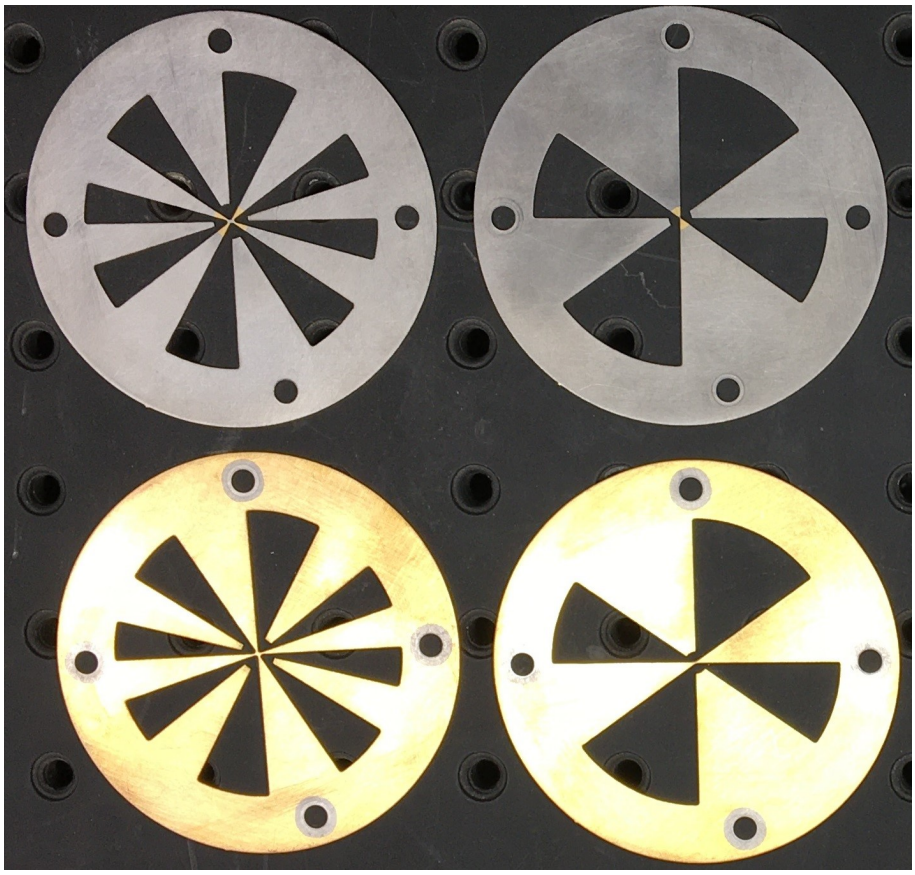

Figure C.2: Pairs of $N = 8, 16$ masks for a 2" OASPM. Note half the spokes have been removed on each mask. Overlapping the masks produces a high quality mask close to axis.

For the masks to line up correctly, the masks are aligned using the holes at the outer edge. Tight fitting screws hold the masks to the substrate holder roughly

$500\mu m$ above the substrate surface. One of the holes is offset such to key the masks orientation so they are always correctly aligned. These offset holes are the lower alignment holes in Fig.C.2. Flipping the masks upside down allows the use to create either $\ell = +$ or $\ell = -$ masks depending on the orientation.

2 inch prototype OASPM's were manufactured for use at 45° for 632, 800 and 1030nm beams - the primary wavelengths used in the university laboratory and all manufactured with $N = 16$. The masks used to generate these OASPM's are shown in Fig.C.3 and were cut from 1/16" aluminum sheet.

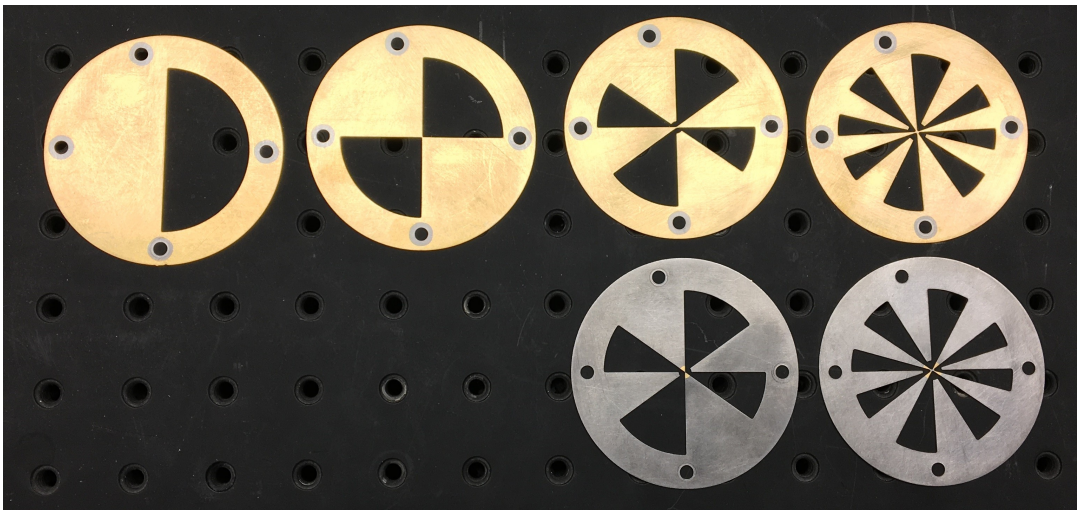

Figure C.3: Aluminum masks for 2" OASPM manufacturing. The masks have been CNC waterjet cut from 1/16" aluminum sheet.

The substrate is mounted in an aluminum holder and held upside down above the electron beam evaporator. It is centred above the gold crucible using a custom machined plate as shown in Fig.C.4 to ensure that the deposited gold is isotropic and does not cause asymmetric bleeding under the mask edges. From the figure, it is also possible to see the key-holes for selecting positive or negative topology on the OASPM.

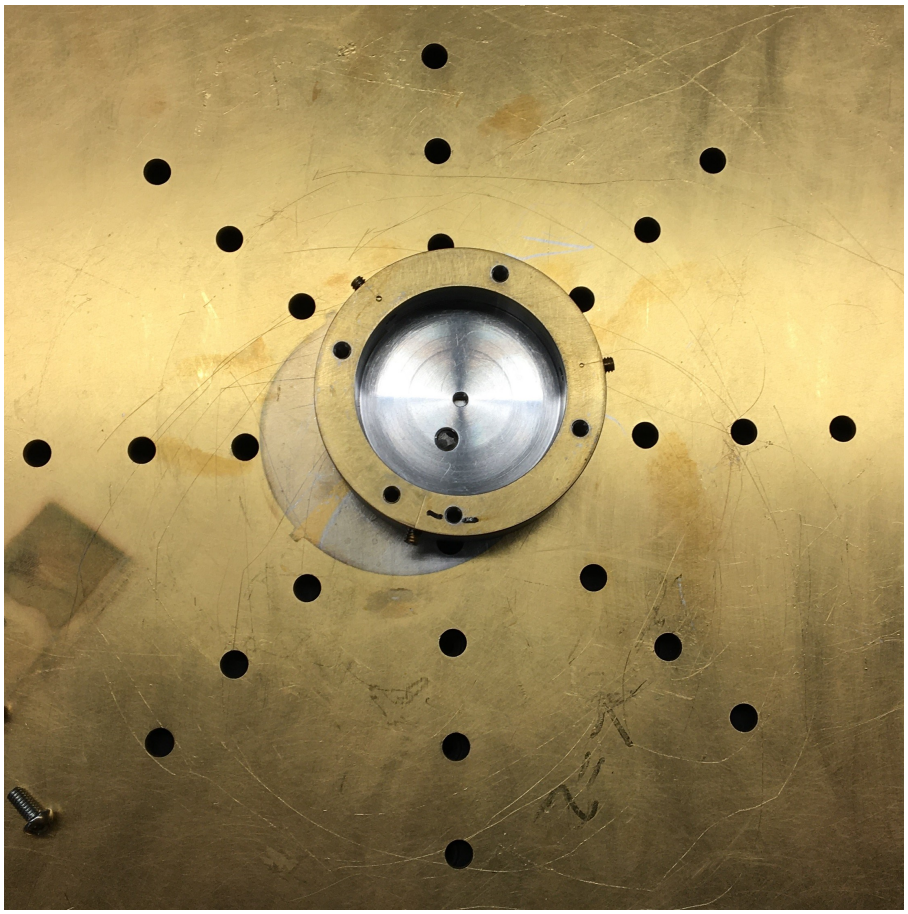

Figure C.4: Substrate holder with keyed holes, mounted on a centering plate for the Gomez electron beam evaporation system at the University of Alberta nanoFAB.

Larger 5" OASPM's were manufactured for use in the CLPU VEGA2 laser beam line. These masks were machined from thicker 1/8" aluminum sheet and were designed for an incidence angle of 17.8° beamline mirror in the laser system. The masks are shown in Fig.C.5 where it is possible to see the change in sector angle.

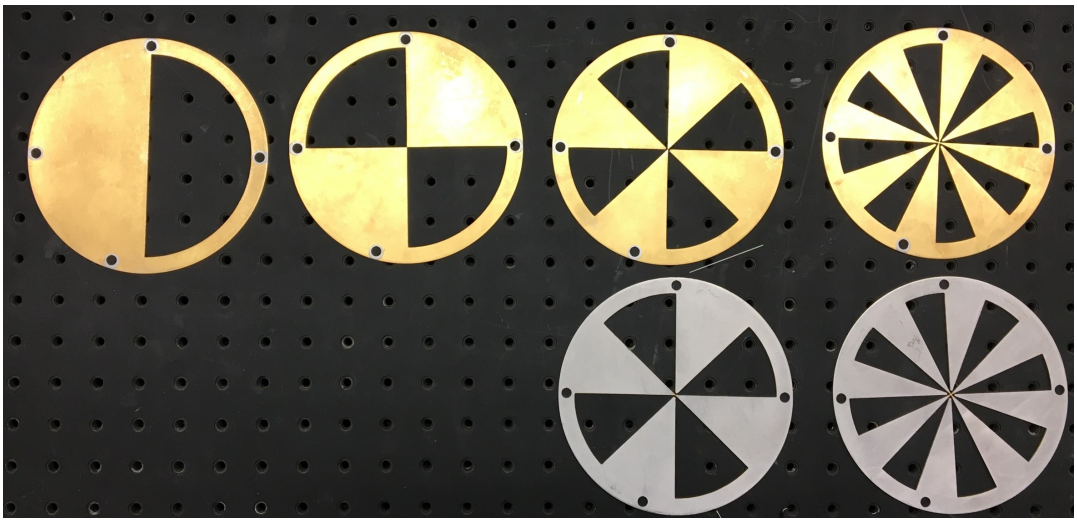

Figure C.5: Aluminum masks for 5” OASPM manufacturing. The masks have been CNC waterjet cut from 1/8” aluminum sheet.

The OASPM’s were manufactured using the University of Alberta’s nanoFAB electron beam evaporator named Gomez. Given the design and size of Gomez, we were essentially limited in manufacturing capabilities to mirrors of 5” or less. Fabrication of larger mirrors would require a larger machine and could likely be commissioned to a commercial manufacturer. The 5” mirrors were sufficient for use in the VEGA2 laser at CLPU, but would not be suitable for beams larger than 4” in diameter. An additional limitation of Gomez is the anisotropy in deposition thickness, and it was found via profilometry that the deposition thickness was approximately 5nm less than that deposited in the centre of the mirror. This is however within the tolerances of the of the calculations performed in the previous section, and will likely lead instead to a slight defocussing in the beam leading to a change in the focal spot location.

To verify the step deposition height and shape, a Zygo optical profilometer was used to images the centre of the staircase and also at select positions along the step edges. The field of view of the profilometer was limited to approximately 2mm x 2mm, and so many images were taken to sample and measure the deposition thickness and standard deviation. An image of the centre of an $L = -1$ OASPM designed for a 632nm beam at 45° taken using the Zygo is given in Fig.C.6. From this image, the spiral staircase is clear, Although it is also clear to see the error in the placement, and bleeding under the masks causing some unclean edges.

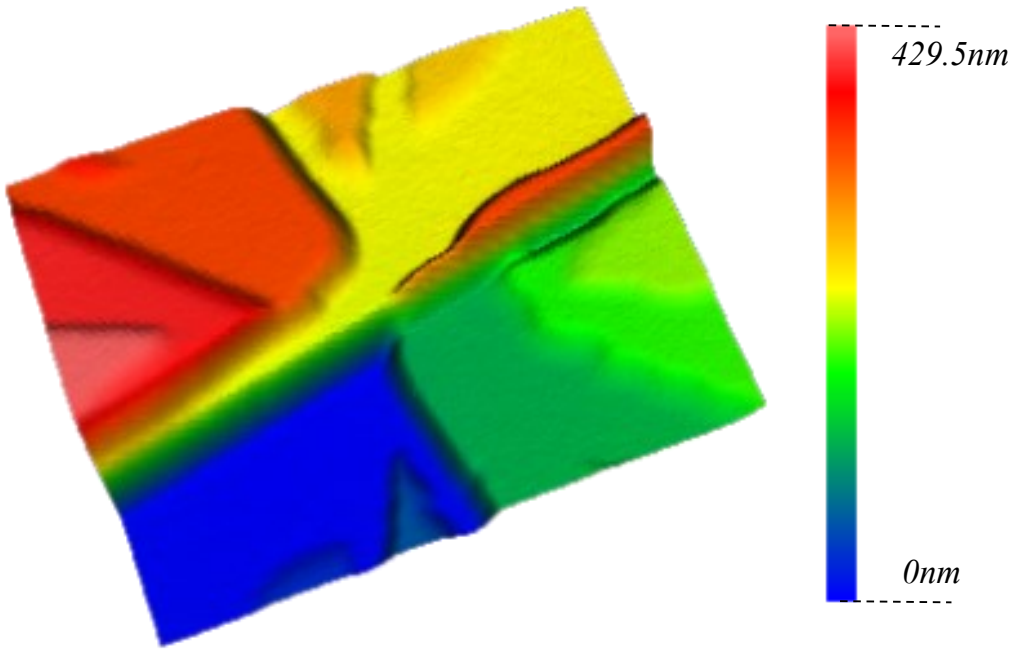

Figure C.6: 3D image of the centre of an $L = -1$, 632nm, $\theta_i = 45°$ OASPM taken on a Zygo optical profilometer. The spatial size of the sample is 2mm x 2mm

Here we find that the step edge width is on the order of $100\mu m$ with values up to $200\mu m$ have been observed as a result of two sources of error. The first source of error comes from bleeding under the mask edge, but given the distance between the gold crucible and the mask ($\approx 1m$), and the mask-mirror gap to be $500\mu m$, we find that in a worst case the gold will bleed approximately $35\mu m$ under the mask.

The second source of edge width comes from uncertainty in the placement of successive masks. This is clear in Fig.C.7 a) where the step edge in blue is found to be approximately $200\mu m$ across as shown in tile b). There were no precision alignment pins used in holding the masks and instead we relied on tight-fitting screws to centre the masks. This seems to be accurate to roughly $100\mu m$, but is certainly the largest source of step edge width and would be a trivial improvement to the manufacturing method in the near future.

A cross section of Fig.C.7 a) is highlighted by the diagonal line in the tile and is given in tile b). The blue and orange dashed orange lines are used for inspecting step edge heights in the Zygo software. Here we find the height between the orange and the green step to be approximately 26nm, and the calculated value from Eq.5.22 is found to be approximately 28nm. This discrepancy leads to a 7% error in the

deposition thickness in this particular instance. According to Fig.5.7, this will lead to a 2% reduction in the $\ell = -1, p = 0$ mode at focus.

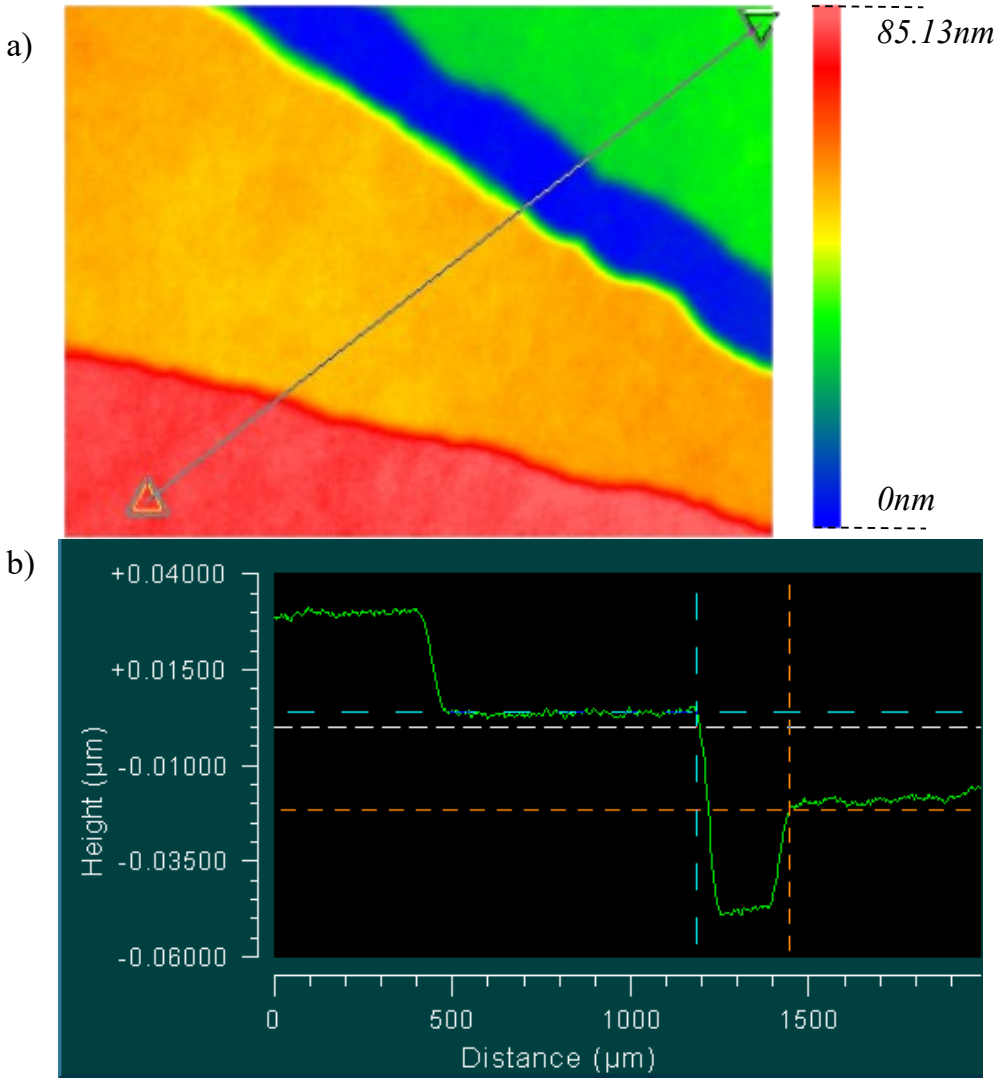

Figure C.7: a) top-down view of a segment of an $L = -1$, 632nm, $\theta_i = 45°$ OASPM highlighting an mask edge misalignment in blue. b) Cross section of a) through the diagonal line on the image. The spatial size of the sample is 2mm x 2mm

Appendix D

Determining Critical X-ray Energy from a Stepped Filter

In determining the critical x-ray energy from the betatron radiation, we employed a step filter as described in chapter 6 and Fig.6.13. To do this, we used the expected betatron spectrum as a function of critical energy,

$$\frac{dI}{dE} \propto \frac{E}{E_c} \int_{E/E_c}^{\infty} K_{5/3}(x)dx \tag{D.1}$$

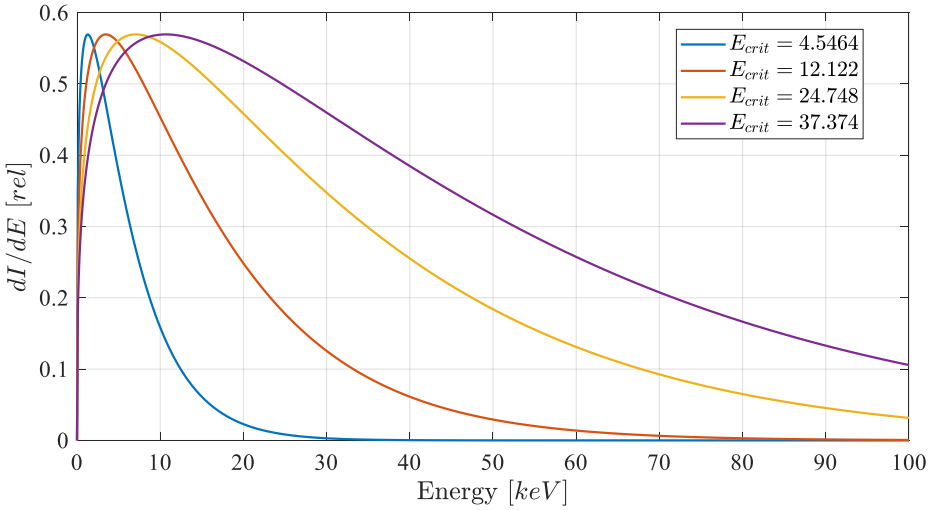

Figure D.1: Betatron energy spectras for various critical energies. Values of the critical energies in the legend are given in keV.

Some example betatron spectras given for various critical energies are given in Fig.D.1. Here we see a clear shift in the peak of the curve as a function of the critical energy.

It is possible to use the shift in spectra to estimate the critical energy using stepped filters. To do this, we first determine what the spectra will look like through different aluminum filters of varying thickness. As the absorption of x-ray photons changes depending on the energy of the photon, the ratio of the transmissions for each thickness of aluminum will change.

For instance, if we integrate over the spectra with no attenuation, and also with a $25\mu m$ aluminum filter in front, we find the ratio of the two values changes as a function of critical energy,

$$R = \frac{\int \frac{dI}{dE}(25\mu m)\, dE}{\int \frac{dI}{dE}(0\mu m)\, dE} \tag{D.2}$$

For example, if the critical energy is $10keV$, then the value of R is found to be 0.131. If the value of E_{crit} is increased to $12.5keV$, then the ratio decreases to 0.126, and 0.122 for $E_{crit} = 15keV$. Using this approach, we can estimate the ratios for multiple channels to a reference channel. According to Fig.6.13, the thinnest reference channel is the $25\mu m$ aluminum with $4\mu m$ of mylar.

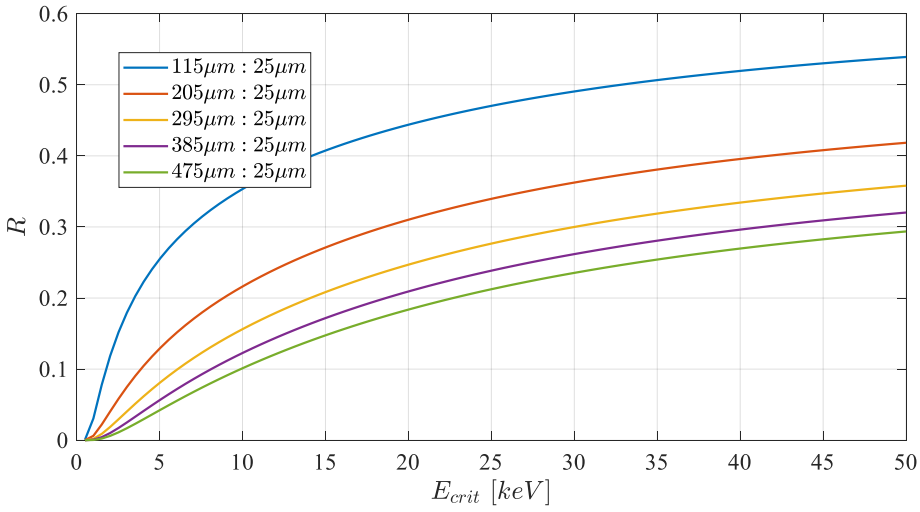

Figure D.2: Ratios of integrated spectrums with transmission filters given in the legend.

The ratios of the total integrated spectrums convolved with different thickness aluminum filters is given in Fig.D.2. The ratios are all taken with respect to $25\mu m$ aluminum and a $4\mu m$ mylar layer. To get these spectra ratios experimentally, we find the average number of counts in each channel, and find the ratios between each of the channels. This is performed after any background gradient or noise is removed from the image.

Once the ratios of several channels (typically three) are found from the experimental data, they are fit to the curves in Fig.D.2 using a least squares analysis. From this we can determine the critical energy of the shot, or averaged set of shots.

After estimating the critical energy of the shot, it is possible to estimate the peak number of photons per 0.1% bandwidth, per unit steradian. After some algebra and incorporating the solid angle of the pixel of the x-ray CCD, we are able to estimate the betatron brightness from the formula,

$$\frac{photons}{0.1\%BW/srad} \approx \frac{\langle C_i \rangle}{75455.75 E_{crit}(keV) R_i} \tag{D.3}$$

where C_i is the count value in a given channel, and R_i is the ratio of the counts in that channel to the full unattenuated spectrum.